Faculté des Sciences Appliquées
Génie Civil et Géologie
Département de Mécanique des matériaux et Structures
Secteur Mécanique des Solides et des Matériaux

Development of Experimental Equipment and Identification Procedures for Sheet Metal Constitutive Laws

PhD Thesis presented by Paulo FLORES
to obtain the degree of
"Docteur en Sciences Appliquées"

November 2005

M & S – BAT. B 52 / 3 – Chemin des Chevreuils, 1. B-4000 Liège 1 (Belgique)
Email : Paulo.Flores@ulg.ac.be

Author's coordinates:
Ir. Paulo FLORES
University of Liege
M&S Department (Mechanics of Materials and Structures), Building B52/3
Chemin des Chevreuils 1
4000 Liege
Belgium
Office phone: +32 (0) 4 366 9523
Secretary phone: +32 (0) 4 366 9260
Fax: +32 (0) 4 366 9192
E-mail: Paulo.Flores@ulg.ac.be

Supervisor's coordinates:
Dr. Anne-Marie HABRAKEN
Senior Research Associated (FNRS)
ESAFORM President (http://www.esaform.ulg.ac.be)
Co-responsible of the MSM team of the M&S Department
University of Liege
M&S Department (Mechanics of Materials and Structures), Building B52/3
Chemin des Chevreuils 1
4000 Liege
Belgium
Office phone: +32 (0) 4 366 9430
Secretary phone: +32 (0) 4 366 9260
Fax: +32 (0) 4 366 9192
E-mail: Anne.Habraken@ulg.ac.be

JURY MEMBERS

Jean-Philippe Ponthot (Président du jury)
Chargé de cours adjoint, University of Liege, ASMA/LTAS Department
Chemin des Chevreuils 1, 4000 Liège
Belgium

Anne-Marie Habraken (Supervisor),
Senior Research Associate FNRS, University of Liege, M&S Department
Chemin des Chevreuils 1, 4000 Liège
Belgium

Salima Bouvier
Maître de conferences, University of Paris 13, LPMTM-CNRS
99 Avenue J.B. Clément, 93430 Villetaneuse
France

Serge Cescotto
Professor, University of Liege, M&S Department
Chemin des Chevreuils 1, 4000 Liège
Belgium

Han Huétink
Professor, University of Twente, Faculty of Engineering Technology
P. O. Box 217, 7500 AE Enschede
The Netherlands

Jacqueline Lecomte-Beckers
Professor, University of Liege, ASMA/Metallurgy and Material Science Department
Chemin des Chevreuils 1, 4000 Liège
Belgium

Xavier Lemoine
Dr. Ir. ARCELOR – Research
Voie Romaine BP 30320, 57283 Maizière-les-Metz
France

ACKNOWLEDGEMENTS

The author of the present work would like to thank:

Dr. Ir. Anne-Marie Habraken for her guidance, encouragement, and critical comments during this work;

The M&S Laboratory staff, especially Etienne Rondia, for sharing his time and knowledge during the development phase of the experimental equipment on which this thesis is based;

Pierre de Montleau, Vincent Mathonet, Laurent Duchêne, Anne-Françoise Gerday, and Thomas Lelotte for their collaboration in the numerical aspects;

The Région Wallonne for the economical support, through the projects PROMETA (RW n°01/1/4710) and PROINDU (RW n°4543b), that made possible the development of this thesis;

Arcelor – RDCS, especially Paul Wouters and Richard Kergen, for providing the materials required to carry out this research;

J.-P. Ponthot, J. Lecomte-Beckers, S. Cescotto, X. Lemoine, S. Bouvier, and H. Huétink for taking part in my public defense and for the time they spent in reading this work;

Ellen Harry for her advises in the manuscript corrections;

The members of the M&S department, especially Catherine Doneux, Christian Perez, Frédéric Pascon, Christophe Henrard, Jean-François Demonceau and Lam Ly, for their support.

SYMBOLS AND ABBREVIATIONS

MATHEMATICAL OPERATORS

$\otimes$	tensor product
:	double contraction
$\lvert \bullet \rvert$	norm of a tensor
$(\ )^T$	transpose of a tensor
det ( )	determinant of a tensor
$(\ )^{-1}$	inverse of a tensor
tr ( )	trace of a tensor
dev ( )	deviatoric part of a tensor
$\overset{\circ}{(\ )}$	Jaumann operator
$\dot{(\ )}$	time derivative
$\bullet\vert_i$	tensor refer to a particular axis i
exp ( )	exponential
ln ( )	natural logarithm
grad ( )	gradient

ABBREVIATIONS

bcc	body-centered cubic
fcc	face-centered cubic
ave	average
exp	experimental
theo	theoretical
BI	bi-axial
GL	Green-Lagrange
PS	plane strain
SH	pure shear
SSH	simple shear
UN	uni-axial
FE	finite elements
IF	interstitial free
ND	normal direction
RD	rolling direction
TD	transversal direction

LATIN CHARACTERS

k	anisotropy parameter
a	Hosford 1979 and Barlat 1991 material parameter
b	specimen dimension
c	Barlat 1991 material parameter
	Prager material parameter
	Armstrong-Frederick material parameter
d	derivative
e	elastic (upper-index)
ep	elasto-plastic (upper-index)
f	
g	Teodosiu and Hu hardening function
h	Teodosiu and Hu hardening function
	specimen dimension
i	sub-index
j	sub-index
k	sub-index
	hardening internal variable
l	sub-index
m	Teodosiu and Hu material parameter
n	exponent, Swift hardening law material parameter
n_L	Teodosiu and Hu material parameter
n_P	Teodosiu and Hu material parameter
o	
p	plastic (upper-index)
	equivalent plastic strain
q	Teodosiu and Hu material parameter
r	Teodosiu and Hu material parameter
	Lankford coefficient
	ratio between two stresses or strains
$\bar{r}$	coefficient of normal anisotropy
Πr	degree of planar anisotropy
s	surface in the current configuration
	Armstrong-Frederick material parameter
t	time
	specimen dimension (thickness)
	tensile (as upper-index)
u	ultimate (as sub-index)
d	rate of deformation
e	orthonormal Cartesian coordinate system
f	resultant force
l	velocity gradient
n	derivate of the yield function with respect to the stress tensor
s	deviatoric stress tensor
t	Cauchy traction vector
u	vector in the Euclidian space

v	left (or spatial) stretch tensor (also used as a vector in the Euclidian space)
w	spin tensor
x	coordinate in the current configuration
n	normal vector in the current configuration
u	current description of displacement field
v	current velocity field
F	yield surface
H	Teodosiu and Hu function
A	area
C_P	hardening material parameter
C_R	hardening material parameter
C_{SD}	hardening material parameter
C_{SL}	hardening material parameter
C_X	hardening material parameter
E	elastic modulus
F	Hill 1948 and Hosford 1979 material parameter
G	Hill 1948 and Hosford 1979 material parameter
H	Hill 1948 and Hosford 1979 material parameter
J	jacobian
K	Swift law hardening material parameter
L	Hill 1948 material parameter
M	Hill 1948 material parameter
N	Hill 1948 material parameter
P_D	Teodosiu and Hu variable
Q	plastic potential function
R	hardening internal variable
R_0	hardening material parameter
R_{SAT}	hardening material parameter
S	surface in the reference configuration
S_D	Teodosiu and Hu variable (strength associated with dislocations of the currently active slip systems)
S_{SAT}	hardening material parameter
W	work
X_{SAT0}	hardening material parameter
Z	$\lvert\mathbf{S}_L\rvert$
A	second order tensor
B	second order tensor
C	forth-order compliance tensor
F	deformation gradient tensor
H	fourth-order tensor defining the anisotropy
I	identity tensor
L	linear operator
N	current direction of the strain-rate tensor
P	first Piola – Kirchhoff stress tensor
	Teodosiu and Hu internal variable

R	rotation tensor
S	forth-order tensor
	Teodosiu and Hu internal variable
$\mathbf{S}_L$	forth-order tensor strength associated with the latent part of the persistent dislocation structures
T	Piola-Kirchhoff traction vector
U	right (or material) stretch tensor
X	coordinate in the reference configuration
	back-stress
	Teodosiu and Hu internal variable
N	normal vector in the reference configuration
U	description of displacement field of a typical particle with respect to the reference configuration

GREEK CHARACTERS

α	angle with respect to the rolling direction
β	Schmitt parameter
∂	partial derivative
γ	shear strain
Γ	principal strains
Π	hardening function
	shear stress
ν	Poisson's coefficient
$\bar{\sigma}$	equivalent stress
$\dot{\Gamma}$	plastic multiplier
Γ^0	hardening material parameter
φ	error function
ε	strain tensor
σ	Cauchy stress tensor

CONTENTS

DEVELOPMENT OF EXPERIMENTAL EQUIPMENT AND IDENTIFICATION PROCEDURES FOR SHEET METAL COSNTITUTIVE LAWS

CHAPTER 1

INTRODUCTION

1.1 General frame

Nowadays, the industrial requirements (e. g., aerospace, car manufacturing and food industries) for lighter parts with high mechanical resistance and, at the same time, high geometrical accuracy, have motivated the study of metals such as high-strength steel and aluminum alloys, along with their appropriate forming processes.
Naturally, the accuracy and quality of the final mechanical parts depend on manufacturing process and material characteristics. The major problems found during the process are, for instance, the number of steps needed in order to obtain the desired shape, the shape of the tools, the displacements and loads associated with the tools and their evolution over time, the material of the tools and the lubrication conditions. Concerning the material, the following variables may also affect the final result: the thickness of the sheet, the material anisotropy and the material plastic properties, namely yield limit, hardening and ductility (Knockaert, 2001).
Additional problems, such as springback, wrinkles and earing behavior, appear as a result of material characteristics.
To avoid these problems, it is necessary to develop a constitutive model for plastic behavior able to predict those phenomena.

To describe the plastic behavior of a material in a general stress state, three elements are needed (Banabic et al., 2000):

- A yield criterion expressing a relationship between the stress components when plastic "yielding" appears;
- An associated flow rule expressing the relationship between the components of the strain rate and stress;
- A hardening rule describing the evolution of the initial yield stress during the forming process.

In general, the yield function may be defined in two different ways:

- By assuming that plastic yield begins when some physical quantity (energy, stress, etc.) attains a critical value. These values are obtained from a calculation based on the crystallographic structure of the material.
- By approximating experimental data using an analytical function (phenomenological description).

A description of a texture-based anisotropic yield locus has been proposed by MTM of K.U. Leuven. This team has developed texture models in strain rate and stress space (Van Bael, 1994, Winters, 1996, Hoferlin 2001, Peeters et al., 2001a), which render the description of initial yield locus possible. Their methods are based on texture measurements by X-Ray diffraction thereby avoiding the performance of several mechanical tests needed to identify the initial yield locus.

The phenomenological yield locus models can be divided into isotropic and anisotropic.
The isotropic models, such as Von Mises and Tresca, require only one material parameter, while anisotropic models can be divided into quadratic and non-quadratic. Hill 1948 belongs to the first group, while Hill 1979, 1990 and 1993, Barlat 1989, 1991 and 1997 and Vegter 1998, to the second one. There are also some yield criteria expressed in polar coordinates (for details, see Habraken, 2001 or Banabic et al., 2000).
In practice, the choice of a yield criterion depends on the material, the experimental constraints, the required accuracy and the FEM code used.
Concerning the materials, it is known that Von Mises and Tresca constitutive laws model quite well ductile isotropic metals, while Hill 1948 is well-adapted for laminated steel and bars, although it cannot describe the plastic behavior of some aluminum alloys. Non-quadratic functions, for their part, can describe a wider range of metals (Banabic et al., 2000).
In Habraken, 2001 and Banabic et al., 2000, the required identification tests are indicated for each of the yield functions mentioned above. The material parameters of these laws can be found using yield stress or Lankford coefficients (Chapter 5).

The evolution of the size and position of this yield locus during the process is defined by macroscopic hardening laws that can be either phenomenological (isotropic and/or kinematic) or those with strong links to microscopic phenomena. Such models generally neglect the geometric (textural) hardening, i.e. the yield locus shape evolution. In some cases, this phenomenon is rather negligible, so using an accurate description of the initial yield locus together with elaborate hardening models yields a high level accuracy at low CPU cost.

A good validation of the constitutive laws used in these simulations is the deep-drawing of a cylindrical cup, because the stress states encountered in the different parts of the blank involve a wide region, extending from uni-axial compression at the edge of the flange to equi-bi-axial tension under the flat part of the punch (Moreira et al., 2000).

The following example, developed by Yoon et al., 2000, shows the importance of an accurate definition of initial yield locus regarding the final results.
In most numerical analyses of sheet metal forming processes, the yield surface is assumed to possess a point-symmetry with respect to the center such that a stress state and its reverse state have the same absolute value. However, the 2090-T3 aluminum alloy does not present this symmetry.
This sheet sample is modeled using Barlat 1996 yield surface (with and without initial yield surface translation) and an isotropic hardening law. No further translation (kinematic hardening) of the yield locus is used in these simulations. Earing formation during a cup drawing test is simulated using FEM and the results are then compared with the experiments.
For example, in Figure 1.1 the measured cup height profile is compared to the predicted cup height profiles. Substantial improvement was achieved with the translated yield surface. The present work indicates that the gain in accuracy obtained in the cup height profile with the translated yield surface appears to be small but is not negligible. Indeed, in the rigid-

packaging industry, this amount of change in the cup height profile is very significant (Yoon et al., 2000).

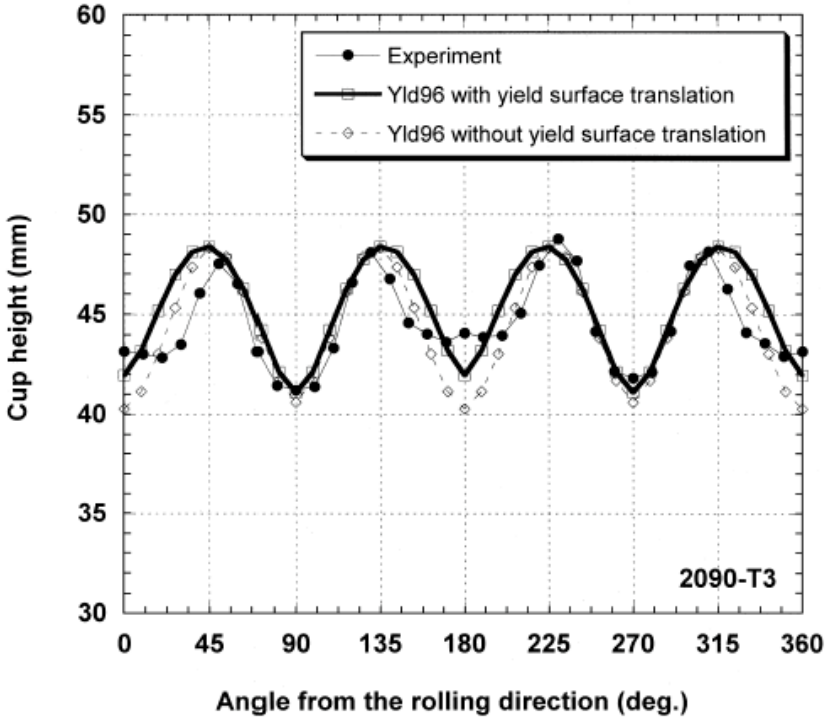

Figure 1.1 Comparison of predicted and measured cup heights: results based on Barlat 1996 yield function with and without yield surface translation for Al 2090-T3. Yoon et al., 2000.

The second example is drawn from Li et al., 2003. A cup drawing test over an interstitial-free (IF) steel sheet of 0,8 mm thickness is performed. The experimental results are compared with four constitutive laws:

- Von – Iso: Von Mises yield function + Swift type isotropic hardening description.
- Von – Mic: Von Mises yield function + Teodosiu and Hu microstructure-based hardening law.
- Tex – Iso: Texture yield function (strain-rate space) + Swift type isotropic hardening description.
- Tex – Mic: Texture yield function (strain-rate space) + Teodosiu microstructure-based hardening law.

The results can be seen in Figure 1.2. The conclusions according to Li et al., 2003 are the following:

- Tex-Mic and Tex-Iso models, although in the experiment the ear at 0° is slightly higher than that at 90°, the predictions show almost equal ear heights in both directions.
- Obviously, the two models based on the Von Mises yield criterion do not predict the earing behavior.
- The cup height is underestimated in all the predictions, indicating that the friction coefficient, as employed in the present simulations, is too low. Nevertheless, it is also interesting to see that the cup heights as predicted by the Tex-Iso and Tex-Mic models are closer to the experimental height than those using the Von Mises criterion.

- This indicates that the consideration of texture is necessary not only for capturing the earing behavior, but also for a better reproduction of the cup height and the thickness distribution in the cup.

Also, it can be seen that the hardening models lack of importance in this test.

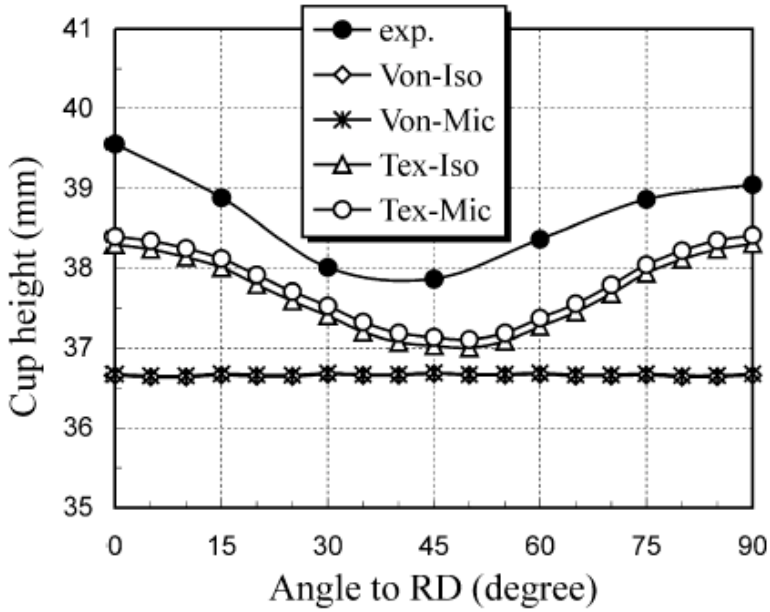

Figure 1.2 Comparison of measured and predicted cup profiles. Li et al., 2003.

Another example presented by Li et al., 2001 compares Tex-Iso and Hill 1948 with the same experimental results as in the former example. The results are shown in Figure 1.3.
It can be seen that the texture-based model Tex-Iso provides a better prediction than Hill 1948.

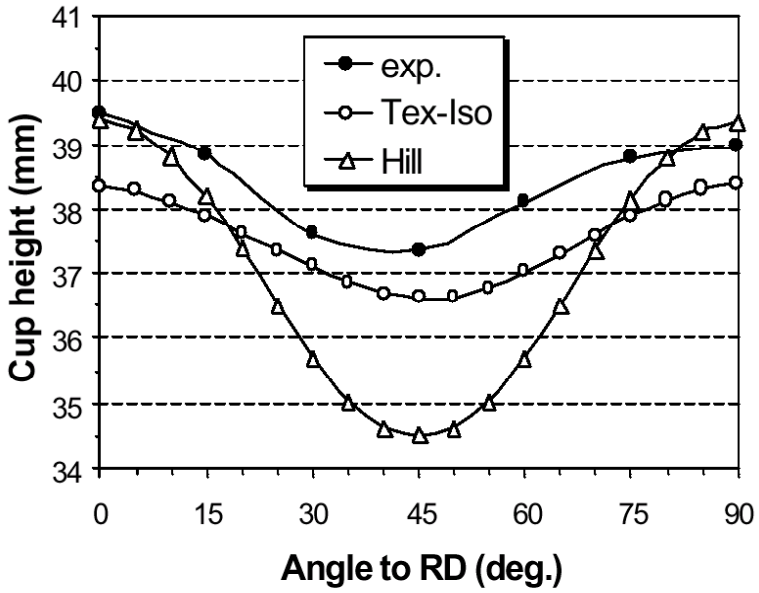

Figure 1.3 Comparison of measured and predicted cup profiles. Li et al., 2001.

A fourth example is shown based on the texture description using a stress-strain interpolation method, in turn based on a polycrystalline model *Minty* (initial texture coupled with Swift isotropic or Teodosiu and Hu hardening laws) and *Evol* (similar to *Minty* but taking into account texture updating due to plastic strains) (Flores et al., 2005). (Details on Minty and Evol can be found in Duchêne et al., 2002 and Habraken and Duchêne, 2004.)
The material is an interstitial-free (IF) steel. The texture has been measured by the K. U. Leuven team, and Teodosiu's isotropic and kinematic hardening model (Bouvier et al., 2002) was identified by Teodosiu's co-workers at University Paris 13 (Duchêne et al. 2005 and Li et al., 2003). The interest of this quite complex hardening model is that it predicts the effect of strain-path changes. In the deep drawing of a cup, the bending and unbending phenomena occurring at the die shoulder deviate significantly from a monotonic strain-path and, as observed in the following results, it requires a good hardening model to predict the earing profile accurately.
Three different yield loci have been applied to simulate the cup deep drawing; these are Hill 1948, Minty and Evol. In the simulations, each one was either coupled with the isotropic Swift model or with Teodosiu's model.
Figure 1.4 presents the earing profile predicted by Minty and Evol coupled with either the Swift or Teodosiu hardening model. Hill results predict for both hardening models a minimum at 45° and a high amplitude of 3,3mm, which modifies scale of Figure 1.4 scale and would prevent analysis of the details of the other laws' predictions, so it is not plotted. The Minty law, which neglects texture evolution, predicts a minimum at 45° and no effect of the hardening model (as is the case for Li et al., 2003). The Evol law shows a different earing when coupled with the Swift or Teodosiu hardening model. The isotropic case (Swift) predicts a minimum at 45° and an amplitude that is too low, while the mixed hardening law of Teodosiu is closer to the experimental amplitude and predicts a shift of the minimum towards 40° in agreement with the experiment. However, an additional maximum not confirmed by the experiment appears in the Evol + Teodosiu case.
In this case, it seems that taking both texture updating and complex isotropic and kinematic hardening into account improves the accuracy of the final geometry computed by finite element models.

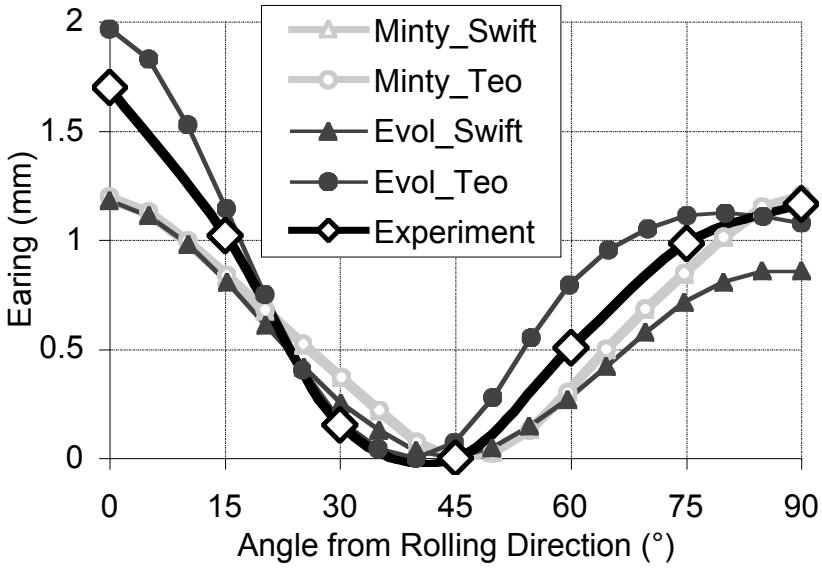

Figure 1.4 Comparison between earing measurements and numerical predictions. Flores et al., 2005.

To study the strain-path induced anisotropy, a last example will be given.
A high-strength steel ZstE180BH is submitted to several tests involving strain-path changes. The Teodosiu microstructure-based hardening law is able to predict the experimental results (Figure 1.5a), unlike a mixed hardening law (combining isotropic and kinematic hardening) (Figure 1.5b).

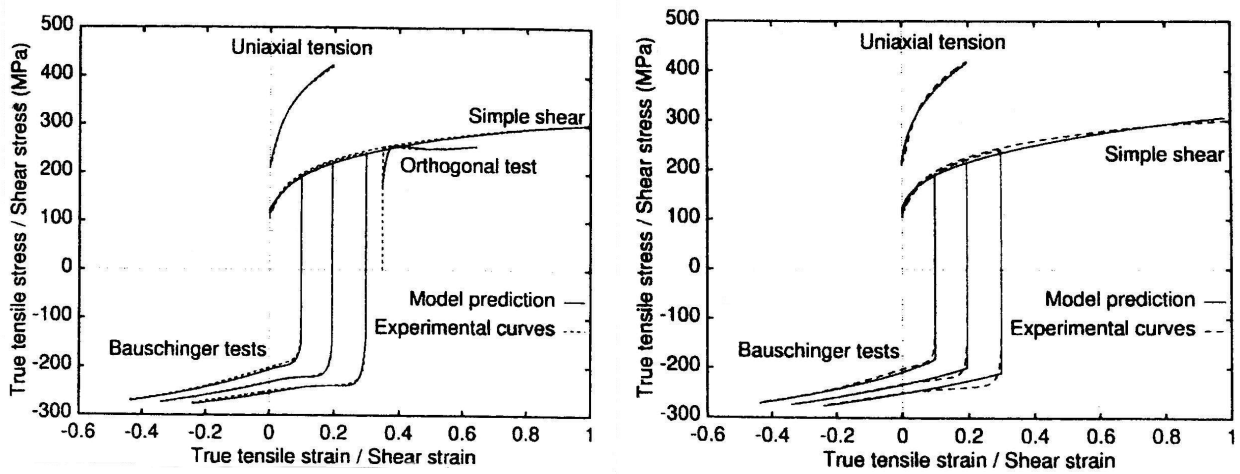

Figure 1.5 High-strength steel ZstE180BH. (a) Modeled by Teodosiu hardening law. (b) Modeled by a Swift law + kinematic hardening using saturation law. (Bouvier and Haddadi, 2001).

The accurate description of the hardening behavior under strain-path changes (e. g., Bauschinger effect and influence of the pre-strain) has a considerable impact on the prediction of the force required in manufacturing processes like single point incremental forming (SPIF), where the material is submitted to cyclic loads (Flores et al., 2005).

In what follows, this work will focused phenomenological yield locus description (initial size, shape and evolution), not taking into account texture description.

1.2 Scopes of the present research work

Within the frame of the projects PROMETA (RW n°01/1/4710) and PROINDU (RW n°4543b) having as objective respectively the numerical prediction of the overforming angle on cold roll forming and the development of a roll forming simulation software, the M&S department (Mechanics of Solids and Materials division) is in charge of the development of experimental equipment, the definition of a test protocol in order to identify the constitutive laws automatically, and the identification of three grades of steel.
The experimental equipment is required to study the initial yield surface at different stress states other than the classical ones (e. g., uni-axial tensile state) as well as the hardening behavior during strain-path changes and combined loads for different materials such as steel, aluminum, titanium and magnesium alloys.

1.3 Contents of the thesis

Following this introduction, Chapter 2 contains the continuum mechanical notions for the description of the plastic behavior of sheet metal under large deformations at room temperature. As such, it includes the kinematics of a continuum body, strain and stress

definitions, and a general elasto-plastic constitutive model description. This last point is complemented by the definition of anisotropy, as well as the description of some yield criteria and hardening laws.
Next, Chapter 3 defines the stress – strain states required to be experimentally reproduced in order to describe the initial yield locus and its displacement in the stress axis representation during plastic deformation. A review of the available experimental equipment capable of reproducing the required stress – strain states is presented in order to choose the best for further construction. After consideration, those deemed the highest performing are the Miyauchi device, able to perform simple shear tests and the bi-axial testing machine, able to perform plane strain and simple shear tests separately or simultaneously. This chapter presents the mechanical features of the Miyauchi device and the bi-axial test machine that were built at the M&S Laboratory, followed by a description of the optical strain gauge chosen that allows the computation of the strain field throughout the specimen's deformation area.
Chapter 4 focuses on the validation of the experimental equipment. First, the homogeneity of the stress and strain fields is verified. Then, the availability of performing the plane strain, simple shear, Bauschinger and orthogonal tests is checked. The repeatability (precision) of the tests is corroborated and the accuracy is validated by comparison with finite elements simulations.
In Chapter 5, the identification methods are proposed and DC06 (0,8mm thick), DP1000 (1,6mm thick) and S320GD (0,69mm thick) steels are identified according to those methods.
The initial yield surface for DC06 is identified by two methods (one using the strain measurements, the other using stress measurements) for two yield criteria, which are then compared with a texture-based yield criterion and the experimental points. The initial yield surface for the other two materials is described by the Hill 1948 yield criterion identified using strain measurements. The yield surface evolution (hardening) for DC06 and S320GD is described by the Teodosiu and Hu hardening law due to the observed mechanical behavior, i.e., the Bauschinger effect and strong influence of the pre-strain when strain-path changes take place. DP1000 exhibits a high Bauschinger effect and its flow stress is not influenced by the amount of pre-strain when reversing the load; hence, its behavior is described by a kinematic hardening law.
Finally, in Chapter 6, conclusions about the present work are established and equipment improvement and further topics for research are proposed, namely, the study of texture evolution, the material axis rotation and the experimental validation of new yield criteria.

CHAPTER 2

PLASTIC BEHAVIOR OF SHEET METAL UNDER LARGE DEFORMATIONS

Most of the metal forming processes involve moderately large or large deformations. Due to the differences in constitutive modeling between finite and infinitesimal deformations, a constitutive model that involves finite deformations is necessary.
The phenomenological constitutive laws used throughout this work, and described in this chapter, deal with finite strain, elasto-plasticity and deformation at room temperature. These constitutive models are based on additive decomposition of the strain rate and hypoelasticity.
This chapter is divided into 7 sections. The first section deals with the algebra of tensors, the second with the kinematics of a continuum body and the third with the concept of stress. The goal of these three sections is to establish a unique notation and concepts used in further chapters. Hence theory of continuum mechanics is referring to Holzapfel, 2000.
Section 4 links the strain rate (defined in Section 2) with the stress rate (defined in Section 3) by a general stress – strain relation for finite deformation. The concepts of yield surface, plastic flow rule and hardening constitutive laws are defined and some particular cases are introduced. A phenomenological micro-structural-based hardening model (Teodosiu and Hu, 1995) able to describe large strains, the influence of strain-path changes and the amount of pre-strain is described in Section 5. Section 6 briefly defines the strain-path change parameter. Some remarks concerning the constitutive laws are included in Section 7.

2.1 Definitions

Throughout this work, vectors and tensors (of second or fourth-order) are written in bold letters (Latin or Greek).
Let us begin with an orthonormal Cartesian coordinate system defined by a set of three-basis unit length vectors $\mathbf{e}_1$, $\mathbf{e}_2$, $\mathbf{e}_3$ (Figure 2.1). Theses vectors are mutually orthogonal, hence:

$$\mathbf{e}_1 \cdot \mathbf{e}_2 = \mathbf{e}_1 \cdot \mathbf{e}_3 = \mathbf{e}_2 \cdot \mathbf{e}_3 = 0 \tag{2.1}$$

and

$$\mathbf{e}_1 \cdot \mathbf{e}_1 = \mathbf{e}_2 \cdot \mathbf{e}_2 = \mathbf{e}_3 \cdot \mathbf{e}_3 = 1. \tag{2.2}$$

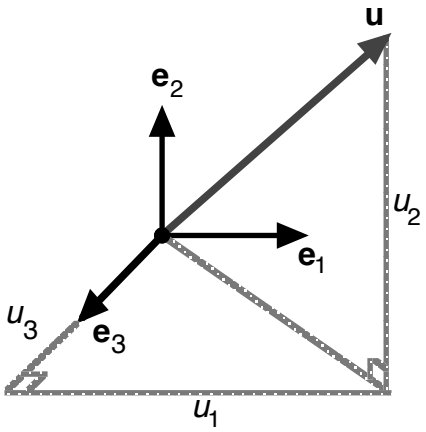

Figure 2.1 Orthonormal Cartesian coordinate system with a vector **u**.

Any vector **u** in the three-dimensional Euclidean space is represented uniquely by a linear combination of the basis vectors $\mathbf{e}_1$, $\mathbf{e}_2$, $\mathbf{e}_3$:

$$\mathbf{u} = u_1\mathbf{e}_1 + u_2\mathbf{e}_2 + u_3\mathbf{e}_3. \tag{2.3}$$

The tensor product or the dyadic product of the vectors **u** and **v** is denoted by $\mathbf{u} \quad \mathbf{v}$.
Any second-order tensor may be represented by a linear combination of dyads formed by the Cartesian basis $\{\mathbf{e}_i\}$:

$$\mathbf{A} = A_{ij}\mathbf{e}_i \quad \mathbf{e}_j \ . \tag{2.4}$$

A fourth-order tensor may also be expressed in terms of the three Cartesian basis vectors:

$$\mathbf{S} = S_{ijkl}\mathbf{e}_i \quad \mathbf{e}_j \quad \mathbf{e}_k \quad \mathbf{e}_l \, . \tag{2.5}$$

The tensor product of two second-order tensors **A** and **B** gives a fourth-order one:

$$\mathbf{S} = \mathbf{A} \quad \mathbf{B} \tag{2.6}$$

or in index notation:

$$S_{ijkl} = A_{ij}B_{kl} \ . \tag{2.7}$$

The double contraction of two tensors is characterized by a colon, i.e.,

$$\mathbf{A} : \mathbf{B} = A_{ij}B_{ij} \ , \tag{2.8}$$

and the double contraction of a fourth-order tensor with a second order one gives a second order tensor:

$$\mathbf{S} : \mathbf{A} = S_{ijkl}A_{kl}\mathbf{e}_i \quad \mathbf{e}_j \, . \tag{2.9}$$

The norm of a tensor is denoted by $\left| \bullet \right|$ and it is a non-negative real number defined by:

$$|\mathbf{A}| = \sqrt{\mathbf{A} : \mathbf{A}} = \sqrt{A_{ij} A_{ij}} \geq 0 \tag{2.10}$$

for a second-order tensor,

$$|\mathbf{S}| = \sqrt{\mathbf{S} : \mathbf{S}} = \sqrt{S_{ijkl} S_{ijkl}} \geq 0 \tag{2.11}$$

for a fourth-order tensor.

The unique transpose of a second-order tensor $\mathbf{A}$, denoted by $\mathbf{A}^T$, is governed by the identity:

$$\mathbf{v} \cdot \mathbf{A}^T \mathbf{u} = \mathbf{u} \cdot \mathbf{A}\mathbf{v} = \mathbf{A}\mathbf{v} \cdot \mathbf{u} \tag{2.12}$$

for any vectors **u** and **v**.
For a fourth-order tensor $\mathbf{S}$ having $\mathbf{S}^T$ as its unique transpose, the following identity must be true:

$$\mathbf{A} : \mathbf{S}^T : \mathbf{B} = \mathbf{B} : \mathbf{S} : \mathbf{A} = (\mathbf{S} : \mathbf{A}) : \mathbf{B} \tag{2.13}$$

for all second-order tensors **A** and **B**.

The determinant of a tensor **A** is defined by the determinant of the matrix **A**, i.e.:

$$\det \mathbf{A} = \det[\mathbf{A}]. \tag{2.14}$$

If a (second-order or fourth-order) tensor **A** is non-singular (det **A** ≠ 0), then there exists a unique inverse $\mathbf{A}^{-1}$ of **A** satisfying the reciprocal relation:

$$\mathbf{A}\mathbf{A}^{-1} = \mathbf{I} = \mathbf{A}^{-1}\mathbf{A} \tag{2.15}$$

where **I** is the identity tensor defined by:

$$\mathbf{I} = \mathbf{e}_j \quad \mathbf{e}_j \,. \tag{2.16}$$

The trace of a tensor **A** is denoted tr **A** and is defined by:

$$\mathrm{tr}\,\mathbf{A} = A_{ii} \,. \tag{2.17}$$

The tensor **A** can be decomposed into its spherical part and its deviatoric part, hence:

$$\mathrm{dev}\,\mathbf{A} = \mathbf{A} - \left(\frac{1}{3}\mathrm{tr}\,\mathbf{A}\right)\mathbf{I}. \tag{2.18}$$

2.2 Kinematics

2.2.1 Deformation gradient

Figure 2.2 illustrates the deformation of a continuum body when it moves from the *reference* (or material) configuration Ω_0 to the *current* (or spatial) configuration Ω. The vectors $d\mathbf{x}$ and $d\mathbf{X}$ are infinitesimal vector elements in the current and reference configurations respectively.
The deformation (second-order) gradient tensor $\mathbf{F}$ defines a linear transformation that transforms a line element $d\mathbf{X}$ into a line element $d\mathbf{x}$ (Equation 2.19). In both cases the line element connects the same material points.
In Figure 2.2, second-order tensors $\boldsymbol{U}$ and $\boldsymbol{u}$ represent respectively the displacement of the material point of coordinate $\mathbf{X}$ (in the initial position Ω_0) in the global coordinate and in the local coordinate base $\mathbf{x}$:

$$d\mathbf{x} = \mathbf{F}(\mathbf{X},t)d\mathbf{X}. \tag{2.19}$$

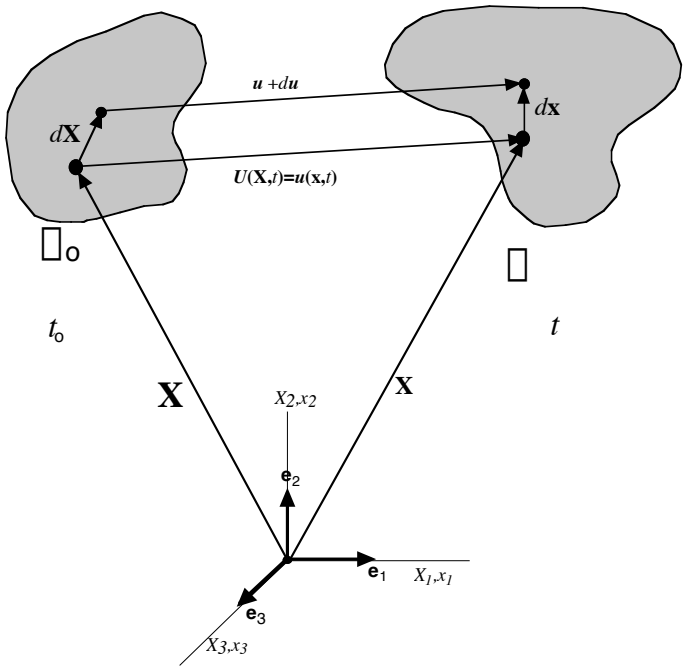

Figure 2.2 Reference and deformed configuration of a continuum body.

2.2.2 Polar decomposition

The Cauchy theorem of polar decomposition establishes that a second-order tensor can be decomposed uniquely into an orthogonal tensor and a symmetric tensor (Khan and Huang, 1995).
The deformation gradient tensor $\mathbf{F}$ is decomposed, then, into a pure stretch and a pure rotation (Equation 2.20):

$$\mathbf{F} = \mathbf{RU} = \mathbf{vR}\ . \tag{2.20}$$

$\mathbf{U}$ and $\mathbf{v}$ define *unique*, *positive definite*, *symmetric* tensors called respectively the right stretch tensor and the left stretch tensor. They measure local stretching (or contraction) along their mutually orthogonal eigenvectors.
$\mathbf{R}$, called *rotation tensor*, is a proper orthogonal tensor (i.e., $\det\mathbf{R} = 1$ and $\mathbf{R}^T\mathbf{R} = \mathbf{I}$) that measures the change in local orientation.

2.2.3 Strain tensors

Several strain tensor definitions can be found in the literature and their choice depends upon the application. A general formula for strain measures in function of the right and left stretch tensors **U** and **v** is:

$$\Pi = \begin{cases} \frac{1}{n}\left(\mathbf{U}^n - \mathbf{I}\right) & ; \quad \frac{1}{n}\left(\mathbf{v}^n - \mathbf{I}\right) \quad ; \quad if \quad n \neq 0 \\ \ln \mathbf{U} & ; \quad \ln \mathbf{v} \quad ; \quad if \quad n = 0 \end{cases} \tag{2.21}$$

where n is a real number.

Throughout this work, the material descriptions for the particular cases $n = 0$ (logarithmic strain tensor) and $n = 2$ (Green – Lagrange strain tensor) will be used, i.e.:

$$\Pi^{n} = \ln \mathbf{U} \ , \tag{2.22}$$

$$\Pi^{GL} = \frac{1}{2}\left(\mathbf{U}^2 - \mathbf{I}\right) . \tag{2.23}$$

The right stretch tensor **U** can be defined as a function of the deformation gradient as follows:

$$\mathbf{U}^2 = \mathbf{F}^T\mathbf{F} \ . \tag{2.24}$$

2.2.4 Rate of deformation tensors

The current velocity field $\boldsymbol{v}(\mathbf{x},t)$ is defined by (see Figure 2.2):

$$\boldsymbol{v} = \dot{\mathbf{x}} = \frac{\partial \mathbf{x}}{\partial t} = \dot{\boldsymbol{u}} \ . \tag{2.25}$$

Then, the derivate of the current velocity field with respect to the current coordinates gives the current velocity gradient:

$$\mathbf{l}(\mathbf{x},t) = \frac{\partial \boldsymbol{v}(\mathbf{x},t)}{\partial \mathbf{x}} = \operatorname{grad} \boldsymbol{v}(\mathbf{x},t) \ . \tag{2.26}$$

The referential velocity gradient is defined by:

$$\dot{\mathbf{F}} = \frac{\partial \mathbf{F}}{\partial t} \ . \tag{2.27}$$

The current velocity gradient can be expressed through the referential velocity gradient in the following way:

$$\mathbf{l}(\mathbf{x},t) = \dot{\mathbf{F}}\mathbf{F}^{-1} . \tag{2.28}$$

The tensor $\mathbf{l}(\mathbf{x},t)$ can be divided into its symmetric part $\mathbf{d}(\mathbf{x},t)$ and its antisymmetric (skew) part $\mathbf{w}(\mathbf{x},t)$:

$$\mathbf{l}(\mathbf{x},t) = \mathbf{d}(\mathbf{x},t) + \mathbf{w}(\mathbf{x},t) \ . \tag{2.29}$$

The symmetric part represents the rate of deformation tensor (or rate of strain tensor) and is defined by:

$$\mathbf{d} = \frac{1}{2}(\mathbf{l} + \mathbf{l}^T) \ . \tag{2.30}$$

The antisymmetric part represents the spin tensor (rate of rotation tensor or vorticity tensor) and is defined by:

$$\mathbf{w} = \frac{1}{2}(\mathbf{l} - \mathbf{l}^T) \ . \tag{2.31}$$

The time derivative of the Green – Lagrange strain tensor gives the so-called strain rate tensor:

$$\dot{\boldsymbol{\Gamma}}^{GL} = \mathbf{F}^T \mathbf{d}\mathbf{F} \ . \tag{2.32}$$

2.3 Stress Tensor

2.3.1 True and nominal stress tensors

Figure 2.3 shows a continuum body occupying a region Ω. Supposing that external arbitrary forces act over its boundary surface, internal distributed forces appear in any internal (imaginary) surface of this body. To understand the idea better, the body is divided (imaginary) into two portions.

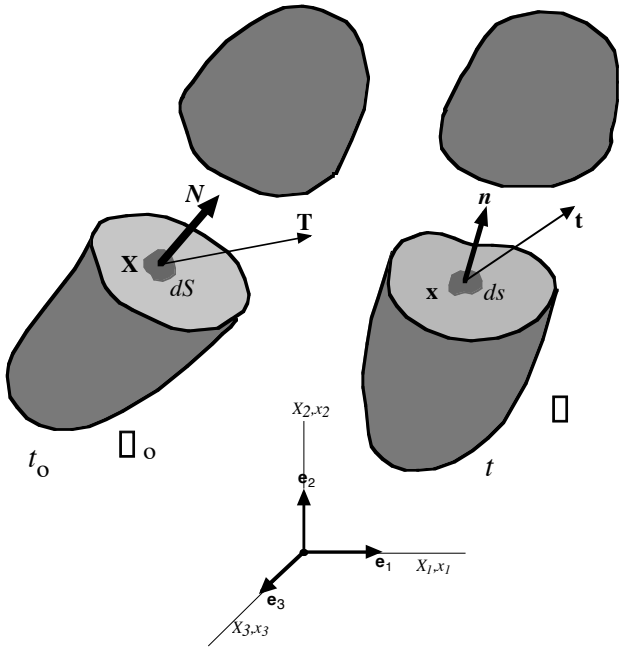

Figure 2.3 Traction vectors in reference and current configuration.

Since these two portions interact, forces are transmitted across the internal plane surface. The infinitesimal resultant force acting on the part dS (ds) is denoted $d\mathbf{f}$ and is defined for every surface element by:

$$d\mathbf{f} = \mathbf{t}ds = \mathbf{T}dS \ , \tag{2.33}$$

where $\mathbf{t} = \mathbf{t}(\mathbf{x},t,\boldsymbol{n})$ is the true (or Cauchy) traction vector defined in the current configuration and $\mathbf{T} = \mathbf{T}(\mathbf{X},t,\boldsymbol{N})$ the nominal (or first Piola – Kirchhoff) traction vector defined in the reference configuration.
These traction vectors act across the surface elements ds and dS with their respective normal vectors $\boldsymbol{n}$ and $\boldsymbol{N}$ (stress vectors).
The stress tensors are then defined by:

$$\mathbf{t}(\mathbf{x},t,\boldsymbol{n}) = \boldsymbol{\sigma}(\mathbf{x},t)\boldsymbol{n} \ , \tag{2.34}$$

$$\mathbf{T}(\mathbf{X},t,\boldsymbol{N}) = \mathbf{P}(\mathbf{X},t)\boldsymbol{N} \ , \tag{2.35}$$

where $\boldsymbol{\sigma}$ represents the symmetric tensor field called true (or Cauchy) stress tensor and $\mathbf{P}$ the nominal (or first Piola – Kirchhoff) stress tensor.
Both tensors can be related by the following expression:

$$\mathbf{P} = J\boldsymbol{\sigma}\mathbf{F}^{-T} \ , \tag{2.36}$$

where $J = \det\mathbf{F}$.

2.3.2 Objective time derivatives – Jaumann rate

Throughout this work, Jaumann rate is used to perform objective time derivatives for non-objective tensors. Jaumann rate is defined by:

$$\overset{\circ}{\boldsymbol{\alpha}} \equiv \dot{\boldsymbol{\alpha}} + \boldsymbol{\alpha}\cdot\boldsymbol{\Omega} - \boldsymbol{\Omega}\cdot\boldsymbol{\alpha} \ , \tag{2.37}$$

where $\boldsymbol{\alpha}$ is any non-objective tensor and $\boldsymbol{\Omega}$ is a spin tensor.
Then the Jaumann stress rate becomes:

$$\overset{\circ}{\boldsymbol{\sigma}} \equiv \dot{\boldsymbol{\sigma}} + \boldsymbol{\sigma}\cdot\mathbf{w} - \mathbf{w}\cdot\boldsymbol{\sigma} \ . \tag{2.38}$$

Here, $\mathbf{w}$ is the spin tensor defined in Equation 2.31.

2.4 Constitutive model: Finite-strain elasto-plasticity

To define the finite-strain elasto-plastic constitutive model, the additive decomposition of the rate deformation and a hypo-elasticity formulation are assumed. The rate of deformation is decomposed into elastic $\mathbf{d}^e$ and plastic $\mathbf{d}^p$ parts:

$$\mathbf{d} = \mathbf{d}^e + \mathbf{d}^p \ . \tag{2.39}$$

Hypo-elasticity relates the elastic rate of deformation to the Cauchy stress rate by a fourth-order tensor (Hook's operator) $\mathbf{C}^e$:

$$\overset{\nabla}{\sigma} = \mathbf{C}^e : \mathbf{d}^e \ . \tag{2.40}$$

To complete the formulation, the notions of yield surface and plastic flow rule must be introduced.

2.4.1 Yield surface

The yield surface divides the stress space into the elastic and plastic domains, i.e., the yield surface being the boundary of these two domains.
A yield criterion F defines the form and the size of the yield surface. The evolution of this surface during the plastic deformation can be described by hardening constitutive equations. Equation 2.41 shows a yield function depending on the stress state σ, and two internal variables $\mathbf{X}$ and k describing respectively the center and the size of the yield surface. The evolution of these internal variables depends on the equivalent plastic strain p (see Section 2.4.5).

$$\mathrm{F}(\sigma, \mathbf{X}, k) = \bar{\sigma}(\sigma - \mathbf{X}) - k(p) = 0 \ . \tag{2.41}$$

$\bar{\sigma}$ represents the equivalent stress and is defined as follows:

$$\bar{\sigma}(\sigma - \mathbf{X}) = \sqrt{(\mathbf{s} - \mathbf{X}) : \mathbf{H} : (\mathbf{s} - \mathbf{X})} \ , \tag{2.42}$$

where $\mathbf{s}$ is the deviatoric part of σ and $\mathbf{H}$ is a fourth-order tensor that defines the anisotropy of the material (see Section 2.4.4 for anisotropy and particular cases of equivalent stress definitions).

2.4.2 Plastic flow rule

The plastic rate of deformation can be derived by making use of a plastic potential function, as is shown in Equation 2.43:

$$\mathbf{d}^P = \dot{\lambda} \frac{\partial Q(\sigma)}{\partial \sigma} \ , \tag{2.43}$$

where $\dot{\lambda}$ is a proportional positive scalar factor called *plastic multiplier*.
For associated plasticity, it is assumed that $Q(\sigma) = \mathrm{F}(\sigma)$. Then Equation 2.43 can be written as:

$$\mathbf{d}^P = \dot{\lambda}\mathbf{n} \ , \tag{2.44}$$

where $\mathbf{n}$ is defined by:

$$\frac{\partial \mathrm{F}}{\partial \sigma} = \mathbf{n} \ . \tag{2.45}$$

Using Equation 2.44 and the power conjugate of the equivalent plastic strain rate $\dot{p}$ as the power conjugate of λ:

$$\dot{p} = \left(\mathbf{s} - \mathbf{X}\right) : \mathbf{d}^p \ , \tag{2.46}$$

the following expression can be obtained:

$$\dot{p} = \dot{\lambda} = \sqrt{\mathbf{d}^p : \mathbf{H}^{-1} : \mathbf{d}^p} \ . \tag{2.47}$$

2.4.3 General stress – strain relation for finite deformations

To obtain a general stress – strain relation for finite deformations the relation established in Equation 2.40 is written, by making use of Equation 2.39 and Equation 2.44, as:

$$\overset{\nabla}{\boldsymbol{\sigma}} = \mathbf{C}^e : (\mathbf{d} - \dot{\lambda}\mathbf{n}) \ . \tag{2.48}$$

According to the consistency condition (see Khan and Huang, 1995 for a multi-internal variable case):

$$\dot{F}(\boldsymbol{\sigma}, \mathbf{X}, k) = \frac{\partial F}{\partial \boldsymbol{\sigma}} : \overset{\nabla}{\boldsymbol{\sigma}} + \frac{\partial F}{\partial \mathbf{X}} : \overset{\nabla}{\mathbf{X}} + \frac{\partial F}{\partial k} \cdot \dot{k} = 0 \ , \tag{2.49}$$

and replacing Equation 2.45 and Equation 2.48,

$$\dot{F}(\boldsymbol{\sigma}, \mathbf{X}, k) = \mathbf{n} : \mathbf{C}^e : \left(\mathbf{d} - \dot{\lambda}\mathbf{n}\right) + \frac{\partial F}{\partial \mathbf{X}} : \frac{d\mathbf{X}}{d\lambda}\dot{\lambda} + \frac{\partial F}{\partial k} \cdot \frac{dk}{d\lambda}\dot{\lambda} = 0 \ , \tag{2.50}$$

the plastic multiplier can be obtained

$$\dot{\lambda} = \frac{1}{f_0}\mathbf{n} : \mathbf{C}^e : \mathbf{d} \ , \tag{2.51}$$

with

$$f_0 = \mathbf{n} : \mathbf{C}^e : \mathbf{n} - \frac{\partial F}{\partial \mathbf{X}} : \frac{d\mathbf{X}}{d\lambda} - \frac{\partial F}{\partial k}\frac{dk}{d\lambda} \tag{2.52}$$

where $\dot{\Gamma} = 0$ for neutral loading, unloading, or in elastic state.
Finally, the stress – strain relation is rewritten as:

$$\overset{\nabla}{\boldsymbol{\Pi}} = \mathbf{C}^{ep} : \mathbf{d} \tag{2.53}$$

and the compliance tensor is:

$$\mathbf{C}^{ep} = \mathbf{C}^e - \frac{\Gamma}{f_0}\left(\mathbf{C}^e : \mathbf{n}\right) \quad \left(\mathbf{C}^e : \mathbf{n}\right) \ , \tag{2.54}$$

where $\Gamma = 0$ in the elastic region and $\Gamma = 1$ in the plastic one.

2.4.4 Anisotropy coefficient and yield criteria

Cold-rolled metal sheets present an anisotropic behavior of their mechanical properties due to the rolling procedure itself and to their crystallographic texture. The phenomenological anisotropic yield criteria described here express this anisotropic behavior in an orthogonal set of material axes. These material axes are taken in the rolling direction (RD), the transverse direction (TD) and the normal (through-thickness) direction of the sheet (ND), coincident respectively with the X_1, X_2 and X_3 axes (Figure 2.3 and Figure 3.1).
The anisotropy coefficient (or Lankford coefficient) is obtained from the ratio between the plastic strain rate in the width and in the thickness directions from uniaxial tensile tests, i.e.:

$$r = \frac{\dot{\varepsilon}_2^p}{\dot{\varepsilon}_3^p}\ , \tag{2.55}$$

$r = 1$ for isotropic materials.
To characterize the plane anisotropy of the metal sheet, the r-values measured in several uniaxial tensile tests at different angles from the RD, must be averaged. For practical reasons, this average value, called the *coefficient of normal anisotropy*, is computed from tests performed at the RD, at the TD and at 45° from the RD. To identify the respective r-values, a sub-index indicating the angle from the RD is used, and then the average coefficient of anisotropy is defined as:

$$\bar{r} = \frac{r_0 + 2r_{45} + r_{90}}{4}. \tag{2.56}$$

A parameter indicating how different the 45° directions are from the symmetry axes is the degree of planar anisotropy:

$$\Delta r = \frac{r_0 + r_{90} - 2r_{45}}{4}. \tag{2.57}$$

Many yield criteria describing the initial anisotropy of a metal sheet can be found in literature. Habraken, 2001 and Banabic, 2000 have put together a wide compilation of those most used in metal forming.

The yield criteria used in this work are now briefly described (in each case σ_y represents the initial yield stress).

Von Mises isotropic yield criterion

This widely used isotropic quadratic criterion is represented by the following equation:

$$\bar{\sigma}(\sigma) \equiv \frac{1}{2}\left[(\sigma_{11} - \sigma_{22})^2 + (\sigma_{11} - \sigma_{33})^2 + (\sigma_{22} - \sigma_{33})^2 + 2\left(\sigma_{12}^2 + \sigma_{13}^2 + \sigma_{23}^2\right)\right] = \sigma_y^2\ . \tag{2.58}$$

Hill 1948 yield criterion (Hill, 1950)

This quadratic yield criterion is a generalization of von Mises criterion. H, G, F, N, L and M are material parameters that are contained in the fourth-order tensor **H** in Equation 2.42. The material is supposed to have an anisotropy with three orthogonal symmetry planes.

$$\bar{\sigma}(\sigma) \equiv \frac{1}{2}\left[H(\sigma_{11}-\sigma_{22})^2 + G(\sigma_{11}-\sigma_{33})^2 + F(\sigma_{22}-\sigma_{33})^2 + 2N\sigma_{12}^2 + 2L\sigma_{13}^2 + 2M\sigma_{23}^2\right] = \sigma_y^2 \quad (2.59)$$

Hosford 1979 yield criterion

The main advantage of this non-quadratic yield criterion is that fitting of the exponent value ensures a good approximation of the experimental data (Banabic, 2000). H, G, F, and a are material parameters. Recommended values for a are a=6 for bcc materials and a=8 for fcc materials (Hosford, 1998). The main drawback is the lack of shear stress.
More information can be found in Hosford and Caddell, 1993.

$$\bar{\sigma}(\sigma) \equiv F|\sigma_{22}-\sigma_{33}|^a + G|\sigma_{33}-\sigma_{11}|^a + H|\sigma_{11}-\sigma_{22}|^a = \sigma_y^a \quad . \quad (2.60)$$

Barlat 1991 yield criterion (Barlat et al. 1991)

This anisotropic yield criterion can be seen as a generalization of the Hosford 1972 (Hosford and Caddell, 1993) isotropic yield criteria to a general stress state. The yield function is written as follows:

$$\bar{\sigma}(\sigma) \equiv |s_1 - s_2|^a + |s_2 - s_3|^a + |s_3 - s_1|^a = \sigma_y^a \quad , \quad (2.61)$$

where s_1, s_2 and s_3 are the principal values of the deviatoric tensor $\mathbf{s}'$ (Equation 2.62). In order to include anisotropy, the following linear transformation must be applied:

$$\mathbf{s}' = \mathbf{L}\sigma \quad , \quad (2.62)$$

where σ is the actual anisotropic stress tensor and **L** is a linear operator depending on the material as defined by:

$$\mathbf{L} = \begin{bmatrix} \frac{c_2+c_3}{3} & -\frac{c_3}{3} & -\frac{c_2}{3} & 0 & 0 & 0 \\ -\frac{c_3}{3} & \frac{c_3+c_1}{3} & -\frac{c_1}{3} & 0 & 0 & 0 \\ -\frac{c_2}{3} & -\frac{c_1}{3} & \frac{c_1+c_3}{3} & 0 & 0 & 0 \\ 0 & 0 & 0 & c_4 & 0 & 0 \\ 0 & 0 & 0 & 0 & c_5 & 0 \\ 0 & 0 & 0 & 0 & 0 & c_6 \end{bmatrix} . \quad (2.63)$$

c_1, c_2, c_3, c_4, c_5, c_6 and a are material parameters.

Minty

Texture evolution is responsible for induced mechanical anisotropy of materials. This phenomenon plays an important role in forming processes; hence it is important in FE codes to implement constitutive models that take this anisotropic behavior into account.
Texture-based models are expensive in CPU-time and in memory storage. Habraken and Duchene, 2004 propose a local yield locus approach able to predict texture evolution during FE modeling.
The model computes only a small zone of the yield locus, which is updated when its position is no longer located in the part of interest in the yield locus or when the yield locus changes due to texture evolution.
Plastic criterion and the stress integration scheme are not defined by a yield locus formulation. It uses a linear stress – strain interpolation in the five-dimensional (5D) stress space described by Equation 2.64:

$$\mathbf{s} = \mathbf{L}\mathbf{u}, \tag{2.64}$$

where **s** and **u** are 5D vectors containing respectively the deviatoric part of the stress (the hydrostatic part being elastically computed according to Hooke's law) and deviatoric plastic strain rate direction (unit vector). $\mathbf{L}$ is a scalar describing the work hardening according to:

$$\sigma = K\left(\varepsilon^0 + \varepsilon\right)^n , \tag{2.65}$$

where K, ε^0, and n are material parameters identified by experimental data and ε is the cumulated polycrystal induced slip.
The macroscopic anisotropic interpolation is included in matrix **L**. Its identification relies on 5 directions of **u** advisedly chosen in the deviatoric strain rate space and their associated deviatoric stress **s** computed by using the polycrystal plasticity model. This micro-macro model uses Taylor's assumption of equal macroscopic strain and microscopic crystal strain (full constraints Taylor's model). It computes the average of the response of a set of representative crystals evaluated with a microscopic model, taking into account the plasticity at the level of the slip systems.
The stress vectors **s** lie on the yield locus. They define the vertices of the interpolation domain and are called *stress nodes*. The matrix **L** is built on the basis of these 5 stress nodes.

A relation between the Lankford coefficient and the material parameters is established in Chapter 5.

2.4.5 Hardening models

Hardening constitutive equations represent the evolution of the yield surface during the plastic deformation process.
Three types of hardening models are described herein. First, there is the isotropic hardening that describes the yield surface size evolution, the kinematic hardening that describes the yield surface displacement while its size remains constant, a combined (or mixed) hardening that contains both elements, i.e., size and displacement evolution. Shape evolution is not studied in this work.

Isotropic hardening

The yield function in Equation 2.41 depends now on one scalar internal parameter that describes the size evolution:

$$F(\boldsymbol{\sigma},k) = \bar{\sigma}(\boldsymbol{\sigma}) - k(p) \le 0 \ . \tag{2.66}$$

Swift type isotropic hardening

$$k(p) = K(\varepsilon_0 + p)^n \tag{2.67}$$

here, K, ε_0 and n are material parameters.

Voce type isotropic hardening

$$k(p) = R_0 + R \tag{2.68}$$

and R is ruled by the following differential equation:

$$\dot{R} = C_R(R_{SAT} - R)\dot{p} \ . \tag{2.69}$$

R_0 represents the initial yield stress, and C_R and R_{SAT} are material parameters defining the flow stress shape.

Kinematic hardening

A second-order tensor **X**, known also as back-stress, describes the displacement of the yield surface during plastic deformation. The size, which remains constant, is given by k_0 in Equation 2.70 and represents the initial yield stress:

$$F(\boldsymbol{\sigma},\mathbf{X},k_0) = \bar{\sigma}(\boldsymbol{\sigma} - \mathbf{X}) - k_0 \le 0 \ . \tag{2.70}$$

The Prager evolution equation for back-stress is:

$$\overset{\nabla}{\mathbf{X}} = c\mathbf{d}^p \ , \tag{2.71}$$

where c is a material parameter.

Ziegler proposes:

$$\overset{\nabla}{\mathbf{X}} = (\boldsymbol{\sigma} - \mathbf{X})\lambda \ , \tag{2.72}$$

where λ is a proportional scalar determined by the consistency condition.

Armstrong – Frederick's evolution equation has the following form:

$$\overset{\nabla}{\mathbf{X}} = c\left(s\mathbf{d}^p - \mathbf{X}\dot{p}\right) \ . \tag{2.73}$$

c and *s* are material parameters.
More details about these hardening constitutive laws can be found in Khan and Huang, 1995.

Combined hardening

This type of hardening describes the size and displacement evolution of the yield surface. The constitutive equations are composed of Equation 2.41 together with a combination of Equation 2.67 or Equation 2.68 and Equation 2.71, Equation 2.72 or Equation 2.73.

2.5 Micro-structural based hardening model (Teodosiu and Hu, 1995)

This is a phenomenological model based on microscopic and macroscopic experimental observations. This model is capable of describing large strains as well as the influence of strain-path changes and the amount of pre-strain over the flow stress.
It was first developed for bcc mono-crystals (Hu, 1992) and it has since been applied successfully to IF steel sheets (Bouvier et Haddadi, 2001, Brasseur et al., 2001, Hoferlin, 2001, Li et al., 2003, etc.). Further applications to dual phase steels and aluminum can be found in Bouvier et al., 2002.
The model uses a set of four internal variables (**X**, **P**, **S**, *R*), and 13 material parameters are required. The back-stress is a second-order tensor **X** having the dimension of the stress. The polarity is a non-dimensional second-order tensor **P**. A fourth-order tensor **S** describes the directional strength of planar persistent dislocation structures. The choice of its order is due to the need to describe the anisotropic contribution of persistent dislocation structures to the flow stress. Finally, a scalar internal variable *R*, with the dimension of the stress, takes into account the isotropic hardening caused by the statistically distributed dislocations.
Annex A describes in further detail the microscopic and macroscopic observations and the role of the internal variables in the phenomenological description.

2.5.1 Yield surface

The yield surface is described by the following equation:

$$F(\boldsymbol{\sigma},\mathbf{X},\mathbf{P},\mathbf{S},R) = f(\boldsymbol{\sigma}-\mathbf{X}) - R_0 - R - m|\mathbf{S}| = 0 \ , \tag{2.74}$$

where R_0 is the initial yield stress and $m|\mathbf{S}|$ is the contribution of the persistent dislocation structures to the isotropic hardening, with $m \in [0,1]$.

2.5.2 Internal variables evolution

The evolution of the scalar internal variable *R* is a Voce type (Equation 2.68 and Equation 2.69).

The back-stress is ruled by the following equation:

$$\overset{\nabla}{\mathbf{X}} = C_X \left(\frac{X_{SAT}}{f} (\mathbf{s}-\mathbf{X}) - \mathbf{X} \right) \dot{p} \ . \tag{2.75}$$

The dependence of **X** on the persistent dislocation structures is included in the scalar function $X_{SAT}(\mathbf{S},\mathbf{N})$:

$$X_{SAT} = X_{SAT0} + (1 - m)|\mathbf{S}|\sqrt{q + (1 - q)\Omega_S^2} \tag{2.76}$$

with

$$\Omega_S = \frac{S_D}{|\mathbf{S}|} \tag{2.77}$$

and

$$S_D = \mathbf{N} : \mathbf{S} : \mathbf{N} \tag{2.78}$$

where

$$\mathbf{N} = \frac{\mathbf{d}^p}{|\mathbf{d}^p|} \tag{2.79}$$

is the current direction of the strain rate tensor.

The internal variable **S** takes into account the directionality of the dislocation structures. For strong path-changes, dislocation structures associated with the subsequent direction of the strain rate evolve quite differently from the rest of the persistent structures (Teodosiu and Hu, 1995). In order to describe such evolution processes, and taking into account the definition of S_D, **S** is broken down into:

$$\mathbf{S} = S_D \mathbf{N} \otimes \mathbf{N} + \mathbf{S}_L \ . \tag{2.80}$$

S_D represents the strength associated with dislocations of the currently active slip systems, whereas $\mathbf{S}_L$ is associated with the latent part of the persistent dislocation structures.

The evolution of S_D follows the equation:

$$\dot{S}_D = C_{SD}\left[g(S_{SAT} - S_D) - hS_D\right]\dot{p} \ . \tag{2.81}$$

Functions *g(***P,N***)* and *h(***X,N***)* are two attenuation coefficients of the evolution of S_D upon stress reversal. *h* is non-negligible only during a micro-plastic stage, and its equation is:

$$h = \frac{1}{2}\left(1 - \frac{\mathbf{X} : \mathbf{N}}{X_{sat}\dfrac{\mathbf{s} - \mathbf{X}}{\Omega} : \mathbf{N}}\right). \tag{2.82}$$

The function *g* describes the work-hardening stagnation and the resumption of work-hardening after a subsequent reverse deformation. Specifically, by denoting P_D=**P:N,** the function is:

$$g = \begin{cases} 1 - \dfrac{C_P}{C_{SD} + C_P}\left|\dfrac{S_D}{S_{SAT}} - P_D\right| & \text{if } P_D \geq 0\ , \\ (1 + P_D)^{n_P}\left(1 - \dfrac{C_P}{C_{SD} + C_P}\dfrac{S_D}{S_{SAT}}\right) & \text{otherwise.} \end{cases} \tag{2.83}$$

The tensor $\mathbf{S}_L$, associated with the latent part of the persistent dislocation structures evolves in the following way:

$$\overset{\nabla}{\mathbf{S}}_L = -C_{SL}\left(\frac{Z}{S_{SAT}}\right)^{n_L}\mathbf{S}_L\dot{p} \tag{2.84}$$

with

$$Z = |\mathbf{S}_L| = \sqrt{|\mathbf{S}|^2 - S_D^2}\ . \tag{2.85}$$

The evolution law for the polarity tensor is:

$$\overset{\nabla}{\mathbf{P}} = C_P(\mathbf{N} - \mathbf{P})\dot{p}\ . \tag{2.86}$$

The set of 13 material parameters is formed by $\{m, R_0, C_R, R_{SAT}, C_X, X_{SAT0}, q, C_{SD}, C_{SL}, S_{SAT}, n_P, n_L, C_P\}$.

2.5.3 Compliance tensor

The value of f_0 in Equation 2.54 is obtained using the consistency condition and becomes:

$$f_0 = \mathbf{n} : \mathbf{C}^e : \mathbf{n} + C_R(R_{SAT} - R) + C_X\left(\frac{X_{SAT}}{\sqrt{2}}(\mathbf{s} - \mathbf{X}) - \mathbf{X}\right) + \mathrm{H} \tag{2.87}$$

where H is

$$\mathrm{H} = \frac{m}{\sqrt{|\mathbf{S}_L|^2 + S_D^2}}\left[-C_{SL}\left(\frac{|\mathbf{S}_L|}{S_{SAT}}\right)^{n_L}|\mathbf{S}_L|^2 + C_{SD}\left[g(S_{SAT} - S_D) - hS_D\right]S_D\right]. \tag{2.88}$$

2.6 Strain-path changes

It has been mentioned in the previous section that the Teodosiu and Hu, 1995 hardening model can describe strain-path changes. To characterize such strain-path changes, Schmitt et al., 1985 propose the following parameter (Schmitt parameter):

$$\beta = \frac{\mathbf{d}_1^P}{|\mathbf{d}_1^P|} : \frac{\mathbf{d}_2^P}{|\mathbf{d}_2^P|}\ , \tag{2.89}$$

where the sub-index 1 and 2 indicate respectively the direction of the rate of deformation during the pre-strain and the subsequent deformation. β_S in Equation 2.77 is a generalization of β (Teodosiu and Hu, 1995).

Classic strain-path changes include the monotonic strain-path change ($\alpha = 1$), the reverse (or Bauschinger) strain-path change ($\alpha = -1$), and the orthogonal strain-path change ($\alpha = 0$). These three particular cases are studied experimentally in the following chapters.

2.7 Conclusions

This chapter establishes the algebra of tensors and their respective notation used throughout this work. The kinematics of a continuum body under large deformations is presented, and the concepts of strain, rate of deformation and stress are defined.
A general constitutive equation, relating stress and deformation in a rate form, is developed by using classic concepts of plasticity theory such as yield function, plastic flow rule and hardening constitutive laws.
The yield functions and hardening laws described in this chapter are programed in the finite element (FE) code *Lagamine* developed at the M&S Department of the University of Liege (Belgium). In 1982, professor Cescotto began the development of a finite element code called Lagamine for modeling the rolling process of steel beams and pile sheets (Cescotto and Grober, 1985). This code is a Lagrangian one taking into account large strains and displacements. Other research projects were conducted that have increased the library of solid elements (Jetteur and Cescotto, 1991, Zhu and Cescotto, 1995, Li and Cescotto, 1997a, and Li and Cescotto, 1997b). and contact elements (Cescotto and Charlier, 1993, Cescotto and Habraken, 1996, and Habraken and Cescotto, 1998). The code is clearly focused on the modeling of material behavior. Researches have studied solid phase transformation or recrystallization (Habraken and Bourdouxhe, 1992, Casotto et al., 2005, and Habraken et al., 1998), damage models to predict crack appearance (Zhu and Cescotto, 1992, Castagne et al., 2002, and Remy et al., 2002), phenomenological laws with gradient plasticity like Li and Cescotto, 1996 or micro-macro laws (Duchêne et al. 2002 and Habraken and Duchêne, 2004). Deep drawing processes (Li et al., 1995 and Duchêne and Habraken, 2005), forging processes (Dyduch et al., 1992) or continuous casting were more specifically simulated.

CHAPTER 3

EXPERIMENTAL EQUIPMENT DEVELOPMENT

To gain a better understanding of the behavior of a metal sheet under different loadings, several tests, machines and devices have been designed. Usually, the results obtained for forces, displacements or strains are used to identify the material parameters required for different phenomenological constitutive laws implemented in FE codes.
This chapter deals with the design and implementation of test equipment. This involves three phases: a general study of the stress – strains states required for identification, a literature review and evaluation of available testing equipment providing the required stress – strain states, and finally, the development of such mechanical equipment.
The first section defines the stress states required to identify the initial yield surface, and describes the required tests needed to identify the different hardening behaviors, the strain state rates required to evaluate the strain-path changes and a comparison between the pure shear state and the simple shear state.
In the second section, different mechanical testing equipment used for sheet metal identification is described. Their ability to reproduce the required stress – strain states is evaluated together with their practical skills (fabrication, control, and required specimen).
The third section describes the fabrication of the Miyauchi simple shear device and the fourth describes the fabrication of a bi-axial testing machine able to perform plane strain and simple shear tests (separately or simultaneously). Section 5 describes the chosen optical system.
Some conclusions are established in Section 6.

3.1 Introduction

This work is based on the study of cold rolled metal sheets; hence, equations developed in the former chapter can be simplified. First, let us define the axis system over the sheet (Figure 3.1):

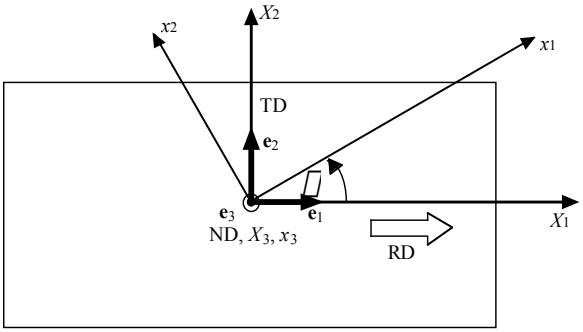

Figure 3.1 Rolled sheet axis definition. θ defines the angle with respect to the rolling direction.

The material axes defined by the rolling direction (RD), the transverse direction (TD) and the normal direction (ND) are coincident with the X_1, X_2 and X_3 axes.
Now, assuming a plane stress state, the stress tensor can be defined as follows:

$$\boldsymbol{\sigma} = \sigma_{11}\mathbf{e}_1 \quad \mathbf{e}_1 + \sigma_{22}\mathbf{e}_2 \quad \mathbf{e}_2 + \sigma_{12}\mathbf{e}_1 \quad \mathbf{e}_2 + \sigma_{12}\mathbf{e}_2 \quad \mathbf{e}_1 , \tag{3.1}$$

and the principal stresses:

$$\boldsymbol{\sigma} = \sigma_1\mathbf{e}_1 \quad \mathbf{e}_1 + \sigma_2\mathbf{e}_2 \quad \mathbf{e}_2 . \tag{3.2}$$

The strain-state tensor is:

$$\boldsymbol{\varepsilon} = \varepsilon_1\mathbf{e}_1 \quad \mathbf{e}_1 + \varepsilon_{22}\mathbf{e}_2 \quad \mathbf{e}_2 + \varepsilon_{33}\mathbf{e}_3 \quad \mathbf{e}_3 + \varepsilon_2\mathbf{e}_1 \quad \mathbf{e}_2 + \varepsilon_2\mathbf{e}_2 \quad \mathbf{e}_1 , \tag{3.3}$$

with its respective principal strains:

$$\boldsymbol{\varepsilon} = \varepsilon_1\mathbf{e}_1 \quad \mathbf{e}_1 + \varepsilon_2\mathbf{e}_2 \quad \mathbf{e}_2 + \varepsilon_3\mathbf{e}_3 \quad \mathbf{e}_3 . \tag{3.4}$$

3.1.1 Initial yield surface identification tests

The yield surface, for a general plane stress case, is illustrated in Figure 3.2, with respect to the principal stresses.

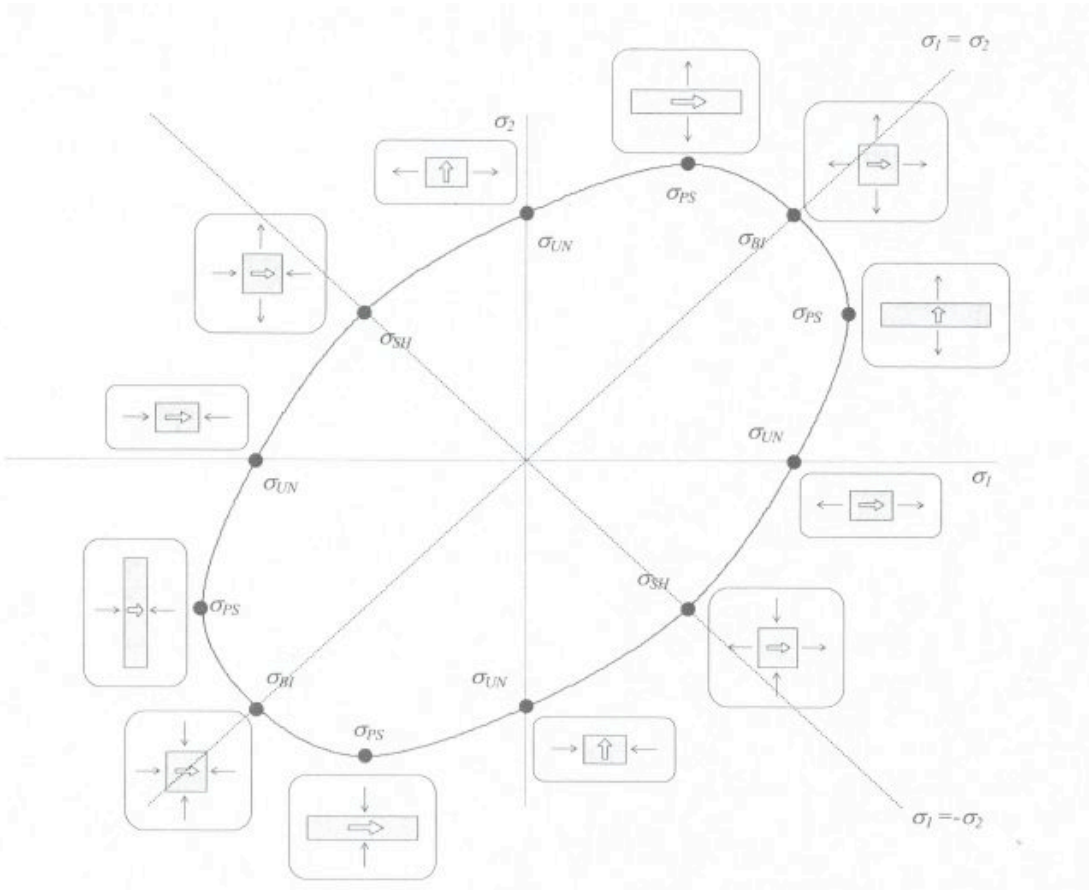

Figure 3.2 Stress states defining the initial yield surface in principal stress axes, Pijlman, 2001.

The yield function is discretized by points that define particular stress states (Figure 3.2). These points define the shape of the function. These stress states are uni-axial (*UN*), plane strain (*PS*), bi-axial (*BI*) and pure shear (*SH*), the single arrows indicating the stress direction and the double ones, the RD.

To represent these stress states in a general way (for any angle α), the following transformation linking a state defined in the x_1, x_2 and x_3 axes with the X_1, X_2 and X_3 axes (orthotropic direction) is used:

$$\boldsymbol{\sigma}_{\mathbf{X}} = \mathbf{R}^T \boldsymbol{\sigma}_{\mathbf{x}} \mathbf{R} \tag{3.5}$$

with **R**:

$$\mathbf{R} = \begin{bmatrix} \cos\alpha & \sin\alpha & 0 \\ -\sin\alpha & \cos\alpha & 0 \\ 0 & 0 & 1 \end{bmatrix} \tag{3.6}$$

where $\boldsymbol{\sigma}$ can be replaced by any second-order tensor.

Then, the general expressions for each stress state mentioned before are defined as follows:

Uni-axial stress state (*UN*) in the x_1 direction

$$\boldsymbol{\sigma} = \left(\sigma_{11}\cos^2\alpha\right)\mathbf{e}_1 \otimes \mathbf{e}_1 + \left(\sigma_{11}\sin^2\alpha\right)\mathbf{e}_2 \otimes \mathbf{e}_2 + \left(\frac{\sigma_{11}}{2}\sin 2\alpha\right)\mathbf{e}_1 \otimes \mathbf{e}_2 + \left(\frac{\sigma_{11}}{2}\sin 2\alpha\right)\mathbf{e}_2 \otimes \mathbf{e}_1 . \tag{3.7}$$

Plane strain stress state (*PS*) in the x_1 and x_2 direction

$$\begin{aligned} \boldsymbol{\sigma} = {} & \left(\sigma_{11}\cos^2\alpha + \sigma_{22}\sin^2\alpha\right)\mathbf{e}_1 \otimes \mathbf{e}_1 + \left(\sigma_{11}\sin^2\alpha + \sigma_{22}\cos^2\alpha\right)\mathbf{e}_2 \otimes \mathbf{e}_2 \\ & + \left(\frac{\sigma_{11} - \sigma_{22}}{2}\sin 2\alpha\right)\mathbf{e}_1 \otimes \mathbf{e}_2 + \left(\frac{\sigma_{11} - \sigma_{22}}{2}\sin 2\alpha\right)\mathbf{e}_2 \otimes \mathbf{e}_1 . \end{aligned} \tag{3.8}$$

Bi-axial stress state (*BI*) in the x_1 and x_2 direction

$$\sigma_{11} = \sigma_{22} = \sigma , \tag{3.9}$$

$$\boldsymbol{\sigma} = \sigma\,\mathbf{e}_1 \otimes \mathbf{e}_1 + \sigma\,\mathbf{e}_2 \otimes \mathbf{e}_2 . \tag{3.10}$$

Pure shear stress state (*SH*) in the x_1 and x_2 direction

$$\sigma_{11} = -\sigma_{22} , \tag{3.11}$$

$$\boldsymbol{\sigma} = \sigma_{11}\left[\cos 2\alpha\,\mathbf{e}_1 \otimes \mathbf{e}_1 - \cos 2\alpha\,\mathbf{e}_2 \otimes \mathbf{e}_2 + \sin 2\alpha\,\mathbf{e}_1 \otimes \mathbf{e}_2 + \sin 2\alpha\,\mathbf{e}_2 \otimes \mathbf{e}_1\right] . \tag{3.12}$$

Simple shear stress state (*SSH*) in the x_1 and x_2 direction

This stress state is not represented in Figure 3.2, but its description is necessary for further developments (Figure 3.7).

$$\begin{aligned}\boldsymbol{\sigma} = &\left(\sigma_{11}\cos^2\theta + \sigma_{22}\sin^2\theta - \sigma_{12}\sin 2\theta\right)\mathbf{e}_1 \quad \mathbf{e}_1 + \left(\sigma_{11}\sin^2\theta + \sigma_{22}\cos^2\theta + \sigma_{12}\sin 2\theta\right)\mathbf{e}_2 \quad \mathbf{e}_2 \\ &+ \left(\frac{\sigma_{11}-\sigma_{22}}{2}\sin 2\theta + \sigma_{12}\cos 2\theta\right)\mathbf{e}_1 \quad \mathbf{e}_2 + \left(\frac{\sigma_{11}-\sigma_{22}}{2}\sin 2\theta + \sigma_{12}\cos 2\theta\right)\mathbf{e}_2 \quad \mathbf{e}_1 .\end{aligned} \tag{3.13}$$

The yield function can be now expressed in terms of the general stress state as shown in Figure 3.3. Three other stress states are included; these are the uni-axial, plane strain, and pure shear applied at 45° from RD.

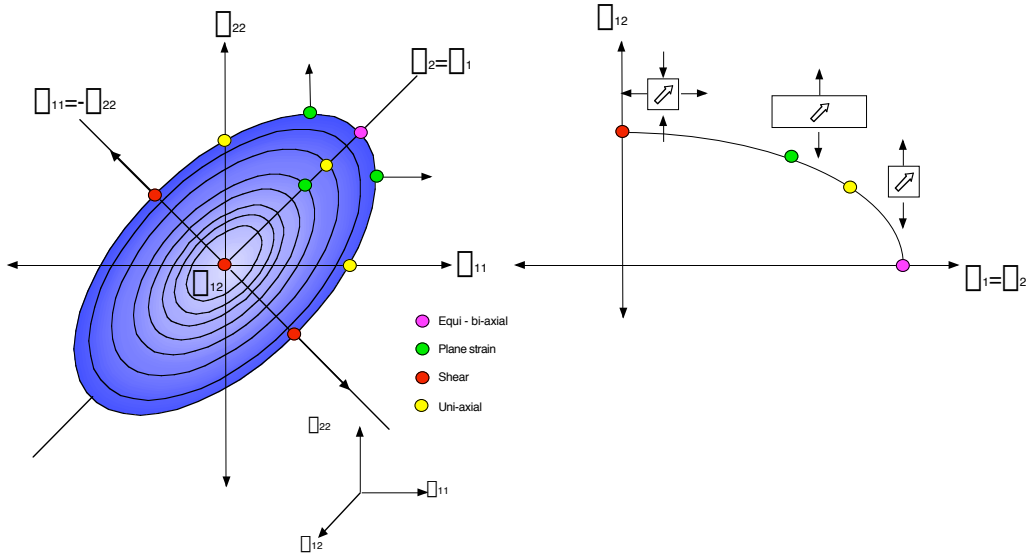

Figure 3.3 Stress states defining the initial yield surface for stress expressed in orthotropy axes X_1, X_2.

3.1.2 Yield surface evolution identification tests

Once the initial surface is defined, it is important to identify the hardening model that best describes the surface evolution. Figure 3.4 illustrates the hardening models defined in Chapter 2.

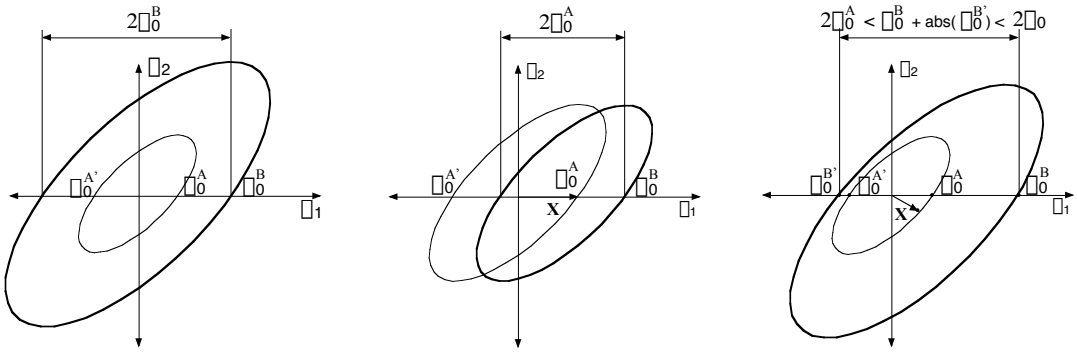

Figure 3.4 Yield surface evolution. **X** represents the back-stress.

The one-dimensional case (Figure 3.5) shows that a reverse (or cyclic) test is necessary to identify the hardening behavior.
Moreover, Figure 3.6 shows the importance to reach large strains in order to identify the hardening constitutive laws able to model the hardening stagnation that some materials might present under that condition (see Equation 2.67 and Equation 2.69).

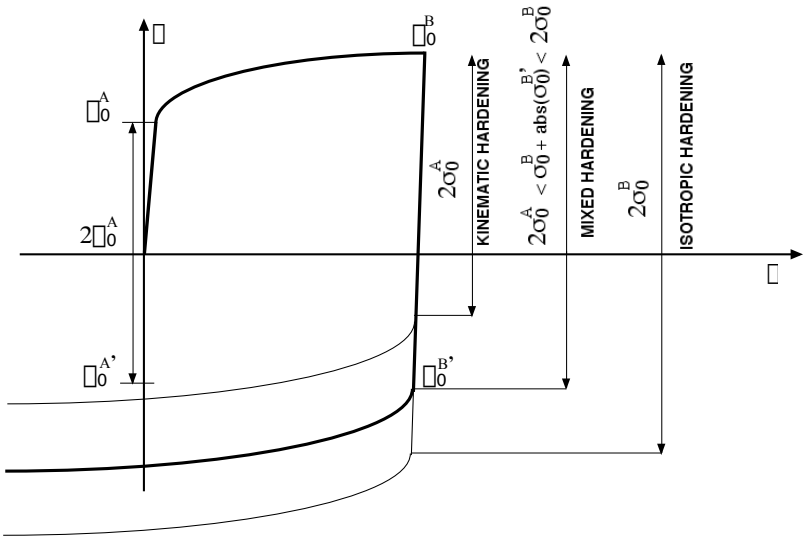

Figure 3.5 Hardening models' effect on the flow stress, one-dimensional case.

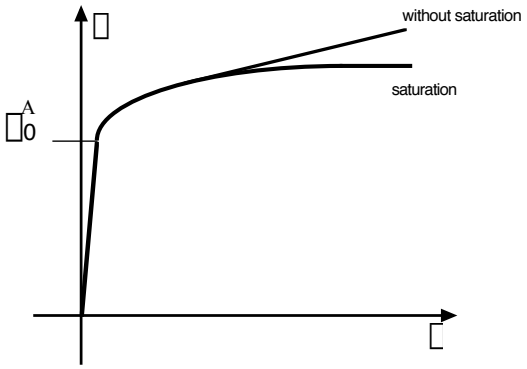

Figure 3.6 Two hardening models, one able to describe saturation of hardening at large strains.

3.1.3 Strain-path changes study

Experimental observations (for IF steels, Bouvier et Haddadi, 2001, Brasseur et al., 2001, Hoferlin, 2001 and Li et al., 2003) show that the flow stress presents a transient behavior after a strong strain-path change. This transient behavior can be softening or stagnation of the flow stress curve. In addition, the length of this transient behavior depends on the amount of pre-strain (hence the use in performing large strains, as also seen in Section 3.1.2).
The Schmitt parameter (Schmitt et al. 1985) is used to characterize the strain-path changes, from Equation 2.89:

$$\alpha = \frac{\mathbf{d}_1^P}{\left|\mathbf{d}_1^P\right|} : \frac{\mathbf{d}_2^P}{\left|\mathbf{d}_2^P\right|} = \mathbf{N}_1 : \mathbf{N}_2 \ , \tag{3.14}$$

where the sub-index 1 indicates the direction of the rate of deformation during the pre-strain and 2 the direction of the rate of deformation during the subsequent strain path.
We can now define the rate of deformation of particular strain states. Equation 3.5 is used and conservation of volume, in plastic deformation, is assumed, i.e.:

$$\mathrm{tr}\,\mathbf{d}^P = 0 \ . \tag{3.15}$$

Uni-axial strain state x_1 direction

Equation 3.15 can be expressed as follows:

$$d_{11}^P + d_{22}^P + d_{33}^P = 0 \ . \tag{3.16}$$

Components 22 and 33 can be written as a function of the rate of deformation in the 11 direction by the parameter k (depending on the anisotropy of the material, k = 0,5 for an isotropic case).

$$d_{11}^P - \mathrm{k} d_{11}^P + (\mathrm{k} - 1) d_{11}^P = 0 \ . \tag{3.17}$$

This parameter can be linked with the Lankford coefficient (Equation 2.55) by the flow rule (Equation 2.44), which depends on the chosen yield criterion (see Chapter 5).
Finally, the general rate of deformation tensor is:

$$\begin{aligned} \mathbf{d}^P = d_{11}^P \Big[& \left(\cos^2\alpha - \mathrm{k}\sin^2\alpha\right)\mathbf{e}_1 \quad \mathbf{e}_1 + \left(\sin^2\alpha - \mathrm{k}\cos^2\alpha\right)\mathbf{e}_2 \quad \mathbf{e}_2 \\ & + (\mathrm{k} - 1)\mathbf{e}_3 \quad \mathbf{e}_3 + \frac{1+\mathrm{k}}{2}\sin 2\alpha\, \mathbf{e}_1 \quad \mathbf{e}_2 + \frac{1+\mathrm{k}}{2}\sin 2\alpha\, \mathbf{e}_2 \quad \mathbf{e}_1 \Big], \end{aligned} \tag{3.18}$$

and its norm:

$$\left|\mathbf{d}^P\right| = \left|d_{11}^P\right| \sqrt{\left(\cos^2\alpha - \mathrm{k}\sin^2\alpha\right)^2 + \left(\sin^2\alpha - \mathrm{k}\cos^2\alpha\right)^2 + (\mathrm{k} - 1)^2 + 2\left(\frac{1+\mathrm{k}}{2}\sin 2\alpha\right)^2} \ . \tag{3.19}$$

Plane strain state in the x_1 and x_2 direction

The plane strain assumes:

$$d_{22}^P = 0 \ , \tag{3.20}$$

then

$$d_{11}^P = -d_{33}^P \ . \tag{3.21}$$

The rate of deformation becomes:

$$\mathbf{d}^P = d_{11}^P \left[\cos^2\theta\, \mathbf{e}_1 \otimes \mathbf{e}_1 + \sin^2\theta\, \mathbf{e}_2 \otimes \mathbf{e}_2 - \mathbf{e}_3 \otimes \mathbf{e}_3 + \frac{\sin 2\theta}{2} \mathbf{e}_1 \otimes \mathbf{e}_2 + \frac{\sin 2\theta}{2} \mathbf{e}_2 \otimes \mathbf{e}_1 \right] \tag{3.22}$$

and its norm:

$$\left|\mathbf{d}^P\right| = \sqrt{2}\left|d_{11}^P\right| . \tag{3.23}$$

Simple shear strain state

Figure 3.7 shows a simple shear case at $\theta = 0$. The development of its kinematics is done for this particular case and its general form is developed.

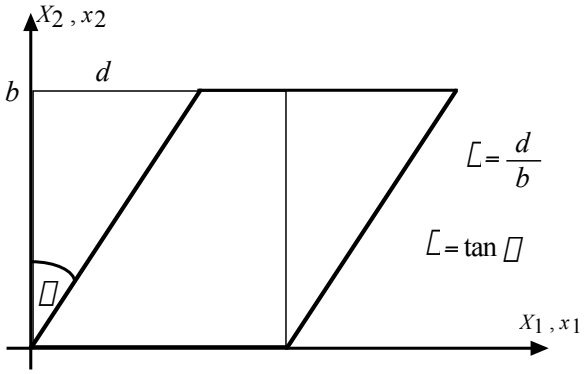

Figure 3.7 Simple shear.

The deformation gradient is defined by

$$\mathbf{F} = \mathbf{e}_1 \otimes \mathbf{e}_1 + \mathbf{e}_2 \otimes \mathbf{e}_2 + \gamma \mathbf{e}_1 \otimes \mathbf{e}_2 \tag{3.24}$$

and its time derivative:

$$\dot{\mathbf{F}} = \dot{\gamma} \mathbf{e}_1 \otimes \mathbf{e}_2 . \tag{3.25}$$

Then, the velocity gradient is:

$$\mathbf{l} = \dot{\mathbf{F}}\mathbf{F}^{-1} = \dot{\gamma} \mathbf{e}_1 \otimes \mathbf{e}_2 \tag{3.26}$$

with a rate of deformation tensor defined as:

$$\mathbf{d} = \frac{\dot{\gamma}}{2}\left(\mathbf{e}_1 \otimes \mathbf{e}_2 + \mathbf{e}_2 \otimes \mathbf{e}_1\right) \tag{3.27}$$

and a spin tensor:

$$\mathbf{w} = \frac{\dot{\gamma}}{2}\left(\mathbf{e}_1 \otimes \mathbf{e}_2 - \mathbf{e}_2 \otimes \mathbf{e}_1\right) . \tag{3.28}$$

In a general case, when $\beta \neq 0$, the rate of deformation tensor is:

$$\mathbf{d}^P = \frac{\dot{\varepsilon}^P}{2}\left[-\sin 2\beta\ \mathbf{e}_1 \otimes \mathbf{e}_1 + \sin 2\beta\ \mathbf{e}_2 \otimes \mathbf{e}_2 + \cos 2\beta\ \mathbf{e}_1 \otimes \mathbf{e}_2 + \cos 2\beta\ \mathbf{e}_2 \otimes \mathbf{e}_1\right] \tag{3.29}$$

having the following norm:

$$\left|\mathbf{d}^P\right| = \sqrt{2}\left|\frac{\dot{\varepsilon}^P}{2}\right| . \tag{3.30}$$

The Schmitt parameter, defined in Section 2.6, is now defined for particular cases; more information can be found in Bacroix at al. 1994, Bouvier et al. 2005 and Rauch and Shmitt, 1989.

Uni-axial strain state at RD followed by simple shear state (general case)

$$\beta = -\mathrm{sgn}\left(\dot{\varepsilon}^P\right)\mathrm{sgn}(d_{11}^P)\frac{1+k}{2\sqrt{1-k+k^2}}\sin 2\beta_2 . \tag{3.31}$$

β_2 represents the angle from the RD of the second strain path.
Figure 3.8 shows the Schmitt parameter in function of β_2 for an isotropic material (k=0,5).
$d_{11}^P > 0$, $\dot{\varepsilon}^P > 0$ (in blue) and $\dot{\varepsilon}^P < 0$ (in red).

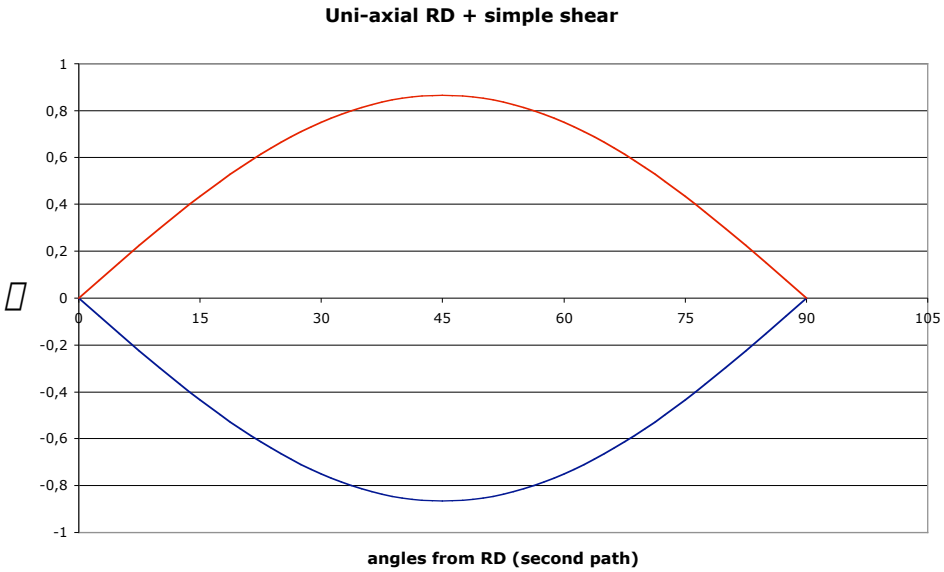

Figure 3.8 Schmitt parameter for a uni-axial strain state at RD followed by a simple shear. Isotropic material (k=0,5). $\dot{\varepsilon}^P > 0$ (in blue) and $\dot{\varepsilon}^P < 0$ (in red).

An orthogonal strain-path change characterized by $\beta = 0$ can be reproduced by a subsequent simple shear at RD or TD.

Plane strain state (general case) followed by a simple shear state (general case)

$$\alpha = \frac{\mathrm{sgn}(d_{11}^{P})\,\mathrm{sgn}(\dot{\gamma}^{P})}{2}\left(\sin 2\theta_1 \cos 2\theta_2 - \sin 2\theta_2 \cos 2\theta_1\right), \tag{3.32}$$

θ_1 and θ_2 represent respectively the angle from the RD of the first and second strain path. Figure 3.9 shows the Schmitt parameter for a pre-strain at RD as a function of θ_2. $d_{11}^{P} > 0, \dot{\gamma}^{P} > 0$ (in blue) and $\dot{\gamma}^{P} < 0$ (in red).

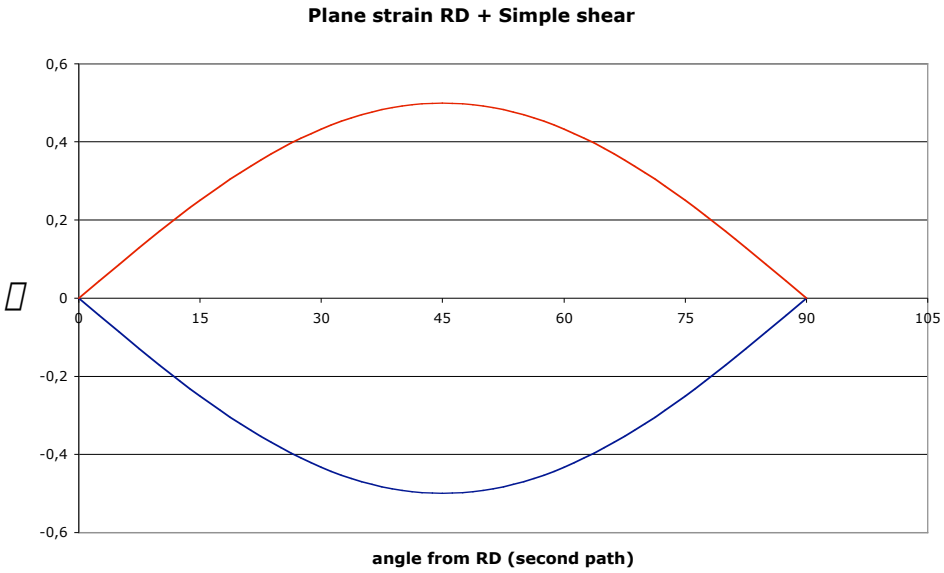

Figure 3.9 Schmitt parameter for a plane strain state at RD followed by a simple shear. $\dot{\gamma}^{P} > 0$ (in blue) and $\dot{\gamma}^{P} < 0$ (in red).

An orthogonal strain-path change can be reproduced by a subsequent simple shear at RD or TD.

Simple shear strain state (general case) followed by a simple shear strain state (general case)

$$\alpha = \mathrm{sgn}(\dot{\gamma}_1^{P})\,\mathrm{sgn}(\dot{\gamma}_2^{P})\left(\sin 2\theta_1 \sin 2\theta_2 + \cos 2\theta_1 \cos 2\theta_2\right). \tag{3.33}$$

Sub-indices 1 and 2 represent respectively the components for the first and second strain path. Figure 3.10 shows the Schmitt parameter for a pre-strain at RD as a function of θ_2. $\dot{\gamma}_1^{P} > 0$, $\dot{\gamma}_2^{P} > 0$ (blue line) and $\dot{\gamma}_2^{P} < 0$ (red line).

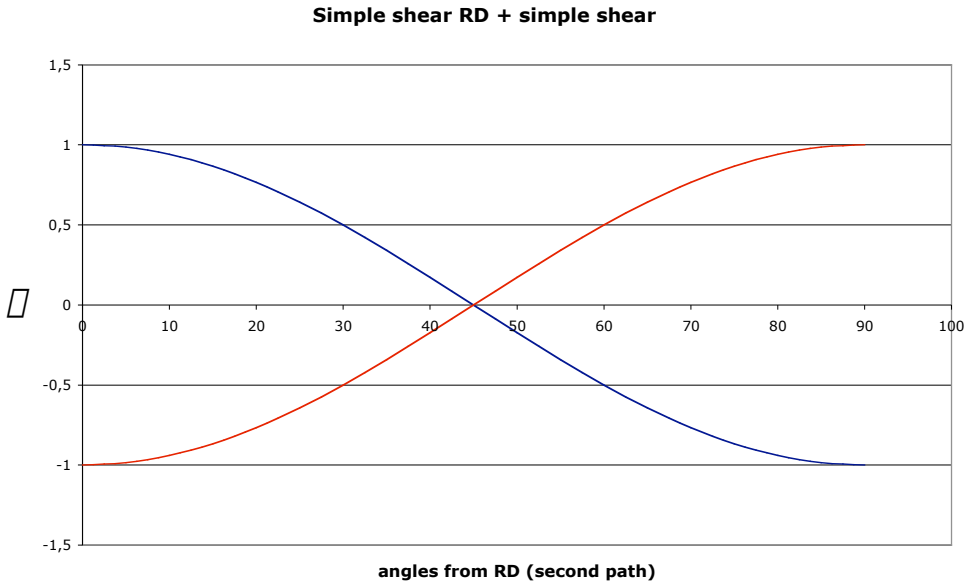

Figure 3.10 Schmitt parameter for a simple shear state at RD followed by a simple shear. $\beta_2^P > 0$ (blue line) and $\beta_2^P < 0$ (red line).

The available strain-path changes are summarized in Table 3.1.

β_2	β			
	$\beta_2^P > 0$		$\beta_2^P < 0$	
0°	1	monotonic	-1	Bauschinger
45°	0	orthogonal	0	orthogonal
90°	-1	Bauschinger	1	monotonic

Table 3.1 Schmitt parameters for different β_2 and β_2^P direction.

3.1.4 Simple shear observations

The simple shear state is much easier to reproduce experimentally reproduce than the pure shear one. For this reason, a deep study is done in this section.
First of all, let us establish the conditions allowing the approach of a pure shear state by a simple shear one.
Figure 3.11 shows what happens in the center of a sample under a simple shear state. One can remark that a simple shear state at RD reproduces a pure shear state at 45° from RD and vice-versa (Pijlman, 2001).

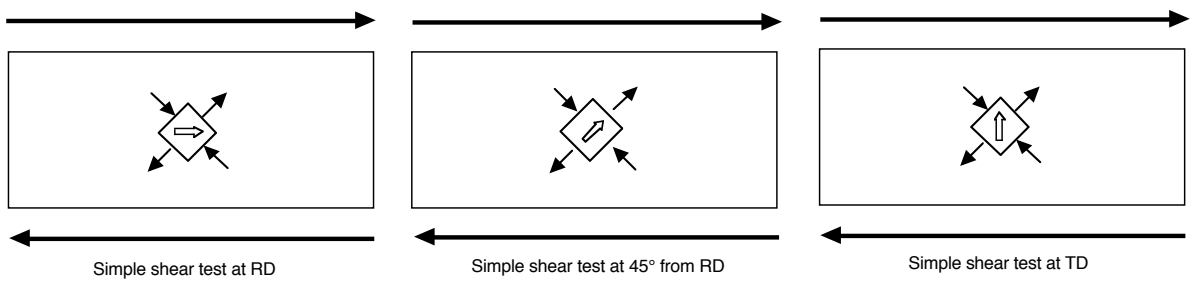

Figure 3.11 Simple shear at RD and 45° from RD.

This is only valid at the beginning of the plastic deformation, when $\sigma_{12} >> (\sigma_{11}, \sigma_{22})$ and the simple shear state at RD can be approached by:

$$\sigma = \sigma_{11}\mathbf{e}_1 \otimes \mathbf{e}_1 + \sigma_{22}\mathbf{e}_2 \otimes \mathbf{e}_2 + \sigma_{12}\mathbf{e}_1 \otimes \mathbf{e}_2 + \sigma_{12}\mathbf{e}_2 \otimes \mathbf{e}_1 \quad (3.34)$$

and the simple shear at 45° from the RD by:

$$\sigma = \left(\frac{\sigma_{11}+\sigma_{22}}{2} - \sigma_{12}\right)\mathbf{e}_1 \otimes \mathbf{e}_1 + \left(\frac{\sigma_{11}+\sigma_{22}}{2} + \sigma_{12}\right)\mathbf{e}_2 \otimes \mathbf{e}_2 + \frac{\sigma_{11}-\sigma_{22}}{2}\mathbf{e}_1 \otimes \mathbf{e}_2 + \frac{\sigma_{11}-\sigma_{22}}{2}\mathbf{e}_2 \otimes \mathbf{e}_1 \quad (3.35)$$

(see Khan and Huang, 1995 for an example with rigid plastic material).

A second point is the symmetry between the simple shear at RD and simple shear at TD. From Equation 3.13, the simple shear stress tensor at RD becomes:

$$\sigma^{RD} = \sigma_{11}\mathbf{e}_1 \otimes \mathbf{e}_1 + \sigma_{22}\mathbf{e}_2 \otimes \mathbf{e}_2 + \sigma_{12}\mathbf{e}_1 \otimes \mathbf{e}_2 + \sigma_{12}\mathbf{e}_2 \otimes \mathbf{e}_1 \quad (3.36)$$

and at TD:

$$\sigma^{TD} = \sigma_{11}\mathbf{e}_1 \otimes \mathbf{e}_1 + \sigma_{22}\mathbf{e}_2 \otimes \mathbf{e}_2 - \sigma_{12}\mathbf{e}_1 \otimes \mathbf{e}_2 - \sigma_{12}\mathbf{e}_2 \otimes \mathbf{e}_1 . \quad (3.37)$$

Clearly, there is symmetry with respect to the $\sigma_{11} = \sigma_{22}$ plane and $\left|\sigma_{12}^{RD}\right| = \left|\sigma_{12}^{TD}\right|$.
The same analysis can be done with the rate of deformation tensor concluding that $\left|d_{12}^{RD}\right| = \left|d_{12}^{TD}\right| = \left|\frac{\sigma}{2}\right|$.

A third point concerns the material axis distortion. Let us place the material coordinates in a new axis system θ_1, θ_2, θ_3 that moves with the material during deformation. Figure 3.12 shows that during a simple shear, the material axes are no longer orthogonal. This can be generalized to any case where deformation takes place out of the principal directions. This axis distortion is neglected in this work and some research involving texture measures and numerical analysis can be found in Lelotte et al., 2005.

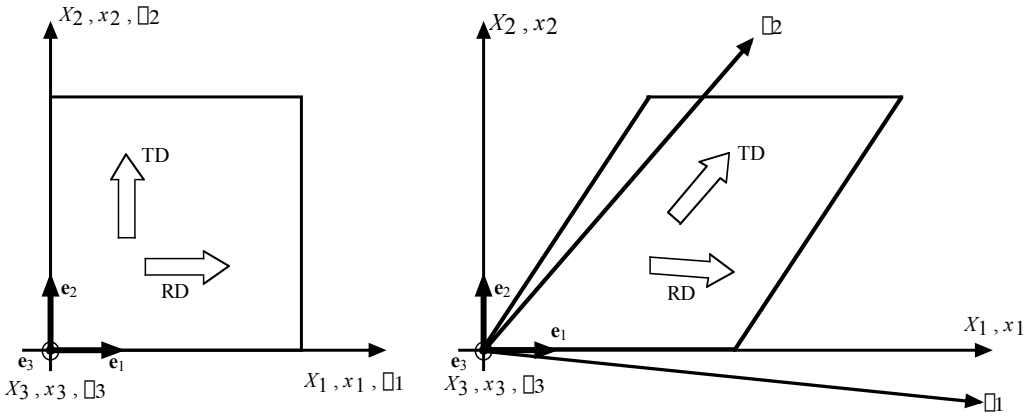

Figure 3.12 Distortion of material axis.

3.2 A general review of mechanical equipment

This section presents a summary of articles that describe sheet metal testing equipment able to represent bi-axial, plane strain, and simple shear stress states. Some of this equipment can also impose different load directions, permitting the study of a more complex deformation path. The performance of the equipment is evaluated according to the flexibility and the simplicity of the design (machine and specimen required).

3.2.1 Experimental devices

Kuwabara test

Figure 3.13a shows the bi-axial tensile testing device used by Kuwabara et al., 1998. Opposing hydraulic cylinders are connected to common hydraulic lines so that they are subjected to the same hydraulic pressure. The hydraulic pressure of each pair of opposing hydraulic cylinders is independently servo-controlled. Displacements of opposing hydraulic cylinders are equalized using a pantograph-type link mechanism. So, the center of the cruciform specimen is always maintained at the center of the testing machine apparatus during bi-axial tests.
A load cell is included in each loading direction. Bi-axial strain components in the gauge section of the specimen are measured using bi-axial strain gauges.

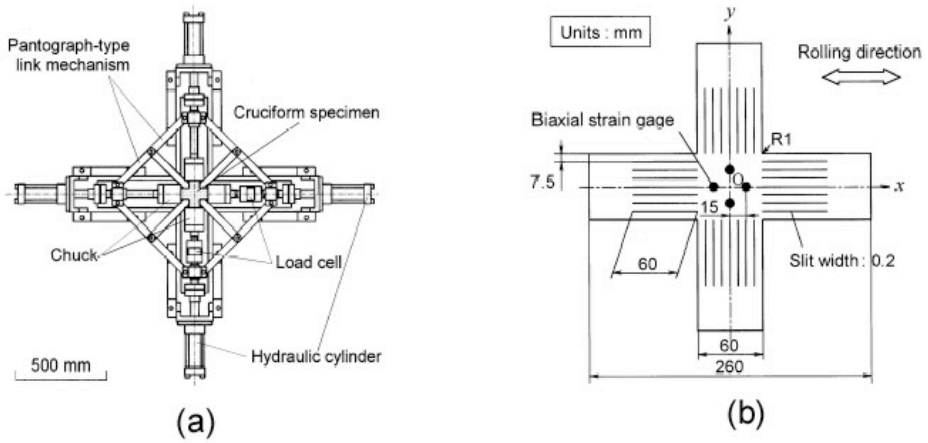

Figure 3.13 Bi-axial testing device. Kuwabara et al. 1998.

Figure 3.13b shows the geometry of the cruciform specimen. The x and y axes are taken parallel to the rolling and transverse directions of the specimen respectively, where the origin of the coordinates is at the center of the specimen.

Inpro test

Hoferlin, 2001 and Pijlman, 2001 describe this multi-axial test setup.
This test uses a cross test setup, which deforms a square piece of sheet metal in two perpendicular directions. The two directions can be controlled separately. The forces applied on the test piece are transmitted through clamping arms. Multiple arms are applied to ensure that a tensile force in one direction does not affect the forces in the perpendicular direction. The specimen is illustrated in Figure 3.14.

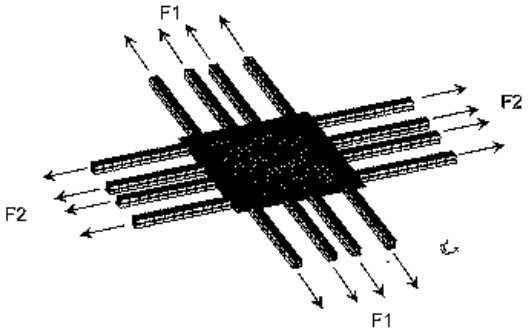

Figure 3.14 Cross test principle. Hoferlin, 2001.

G'Sell-Rauch shear test

This specimen was first proposed by G'Sell et al., 1983 to determine the plastic behavior of solid polymers under large strains. It was later adapted by Rauch, 1998 to study the plastic anisotropy of sheet metals, and has been widely used by many authors due to the absence of necking development, the large range of achievable homogeneous strains, the extreme simplification of the sample geometry (Figure 3.15), and the possibility of reversing the load direction during the course of the experiment.

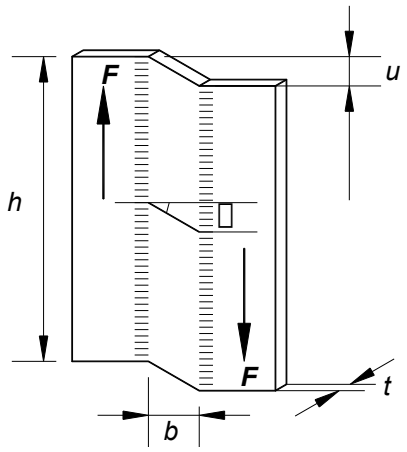

Figure 3.15 Geometry of a shear sample. The deformed volume is defined by the indentations resulting from the clamping of lateral grips. Rauch, 1998.

In order to obtain a quasi-homogenous shear stress distribution in the measurable part (deformed volume in Figure 3.15), some considerations from Hu, 1992 have to be taken:

- To minimize the influence of free ends, the ratio between the length and the width has to be as large as possible, that is $h/b >> 1$.
- To minimize the stress perturbation due to the grip force, the ratio between the width and the thickness has to be greater than 2, that is, $b/t > 2$.
- To avoid buckling effects, the ratio between the width and the thickness has to be less than 10 for steel, $b/t < 10$.

The device to carry out this test was designed in order to impose a parallel displacement of two lateral grips. Some information for test apparatus construction can be found in G'Sell et al., 1983 and Hu, 1992.

Miyauchi shear test

This test was proposed by Miyauchi, 1984 and is presented in Figure 3.16 and Figure 3.17.
This test is used to study the Bauschinger effect (reversing the test), to reach high deformation levels and to pre-strain the material for further tests.
Genevois, 1992 recommends the following sizes for the deformed areas: $h \geq 40$ mm and $b = 2$ to 10 mm. The geometry sketched in Figure 3.16 is used by Bacroix et al., 1994, i.e., a specimen of 200 mm long and 230 mm wide, and has two 200x40 mm gauge zones. This last specimen is used mainly to pre-strain the metal sheet for later deformations. (Smaller specimens can be cut from the deformation gauge areas and then deformed in another test machine.)

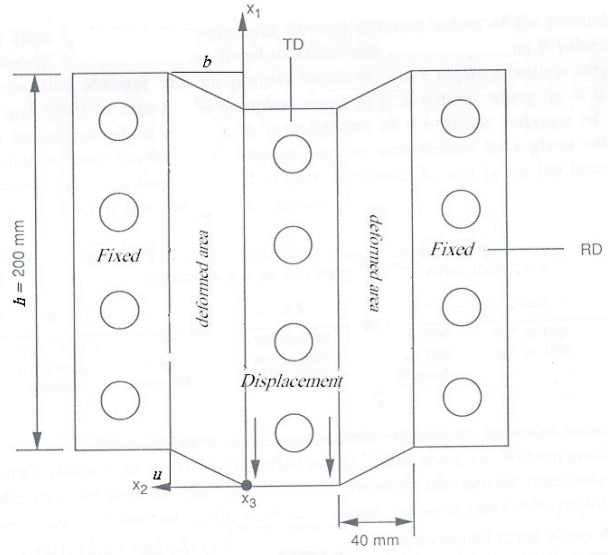

Figure 3.16 Geometry of the samples used in the pre-strain and simple shear device. Bacroix et al., 1994.

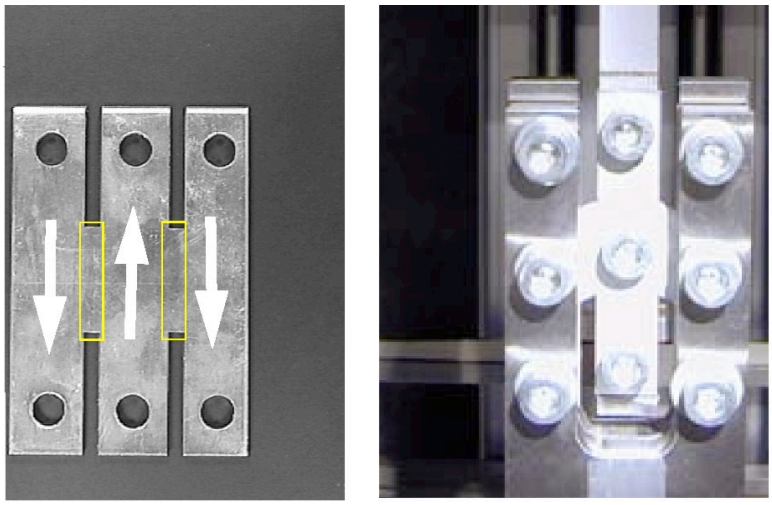

Figure 3.17 Shear test according to Miyauchi: (left) test specimen, (right) specimen fixture. Hora et al., 2000.

In this test, the two deformed areas must have a symmetric behavior, which is not the case for anisotropic materials under simple shear state. It is possible to recover the symmetrical behavior of the sheet metal by cutting the specimen and turning over one of the parts, as shown in Figure 3.18 (Genevois, 1992).

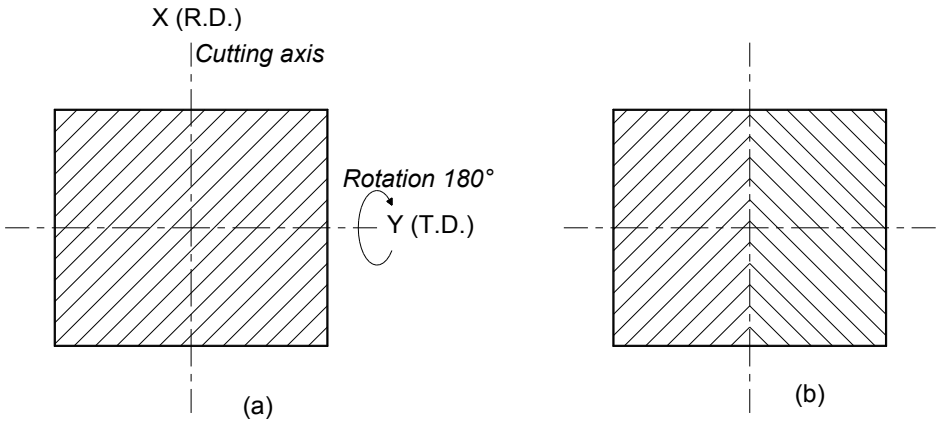

Figure 3.18 Miyauchi test specimen. (a) Cutting and turning. (b) Symmetric specimen. Genevois, 1992.

According to Rauch, 1998, for material in an orthotropic state, by symmetry across the YZ plane (or equivalently across the XZ plane) a test at (180° – α) is strictly equivalent (at and after yielding) to the reverse test at α (α: angle from the rolling direction), Figure 3.19.

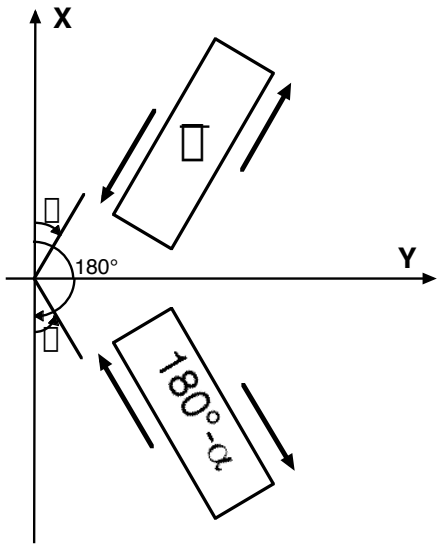

Figure 3.19 Experiment performed at (180° – α) corresponds to α (orthotropic sheets). Rauch, 1998.

Twente bi-axial test

This test was developed at the University of Twente (Pijlman, 2001). It consists of a bi-axial machine, able to combine shear with plane strain deformation. The main advantage of using a bi-axial machine is that it is possible to test sheet material behavior under multi-axial and non-proportional loads, and to study of the effect of path changing without removing the test piece.
The scheme of this test machine is presented in Figure 3.20. The arrows indicate the direction of movement caused by electrical motors. The horizontal movement imposes a simple shear test, while vertical movement, a plane strain one.

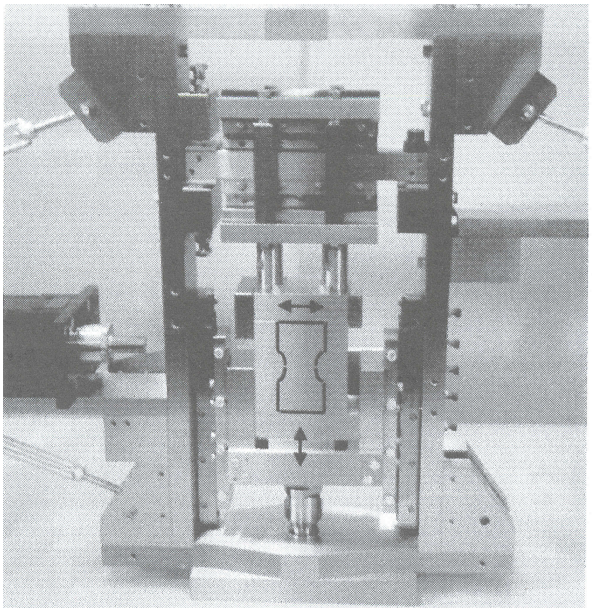

Figure 3.20 Picture of the bi-axial test equipment. Pijlman, 2001.

The test piece that is used in this machine is shown in Figure 3.21, from Pijlman, 2001. Over this specimen, a plain strain (monotonic) and a simple shear (monotonic or cyclic) test can be carried out, separately or simultaneously. The main advantages of the specimen's shape are the same as those for the Rauch, 1998 test piece.

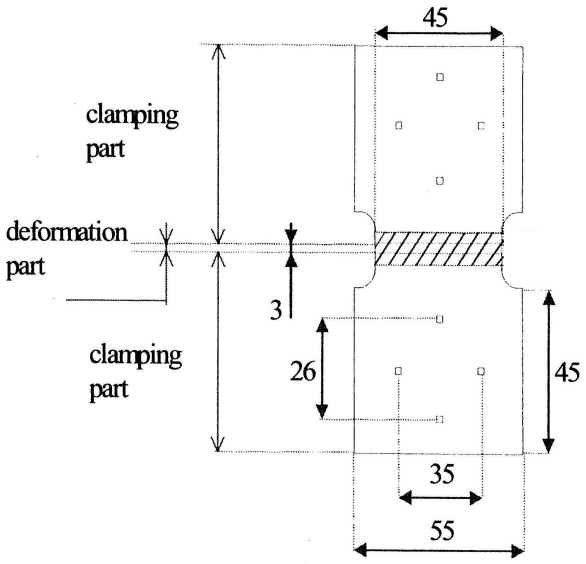

Figure 3.21 Dimensions and shape of Twente's specimen. Pijlman, 2001.

Hydraulic bulge test

This well-known test is described, for instance, in Banabic et al., 2000, and consists of a circular specimen clamped along its circumference and exposed to hydraulic pressure. For test evaluation, it should be sufficient to measure two quantities: the hydraulic pressure and the height of the dome. In practice, at least three quantities are measured to obtain more accurate results. Strains up to the order of 50% can be obtained.

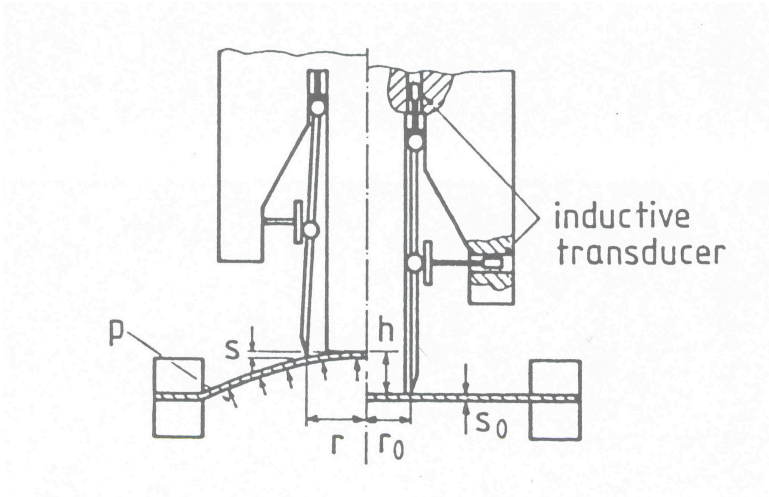

Figure 3.22 Hydraulic bulge test. Banabic et al., 2000.

Arcan apparatus

This apparatus was originally designed to investigate the bi-axial failure of unidirectional fiber-reinforced composites (Arcan et al., 1978). Many adaptations have been made ever since in order to study different materials or loadings (Petras and Sutcliffe, 2000, Mahgoub et al., 2003, Doyoyo and Mohr, 2003, or Doyoyo and Wierzbicki, 2003). The test description presented in the following paragraph is summarized from the last reference.
The Doyoyo and Wierzbicki, 2003 modified Arcan apparatus is shown in Figure 3.23a. A "butterfly-shaped" specimen is attached to two half-circular metal plates with smaller antisymmetric "cut-outs", at a 45° orientation. The plates are connected to a universal testing machine by intermediate grips via two loading pins. The two pins prohibit rotation between the Arcan assembly and the intermediate grips. Thus, when the machine applies a vertical force V, a perpendicular reaction force R, is generated. The resulting state of plane stress at the central section is shown in Figure 3.23b; x and y denote respectively coordinates perpendicular and parallel to the central section, and is the loading angle.

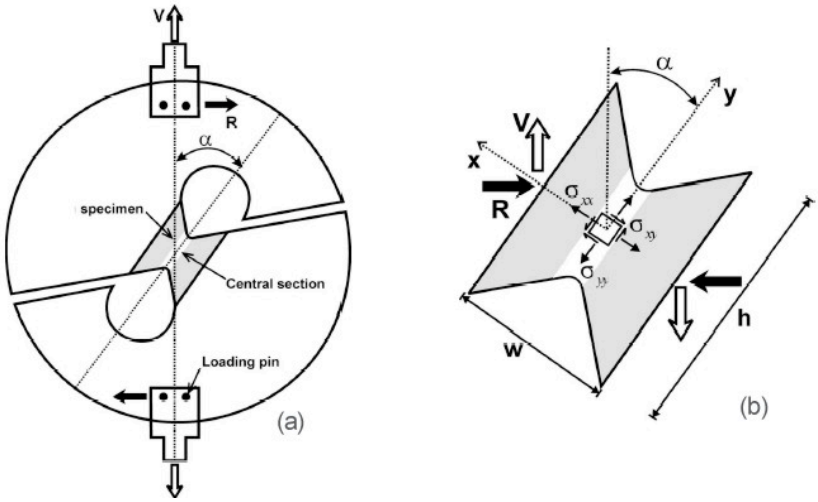

Figure 3.23 (a) A schema of the modified Arcan apparatus with a "butterfly – shaped" specimen. (b) Bi-axial state of stress at the central section of the specimen. Doyoyo and Wierzbicki, 2003.

The presence of a reaction force is the basic difference between the current setup and the original Arcan apparatus. In the original design (Arcan et al., 1978) the apparatus is joined to

the testing machine by a single loading pin, thus allowing rotations, which results in zero reaction forces. This may be appropriate for fiber-reinforced composites, which are relatively stiff solids, but for softer material, it is a disadvantage because the deformations tend to concentrate in undesirable regions of the specimen. This apparatus must include a loading cell in order to measure the reaction force during bi-axial loading.

3.2.2 Discussion

In this section, a discussion about the skills and limitations of the former described tests and a comparison between same purpose tests are presented (summarized in Table 3.2).

Kuwabara test – Inpro test

Both tests are designed on the same principle; specimens present some differences in the clamping zone. For both tests, it is important that the center of the cruciform specimen is always maintained at the center of the testing machine apparatus, so special care must be taken in the design of the centering device.
The advantages of these tests are that by altering the ratio of the forces in both directions (F1 and F2 in Figure 3.14), the stresses range from uni-axial to equi-bi-axial states. Moreover this setup can impose different deformations on the same test piece. A successive pattern of deformations can also be applied. This test has a good performance in determining initial yield locus. On the other hand, this setup permits neither a compression load in either direction, nor high strains.

Miyauchi test – G'Sell-Rauch test

One of the advantages of the Miyauchi test over the G'Sell-Rauch is that Miyauchi has a better estimation of the shear stress due to the symmetric behavior, which decreases the friction in the guiding system. Another advantage is that Miyauchi test can be performed using a standard tensile test machine by adapting an easy fabrication device. On the other hand, the G'Sell-Rauch test specimen is more favorable to the strain filed homogeneity.
An important remark has to be made if the specimen used for the Miyauchi test has the dimensions shown in Figure 3.16. In that case, a special device has to be designed in order to avoid buckling due to the deformation gauge geometry. As a result, deformation areas can no longer be visualized, preventing the use of external displacement sensors. The use of a grid or the strain calculus from the displacement piston data are two solutions. An advantage of this Miyauchi specimen geometry is that it allows cutting off smaller specimens from its deformed areas to use them as pre-strain specimens.
Besides this, both tests perform well in calculating high stress or cyclic tests.
Characteristics of G'Sell-Rauch test are identical to the simple shear test performed by Twente's bi-axial machine.

Simple shear test – hydraulic bulge test

Hora et al., 2000, recalled two disadvantages of the bulge test compared to the simple shear test. The first one is that in order to determine the stresses as a function of internal hydraulic pressure, it is necessary to know the curvature at the vertex of the cup. This measurement is often subject to large measurement errors. The second difficulty comes from the transformation of the multi-axial state into an equivalent stress state, which requires exact

knowledge of the flow locus. This locus, however, is not known precisely. Obviously, a simple shear test is not subject to these difficulties.
Both tests present a satisfactory ability to reach high strains.

Twente bi-axial test – Arcan test

Both tests allow for the study of the plane strain and shear state, either separately or simultaneously, and both specimen tests are extremely simple.
In the Arcan system, the ratio between the tensile load and the shear load is controlled by (Figure 3.23), so to change this ratio during the test is not an easy task. Twente bi-axial machine forces are controlled separately.
The Arcan apparatus is easily constructed and can be adapted into a standard tensile test machine.

Test	Kuwabara	G'Sell Rauch	Miyauchi	Twente	Bulge	Arcan
High strains	–	√	√	√	√	√
Reverse loading	–	√	√	√	–	√
Path changes	√	–	–	√	–	√
Combined loads	√	–	–	√	–	√
Easy fabrication specimen	–	√	√	√	√	√
Easy fabrication apparatus	–	–	√	–	–	√
Easy control of applied loads	√	√	√	√	√	–

Table 3.2 Summary of test skills.

3.2.3 Selection

The most adapted tests in agreement with the objective of this work are the Arcan test and the Twente bi-axial test. Even if Arcan apparatus fabrication is simpler, the control of the loads, for the purpose of this work, is much more important.
The fabrication simplicity and the small size of the Twente specimen enable us to cut them off from the Miyauchi specimen deformation areas (Figure 3.24). Due to this point and the fact that Miyauchi device is easy to make, this apparatus will be taken into consideration for further analyses.

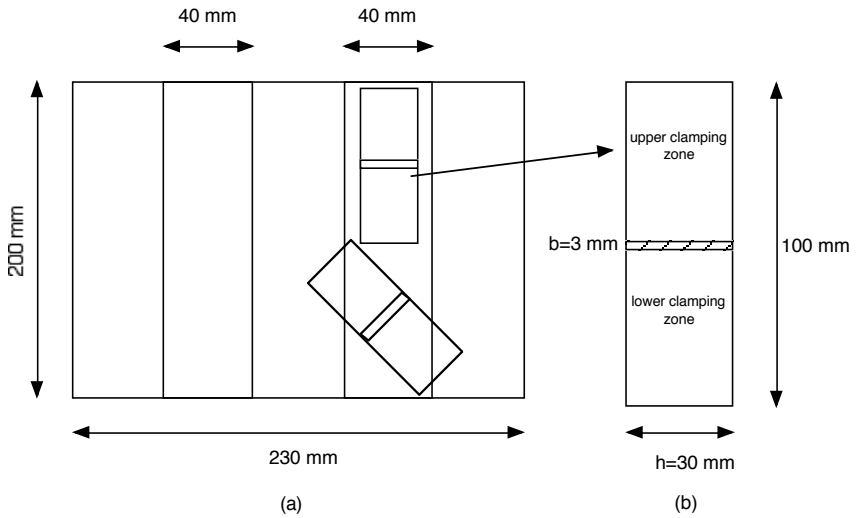

Figure 3.24 (a) Sketch of the cutting-off process, (b) specimen for the bi-axial test. The deformation area is hatched, values in mm.

Even if the bi-axial test has the best performance in the determination of the initial yield locus, it will not be taken into consideration due to its poor contribution in the determination of hardening parameters and its high implementation cost.
A more detailed analysis of Twente bi-axial and Miyauchi tests will be developed throughout this work.

3.3 Miyauchi device design and features

This device allows for a reverse simple shear test and can be implemented in any tensile test machine. The specimen geometry used here is designed to have a wide deformation zone in order to allow for the extraction of pre-strained specimens to be deformed in the bi-axial machine (Bacroix et al., 1994).
Due to the required geometry of the specimen, buckling might develop. To avoid this, it is necessary to prevent the out-of-plane deformation. The design sketches are shown in Figure 3.25 and Figure 3.26. To impede the out-of-plane deformation and friction between parts 1 (or 2) and the specimen, a 1 mm gap is maintained in order to add Teflon® sliding sheets (Figure 3.26).

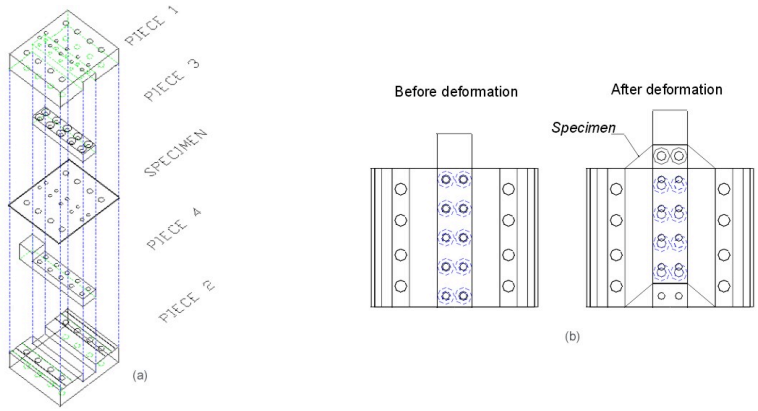

Figure 3.25 (a) Sketch of the device, (b) Scheme of the deformation procedure.

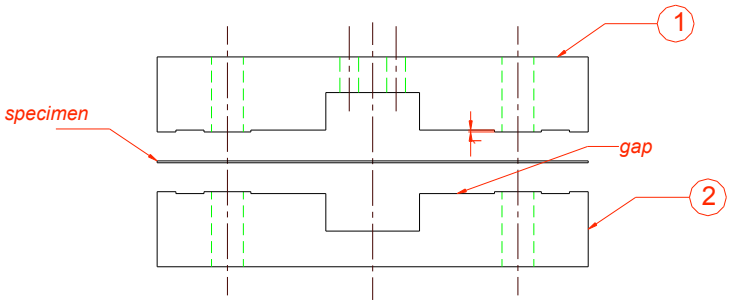

Figure 3.26 Gap between part 1 (or 2) and the specimen in order to add lubrication sheets.

The finished device and its adaptation to a tensile test machine are shown respectively in Figure 3.27 and Figure 3.28.

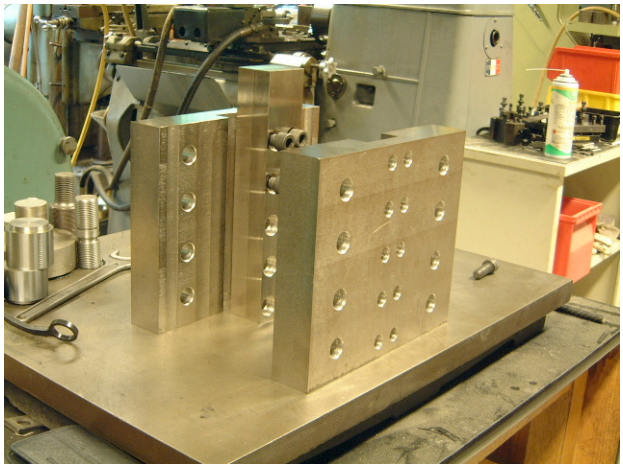

Figure 3.27 Miyauchi device.

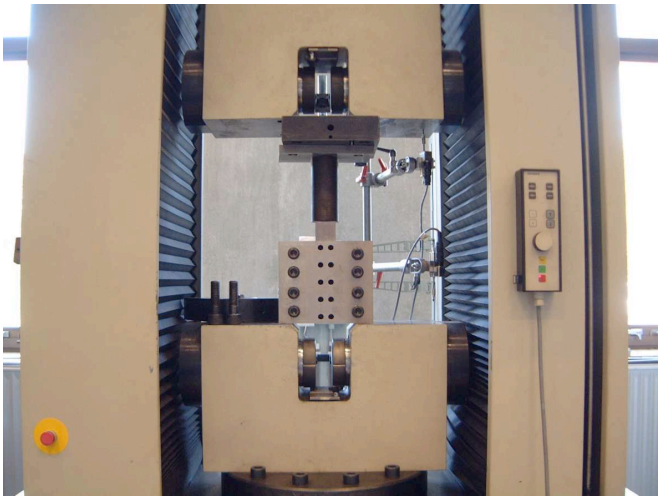

Figure 3.28 Miyauchi device in a tensile test machine

Figure 3.29 shows various samples after deformation. The non-deformed specimen is presented in Figure 29a. Figure 29b shows buckling produced in the absence of Teflon sheets. Undesirable plastic deformation at the grip zones is observed in Figure 29b and Figure 29c.

To avoid this undesirable effect, the grip zones were sanded to increase friction. A satisfactory result is displayed in Figure 29d.

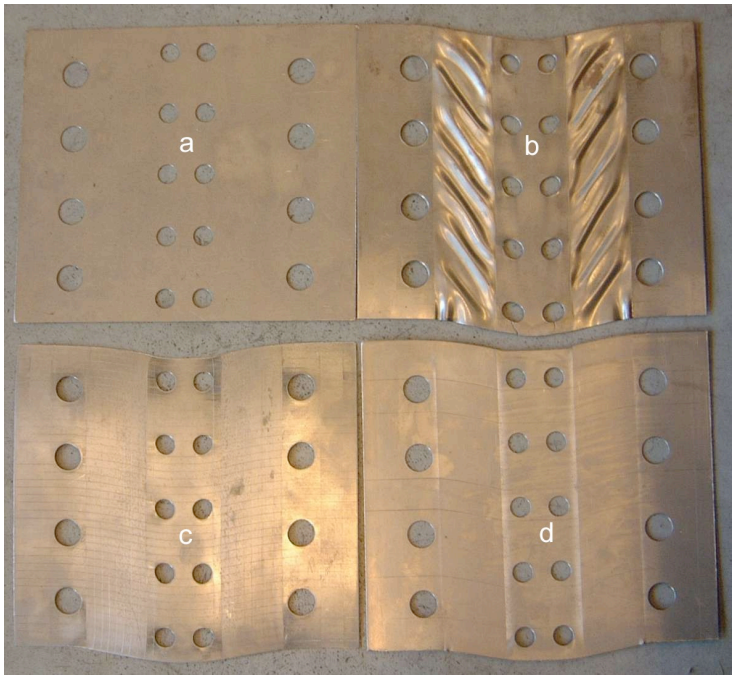

Figure 3.29 a) Undeformed specimen (200 mm x 240 mm), b) buckling, c) plastic deformation around the holes, d) deformation only in strain gauges device

More details on the test design can be found in (Flores 2003).

The force required to attain the desired deformation depends on the material resistance and on the sheet thickness. To compute the approximate ultimate force, the following formula, obtained from the von Mises equivalent stress definition (Equation 2.58), is used:

$$F_u \approx \frac{1}{\sqrt{3}} \sigma_u^t (2 \cdot h \cdot t) \,, \tag{3.38}$$

where t and h are depicted in Figure 3.30 and σ_u^t is the value of the ultimate uni-axial stress obtained from a tensile test.

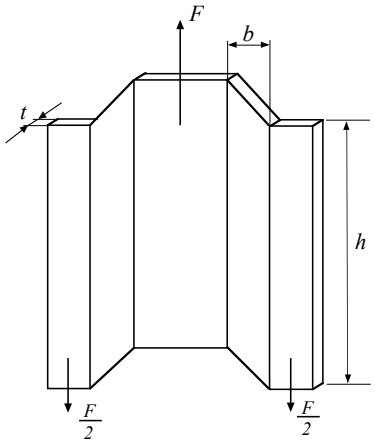

Figure 3.30 Forces on a Miyauchi specimen.

Table 3.3 shows the required forces for different sheet thicknesses and for different material resistances.

Specimen geometry		**Ultimate force kN**		
Thickness *t*	Deformed area	σ_u^t = 600 MPa	σ_u^t = 800 MPa	σ_u^t = 1400 MPa
0,7 mm	*h* = 200 mm *b* = 40 mm	96,99	129,33	226,32
1,5 mm	*h* = 200 mm *b* = 40 mm	207,85	277,13	484,97
2 mm	*h* = 200 mm *b* = 40 mm	277,13	369,50	646,63
3 mm	*h* = 200 mm *b* = 40 mm	415,69	554,26	969,95

Table 3.3 Required forces for Miyauchi simple shear test.

3.4 Bi–axial machine design and features

The original idea of this machine is taken from Pijlman, 2001. The mechanical design is based on stocked equipment such as hydraulic grips (originally designed for a tensile test) and hydraulic pistons of 10MPa capacity that serve as the reference for the dimension of the structure and the selection of guiding systems and load cells.
The arrows in Figure 3.31 show the machine movement axes. The motion is generated by two hydraulic pistons, which can be controlled in displacement or force simultaneously or independently. These motions enable us to perform simple shear and plane strain tests.
The acquisition system allows us to stock mechanical data such as piston force, piston displacement and the strain field.
The complete design can be found in Flores, 2003.

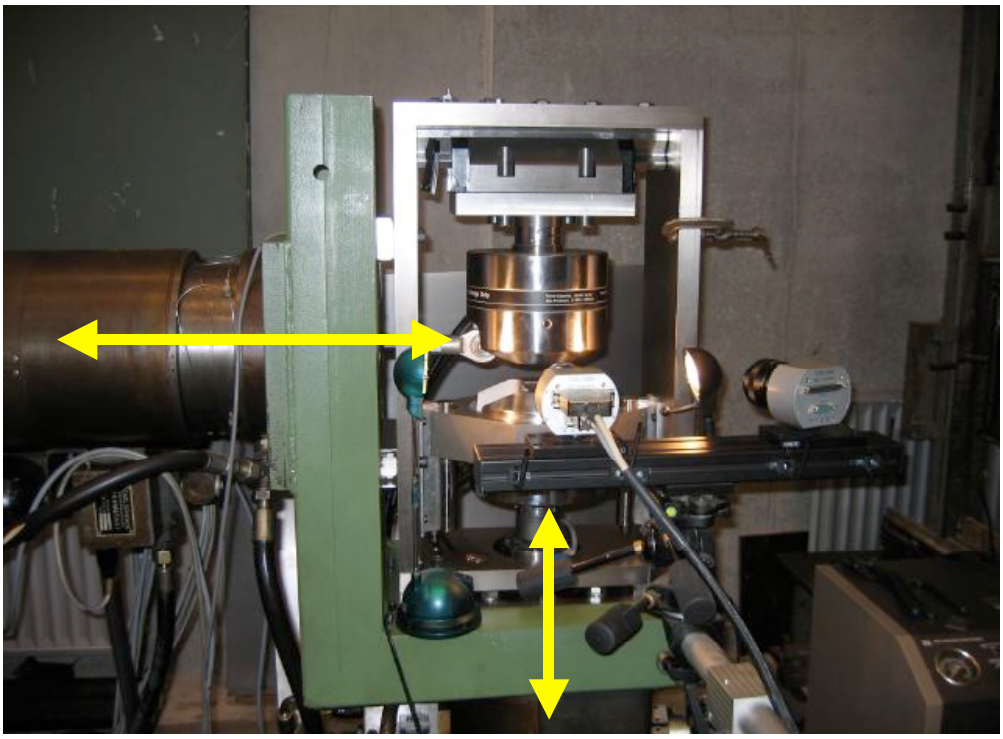

Figure 3.31 Bi-axial machine designed at the M&S Laboratory, University of Liege.

Figure 3.32 shows some close-up pictures of important mechanical elements of the testing machine.

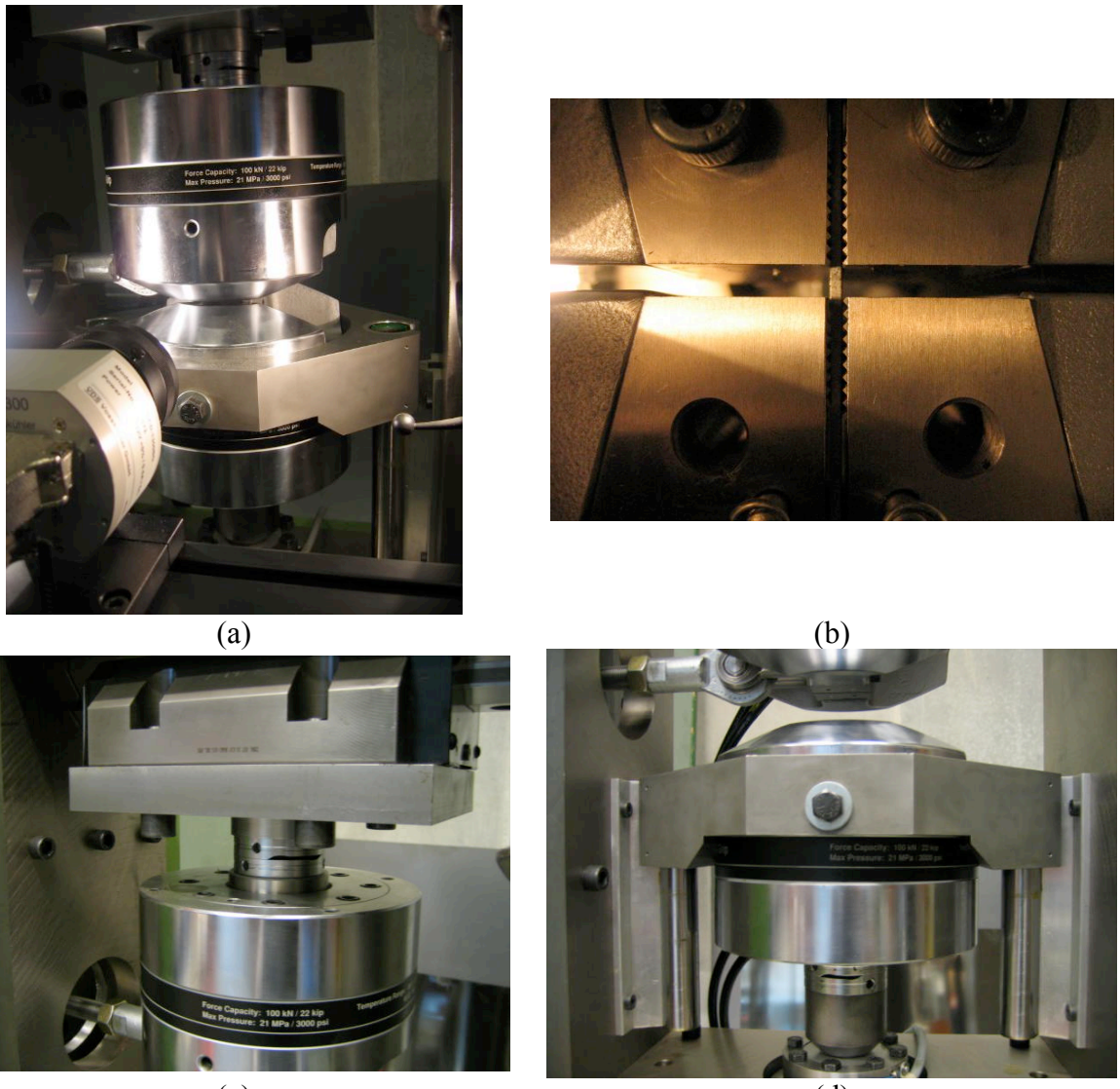

Figure 3.32 (a) Detailed view of the installed grips. (b) Specimen clamped by the grip's wedges. (c) Horizontal linear guide system INA series RUE 65 installed. (d) Vertical linear guide system.

The control system schema is shown in Figure 3.33. The force and displacement signals come from the respective sensors (load cells and displacement sensors) to the processor (PC) passing through an amplifier and analog/digital (A/D) converter. The processor has several functions such as, the data acquisition, security limit definition, hydraulic power control, function generator and PID tuning. The output signals coming from the processor pass through a D/A converter to act on the servo-valves (SV) that feed the pistons.

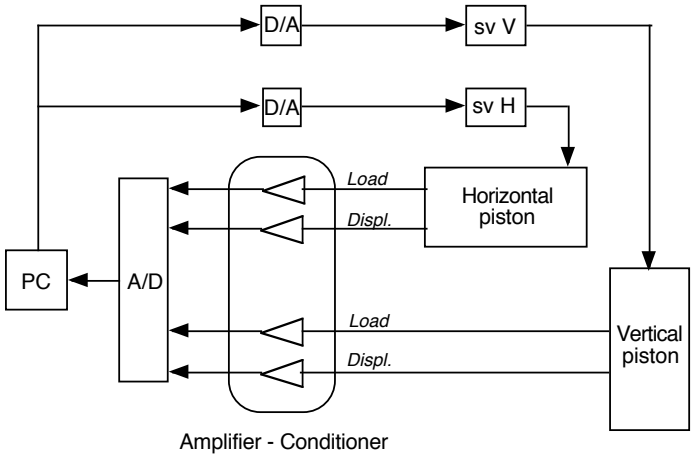

Figure 3.33 Control system schema.

A software application enables the user to manage the controlled variable used (force or displacement of the pistons) and the active piston (one or two, vertical or horizontal), among other tasks.
Mechanical features of the control system are summarized in Table 3.4 for the displacements and Table 3.5 for the forces.

	Maximum displacement mm	Minimum displacement mm	Maximum velocity mm/s	Minimum velocity mm/s
Horizontal motion	50	-50	1000	0,00005
Vertical motion	10	-10	1000	0,00005

Table 3.4 Features of the displacement control.

	Maximum force kN	Minimum Force kN	Maximum velocity kN/s	Minimum velocity kN/s
Horizontal motion	50	-50	2	$1x10^{-7}$
Vertical motion	50	-50	2	$1x10^{-7}$

Table 3.5 Features of the force control.

Vertical load capacity is limited by the vertical load cell, i.e., 50kN. Horizontal load is mainly limited by the grips' performance since these are originally designed for tensile tests (vertical load). Annex B shows that horizontal load should not be greater than 25kN. Table 3.6 contains the values of the actual loads that can be imposed by the machine.

	Maximum force kN	Minimum Force kN	Maximum velocity kN/s	Minimum velocity kN/s
Horizontal motion	25	-25	2	$1x10^{-7}$
Vertical motion	50	-50	2	$1x10^{-7}$

Table 3.6 Actual applicable loads.

The specimen thickness is limited by the grip's wedges geometry as is shown in Figure 3.34. It can be seen that the grips completely cover the grip's wedges and part of the specimen, impeding the measurement of the whole strain field.
The maximum specimen thickness is then limited to 1,6mm (experimentally tested). The minimum thickness is recommended to be greater than 0,5mm.

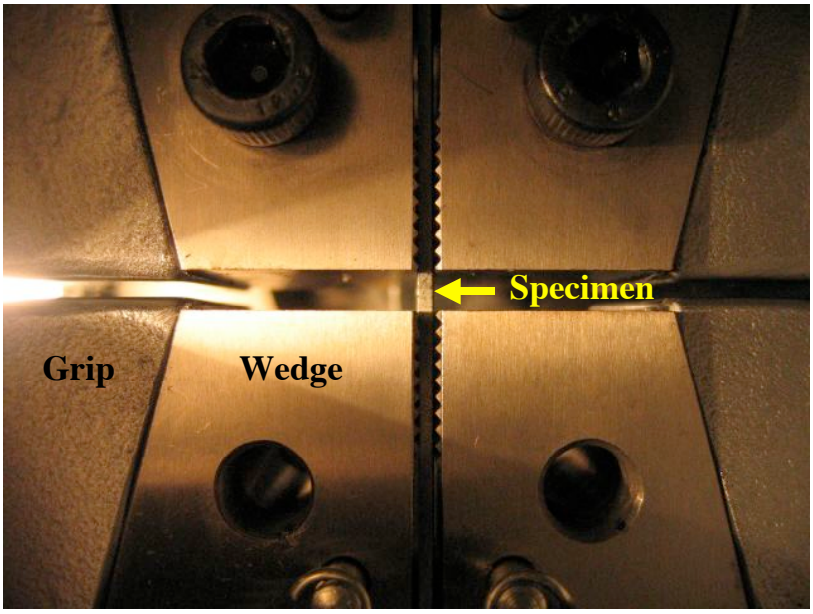

Figure 3.34 Thickness limiting factor. Grips cover part of the specimen measurable zone.

Von Mises criterion (Equation 2.58) is used to compute the approximate ultimate tensile strength in order to identify the grades of materials that can be tested in this testing machine. The simple shear test is approximated by the pure shear stress state:

$$\sigma_u^t = \sqrt{3}\frac{F_{horizontal}}{h \cdot t} \tag{3.39}$$

then, the ultimate strength for the limiting thickness are:

$$\begin{aligned} \sigma_u^t(t = 0{,}5mm) &= 3460MPa \\ \sigma_u^t(t = 1{,}6mm) &= 900MPa \end{aligned} . \tag{3.40}$$

Plane strain stress state is approximated by (Flores, 2003):

$$\sigma_u^t = \frac{\sqrt{3}}{2}\frac{F_{vertical}}{h \cdot t} \tag{3.41}$$

giving the following maximal strength values:

$$\begin{aligned} \sigma_u^t(t = 0{,}5mm) &= 2880MPa \\ \sigma_u^t(t = 1{,}6mm) &= 900MPa \end{aligned} . \tag{3.42}$$

The specimen geometry appears in Figure 3.24b. This geometry is compared with the one presented in Figure 3.21 in Annex C.

3.5 Measurement system description

An optical measurement system called Aramis® (Gom, 2001) is chosen to measure the deformations of the specimen. It has been demonstrated that the performance of such a system is optimal for measuring complex deformation paths (Knockaert, 2001, Mistou et al., 2003 and Orteu, 2003). In addition, the optical system avoids the possible errors that migth appear due to sliping of the specimen under the grips. This section aims to describe the features and functional principles of the chosen system.
Annex D shows the tuning up of this application for measuring the strain field in bi-axial type specimens.

3.5.1 Technical characteristics

- Simple preparation of the specimen: high contrast pattern.
- Large measuring area: mm^2 – m^2.
- Strain range of 0,05% up to several 100%.
- 2D analysis (1 camera).
- 3D analysis (2 cameras).
- Flexibility, mobility.

3.5.2 Functional Principle

The application Aramis® detects displacements using optical measurement techniques. Once the displacement has been determined the material's strains can be computed.
Aramis® recognizes the surface structure in digital images and can allocate coordinates to every pixel in the image. The initial coordinates are recorded as the reference image, displaying the object of measurement in its undeformed state. After the object of measurement has been deformed, a second image is recorded. At that point, Aramis® compares the images and can register any displacement of object-characteristics (Gom, 2001).
All images correlation systemes use a random pattern so that the aspect of the surface at one point is, at least locally, unique. It is then possible to recognize and to locate a given point in several images. In practice, the images are divided into small squares called "facets". These facets are characterized by their grey level distribution. This procedure can be summarized as follows (Knockaert, 2001):

- Pictures of the part are taken before and after the deformation.
- As mentioned previously, an image of the undeformed configuration is taken as a reference and divided into small squares called "facets". The size of the facets has to be chosen with respect to the aspect of the surface.
- Then, the system tries to match the grey level distribution of these facets with the grey level distribution around one point of the deformed image. This matching operation is possible thanks to a transformation applied to the facets. This transformation is a combination of a translation, a rotation and a distortion.

The analysis can be done in 2D or 3D. For the 2D case, the analyzed surface must remain planar and at a constant distance from the camera, Figure 3.35.

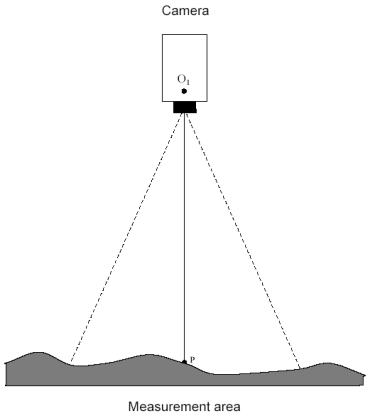

Figure 3.35 Functional principle of Aramis® 2D. Gom, 2001.

The 3D measurements require two cameras, which reconstitute a 3D image using 2D images (Figure 3.36). The locations of the points in space are determined by triangulation of directional bundles. The 3D coordinates of an object-point can then be determined by the intersection point of straight lines (Figure 3.37).

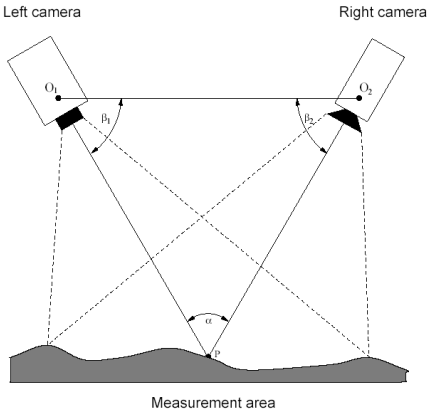

Figure 3.36 Functional principle of Aramis® 3D. Gom, 2001.

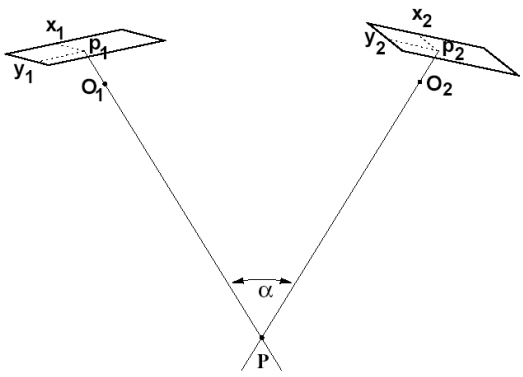

Figure 3.37 Principle of a 3D measuring arrangement. Gom, 2001.

It is necessary to calibrate before performing image acquisition. The calibration is used to identify the geometric parameters required for the transformation (distance and angle between cameras), and to quantify the optical errors in order to take them into account in computing displacements or strains. A calibration object with a given arrangement of points is measured and recorded from different positions with respect to the measuring system (Figure 3.38).

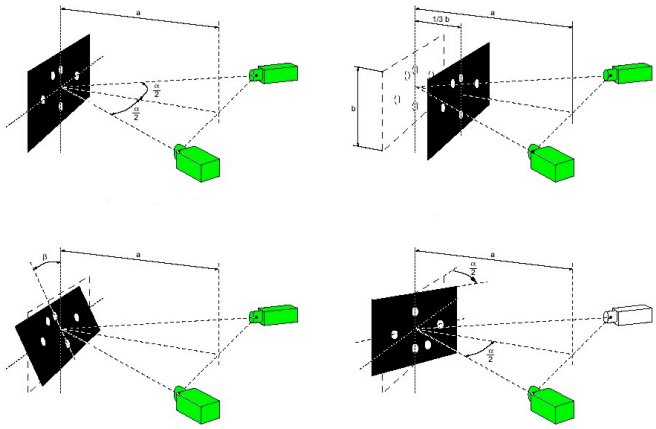

Figure 3.38 Different positions for the calibration object. Gom, 2001.

The individual points of the calibration object are identified and their respective coordinates are determined with high sub-pixel accuracy. Then, the parameters of the cameras and the coordinates of all points involved in the calibration are determined using the least squares adjustment method.
In the 3D case, two images of the undeformed part and two images of the deformed part are taken. Three steps of correlation are carried out between one of the images considered as a reference image and the three others ones. Then, the system is able to compute the 3D displacement field on the surface of the part.

3.5.3 Strain computation

The relative displacements of neighboring points are used for the computation of the strains on the specimen's surface. Several methods are available in Aramis®. One of these is to compute the length of the sides of a facet defined by four nodes. For that purpose, splines are constructed around nodes of the facet and neighboring nodes. This approach allows for an accurate computation of the real length of the sides. These lengths are used to construct a quadrangle in two-dimensional space. The deformation gradient **F** is then computed for the center of gravity of the facet by least square adjustment (Knockaert, 2001); see Figure 3.39.

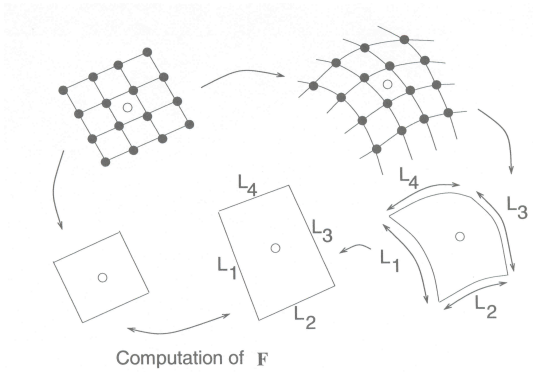

Figure 3.39 Measurement of the effective distortion of a facet using spline interpolation. Knockaert, 2001.

Then polar decomposition of **F** makes it possible to compute the stretch tensor **U** (Equation 2.20), which has the following form defined by Gom, 2001 (see also Equation 2.21 for $n = 1$):

$$\mathbf{U} = \begin{bmatrix} u_{11} & u_{12} \\ u_{12} & u_{22} \end{bmatrix} = \begin{bmatrix} 1+\varepsilon_{xx} & \varepsilon_{xy} \\ \varepsilon_{xy} & 1+\varepsilon_{yy} \end{bmatrix}. \tag{3.43}$$

Transformation of **U** in diagonal form leads to the computation of the principal stretch ratios λ_1 and λ_2 :

$$\lambda_1 = 1 + \frac{\varepsilon_{xx}+\varepsilon_{yy}}{2} + \sqrt{\left(\frac{\varepsilon_{xx}+\varepsilon_{yy}}{2}\right)^2 + \left(\varepsilon_{xx}\varepsilon_{yy} - \varepsilon_{xy}^2\right)}, \tag{3.44}$$

$$\lambda_2 = 1 + \frac{\varepsilon_{xx}+\varepsilon_{yy}}{2} - \sqrt{\left(\frac{\varepsilon_{xx}+\varepsilon_{yy}}{2}\right)^2 + \left(\varepsilon_{xx}\varepsilon_{yy} - \varepsilon_{xy}^2\right)}. \tag{3.45}$$

The principal strains can then be computed using various strain definitions:

- Technical strains: $\varepsilon_i^T = \lambda_i - 1$, (3.46)
- Logarithmic strains: $\varepsilon_i^{ln} = \ln(\lambda_i)$, (3.47)
- Green-Lagrange strains: $\varepsilon_i^{GL} = \frac{1}{2}\left(\lambda_i^2 - 1\right)$, (3.48)

where i=1 or 2.
The third component is computed assuming conservation of volume while plastic deformation takes place, i.e.:

$$\lambda_1\lambda_2\lambda_3 = 1. \tag{3.49}$$

3.6 Conclusions

Throughout this chapter, the study of the stress – strain states needed to identify material behavior has been addressed; in addition, a review of testing equipment used to reproduce the required mechanical states is presented.
A Miyauchi device for simple shear testing has been fabricated. This device allows for a reverse simple shear test and can be implemented in any tensile test machine. The specimen geometry used here has been designed to have a wide deformation zone in order to allow the extraction of pre-strained specimens to be tested in the bi-axial machine.
A bi-axial testing machine able to perform plane strain and simple shear tests separately or simultaneously has been fabricated. The small size of its specimen enables to cut them off from the Miyauchi specimen deformation areas.
The testing machine load limits are 50kN in tension and 30kN in simple shear. The specimen's thickness must be higher than 0,5mm and smaller than 1,6mm. To test thicker specimens, the grip wedges must be replaced and the required load must be verified.
An optical strain gauge is used to measure the strain field. This non-contact method directly measures the material strain, avoiding error sources such as sliding or machine rigid displacements.

CHAPTER 4

EXPERIMENTAL EQUIPMENT VALIDATION

The mechanical equipment presented in the former chapter is designed to reproduce two particular stress – strain states: the plane strain state and the simple shear state. An optical strain gauge is adopted to measure the strain field in the specimen. Annex D shows the tests performed to study the performance of the optical measurement in small and moderately large strains.
This chapter verifies that the mechanical equipment, together with the chosen specimen's geometry, can reproduce the required stress – strain states.

The first analysis consists in verifying the stress – strain field homogeneity in the measurable zone of the bi-axial machine specimen. The first step is to measure the strain field experimentally using the optical strain gauge for both types of tests, i.e., plane strain and simple shear. The second step is focused on the stress field. This step is carry out numerically by a finite element analysis and it consists in comparing the stress field values (by taking an average value from each finite element) with the global stress obtained from the force per unit of area. The idea is to show that this last measure can represent the stress average value. These results are also compared with the results obtained for a single element analysis.

Once the stress – strain field homogeneity is verified, the second analysis consists in comparing the mechanical test results (plane strain, simple shear, Bauschinger, and orthogonal) performed by the bi-axial machine or the Miyauchi device with finite element simulations. Mechanical tests have been performed for a dual phase steel DP600 of 0,7mm thickness. Bouvier et al., 2002 identified the Hill 1948 and Teodosiu and Hu parameters for this material. Numerical simulations of the mechanical tests mentioned before, performed with those material parameters, are used to check the forces measured by our equipment. The numerical simulations are done over a single element mesh due to the results obtained in the previous analysis. The mechanical flow stress obtained from the load cell data and from the current specimen's area is compared with the one obtained at the integration point of the finite element.
Dual phase steel DP600 is chosen for validation due to its mechanical behavior. It presents a significant Bauschinger effect and work hardening stagnation dependent on the amount of pre-strain when strain-path changes take place. Bouvier et al., 2002 show that this hardening law can predict DP600 behavior even if it was developed for monophase steels.

A third analysis consists in studying the bi-axial testing machine performance when testing different materials with different strength limits. This analysis gives an idea of the machine performance at low force levels.

Finally, some conclusions are established and some improvements are proposed.

4.1 Stress – strain field distribution

The specimen geometry designed for the bi-axial testing machine (Figure 3.31) is shown in Figure 4.1 where the dotted area is the measurable zone. The deformation is imposed by the pistons (vertical or horizontal) of the bi-axial testing machine.
The strain field can be measured in the whole deformation zone (due to the optical strain gauge), and the average stress is computed from the load cell data and the actual area. This last assumption is only valid if the stress field is homogeneous.
This section verifies whether the chosen geometry shows the conditions under which the stress and strain fields can be considered homogeneous and the free edge effect neglected (Genevois, 1992 and Bouvier et al., 2005).

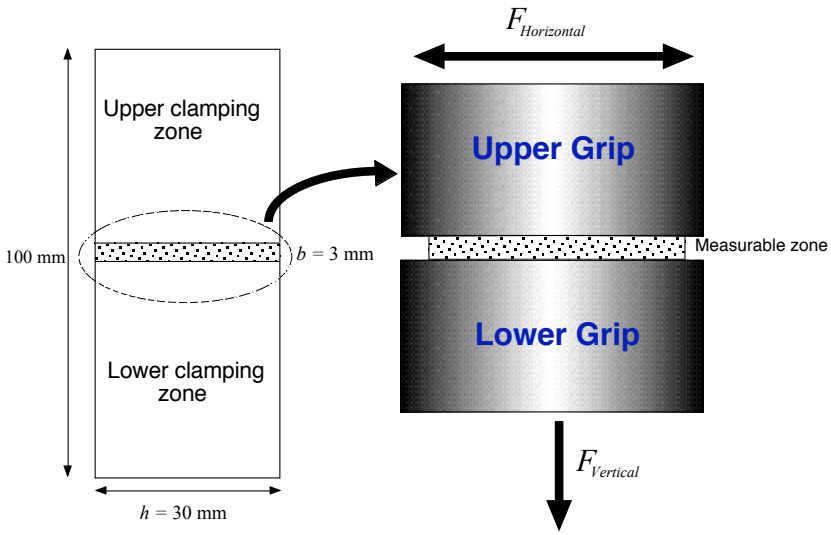

Figure 4.1 Specimen geometry and deformation area.

4.1.1 Plane strain test

The plane strain test diagram is shown in Figure 4.2. The stress tensor is represented by:

$$\boldsymbol{\sigma} = \sigma_{11}\mathbf{e}_1 \otimes \mathbf{e}_1 + \sigma_{22}\mathbf{e}_2 \otimes \mathbf{e}_2 \tag{4.1}$$

with

$$\sigma_{11} = \frac{F_{vertical}}{A_{actual}} \begin{matrix} \text{vertical load cell} \\ \text{optical strain measurements} \end{matrix} . \tag{4.2}$$

$F_{vertical}$ is the load measured by the load cell and A_{actual} is the actual area of the specimen measured at the central line. The stress measured in that way will be called “global” stress and represents the average stress over the deformation zone.
The component σ_{22} cannot be measured with this mechanical configuration.

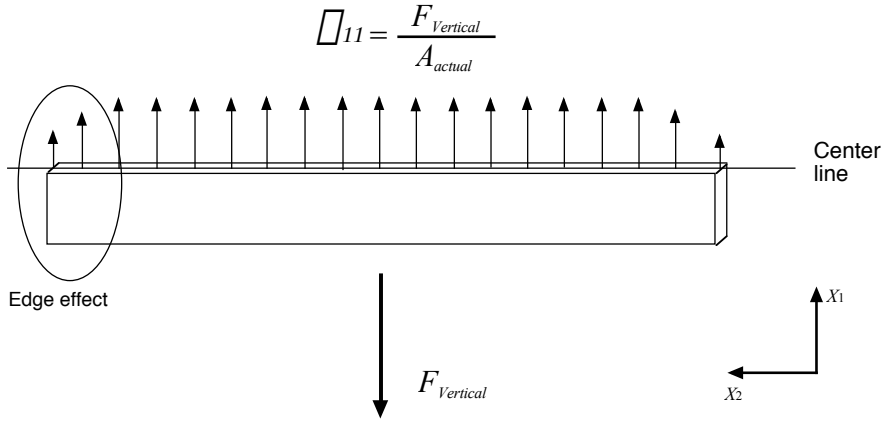

Figure 4.2 Plane strain test diagram.

A_{actual} is computed from the thickness reduction at the centerline level (Figure 4.2). This thickness reduction is computed by using the conservation of volume assumption (Equation 3.49).
The strain tensor is written as:

$$\boldsymbol{\varepsilon} = \varepsilon_1 \mathbf{e}_1 \otimes \mathbf{e}_1 + \varepsilon_{22} \mathbf{e}_2 \otimes \mathbf{e}_2 + \varepsilon_{33} \mathbf{e}_3 \otimes \mathbf{e}_3 \,. \tag{4.3}$$

In Section 3.1.3 the condition $\varepsilon_{22} = 0$ is established; hence, from plastic volume conservation and using the logarithmic strain tensor (Equation 2.22) we have:

$$\varepsilon_{33}^{\ln} = -\varepsilon_{11}^{\ln} \tag{4.4}$$

then

$$A_{actual} = A_0 \cdot \exp\left(-\varepsilon_{11}^{\ln}\right) , \tag{4.5}$$

where A_0 is the initial area of the undeformed specimen defined by $A_0 = h \cdot t$ (t being the specimen thickness).
Figure 4.3 shows the experimental $\varepsilon_{11}^{\ln}$ strain distribution in the whole deformation area. Figure 4.4, Figure 4.5, Figure 4.6 and Figure 4.7 show the experimental strain field distribution at the centerline level for the respective strain components $\varepsilon_{11}^{\ln}$, $\varepsilon_{22}^{\ln}$, $\varepsilon_{33}^{\ln}$ and the von Mises equivalent strain $\varepsilon_{vonMises}$ (Equation 4.6) at different strain levels (until $\varepsilon_{11}^{\ln} = 0{,}11$). The test is done over a DP600 dual-phase steel of 0,7mm thickness.

$$\varepsilon_{vonMises} = \sqrt{\frac{2}{3}\boldsymbol{\varepsilon} : \boldsymbol{\varepsilon}} \,. \tag{4.6}$$

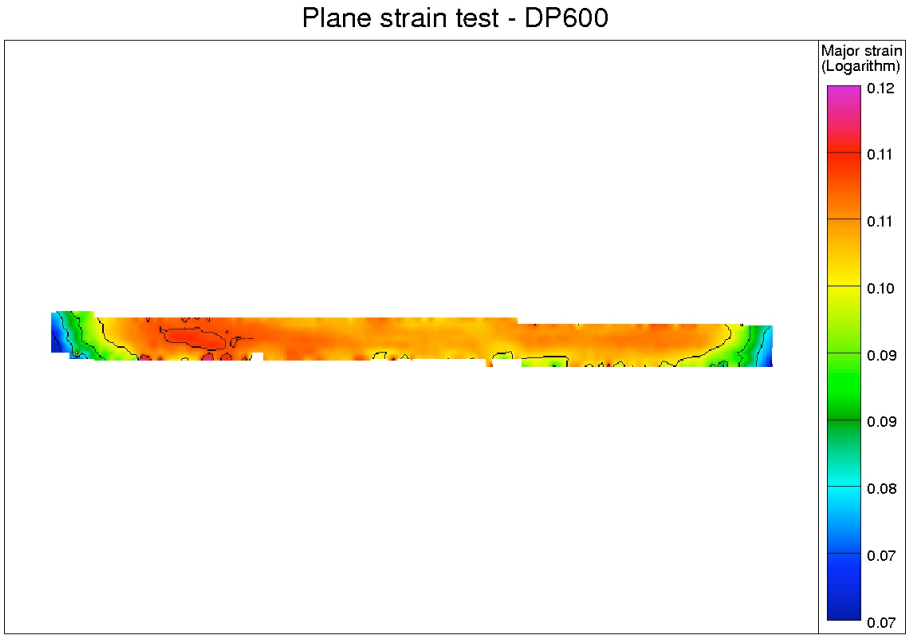

Figure 4.3 Major strain field for a plane strain test. DP600 0,7mm.

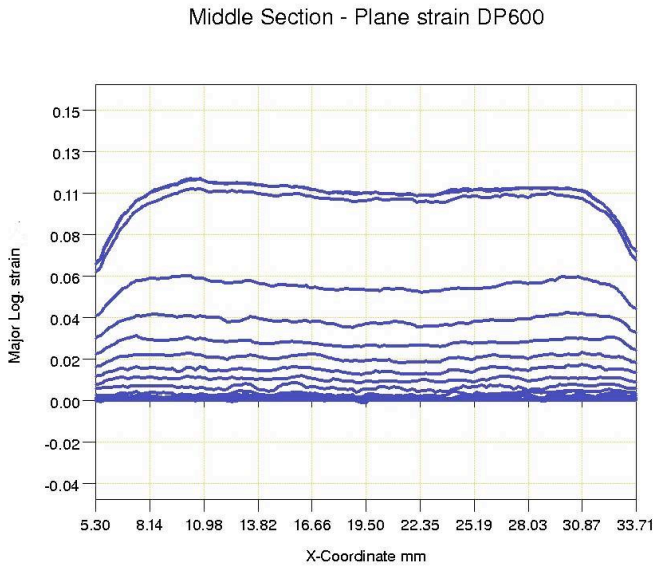

Figure 4.4 ε_{11}^{ln} component at the centerline for different levels of major strains in plane strain test (DP600 0,7mm thick).

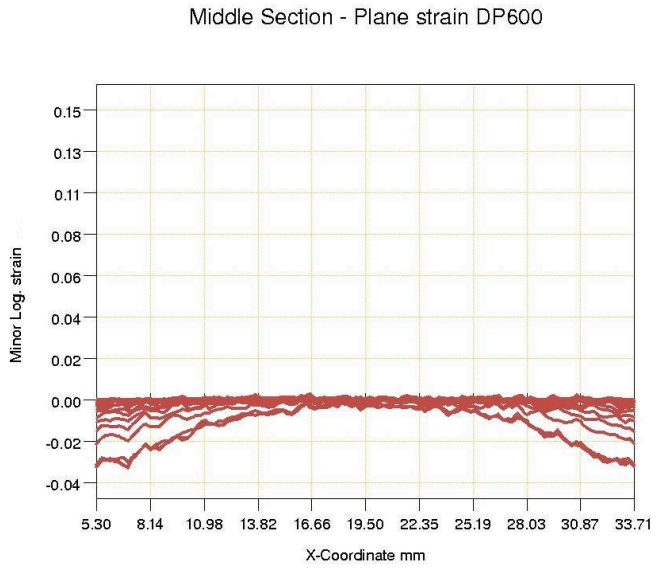

Figure 4.5 ε_{22}^{ln} component at the centerline at different levels of major strains in plane strain test (DP600 0,7mm thick).

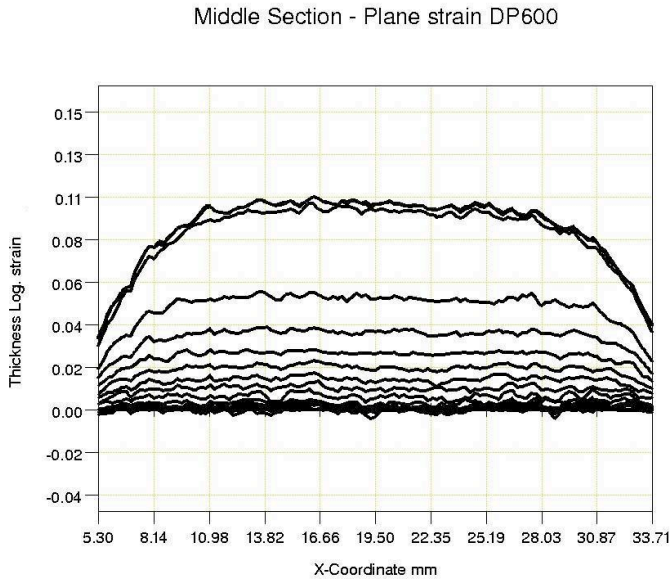

Figure 4.6 ε_{33}^{ln} component at the centerline for different levels of major strains in plane strain test (DP600 0,7mm thick).

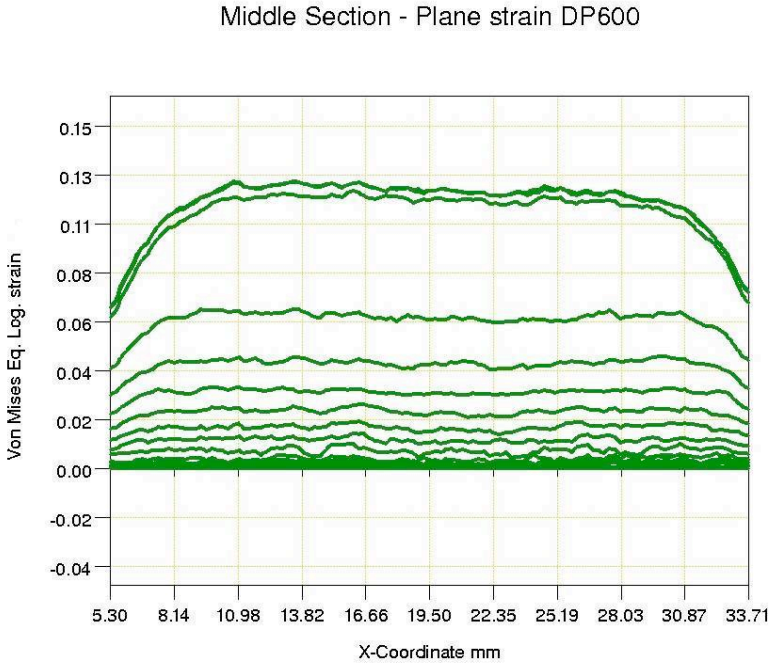

Figure 4.7 $\varepsilon_{vonMises}$ component at the centerline at different levels of strains in plane strain test (DP600 0,7mm thick).

The following conclusions can be drawn from these results:

- The strain tensor is homogeneous over the deformation area except at the free edges.
- The homogeneity depends on the amount of strain ε_{11}^{ln}.
- The strain component ε_{22}^{ln} is negligible in the homogeneous zone of the deformation area.
- The condition $\varepsilon_{33}^{ln} = -\varepsilon_{11}^{ln}$ is valid over the homogeneous zone of the deformation area.

The influence of the free edges over the stress field is studied in what follows by a finite element simulation of a plane strain test. DP600 (0,7mm thickness) material data are obtained from Bouvier et al., 2002. Two studies have been done: a single element simulation and a 707-element simulation (Figure 4.8). Table 4.1 summarizes the finite element simulation data, and Table 4.2, the material parameters for the constitutive law. The chosen element for these simulations is an eight-node mixed-type brick element with one integration point called BWD3D (Duchene et al., 2005), using the new approach for suppressing locking and hourglassing developed by Wagoner and Wang, 2004. It is an improvement on the BLZ3D element (Zhu and Cescotto, 1994).

Finite element simulation data	
Code	Lagamine
Element type	BWD3D – 1 integration point
Constitutive law	Hill3D_KI (Hill 1948 + Teodosiu and Hu hardening law)
Material	DP600 0,7mm thick

Table 4.1 Finite element strategy.

Hill 1948 material parameters (Equation 2.59)												
F			G			H			$N=M=L$			
0,898			1,143			0,857			3,06			
Teodosiu and Hu hardening parameters (Section 2.5)												
R_0	C_R	R_{SAT}	C_X	X_{SAT0}	m	q	C_{SD}	C_{SL}	S_{SAT}	n_p	n_L	C_P
285 MPa	37,6	110,8 MPa	55,7	169,4 MPa	0,631	0	5,6	0	330,7	664,5	0	0,54

Table 4.2 DP600 material parameters.

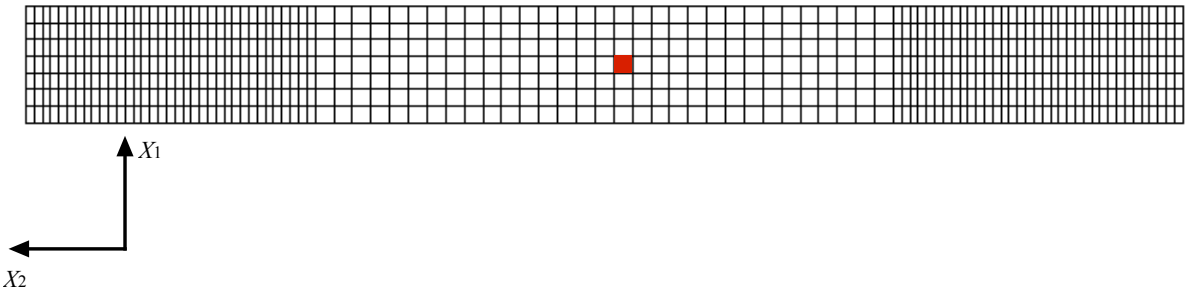

Figure 4.8 707-element mesh. Central element in red.

The variables to be analyzed are defined as follows:

- σ^{1el} (ε^{1el}) is the stress (strain) component σ_{11}, (ε_{11}) at the element integration point of the single element mesh.
- σ^{707el}_{center} ($\varepsilon^{707el}_{center}$) is the stress (strain) component σ_{11} (ε_{11}) at the center element integration point (Figure 4.8) of the 707-element mesh.
- σ^{707el}_{ave} ($\varepsilon^{707el}_{ave}$) is the average stress (strain) component σ_{11} (ε_{11}) computed from each element integration point of the 707-element mesh.
- σ^{707el}_{global} is the stress obtained from the resulting force per unit of area (Equation 4.2). The actual area (Equation 4.5) is computed from the strain at the central element.

Figure 4.9 and Figure 4.10 respectively show the stress and the strain field in the measurable zone for a $\varepsilon_{11} = 20\%$. Figure 4.11 shows the stress – strain curves obtained for the previously mentioned variables.

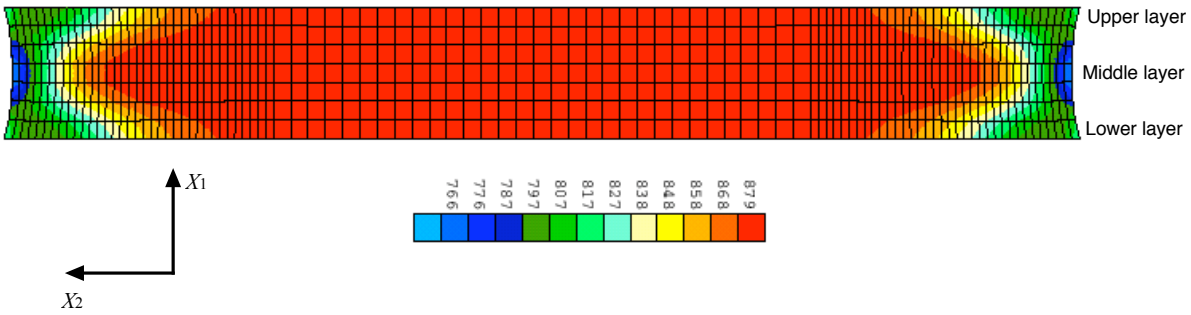

Figure 4.9 Stress (σ_{11}) field for plane strain test. DP600 0,7mm.

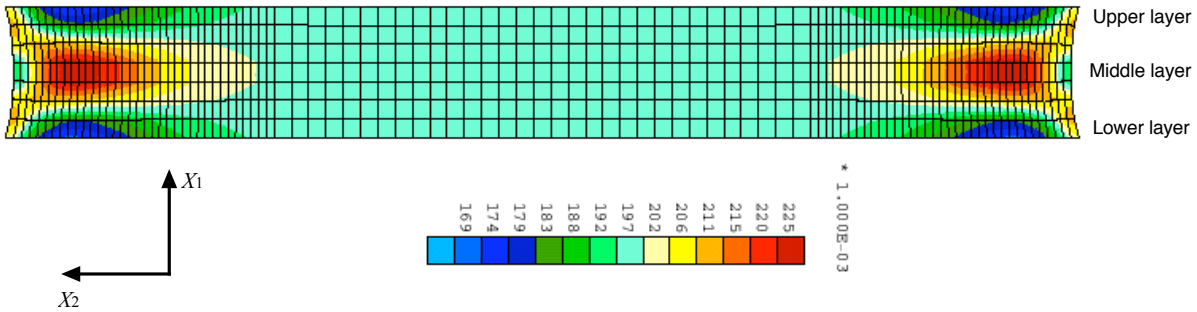

Figure 4.10 Strain (ε_{11}) field for plane strain test. DP600 0,7mm.

It can be seen that curves obtained from $\varepsilon^{1el} - \varepsilon^{1el}$ and $\varepsilon^{707el}_{center} - \varepsilon^{707el}_{center}$ are coincident. This is verified in Figure 4.12 by plotting the stress (Equation 4.7) and strain (Equation 4.8) ratios as a function of the simulation time.

$$r_{stress}(707el\_1el) = \frac{\sigma^{707el}_{center}}{\sigma^{1el}}\ , \tag{4.7}$$

$$r_{strain}(707el\_1el) = \frac{\varepsilon^{707el}_{center}}{\varepsilon^{1el}}\ . \tag{4.8}$$

The plane strain state at the center of the specimen is not affected by free edges. The stress shows and error average of 0,12%, and the strain, an error average 0,64% (Table 4.3).

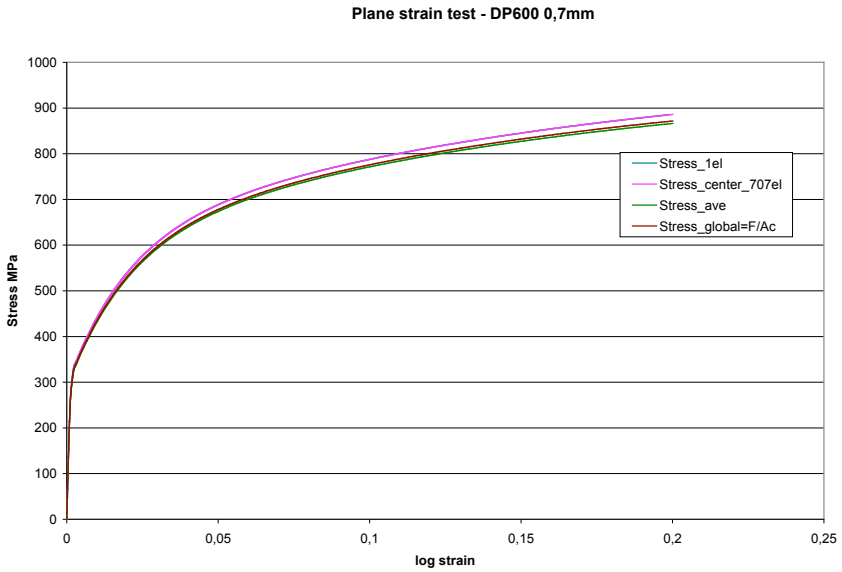

Figure 4.11 Stress –strain curves for a plane strain simulation.

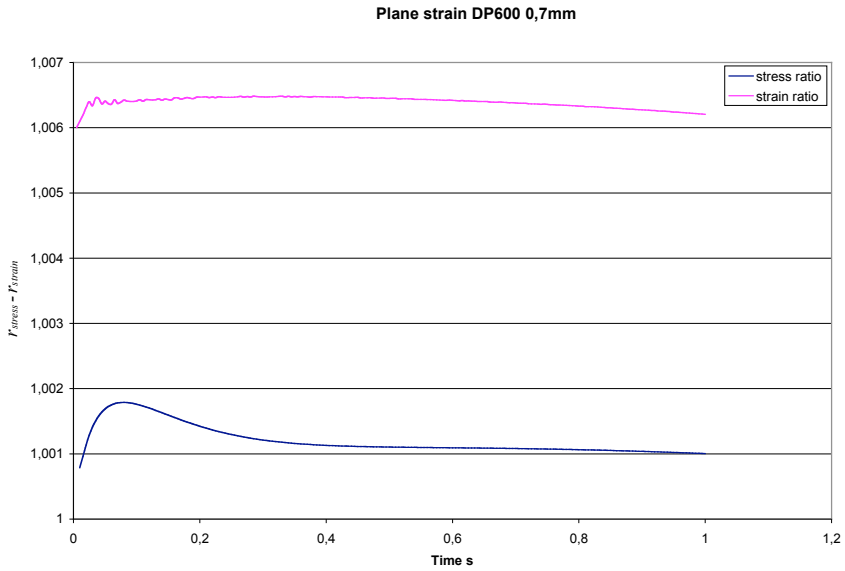

Figure 4.12 Ratios between stress – strain results obtained from 1-element mesh and at the center of a 707-element mesh for a plane strain case.

The difference between $\sigma_{ave}^{707el} - \varepsilon_{ave}^{707el}$ and $\sigma_{global}^{707el} - \varepsilon_{center}^{707el}$ in Figure 4.11 presents an error of approximately 0,6% as can be seen in Figure 4.13 for a stress ratio plot as a function of the strain $\varepsilon_{center}^{707el}$.

The stress σ^{1el} result obtained from a 1-element simulation presents an error average of 2,03% with the global stress σ_{global}^{707el} and an error average of 1,43% with the average stress (Figure 4.13). These results are summarized in Table 4.3.

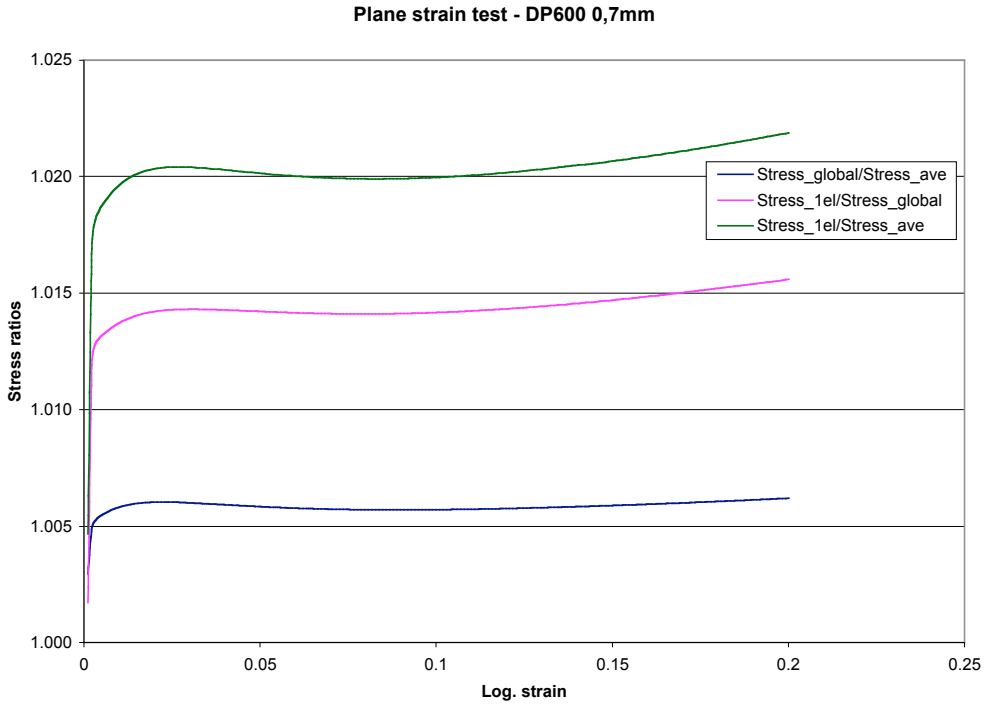

Figure 4.13 Stress ratios as a function of the accumulated strain for a plane strain case.

$\sigma_{center}^{707el} - \sigma^{1el}$		$\sigma_{center}^{707el} - \sigma^{1el}$		$\sigma_{global}^{707el} - \sigma_{ave}^{707el}$		$\sigma^{1el} - \sigma_{global}^{707el}$		$\sigma^{1el} - \sigma_{ave}^{707el}$	
Ratio (average)	Relative error	Ratio (average)	Relative error	Ratio (average)	Relative error	Ratio (average)	Relative error	Ratio (average)	Relative error
1,0012	0,12%	1,0064	0,64%	1,0058	0,58%	1,0143	1,43%	1,0203	2,03%

Table 4.3 Ratio and relative errors for a plane strain test.

Figure 4.14, Figure 4.15 and Figure 4.16 respectively show the stress components σ_{11}, σ_{22}, and σ_{12} at the lower, middle, and upper layers of the mesh for a $\varepsilon_{11}^{ln} = 20\%$ (Figure 4.9).

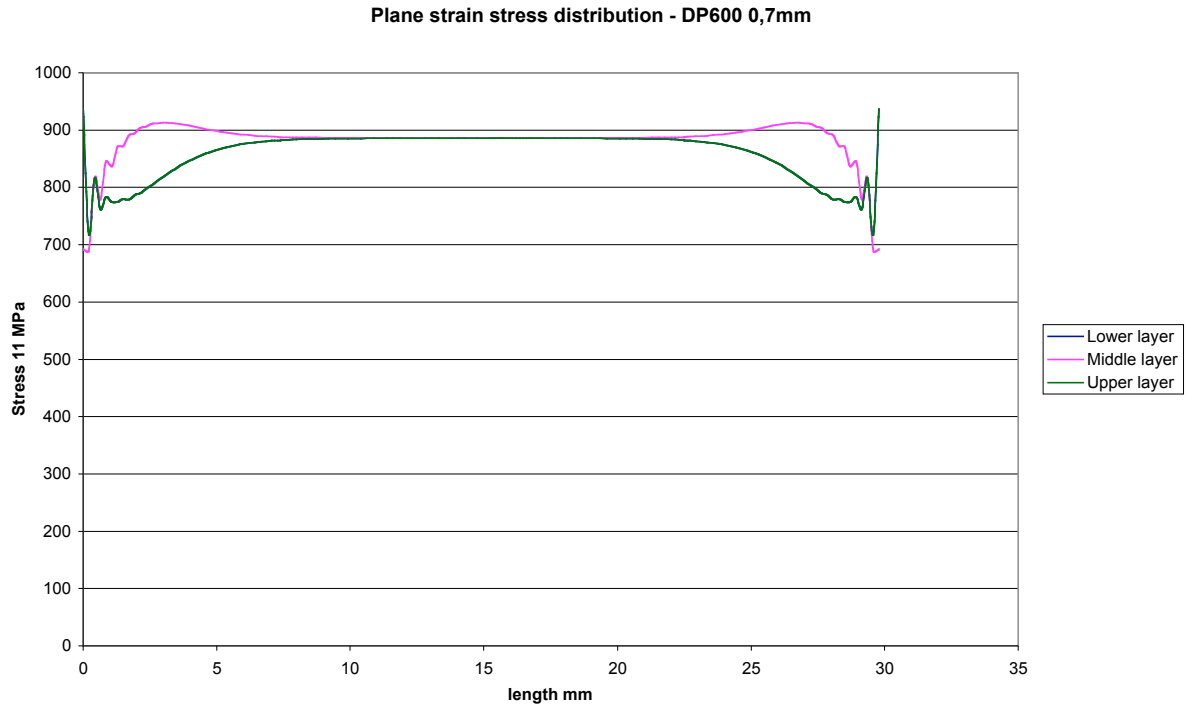

Figure 4.14 σ_{11} distribution at the lower, middle, and upper layers of the mesh for a plane strain test (DP600 0,7mm thick).

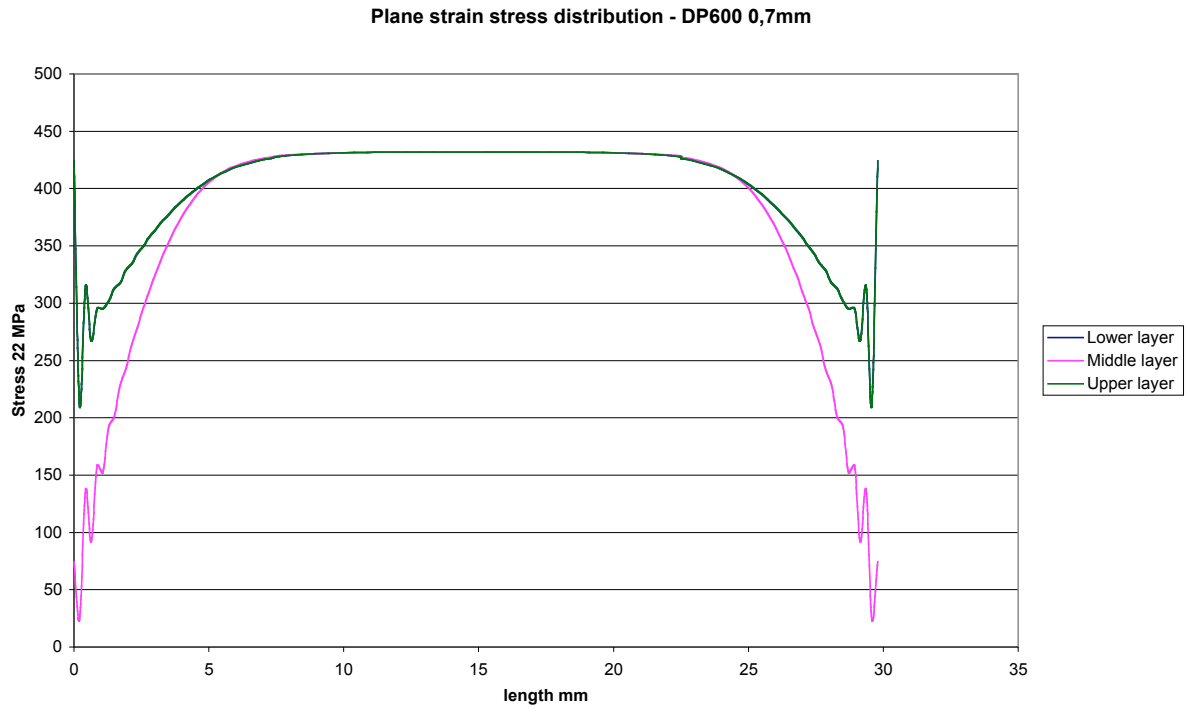

Figure 4.15 σ_{22} distribution at the lower, middle, and upper layers of the mesh for a plane strain test (DP600 0,7mm thick).

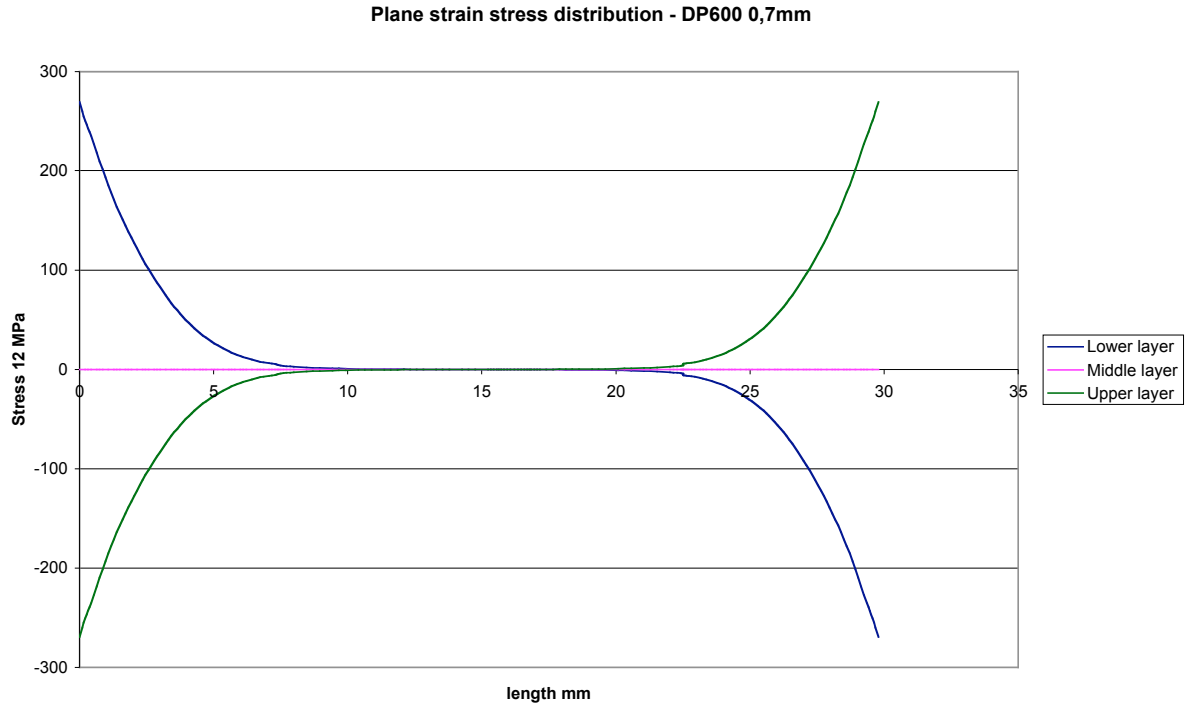

Figure 4.16 σ_{12} distribution at the lower, middle, and upper layers of the mesh for a plane strain test (DP600 0,7mm thick).

The following conclusions can be established:

- The numerical results show a homogeneous stress field outside of the free edges.
- A single finite element mesh can model the material behavior at the center of the specimen with an average error of 0,12%.
- The average stress σ_{ave}^{707el} can be approximated by the global stress σ_{global}^{707el} (computed from the load data) with an average error of 0,58%.
- A factor of 1,014 between the global stress σ_{global}^{707el} and the single element stress σ^{1el} is obtained. This result is important for determining the material parameters (Chapter 5).
- The homogeneity of the test depends strongly on the specimen geometry. Genevois, 1992 and Khalfallah et al., 2002 performed similar tests with specimens where the ratio between length and width was inferior to 6 obtained heterogeneous stress and strain fields.
- Results have the same magnitude as observed in Pijlman, 2001 for the same specimen geometry.

4.1.2 Simple shear test

A similar analysis is done for this test. The simple shear test diagram is shown in Figure 4.17 and Figure 3.7. The stress tensor is:

$$\boldsymbol{\sigma} = \sigma_{11}\mathbf{e}_1 \otimes \mathbf{e}_1 + \sigma_{22}\mathbf{e}_2 \otimes \mathbf{e}_2 + \sigma_{12}\mathbf{e}_1 \otimes \mathbf{e}_2 + \sigma_{12}\mathbf{e}_2 \otimes \mathbf{e}_1 \tag{4.9}$$

where

$$\sigma_{12} = \frac{F_{horizontal} \quad \text{horizontal load cell}}{A_{actual} \quad \text{optical strain measurements}} . \tag{4.10}$$

$F_{horizontal}$ is the load measured by the load cell and A_{actual} is the actual area of the specimen measured at the central line. The stress measured in that way will be called “global” stress and represents the average stress over the deformation zone.
The component σ_{11} can be measured using the vertical load cell, hence:

$$\sigma_{11} = \frac{F_{vertical} \quad \text{vertical load cell}}{A_{actual} \quad \text{optical strain measurements}} , \tag{4.11}$$

σ_{22} can not be measured.

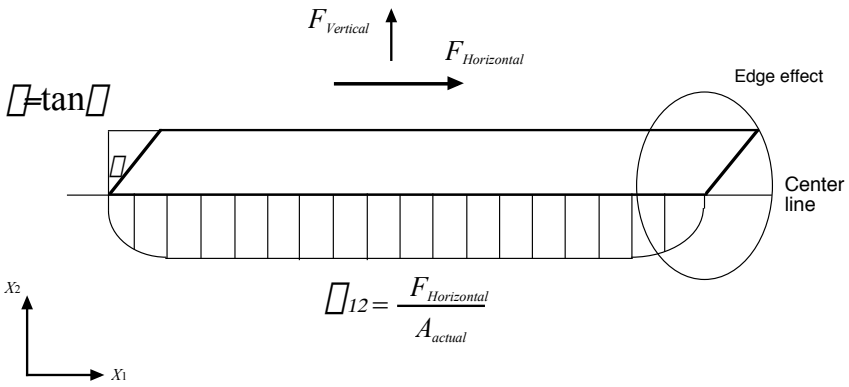

Figure 4.17 Simple shear test diagram.

The A_{actual} is computed from the thickness reduction at the center-line level (Figure 4.17). This thickness reduction is computed from the conservation of volume assumption (Equation 3.49).
The strain tensor is written as:

$$= {}_1\mathbf{e}_1 \quad \mathbf{e}_1 + {}_{22}\mathbf{e}_2 \quad \mathbf{e}_2 + {}_{33}\mathbf{e}_3 \quad \mathbf{e}_3 + {}_2\mathbf{e}_1 \quad \mathbf{e}_2 + {}_2\mathbf{e}_2 \quad \mathbf{e}_1 \ . \tag{4.12}$$

Using the Green-Lagrange strain tensor definition (Equation 2.23) and the deformation gradient for the simple shear case (Equation 3.24), the strain tensor as a function of the test geometry (Figure 4.17) is:

$$^{GL} = \frac{1}{2}\left(^2\mathbf{e}_2 \quad \mathbf{e}_2 + \mathbf{e}_1 \quad \mathbf{e}_2 + \mathbf{e}_2 \quad \mathbf{e}_1 \right) . \tag{4.13}$$

The strain distribution is measured from a simple shear test over a DP600 of 0,7mm thickness. Figure 4.18 shows the $^{GL}_{12}$ distribution over the measurable zone of the specimen for an imposed $|_{\max}| = 0{,}47$.

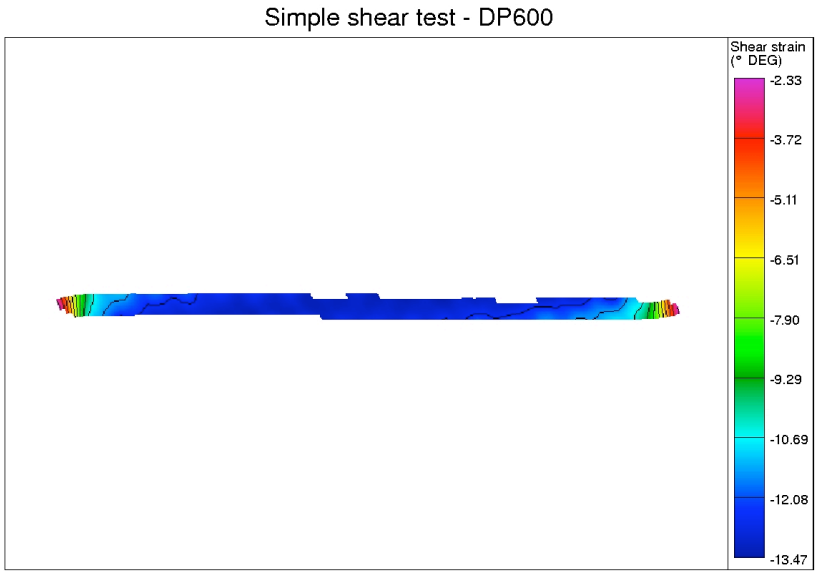

Figure 4.18 $^{GL}_{12}$ strain distribution over the measurable zone (in degrees), for $|_{\max}| = 0{,}47$.

The distribution of the components of the strain tensor are plotted over a center-line of the measurable zone for an imposed □= 0,47. Figure 4.19, Figure 4.20, Figure 4.21, Figure 4.22 and Figure 4.23 respectively show $\square_{11}^{GL}$, $\square_{22}^{GL}$, $\square_{12}^{GL}$, the thickness reduction and the von Mises equivalent stress at different amounts of strains.

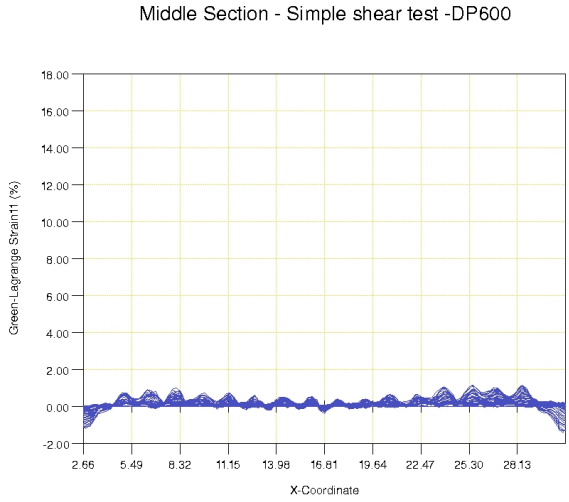

Figure 4.19 $\square_{11}^{GL}$ strain distribution over the specimens middle line for different amount of strains.

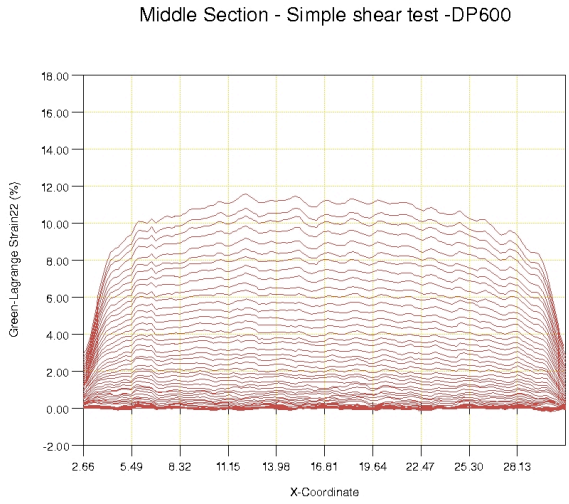

Figure 4.20 $\square_{22}^{GL}$ strain distribution over the specimen's middle line for different amounts of strains.

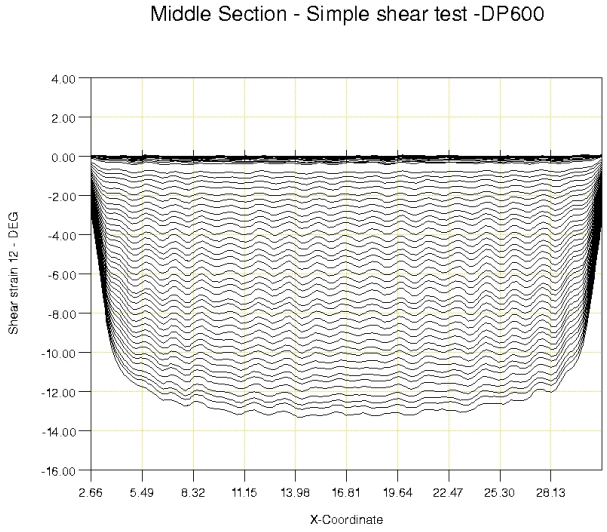

Figure 4.21 ε_{12}^{GL} strain distribution over the specimen's middle line for different amounts of strains (in degrees), for $|\varepsilon_{\max}| = 0{,}47$.

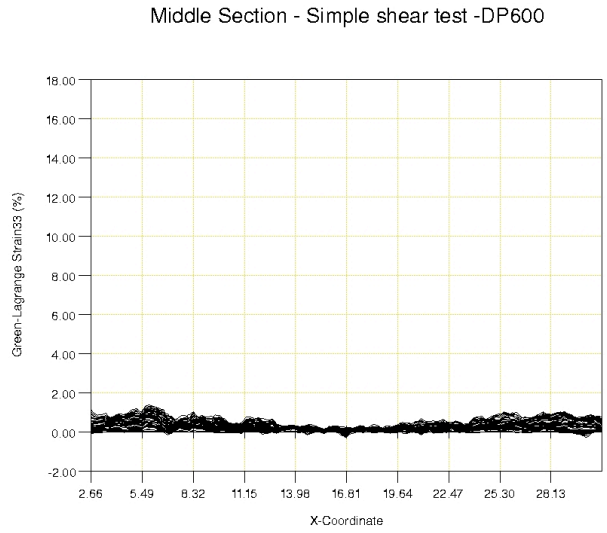

Figure 4.22 ε_{33}^{GL} (thickness reduction) strain distribution over the specimen's middle line for different amounts of strains.

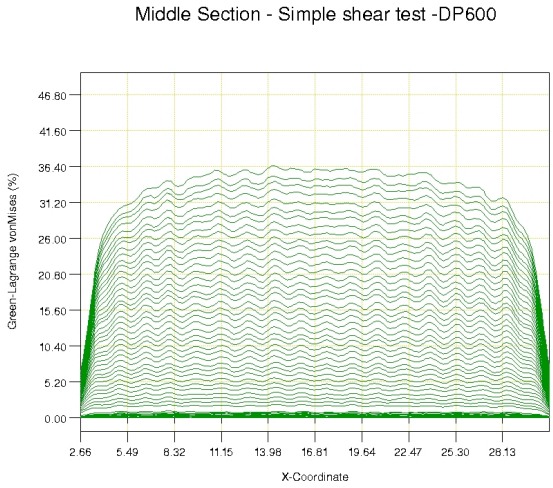

Figure 4.23 von Mises strain distribution over the specimen's middle line for different amounts of strains.

The following conclusions can be drawn from these results:

- The specimen geometry restricts the influence of the free edges, hence a wide homogenious deformation zone is obtained.
- The theoretical Green-Lagrange strain tensor (Equation 4.13) is reproduced if the components ε_{11}^{GL} and ε_{33}^{GL} are neglected (they are less than 1% for a $|\varepsilon_{max}| = 0{,}47$).
- To complement this last remark, Figure 4.24 shows the experimental deformation gradient tensor **F** evolution at the center of the specimen in function of γ. The theoretical deformation gradient established in Equation 3.24 is verified.
- If thickness reduction is neglected (i.e. $\varepsilon_{33}^{GL} \approx 0$), the actual area A_{actual} of Equation 4.10 can be approximated from the initial area A_0.

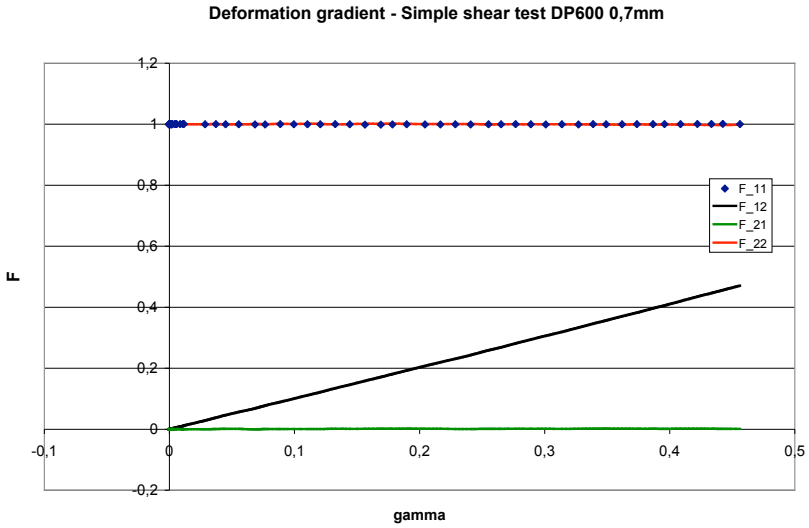

Figure 4.24 Deformation gradient at the center of the specimen. DP600 0,7mm.

To study the stress distribution, a finite element analysis is done using the same data as in the former section, i.e., Table 4.1 and Table 4.2 and two meshes, one using a single element and the other of 707 elements, as is shown in Figure 4.8.
The variables to be studied are:

- σ^{1el}, the stress component σ_{12} at the element integration point of the single element mesh.
- σ^{1el}, defined in Figure 3.7.
- σ^{707el}_{center} (σ^{707el}_{center}), the stress (strain) component σ_{12} ($2\varepsilon^{GL}_{12}$) at the center element integration point of the 707-element mesh.
- σ^{707el}_{ave} (σ^{707el}_{ave}), the average stress (strain) component σ_{12} ($2\varepsilon^{GL}_{12}$) computed from each element integration point of the 707-element mesh.
- σ^{707el}_{global}, the stress obtained from the resulting force per unit of area (Equation 4.10). The actual area is computed from the thickness reduction at the central element.
- σ^{707el}_{global}, defined in Figure 4.17.

Figure 4.25 and Figure 4.26 respectively show the stress and the strain fields at the deformed mesh for an imposed γ= 0,7. Figure 4.27 shows the stress – strain curves obtained for the previously mentioned variables.

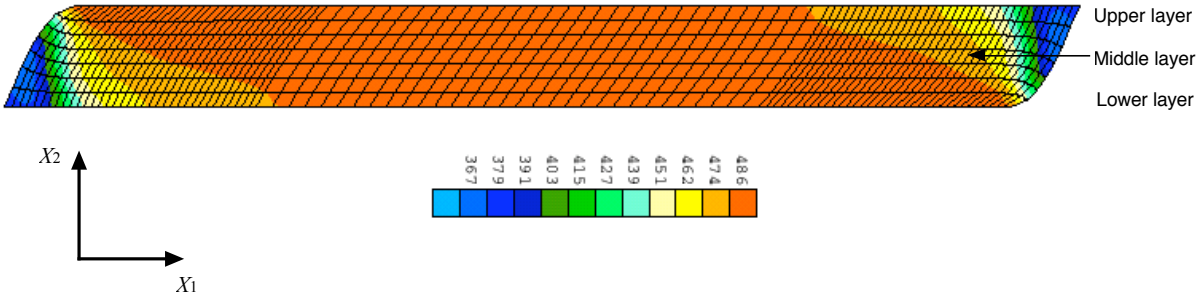

Figure 4.25 Stress (σ_{12}) field for a simple shear test with an imposed γ= 0,7 (DP600 0,7mm thick).

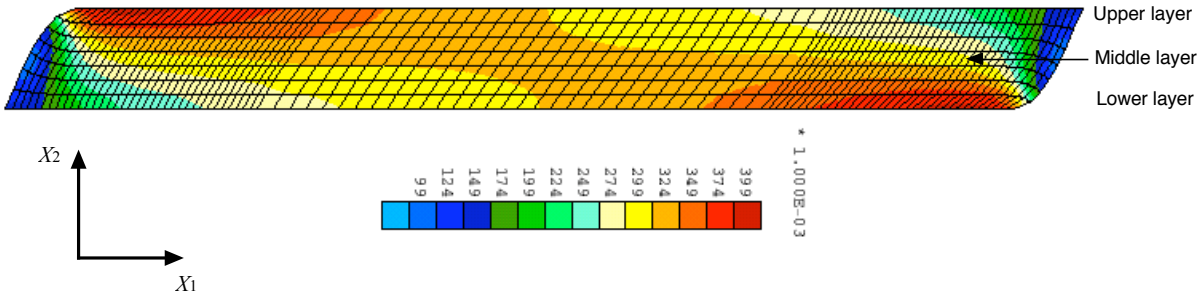

Figure 4.26 Strain (ε_2) field for a simple shear test with an imposed γ= 0,7 (DP600 0,7mm thick).

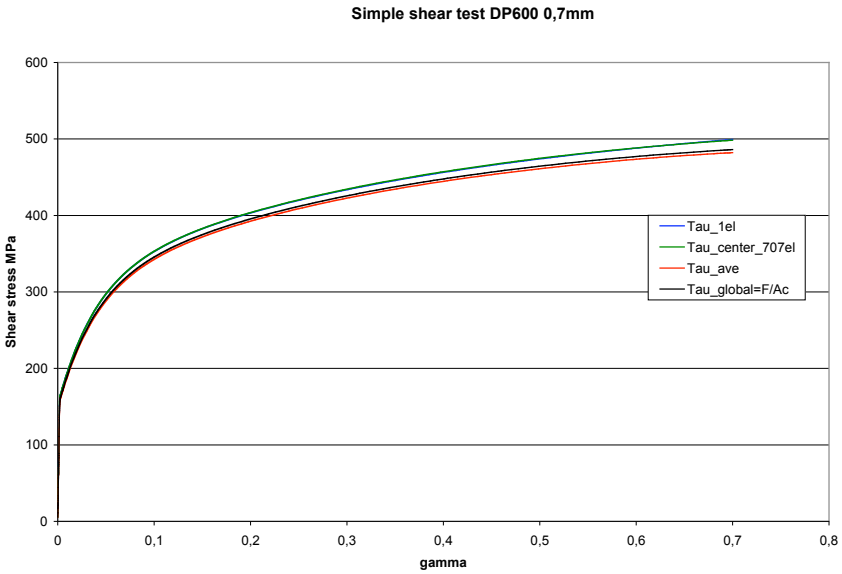

Figure 4.27 Stress – strain curves for a simple shear test.

Table 4.4 summarizes the errors and ratios between the different strain definitions. Figure 4.28 shows the ratio evolution as a function of the amount of the global shear strain.

$\gamma_{center}^{707el} - \gamma^{1el}$		$\gamma^{1el} - \gamma_{ave}^{707el}$		$\gamma_{center}^{707el} \gamma_{ave}^{707el}$		$\gamma^{1el} - \gamma_{global}^{707el}$	
Ratio (average)	Relative error	Ratio (average)	Relative error	Ratio (average)	Relative error	Ratio (average)	Relative error
0,999	0,1%	1,04	4%	1,033	3,3%	1	0%

Table 4.4 Ratio and relative errors for γ_2 in a simple shear test.

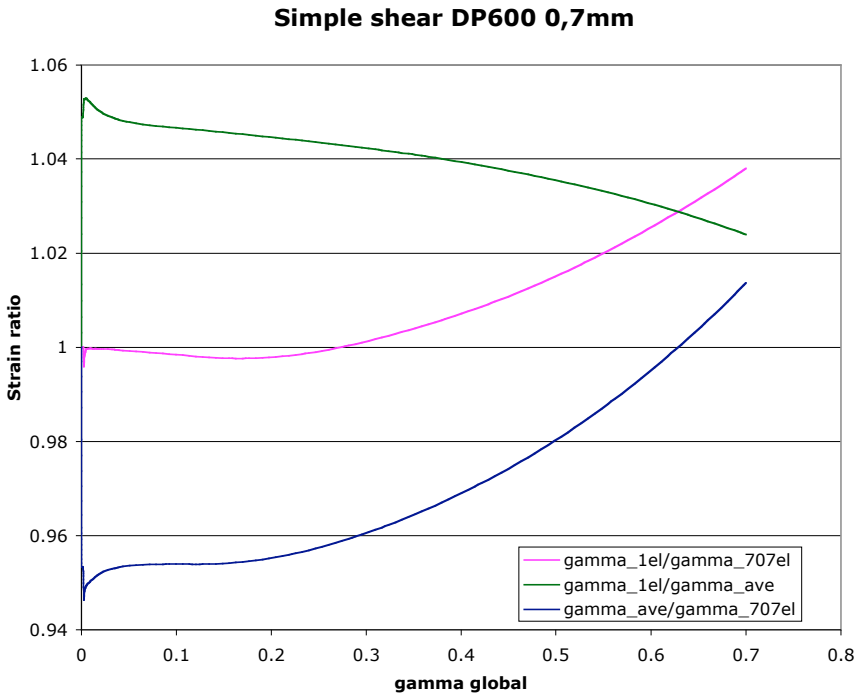

Figure 4.28 Ratios between stress – strain results obtained from 1-element mesh and at the center of a 707-element mesh for a simple shear case.

Figure 4.29 shows the ratio and error evolutions of the stress component as a function of the amount of shear strain. Average values are in Table 4.5.

$\sigma^{1el} - \sigma^{707el}_{center}$		$\sigma^{707el}_{global} - \sigma^{707el}_{ave}$		$\sigma^{1el} - \sigma^{707el}_{global}$		$\sigma^{1el} - \sigma^{707el}_{ave}$	
Ratio (average)	Relative error	Ratio (average)	Relative error	Ratio (average)	Relative error	Ratio (average)	Relative error
0,999	0,1%	1,008	0,8%	1,023	2,3%	1,031	3,1%

Table 4.5 Ratio and relative errors for the σ_{12} component in a simple shear test.

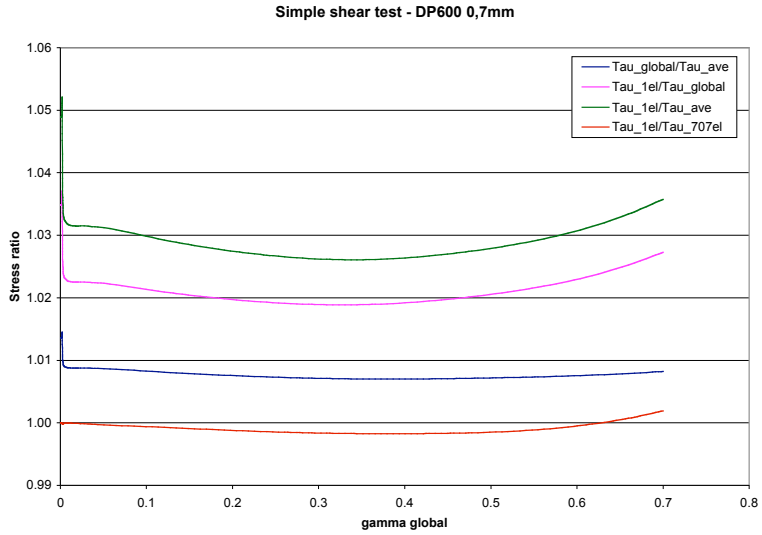

Figure 4.29 Stress ratios as a function of the accumulated strain for a simple shear case.

The stress tensor components σ_{11}, σ_{22} and σ_{12} are plotted at the lower, middle and upper layers of the deformation zone mesh in Figure 4.30, Figure 4.31, and Figure 4.32, for an imposed $\gamma = 0,7$.

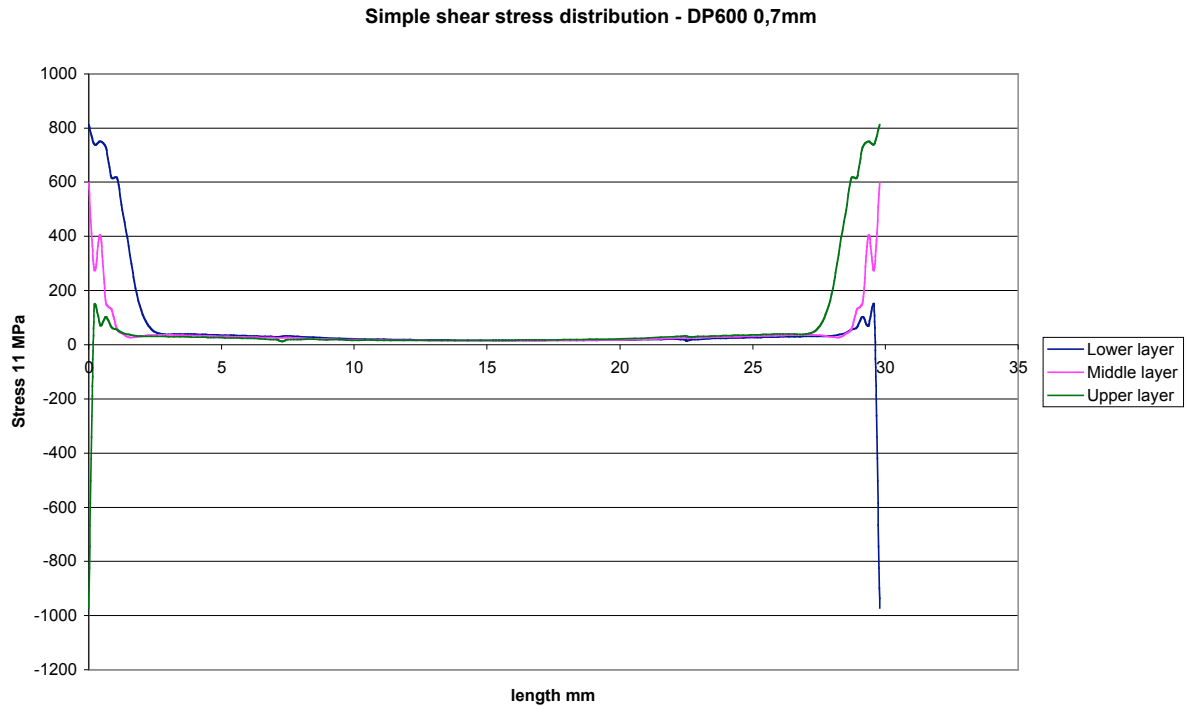

Figure 4.30 σ_{11} distribution at the lower, middle, and upper layers of the mesh for simple shear test.

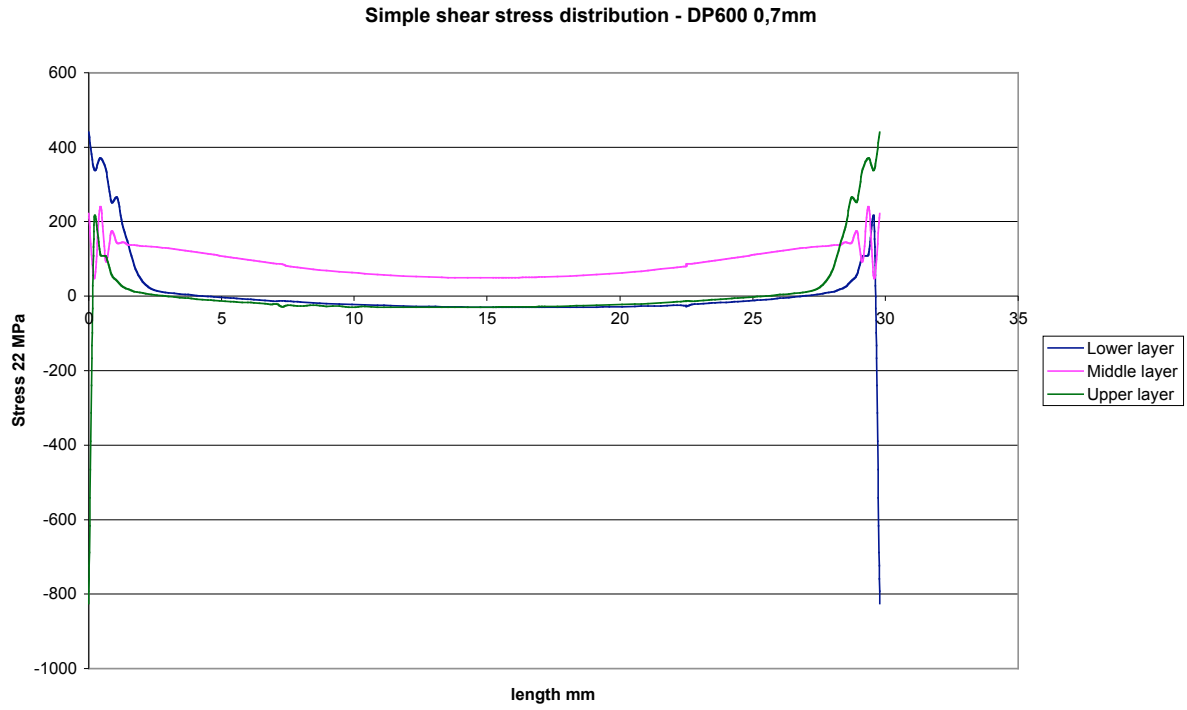

Figure 4.31 σ_{22} distribution at the lower, middle and upper layers of the mesh for simple shear test.

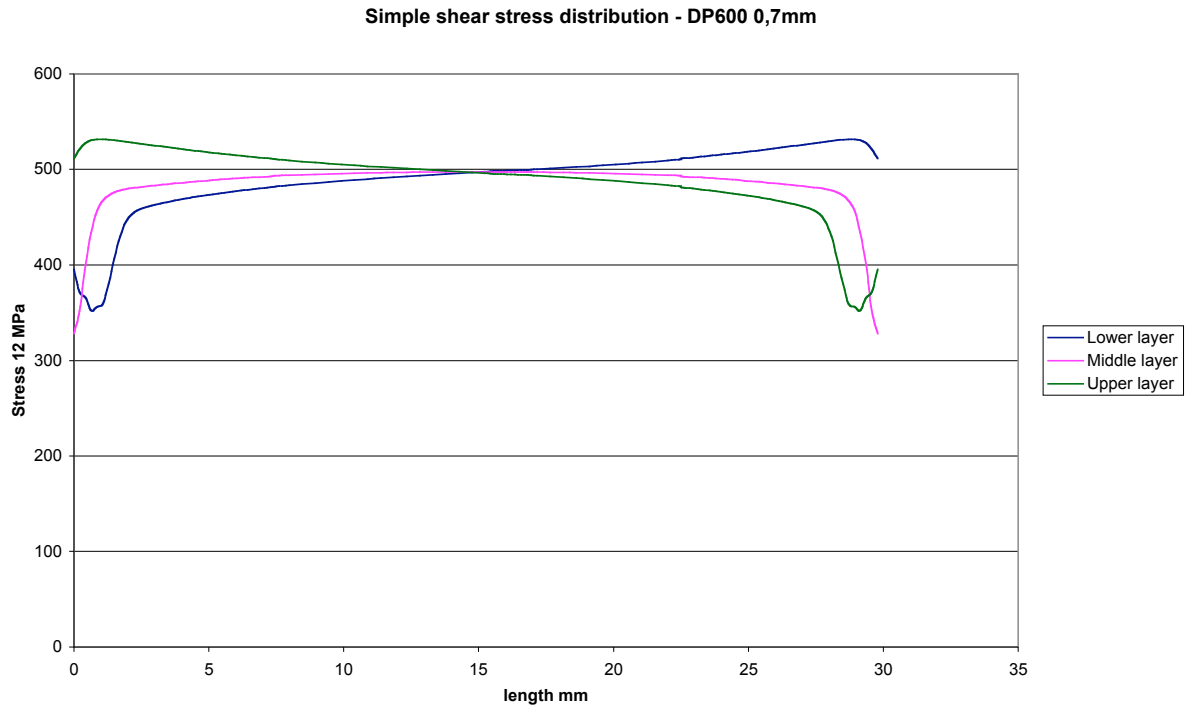

Figure 4.32 σ_{12} distribution at the lower, middle, and upper layers of the mesh for simple shear test.

The following conclusions can be established:

- The numerical results show a homogeneous stress field outside of the free edges.
- A single finite element mesh can model the material behavior at the center of the specimen with an average error of 0,1%.
- The average stress σ_{ave}^{707el} can be approximated by the global σ_{global}^{707el} stress (computed from the load data) with an average error of 0,8%.
- A factor of 1,023 between the global stress σ_{global}^{707el} and the single element stress σ^{1el} is obtained. This result is important for determining the material parameters (Chapter 5).
- This last point coincides with the results obtained in Bouvier et al, 2005 where the influence of the geometry and the amount of shear strain in the homogeneity of the stress field is studied.
- Results have the same magnitude as observed in Pijlman, 2001 for the same specimen geometry.

4.2 Mechanical tests

A bi-axial machine, as it is mentioned in Chapter 3, is able to perform plane strain tests, simple shear tests and a combination of both. The results given by the machine captors (load cell and the optical strain gauge) are validated by comparison with the respective finite element simulation tests for a DP600 material of 0,7mm thickness.
The simulation parameters are summarized in Table 4.1 and Table 4.2 and only one element is used for each test simulation due to stress – strain field homogeneity (shown in the previous section).

4.2.1 Plane strain test

The plane strain test is performed by an imposed displacement of the vertical piston. The stress is computed with Equation 4.2 by the load cell and strain data. The actual area is computed as shown in Equation 4.5. The major strain is the strain computed in the center of the specimen in the loading direction.
Figure 4.33 compares two experimental results with the simulated one.

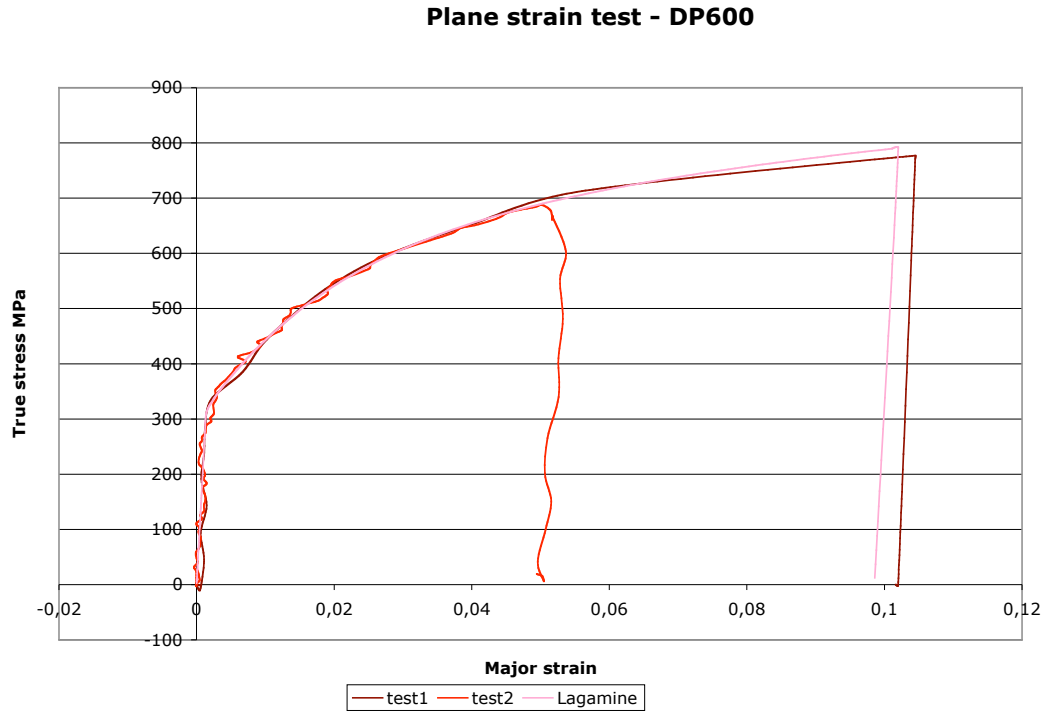

Figure 4.33 Plane strain test. DP600 0,7mm.

4.2.2 Simple shear and Bauschinger test

A simple shear test is performed by imposing a displacement of the horizontal piston. The gap between grip wedges must remain constant.
A Bauschinger test is obtained by imposing a displacement in one direction and then imposing a displacement in the opposite direction. The idea is to investigate the reverse loading effect in a way easier way than by a tension – compression test as in sheet compression would directly yield buckling (Figure 4.34).

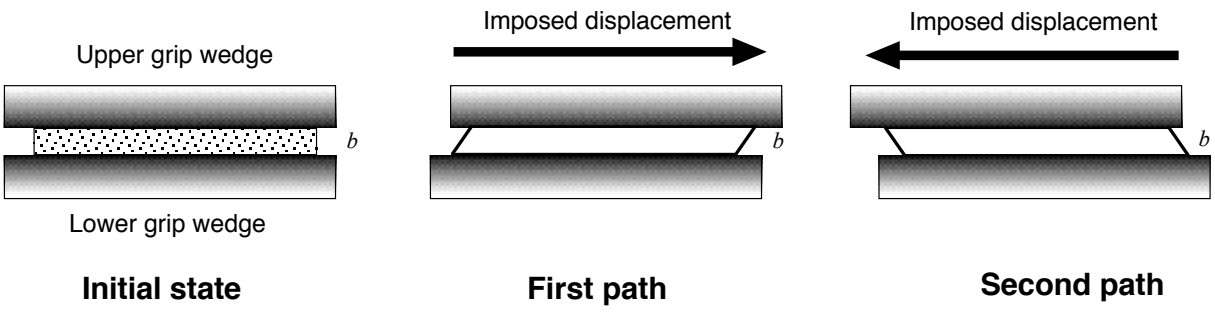

Figure 4.34 Bauschinger test diagram.

Figure 4.35 compares the results of three experimental tests at different amounts of pre-strain. It can be clearly seen that the amount of pre-strain has an influence on the length of the work hardening stagnation observed at the reverse load. This phenomenon can be predicted by the Teodosiu and Hu hardening law (Chapter 2 and Annex A).

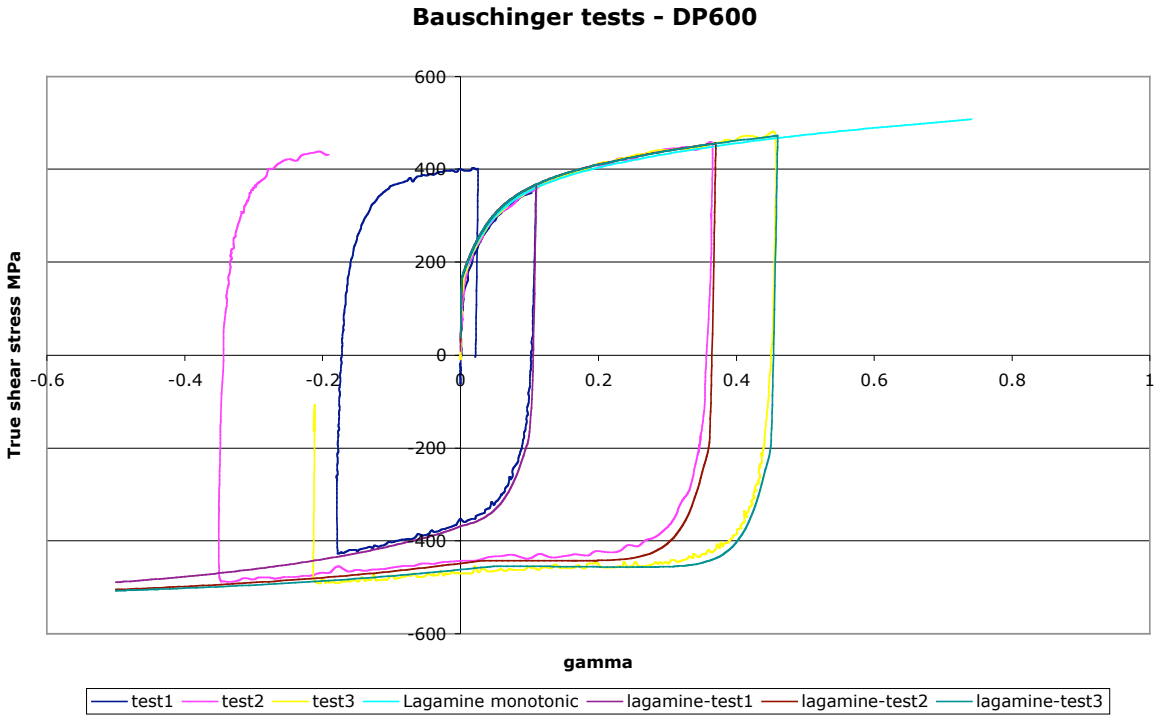

Figure 4.35 Simple shear and Bauschinger tests. DP600 0,7mm thickness.

4.2.3 Orthogonal test

First, a load is applied in the vertical direction (plane strain test) and a subsequent load is applied in the horizontal direction (pre-strained simple shear).
Two ways to proceed are shown:

- (U) Vertical Load – Elastic Unload – Horizontal Load (Figure 4.36).
- (L) Vertical Load – Horizontal Load (Figure 4.37).

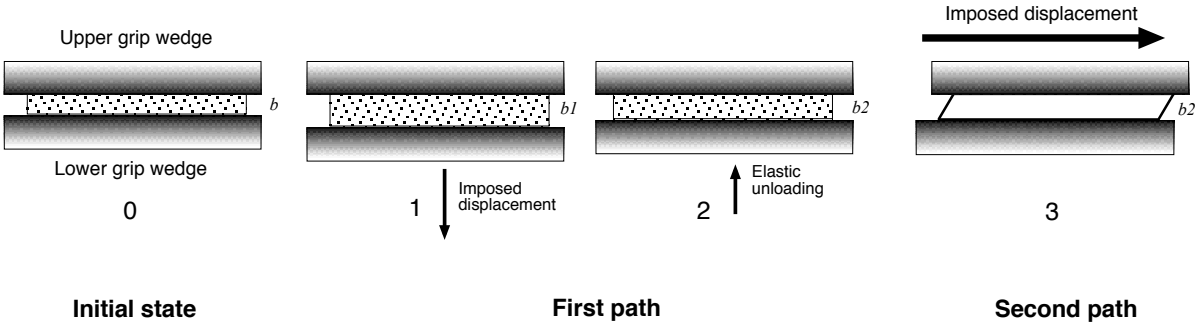

Figure 4.36 Orthogonal test with elastic unloading. U curve in Figure 4.38.

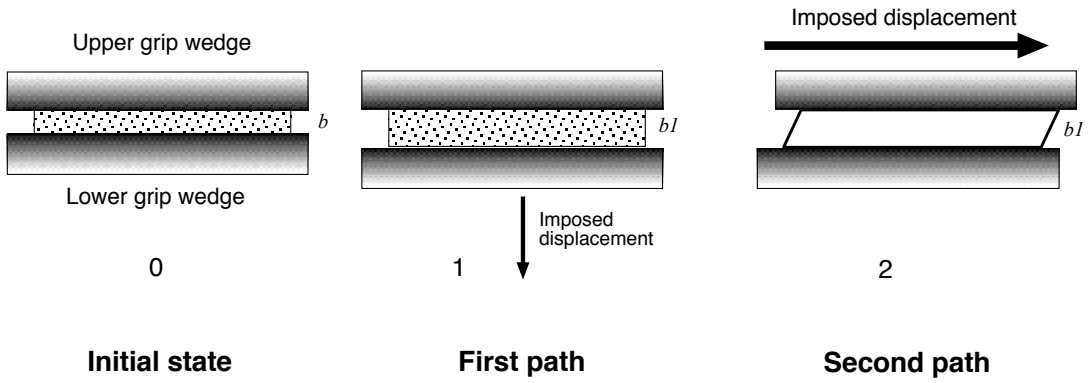

Figure 4.37 Orthogonal test without elastic unloading. L curve in Figure 4.38.

Figure 4.38 shows the experimental results for both cases. It can be seen that their difference takes root at the beginning of the subsequent load, but both curves converge to the monotonic simple shear one. The difference comes from the elastic unload. Figure 4.39 describes, in a yield surface view (simplified from Figure 3.3), the "U" case and the "L" case. For simplicity, an elastic-perfectly-plastic model is chosen for this representation.

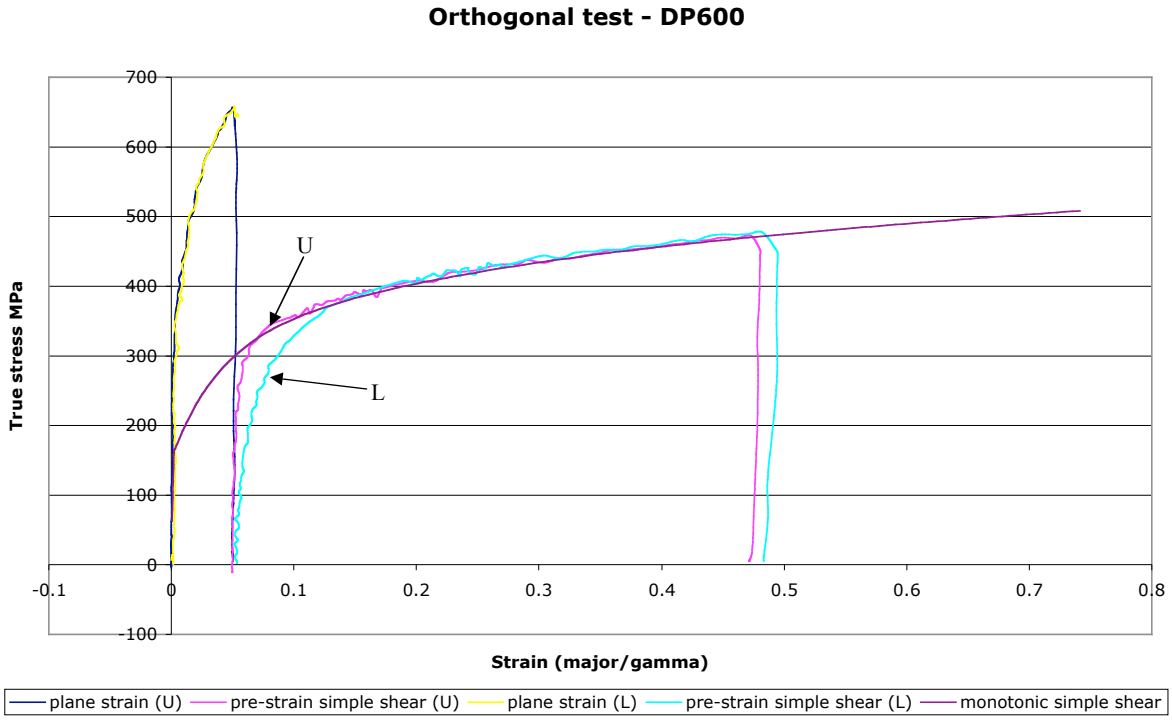

Figure 4.38 Orthogonal test. DP600 0,7mm.

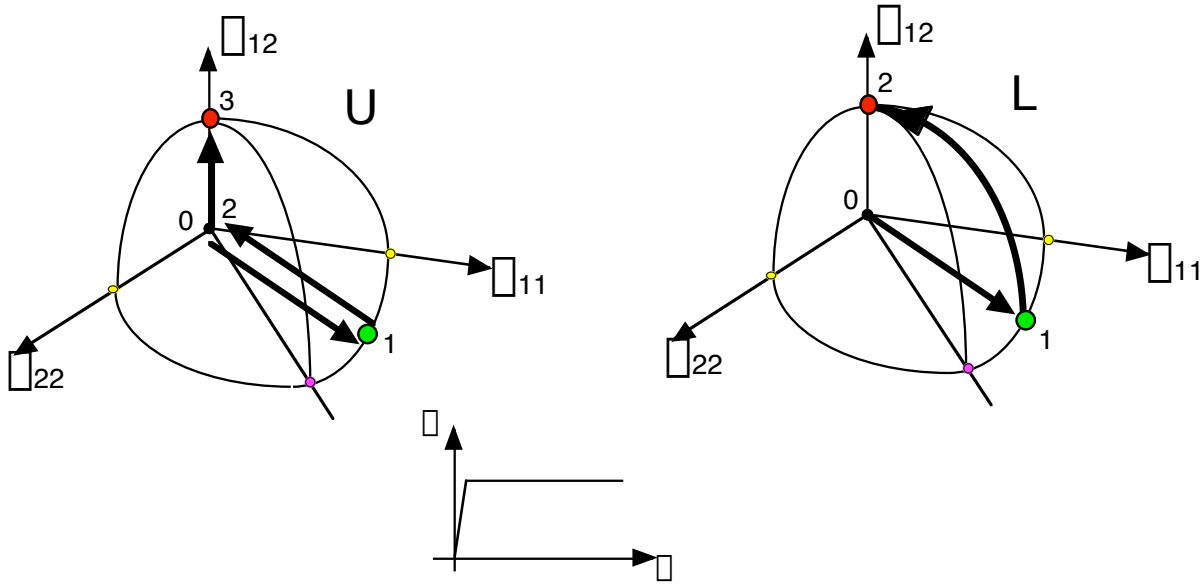

Figure 4.39 "U" and "L" cases in a yield surface representation for elastic-perfectly-plastic model.

Figure 4.40 compares the subsequent load stage with the finite element simulations. The results differ slightly at the beginning of the plastic deformation, converging later to the same value. This difference can take root in the identification procedure. The orthogonal test used for the identification done in Bouvier et al., 2002 is done with a uni-axial tensile test followed by a simple shear test, which differs from the orthogonal test performed here.

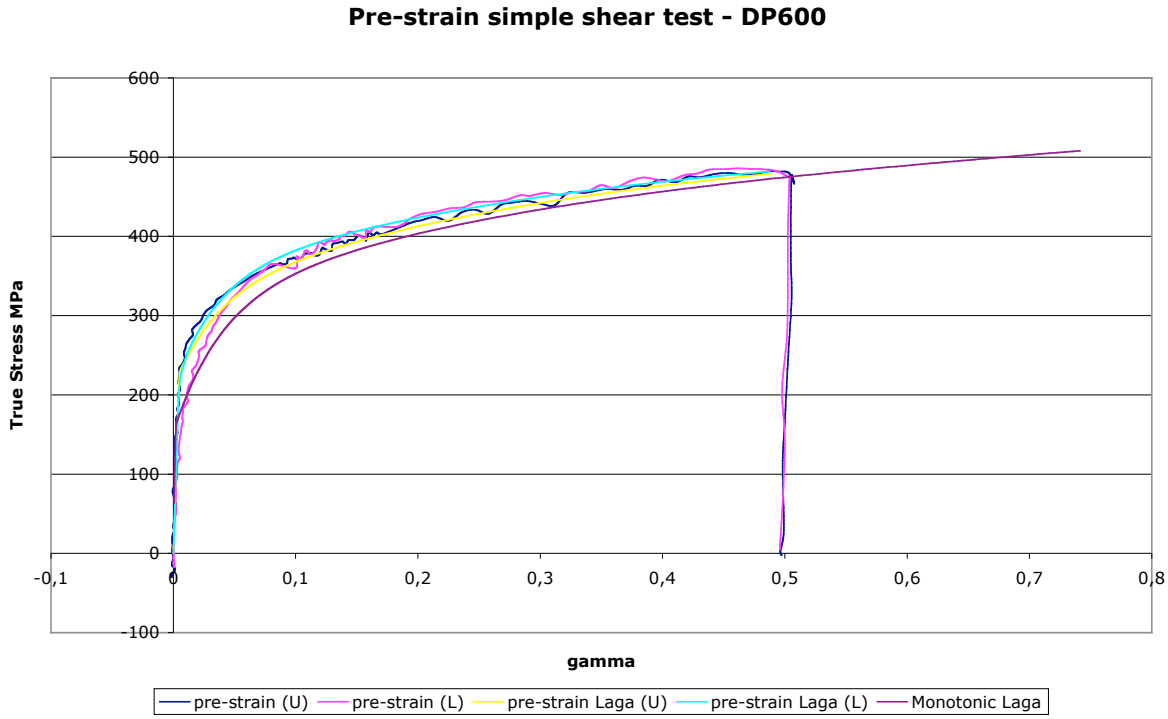

Figure 4.40 Second load of the orthogonal test. DP600 0,7mm.

4.2.4 Combined test

In this test the two loads are applied at the same time throughout the test (Figure 4.40). The results shown in Figure 4.42 come from a test having the characteristics described in Table 4.6.

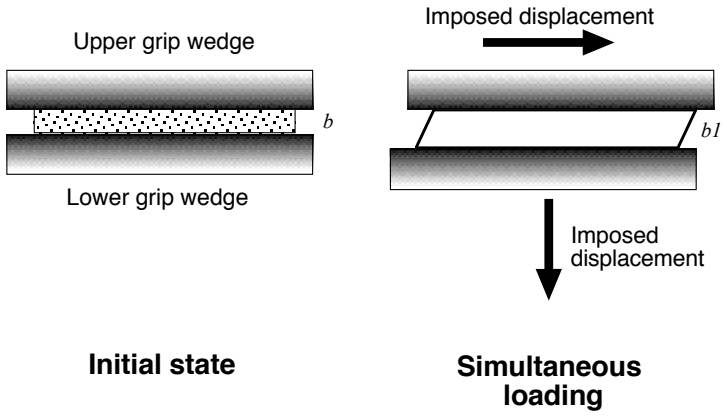

Figure 4.41 Combined test diagram.

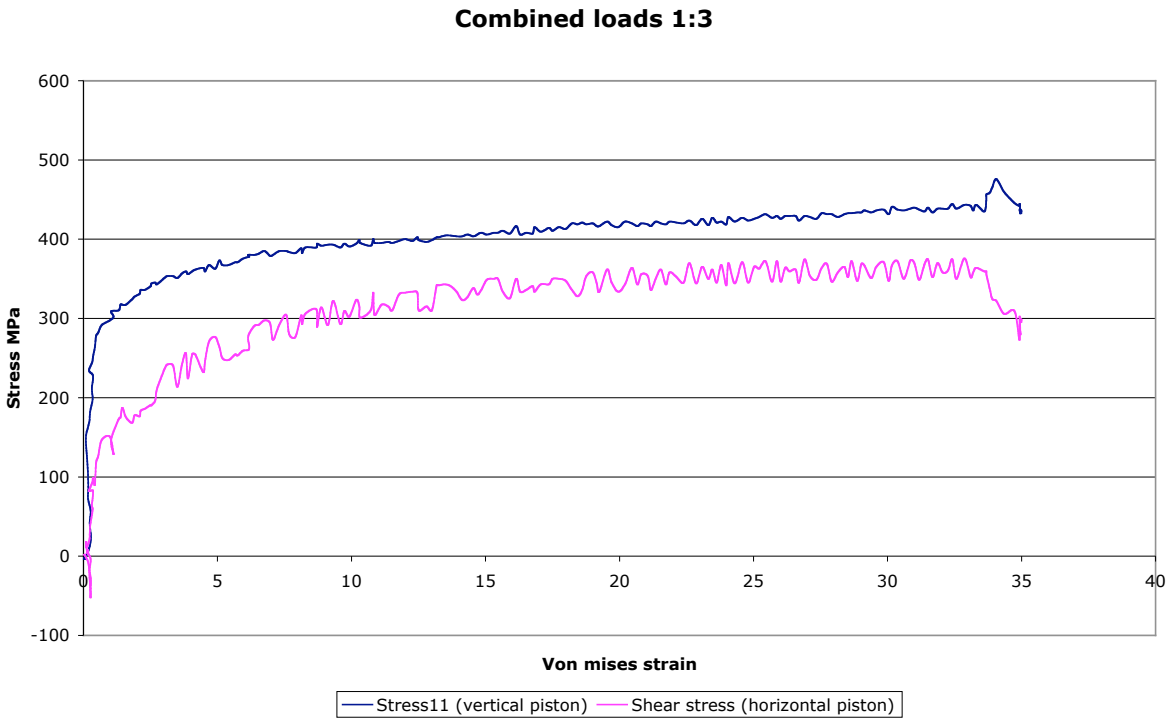

Figure 4.42 Combined test. DP600 0,7mm.

Vertical piston		Horizontal piston	
Displacement mm	Speed mm/s	Displacement mm	Speed mm/s
1	0,0016	3	0,005

Table 4.6 Combined test characteristics.

The purpose of this test is to show the feasibility of performing a combined test with the bi-axial testing machine. Other combination of piston displacements can be performed.

These load combinations permit us to determine new discrete points belonging to the yield surface. These points are physically placed in the red arrows shown in Figure 4.43.

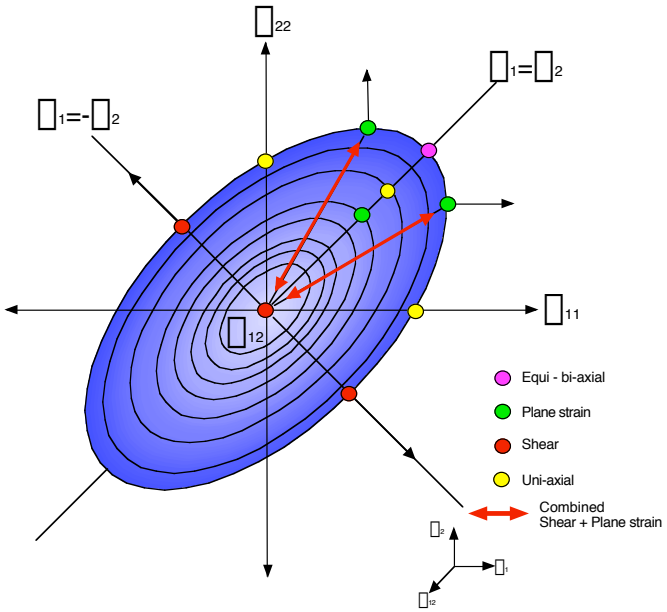

Figure 4.43 Stress states defining the initial yield surface in general stress axes.

4.2.5 Miyauchi device

Experimental setup is shown in Figure 4.44. The force values are obtained from the dynamometer while the displacement values are measured at the lower part of the guiding piece (point A in Figure 4.44) with a displacement sensor.

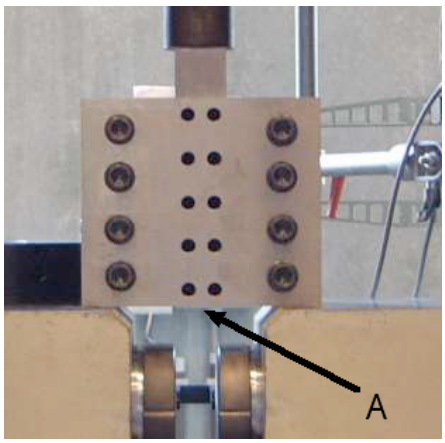

Figure 4.44 Displacement measurement point.

Figure 4.45 compares numerical with experimental results showing a good correlation.

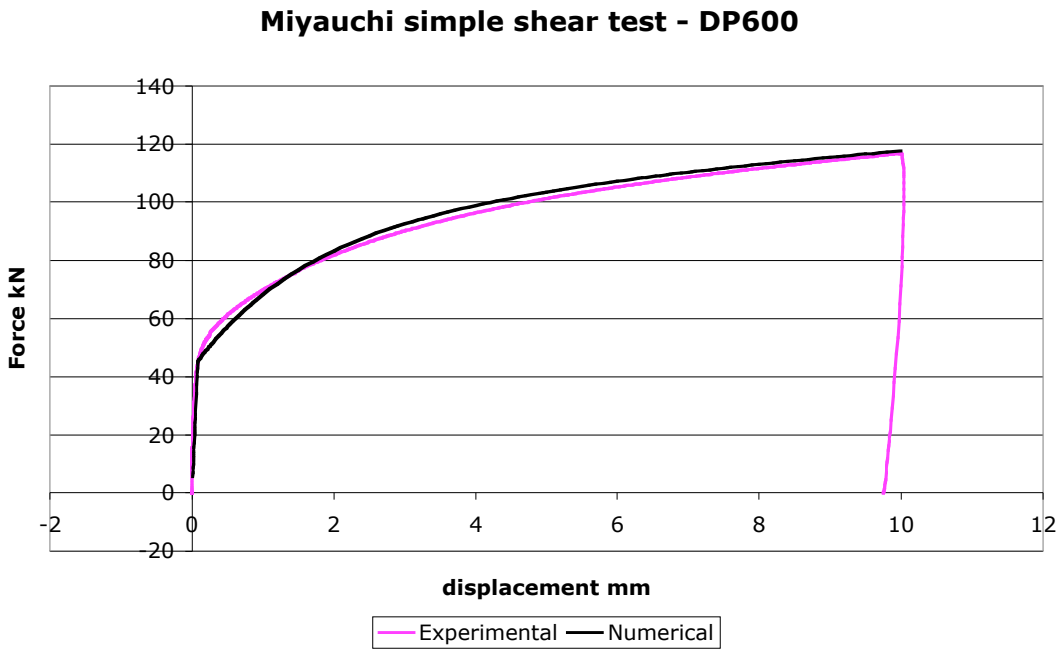

Figure 4.45 Miyauchi simple shear test. DP600 0,7mm.

4.3 Performance at different loads

The bi-axial testing machine is designed with hydraulic pistons of a 10MPa capacity, the purpose being to study the performance of the testing machine mainly at low-levels loads. Several simple shear tests have been performed on different materials and the force – deformation curves are shown in Figure 4.46.
Figure 4.47 is focused on the lower loads. It can be observed that the oscillations become larger and further filtering and averaging work must be done. The optimal loads are between 5kN and 30kN for the current bi-axial machine.

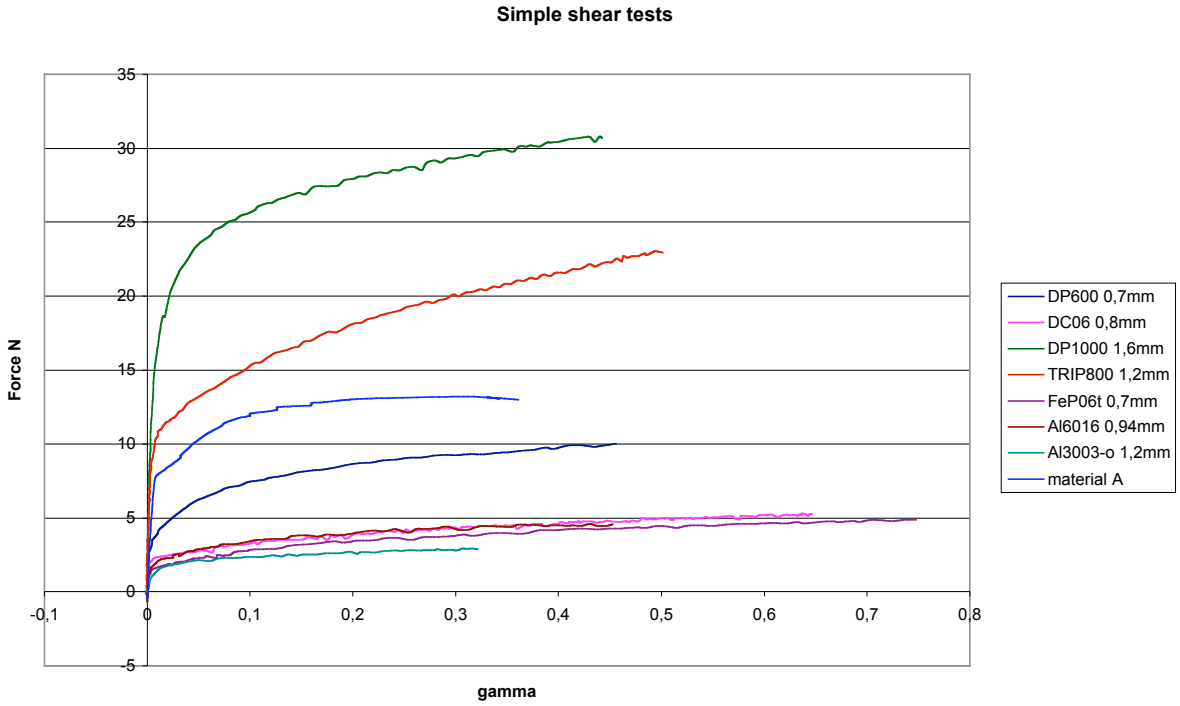

Figure 4.46 Simple shear test for different materials. Material A unidentified for confidentiality reasons.

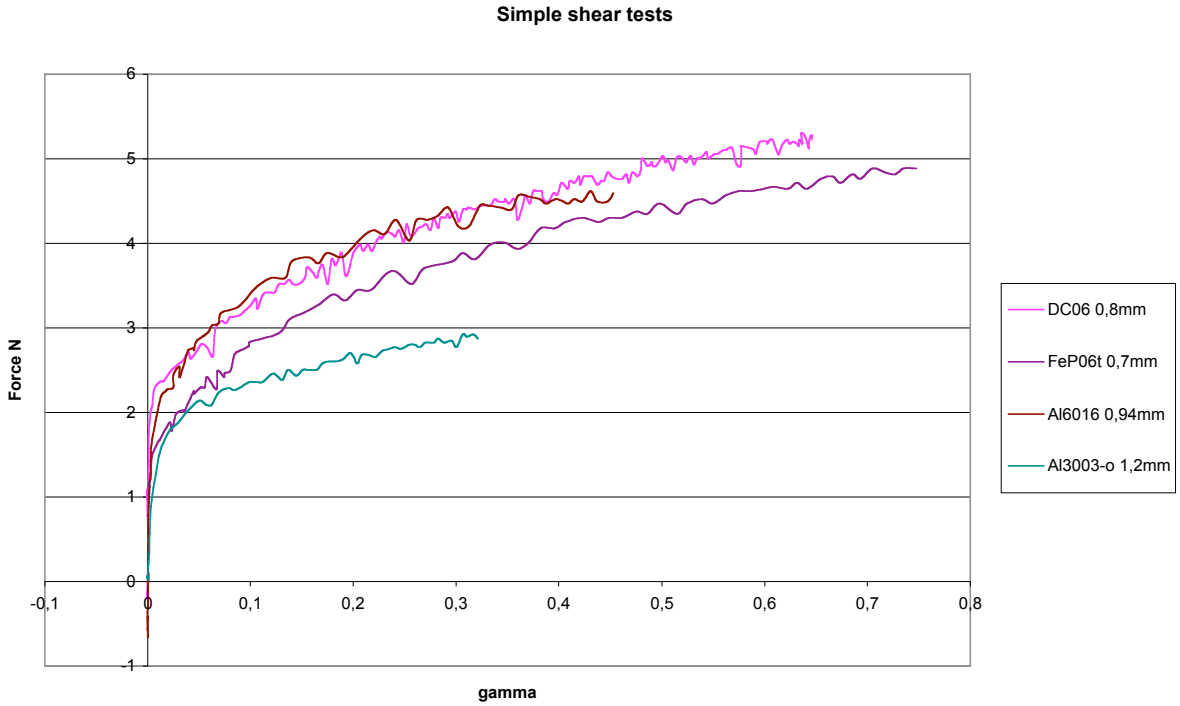

Figure 4.47 Simple shear test for different materials. Detail of the lower loads.

4.4 Conclusions

The homogeneity test confirms that the stress computation can be directly obtained from available data such as load and current area; in addition, the central point can be taken as a representative point of the specimen deformation area. If other geometries are required a similar analysis has to be done (as the one performed in Bouvier et al., 1995).
This test also demonstrates that a single-element finite element analysis represents the material behavior at the center of the specimen quite well and that the relative error with respect to the average value is negligible. This last point is important since the hardening material parameter identification will be carried out using the inverse method from one finite element simulation (Chapter 5).
The availability of different kinds of tests has been shown, and the results are coincident with those computed by FEM codes with parameters identified by another laboratory. The results shown in this chapter are validated by this approach. The combined simultaneous shear and plain strain tests enable us to include new experimental points in the yield surface description shown in Figure 3.3. Figure 4.43 includes the loci where new experimental points can be added.
It has also been shown that the performance at low loads is not optimal. To have satisfactory results in the range under 5kN, a greater number of tests must be done in order to obtain good average results that facilitate the data filter. The possibility of changing the pistons is being studied at the present.

CHAPTER 5

MATERIAL CHARACTERIZATION

One of the applications of the designed bi-axial machine is the calibration of material parameters of complex constitutive laws.

Let us recall that DP600 steel grade was used in Chapter 4 as a validation of our equipment as it was already identified by the laboratory of Paris 13 (Bouvier et al., 2002). Discussions with the partners of this project have defined three other materials to be characterized:

- DC06 (0,8mm thick) was known to be quite anisotropic and complex kinematic, isotropic hardening sensitive to strain-path changes. It was chosen to check our ability to identify the yield locus and hardening model.
- DP1000 (1,6mm thick) is a material used in cold forming whose characterization was required for the PROMETA/PROINDU project which finances this research.
- S320GD (0,69mm thick) is a steel grade used by ARCELOR but whose complete behavior was not identified, so it was chosen as the third material by the PROMETA/PROINDU partners.

The choice of an appropriate constitutive law depends on the observed mechanical behavior. Regardless of the chosen constitutive law, the identification is divided into three parts: elastic behavior, initial yield surface and work hardening model.

Isotropic elasticity is assumed, and the *elastic modulus* and *Poisson's coefficient* are determined by a uni-axial tensile test.

The initial yield function is classically identified using the *anisotropy coefficients* (or *Lankford coefficients*) based on strain measurements. An alternative identification, based on stress measurements, is proposed. Several yield stress points are measured for different stress states and *contours of equivalent plastic work* are defined. This method consists of the optimization of material parameters in order to define a function that represents those contours. In order to include the influence of strain and stress measurements, both methods can be combined.

The hardening constitutive laws are identified by an optimization procedure between the experimental curves and finite element simulation of the required tests. The optimization code is based on the *main Levenberg* algorithm and coupled with the finite element code *Lagamine*.

This chapter is divided into five sections. The first section briefly describes the identification of elastic parameters. The second section describes the initial yield locus identification using the two previously mentioned methods. The third section describes the identification of the material parameters of the different hardening laws. The material identification for the three materials is examined in the fourth section. Finally, some conclusions are established in the fifth section.

5.1 Elastic parameters' identification

The elastic parameters are measured from tensile tests at different angles from the RD (Figure 5.1). In addition, isotropic elasticity is assumed; hence, average values, for elastic modulus (E) and Poisson's coefficient (ν), are used.
These average values are computed as follows:

$$E = \frac{E_0 + 2 \cdot E_{45} + E_{90}}{4} . \tag{5.1}$$

$$\nu = \frac{\nu_0 + 2 \cdot \nu_{45} + \nu_{90}}{4} . \tag{5.2}$$

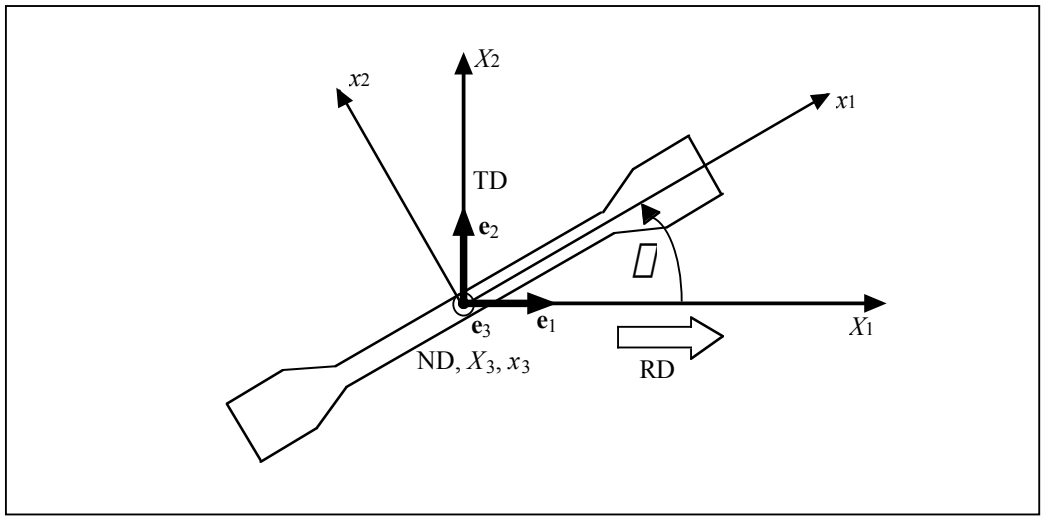

Figure 5.1 Uni-axial tensile test specimen.

5.2 Initial yield surface identification

5.2.1 Strain measurements method

This method is based on the anisotropic coefficients (Lankford coefficients) defined in Section 2.4.4. These coefficients are derived from strain measurements obtained from uni-axial tensile tests performed at different degrees from the RD (Figure 5.1). These coefficients can be linked with the yield surface material parameters by using the plastic flow rule defined in Equation 2.44.

Anisotropy coefficients

The rate of deformation tensor **d** (Equation 2.30) can be linked to the logarithmic strain tensor by:

$$\boldsymbol{\varepsilon}^{\ln} = \left(\mathbf{F}^T\mathbf{F}\right)^{-1}\mathbf{F}^T\mathbf{dF} \ . \tag{5.3}$$

It can be shown that when there are no rotations involved,

$$\boldsymbol{\varepsilon}^{\ln} = \mathbf{d} \ . \tag{5.4}$$

Then, for the uni-axial tensile state, the additive decomposition assumption (Equation 2.39) can be used for the logarithmic strain tensor, i.e.:

$$\boldsymbol{\varepsilon}^{\ln} = \boldsymbol{\varepsilon}^{e} + \boldsymbol{\varepsilon}^{p} \ . \tag{5.5}$$

Finally, the following approach is used:

$$\boldsymbol{\varepsilon}^{p} = \mathbf{d}^{p} \tag{5.6}$$

and the flow stress rule can be written as:

$$\boldsymbol{\varepsilon}^{p} = \dot{\lambda}\frac{\partial F}{\partial \boldsymbol{\sigma}} = \dot{\lambda}\mathbf{n} \ . \tag{5.7}$$

With respect to the orthotropic material axes (X_1, X_2, X_3) and using the general expression for the uni-axial stress state (Equation 3.7), **n** can be written for the Hill 1948 criterion (Equation 2.59) as:

$$\begin{aligned}\mathbf{n} = \sigma_{11}\Big\{&\left[(H+G)\cos^2\theta - H\sin^2\theta\right]\mathbf{e}_1 \quad \mathbf{e}_1 + \left[-H\cos^2\theta + (H+F)\sin^2\theta\right]\mathbf{e}_2 \quad \mathbf{e}_2 + \\ &\left[-G\cos^2\theta - F\sin^2\theta\right]\mathbf{e}_3 \quad \mathbf{e}_3 + N\frac{\sin 2\theta}{2}\,\mathbf{e}_1 \quad \mathbf{e}_2 + N\frac{\sin 2\theta}{2}\,\mathbf{e}_2 \quad \mathbf{e}_1\Big\} \ ,\end{aligned} \tag{5.8}$$

where σ_{11} indicates the uni-axial stress at the angle θ from the RD (in the **x** base, Figure 5.1). Lankford coefficients are measured in the (x_1, x_2, x_3) axes, then the following transformation is used to define the strain rate tensor in these axes (see Equation 3.5):

$$\boldsymbol{\varepsilon}_{\mathbf{x}} = \mathbf{R}\boldsymbol{\varepsilon}_{\mathbf{X}}\mathbf{R}^T \tag{5.9}$$

with

$$\mathbf{R} = \begin{bmatrix} \cos\theta & \sin\theta & 0 \\ -\sin\theta & \cos\theta & 0 \\ 0 & 0 & 1 \end{bmatrix}. \tag{5.10}$$

This gives the general expression for the Lankford coefficients:

$$r_\theta = \frac{\varepsilon^p_{22}}{\varepsilon^p_{33}} = \frac{H + (2N - F - G - 4H)\sin^2\theta\cos^2\theta}{G\cos^2\theta + F\sin^2\theta} \ . \tag{5.11}$$

r_{α} indicates the Lankford coefficient at the angle α from the RD.

Strain rate measures are taken with the optical extensometer (Chapter 3) in the x_1 direction (longitude) and in the x_2 direction (width) in Figure 5.1. The plastic strain rate in the x_3 (thickness) direction is computed from volume conservation. A logarithmic strain rate tensor, obtained from the temporal derivate of Equation 2.22, gives:

$$\dot{\varepsilon}_{33}^{p} = -\left(\dot{\varepsilon}_{11}^{p} + \dot{\varepsilon}_{22}^{p}\right) , \tag{5.12}$$

for the uni-axial tensile state. See also Equation 3.47 and Equation 3.49.

The Hill 1948 material parameters can then be characterized by uni-axial tensile tests at RD, TD and 45° from the RD.

$$r_0 = \frac{H}{G} \tag{5.13}$$

$$r_{90} = \frac{H}{F} \tag{5.14}$$

$$r_{45} = \frac{2N - F - G}{2\left(G + F\right)} \tag{5.15}$$

A final condition stems from the manner in which the yield stress σ_y is chosen. Combining Equation 2.59 and Equation 3.7 the Hill 1948 yield criterion can be written for a general uni-axial tensile case as:

$$\frac{\sigma_{11}^2}{2}\left[\left(H + G\right)\cos^4\alpha + \left(H + F\right)\sin^4\alpha + 2\left(N - H\right)\sin^2\alpha\cos^2\alpha\right] = \sigma_y^2 . \tag{5.16}$$

This equation directly implies that:

$$\text{if } \alpha = 0° : \; H + G = 2 , \tag{5.17}$$

$$\text{if } \alpha = 90° : \; H + F = 2 , \tag{5.18}$$

$$\text{if } \alpha = 45° : \; G + F + 2N = 8 . \tag{5.19}$$

Generally, the RD is chosen as the reference yield stress σ_y as in Equation 5.17.
Finally, parameters *M* and *L* are set equal to *N*, i.e.:

$$N = M = L . \tag{5.20}$$

The Hosford 1979 yield criterion (Equation 2.60) does not describe the shear stress; hence, the material parameters are characterized by tensile tests in the RD and TD. Recommended values for *a* are $a = 6$ for bcc and $a = 8$ for fcc materials (Hosford, 1998). Performing the same analysis also reveals the link between anisotropy coefficients and material parameters is done. The tensor **n** can be written as:

$$\mathbf{n} = \left[aG\left|\sigma_{11}\cos^2\theta\right|^{a-1}\frac{\left|\sigma_{11}\cos^2\theta\right|}{\sigma_{11}\cos^2\theta} + aH\left|\sigma_{11}\left(\cos^2\theta-\sin^2\theta\right)\right|^{a-1}\frac{\left|\sigma_{11}\left(\cos^2\theta-\sin^2\theta\right)\right|}{\sigma_{11}\left(\cos^2\theta-\sin^2\theta\right)}\right]\mathbf{e}_1 \quad \mathbf{e}_1 +$$
$$\left[aF\left|\sigma_{11}\sin^2\theta\right|^{a-1}\frac{\left|\sigma_{11}\sin^2\theta\right|}{\sigma_{11}\sin^2\theta} + aH\left|\sigma_{11}\left(\cos^2\theta-\sin^2\theta\right)\right|^{a-1}\frac{\left|\sigma_{11}\left(\cos^2\theta-\sin^2\theta\right)\right|}{\sigma_{11}\left(\cos^2\theta-\sin^2\theta\right)}(-1)\right]\mathbf{e}_2 \quad \mathbf{e}_2 +$$
$$\left[-aF\left|\sigma_{11}\sin^2\theta\right|^{a-1}\frac{\left|\sigma_{11}\sin^2\theta\right|}{\sigma_{11}\sin^2\theta} - aG\left|\sigma_{11}\cos^2\theta\right|^{a-1}\frac{\left|\sigma_{11}\cos^2\theta\right|}{\sigma_{11}\cos^2\theta}\right]\mathbf{e}_3 \quad \mathbf{e}_3 \tag{5.21}$$

where $\theta = 0°$ or $\theta = 90°$.

The anisotropy coefficients become:

$$r_0 = \frac{H}{G} \tag{5.22}$$

$$r_{90} = \frac{H}{F} \tag{5.23}$$

with the following assumptions:

if $\theta = 0°$: $H + G = 1$, (5.24)

if $\theta = 90°$: $H + F = 1$. (5.25)

Plastic strain rate computation

The plastic strain rate is computed from the total strain measured and the computation of the elastic strain (Equation 5.26) using the linear elastic constitutive model (Equation 5.27), where E is the elastic modulus and ν is the Poisson's coefficient measured from uni-axial tensile tests. Using Equation 5.5:

$$\boldsymbol{\varepsilon}^p = \boldsymbol{\varepsilon} - \boldsymbol{\varepsilon}^e \tag{5.26}$$

where

$$\boldsymbol{\varepsilon}^e = \frac{\sigma_{11}}{E}\left(\mathbf{e}_1 \otimes \mathbf{e}_1 - \nu\,\mathbf{e}_2 \otimes \mathbf{e}_2 - \nu\,\mathbf{e}_3 \otimes \mathbf{e}_3\right) . \tag{5.27}$$

Then, the plastic strain rate is computed by:

$$\dot{\boldsymbol{\varepsilon}}^p = \frac{d\boldsymbol{\varepsilon}^p}{dt} \tag{5.28}$$

If the elastic part is much smaller than the plastic one, the plastic strain rate can be approximated by the total strain rate:

$$\dot{\varepsilon}^p \approx \dot{\varepsilon} = \frac{d\varepsilon}{dt}. \tag{5.29}$$

This is not the case in this work, but it is worth mentioning due to its simplification of the measurements. An example can be seen in Table 5.5 and Table 5.6.

5.2.2 Stress measurements method

Figure 3.3 shows the initial yield surface as a function of the stress components present in a plane stress state. It also shows, by discrete points, some particular stress states (uni-axial tensile, plane strain and pure shear at the RD, TD and 45° from RD).
These stress states can be reproduced with the bi-axial machine described in Chapter 3 and Chapter 4, as well as with a tensile test machine.

Yield stress definition

The yield stress is defined by the offset method and it is determined from a stress – strain diagram obtained from a uni-axial tensile test (in this work, at the RD, see Figure 5.2). The choice of the offset is set to an arbitrary plastic strain value $\varepsilon^p = \varepsilon_0^p$.

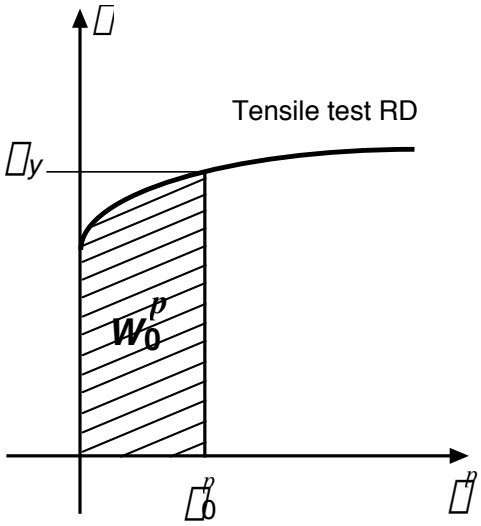

Figure 5.2 Yield stress for a uni-axial tensile test at the RD.

The yield stress for other stress states is defined by the plastic work W^p (Equation 5.30) computed from the uni-axial stress – strain curve in the RD for σ_y and ε^p (Figure 5.3). The offset plastic work W_0^p is associated with the offset strain ε_0^p.

$$W^p = \int \boldsymbol{\sigma} : d\boldsymbol{\varepsilon}^p \tag{5.30}$$

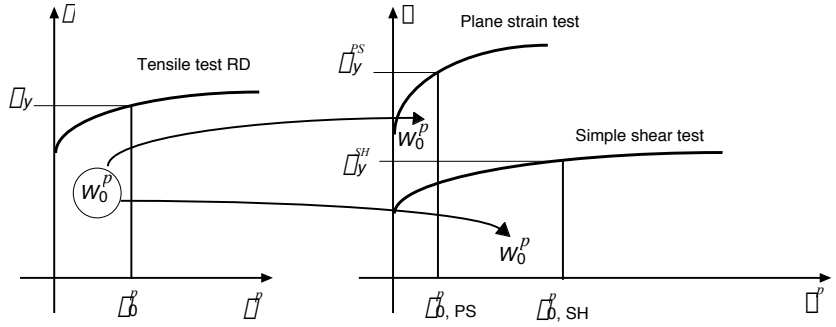

Figure 5.3 Yield stresses for different stress states.

Contours of plastic work

The contours of plastic work are defined from several yield stress states (tensile, plane strain and simple shear in the RD, TD and 45° from the RD) computed at equal $\bar{\varepsilon}_0^p$.
These points are plotted in a $(\sigma_{11},\sigma_{22},\sigma_{12})$ axis (as in Figure 3.3) and they belong to a surface defined for the chosen plastic strain offset. For small plastic strain levels, this surface approximates the yield locus.
To define contours of plastic work, the following hypothesis must be assumed:

- At small deformations a simple shear test can represent a pure shear state as is shown in Figure 3.11 (Section 3.1.4).

- Mechanical configuration of the bi-axial testing machine renders the measurement the whole plane strain stress state impossible. The missing stress component is obtained using the flow rule and the strain field measurements. Then, the component σ_{22}, for a plane strain test performed in the x_1 direction (angle θ from the RD), is related to the measured one σ_{11} by:

$$\dot{\bar{\varepsilon}}_{22}^p = \dot{\lambda}\frac{\partial F}{\partial \sigma_{22}} = 0. \tag{5.31}$$

(See also Equation 3.20 and the experimental results of Figure 4.5.)
The Hill 1948 criterion is used to establish a general expression that relates σ_{22} with σ_{11}. **n** is represented in Equation 5.32 in the orthotropic material axis (X_1, X_2, X_3) by using the general expression for the plane strain stress state (Equation 3.8). Then, using the transformation matrix of Equation 5.9, the strain is represented in the (x_1, x_2, x_3) axis and the relation established in Equation 5.33 can be obtained.

$$\begin{aligned}\mathbf{n} = &\left[(H+G)\left(\sigma_{11}\cos^2\theta + \sigma_{22}\sin^2\theta\right) - H\left(\sigma_{11}\sin^2\theta + \sigma_{22}\cos^2\theta\right)\right]\mathbf{e}_1 \quad \mathbf{e}_1 + \\ &\left[-H\left(\sigma_{11}\cos^2\theta + \sigma_{22}\sin^2\theta\right) + (H+F)\left(\sigma_{11}\sin^2\theta + \sigma_{22}\cos^2\theta\right)\right]\mathbf{e}_2 \quad \mathbf{e}_2 \\ &\left[-G\left(\sigma_{11}\cos^2\theta + \sigma_{22}\sin^2\theta\right) - F\left(\sigma_{11}\sin^2\theta + \sigma_{22}\cos^2\theta\right)\right]\mathbf{e}_3 \quad \mathbf{e}_3 + \\ &N(\sigma_{11}-\sigma_{22})\sin 2\theta\,\mathbf{e}_1 \quad \mathbf{e}_2 + N(\sigma_{11}-\sigma_{22})\sin 2\theta\,\mathbf{e}_2 \quad \mathbf{e}_1 .\end{aligned} \tag{5.32}$$

$$\sigma_{22} = \underbrace{\left[\frac{H + (2N - 4H - G - F)\cos^2\theta\sin^2\theta}{(H+G)\sin^4\theta + (H+F)\cos^4\theta + 2(N-H)\cos^2\theta\sin^2\theta}\right]}_{k_\theta}\sigma_{11} . \tag{5.33}$$

$$\text{If } \theta = 0°: \; k_0 = \frac{H}{H+F} \;, \tag{5.34}$$

$$\text{if } \theta = 90°: \; k_{90} = \frac{H}{H+G} \;, \tag{5.35}$$

$$\text{if } \theta = 45°: \; k_{45} = \frac{2N+G+F}{2N+G+F} \;. \tag{5.36}$$

The same analysis for the Hosford 1979 criterion gives the following relations:

$$\text{If } \theta = 0°: \; k_0 = \frac{1}{1+\left(\frac{F}{H}\right)^{a-1}} \;, \tag{5.37}$$

$$\text{if } \theta = 90°: \; k_{90} = \frac{1}{1+\left(\frac{G}{H}\right)^{a-1}} \;. \tag{5.38}$$

Optimization of material parameters

The experimental points define discrete points over the yield surface. The material parameters that define the shape of this surface are optimized in order to minimize the following function:

$$\Phi = \underbrace{\sum_{i=1,l} (1-w)\left(\frac{\sigma_{Theo\_i} - \sigma_{exp\_i}}{\sigma_y}\right)^2}_{\Phi_\sigma} + \underbrace{\sum_{j=1,m} w\left(\frac{r_{Theo\_j} - r_{exp\_j}}{\bar{r}}\right)^2}_{\Phi_r} \tag{5.39}$$

where the sub-index *l* defines the number of experimental tests used to measure stress points, and sub-index *m* the number of tests used to define anisotropy parameters. The sub-index *Theo* and *exp* refer respectively to the theoretical and experimental values. w is a weight factor for the stress and strain measurements.
The theoretical value for a uni-axial tensile test defined by Hill 1948 is:

$$\sigma_{11} = \sqrt{\frac{2}{(H+G)\cos^4\theta + (H+F)\sin^4\theta + 2(N-H)\cos^2\theta\sin^2\theta}}\,\sigma_y \tag{5.40}$$

for the plane strain test:

$$\sigma_{11} = \sqrt{\frac{2}{\left[(1-k_\theta)^2 H + G + k_\theta^2 F\right]\cos^4\theta + \left[(1-k_\theta)^2 H + k_\theta^2 G + F\right]\sin^4\theta + \left[N(1-k_\theta)^2 + k(G+F) - (1-k_\theta)^2 H\right]2\cos^2\theta\sin^2\theta}}\,\sigma_y \tag{5.41}$$

and for the simple shear test (approximated by a pure shear test, i.e., $\sigma_{11}, \sigma_{22} \approx 0$):

$$\sigma_{12} = \sqrt{\frac{2}{(4H+G+F)\sin^2 2\theta + 2N\cos^2 2\theta}} \,. \tag{5.42}$$

The Hill 1948 material parameters are identified by the eight experimental tests of Table 5.1.

Test	Experimental point	Theoretical value
Uni-axial tensile RD	$\sigma_{exp\_1} = \sigma_{11}(\theta = 0°)$	$\sigma_{11} = \sigma_{Theo\_1} = \sqrt{\frac{2}{H+G}}\sigma_y$
Uni-axial tensile TD	$\sigma_{exp\_2} = \sigma_{11}(\theta = 90°)$	$\sigma_{11} = \sigma_{Theo\_2} = \sqrt{\frac{2}{H+F}}\sigma_y$
Uni-axial tensile 45°	$\sigma_{exp\_3} = \sigma_{11}(\theta = 45°)$	$\sigma_{11} = \sigma_{Theo\_3} = \sqrt{\frac{8}{2N+G+F}}\sigma_y$
Plane strain RD	$\sigma_{exp\_4} = \sigma_{11}(\theta = 0°)$	$\sigma_{11} = \sigma_{Theo\_4} = \sqrt{\frac{2}{H(1-k_0)^2 + G + k_0^2 F}}\sigma_y$
Plane strain TD	$\sigma_{exp\_5} = \sigma_{11}(\theta = 90°)$	$\sigma_{11} = \sigma_{Theo\_5} = \sqrt{\frac{2}{H(1-k_{90})^2 + k_{90}^2 G + F}}\sigma_y$
Plane strain 45°	$\sigma_{exp\_6} = \sigma_{11}(\theta = 45°)$	$\sigma_{11} = \sigma_{Theo\_6} = \sqrt{\frac{8}{2N(1-k_{45})^2 + (1+k_{45})^2(G+F)}}\sigma_y$
Simple shear RD	$\sigma_{exp\_7} = \sigma_{12}(\theta = 0°)$	$\sigma_{12} = \sigma_{Theo\_7} = \sqrt{\frac{1}{N}}\sigma_y$
Simple shear 45°	$\sigma_{exp\_8} = \sigma_{12}(\theta = 45°)$	$\sigma_{12} = \sigma_{Theo\_8} = \sqrt{\frac{2}{4H+G+F}}\sigma_y$

Table 5.1 Experimental points and theoretical values for Hill 1948 yield criterion.

The Hosford 1979 material parameters are identified by the five experimental tests of Table 5.2.

Test	Experimental point	Theoretical value
Uni-axial tensile RD	$\sigma_{exp\_1} = \sigma_{11}(\theta = 0°)$	$\sigma_{11} = \sigma_{Theo\_1} = \left(\frac{1}{H+G}\right)^{\frac{1}{a}}\sigma_y$
Uni-axial tensile TD	$\sigma_{exp\_2} = \sigma_{11}(\theta = 90°)$	$\sigma_{11} = \sigma_{Theo\_2} = \left(\frac{1}{H+F}\right)^{\frac{1}{a}}\sigma_y$
Plane strain RD	$\sigma_{exp\_3} = \sigma_{11}(\theta = 0°)$	$\sigma_{11} = \sigma_{Theo\_3} = \left(\frac{1}{H\lvert 1-k_0\rvert^a + G + \lvert k_0\rvert^a F}\right)^{\frac{1}{a}}\sigma_y$
Plane strain TD	$\sigma_{exp\_4} = \sigma_{11}(\theta = 90°)$	$\sigma_{11} = \sigma_{Theo\_4} = \left(\frac{2}{H\lvert k_{90}-1\rvert^a + \lvert k_{90}\rvert^a G + F}\right)^{\frac{1}{a}}\sigma_y$
Simple shear 45°	$\sigma_{exp\_5} = \sigma_{12}(\theta = 45°)$	$\sigma_{12} = \sigma_{Theo\_5} = \left(\frac{1}{2^a H + G + F}\right)^{\frac{1}{a}}\sigma_y$

Table 5.2 Experimental points and theoretical values for Hosford 1979 yield criterion.

5.3 Hardening parameters identification

The calibration of the hardening constitutive laws is performed using an optimization procedure, regardless of its complexity.
An optimization code called *Optim* based on the main Levenberg algorithm (Mathonet and Habraken, 2003) is coupled with the finite element code *Lagamine*. Finite element simulations of the required identification tests are performed in order to optimize experimental stress – strain curves. Due to the homogeneity of the stress and strain fields (shown in Chapter 4) only one finite element mesh is required.
This method consists in minimizing an objective function (based on the addition of square difference) obtained from the difference between the simulated curves and experimental ones.

Optim works in the following way:

- Read the experimental data.
- Run *Lagamine* with the given material parameters.
- Compute the *sensibility matrix* built up by the function and its derivatives with respect to the parameters. More details can be found in Mathonet and Habraken 2003.
- Compute the norm.
- New set of parameters is proposed.

* loop continues until 1 – ($norm_1$/norm) > tolerance, where $norm_1$ is the norm computed with guest parameters, and norm is the lowest norm calculated.

The number of mechanical tests required for the material identification depends on the complexity of the model.
The texture evolution that induces modification in the yield function shape is not taken into account. Hence, throughout this work, only tests performed in the RD are used for the identification of hardening materials parameters.

5.3.1 Isotropic hardening identification

For a three-parameter isotropic hardening law (Swift or Voce type, studied in Chapter 2), a single uni-axial stress – strain curve is required for identification.
The study of the influence of the material parameters on the flow rule is necessary to facilitate the tuning of material parameters.
Figure 5.4, Figure 5.5 and Figure 5.6 show the influence on the uni-axial stress – strain curve of the different parameters of the Swift type hardening law (Equation 2.67). Once set, the optimized parameters set must agree with the initial yield stress given by:

$$\sigma_y = K\varepsilon_0^n \,, \tag{5.43}$$

or, if an offset is used to determine the initial yield stress:

$$\sigma_y\left(\varepsilon_0^p\right) = K\left(\varepsilon_0 + \varepsilon_0^p\right)^n . \tag{5.44}$$

This equation uses only the plastic strain computed as in Equation 5.26.

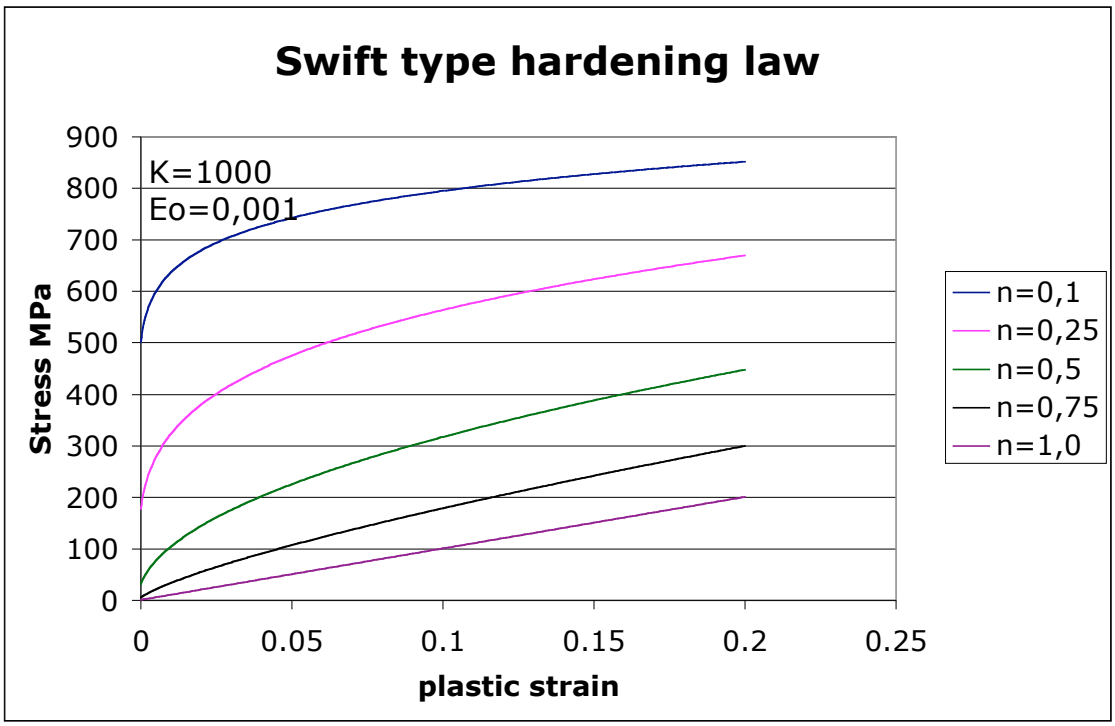

Figure 5.4 Variation of parameter *n*. Swift type isotropic hardening law.

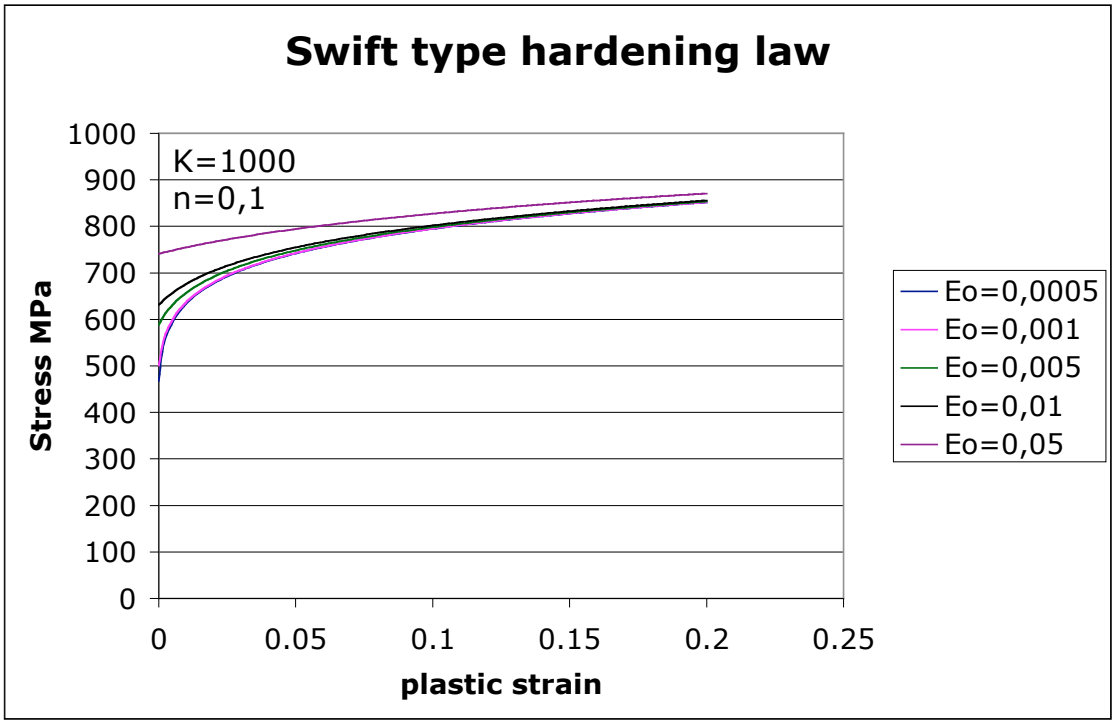

Figure 5.5 Variation of parameter ε_0. Swift type isotropic hardening law.

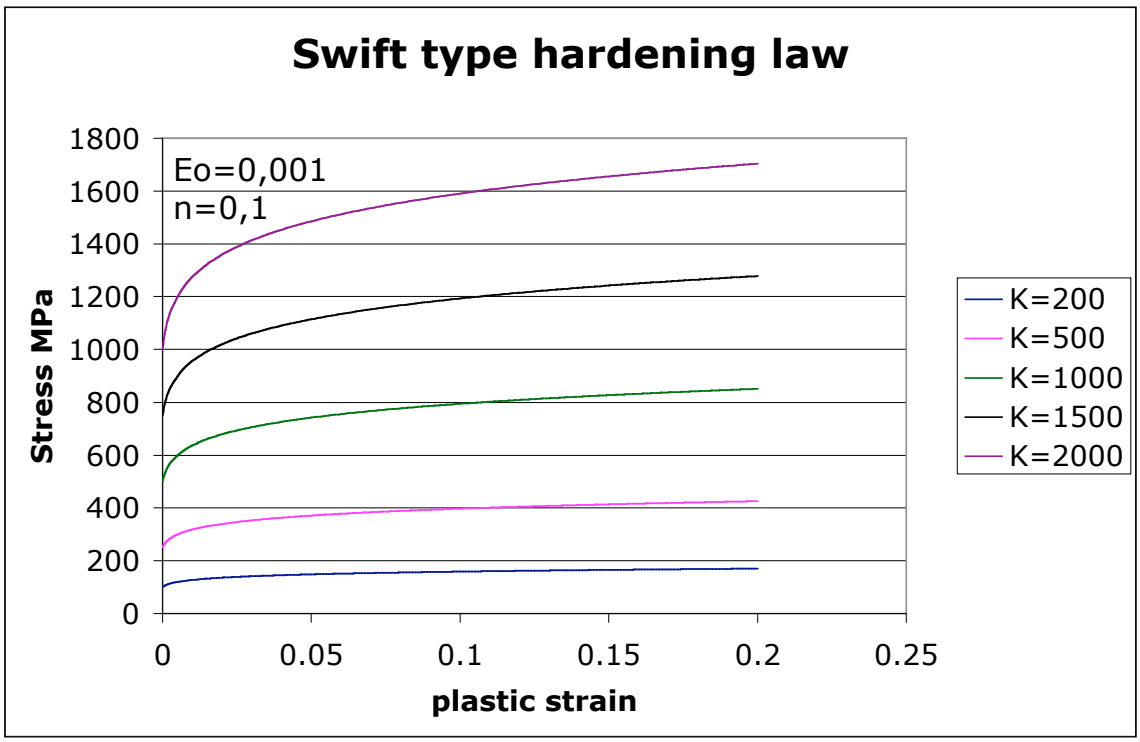

Figure 5.6 Variation of parameter *K*. Swift type isotropic hardening law.

A Voce type isotropic hardening law (Equation 2.69) counts also 3 material parameters: R_0, R_{SAT} and C_R.
The parameter R_0 represents the initial yield stress and is obtained from the tensile test using the offset method. The other parameters describe the saturation of the flow stress (R_{SAT}) and its respective saturation speed (C_R) as it can be seen respectively in Figure 5.7 and Figure 5.8.

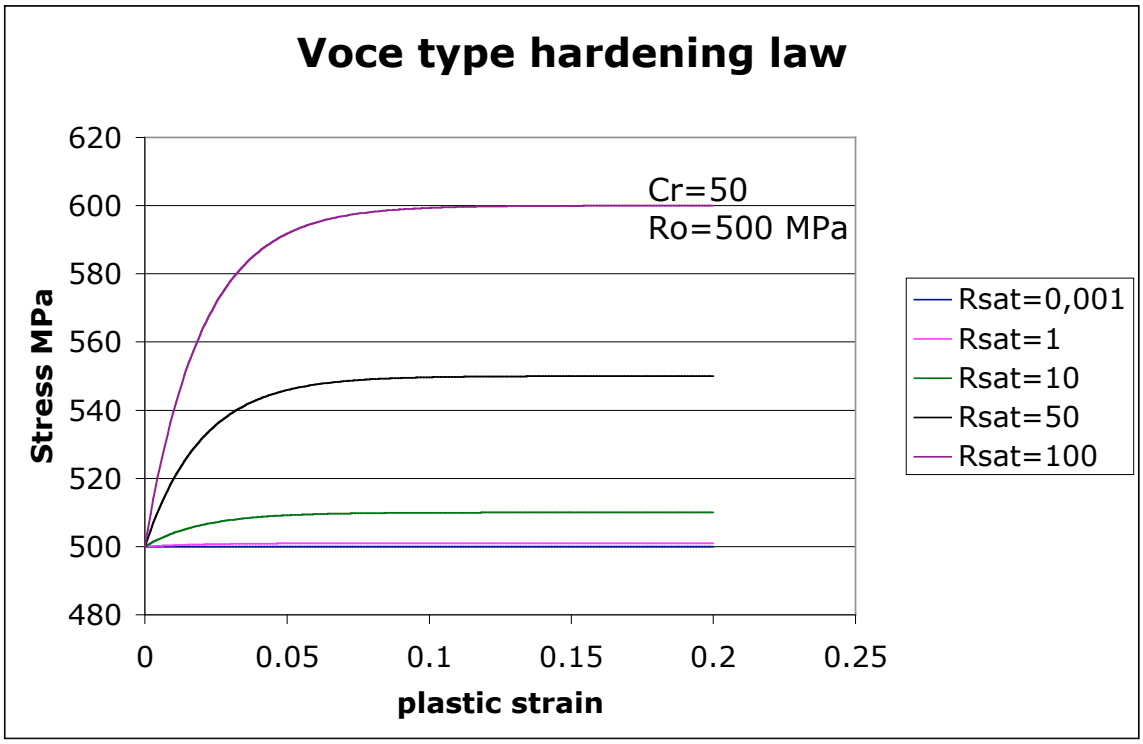

Figure 5.7 Variation of parameter R_{SAT}. Voce type isotropic hardening law.

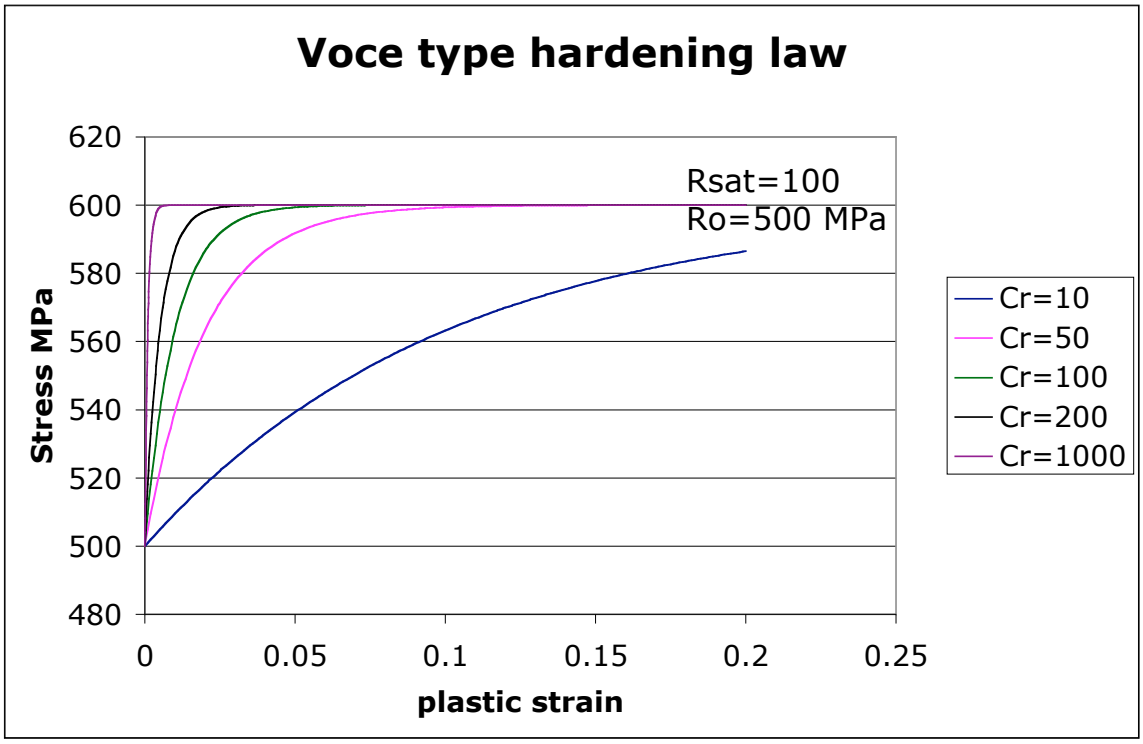

Figure 5.8 Variation of parameter C_R. Voce type isotropic hardening law.

5.3.2 Kinematic hardening identification

Kinematic hardening, as it is mentioned in Section 2.4.5, describes the displacement of the yield surface, while the size and shape remain constant. Kinematic hardening predicts the Bauschinger effect (Figure 3.5), which can be observed after a reversed load test (i.e. tension followed by a compression). In this work, the Bauschinger effect is visualized by reverse simple shear tests as seen in Chapter 4.
The Armstrong-Frederick kinematic hardening law presented in Equation 5.45 combined with Equation 2.73 has three material parameters. The initial yield stress is obtained form a uni-axial tensile test and it defines the constant yield surface size. The other two parameters represent the saturation of the back-stress ($s = X_{SAT}$) and its respective saturation speed ($c = C_X$). The back-stress evolution equation is written as:

$$\overset{\square}{\mathbf{X}} = C_X\left(X_{SAT}\mathbf{d}^p - \mathbf{X}\dot{p}\right). \tag{5.45}$$

The influence of these material parameters over a reverse simple shear test (shear stress – gamma curve) can be seen in Figure 5.9 and Figure 5.10.

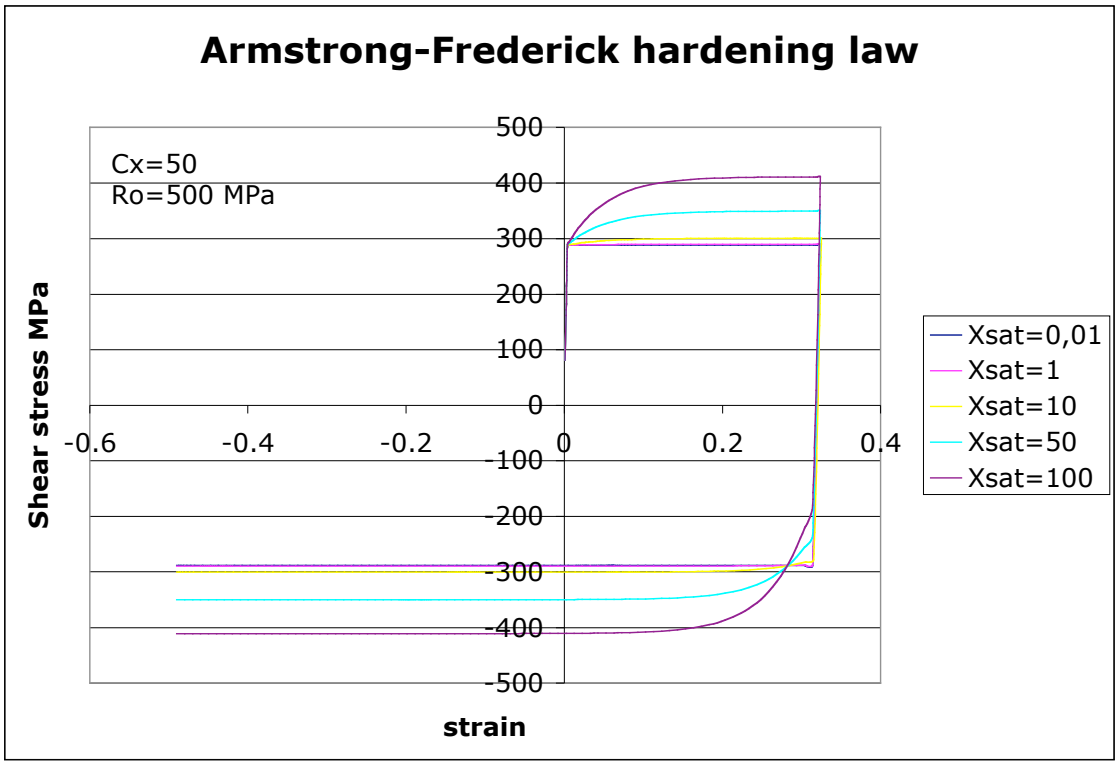

Figure 5.9 Variation of parameter X_{SAT}. Armstrong-Frederick kinematic hardening law.

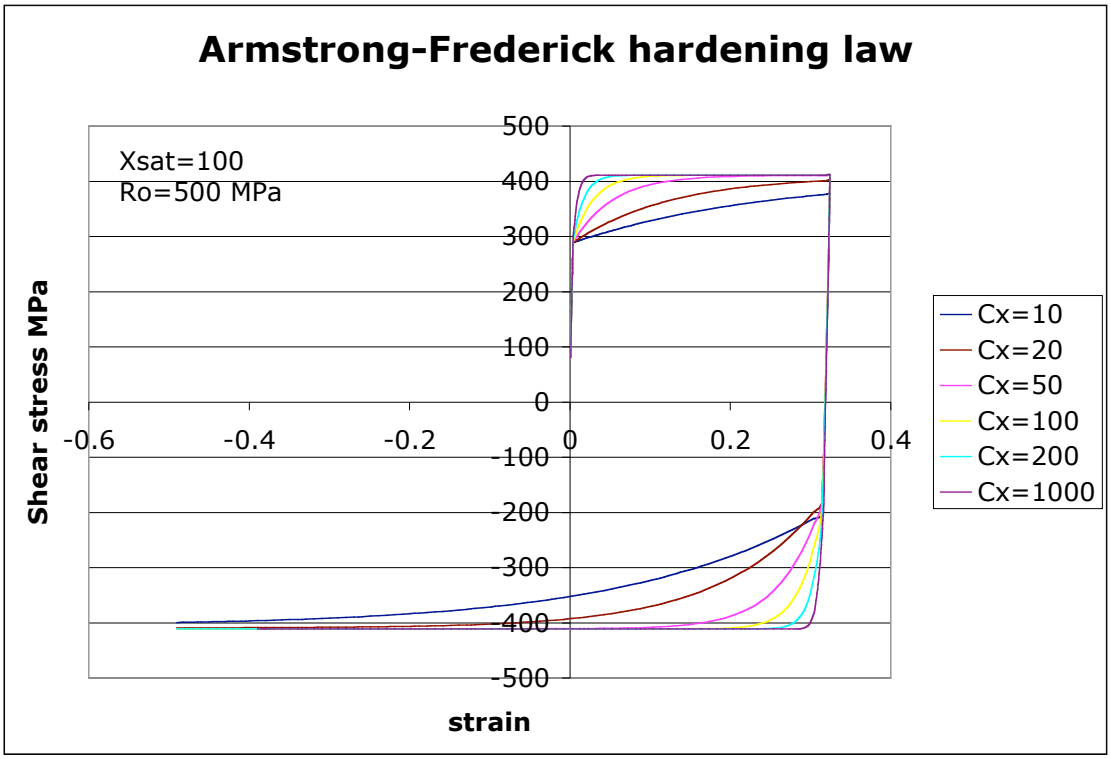

Figure 5.10 Variation of parameter C_X. Armstrong-Frederick kinematic hardening law.

5.3.3 Mixed hardening identification

The size and displacement of the yield surface evolution can be described combining both hardening constitutive laws. This new constitutive law entails 5 material parameters, which

must be optimized by at least two mechanical tests: a uni-axial tensile test and a reverse simple shear test.

5.3.4 Teodosiu and Hu hardening law identification

The Teodosiu and Hu micro-structural based hardening law is described in Section 2.5. A review, concerning the micro-structural roots, the required mechanical tests and the phenomenological constitutive equations, is presented in Annex A.
This constitutive law is able to predict the transient effect on the flow rule due to strain-path changes (Section 2.6 and Section 3.1.3).
For example, the strain path for which $\alpha = 1$ can be reproduced by any monotonic test (uni-axial tensile or simple shear).
The strain path for which $\alpha = -1$ is reproduced by a reverse simple shear test. Here, a transient stagnation of the work hardening followed by a resumption of the flow stress can be observed. The size of this transient zone depends on the pre-strain.
The strain path for which $\alpha = 0$ is reproduced by a plane strain test followed by a simple shear test (orthogonal test). Depending on the amount of pre-strain, the flow stress of the subsequent path will have a positive work hardening rate (if the pre-strain is small) or a work softening followed by a resumption of the work hardening (if the pre-strain is large).
This hardening law entails 13 material parameters $\{m, R_0, C_R, R_{SAT}, C_X, X_{SAT0}, q, C_{SD}, C_{SL}, S_{SAT}, n_P, n_L, C_P\}$ and requires four kinds of mechanical tests for its identification: uni-axial tensile, monotonic simple shear, reverse simple shear and orthogonal tests. The reverse simple shear and orthogonal tests must be performed at different levels of pre-strain.
This section is focused on the identification of material parameters in Teodosiu and Hu's law.

According to this law, the material parameter R_0 represents the initial yield stress and is obtained by the offset method from a uni-axial tensile test.
Next, m, C_R, R_{SAT}, C_X, X_{SAT0}, C_{SD}, S_{SAT}, C_P are optimized using the uni-axial tensile, the simple shear and Bauschinger tests at a small pre-strain. Parameters C_{SL}, n_L and q are activated only when $\alpha \neq \pm 1$ as can be seen in Equation 2.84 for the tensor $\mathbf{S}_L$ evolution and in Equation 2.76 for the back-stress saturation X_{SAT} (α_S is a generalization of α). The parameter n_P, that describes the work hardening stagnation after a reverse load ($\alpha = -1$), has a small influence on the flow stress for small pre-strain levels (Figure 5.14 and Figure 5.15); therefore, this parameter can be set to an arbitrary value.
The saturation speed parameters C_R , C_X, C_{SD}, C_P are adjusted using the stress – strain data at small strains (where the work hardening is higher) from the uni-axial tensile test, the monotonic simple shear test and the reversed part of one Bauschinger test (at a small pre-strain level) (see Figure 5.11).

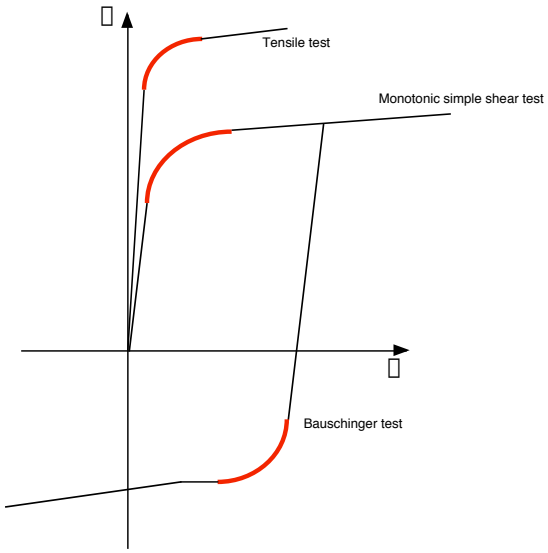

Figure 5.11 Saturation speed parameter identification: C_R, C_X, C_{SD}, C_P. Higher work hardening, at small strains.

The saturation parameters R_{SAT}, X_{SAT0}, S_{SAT} are adjusted according to the stress – strain data at final strains (where the work hardening tends to zero) from the uni-axial tensile test, the monotonic simple shear test and the reversed part of one Bauschinger test (at a small pre-strain level) (see Figure 5.12).

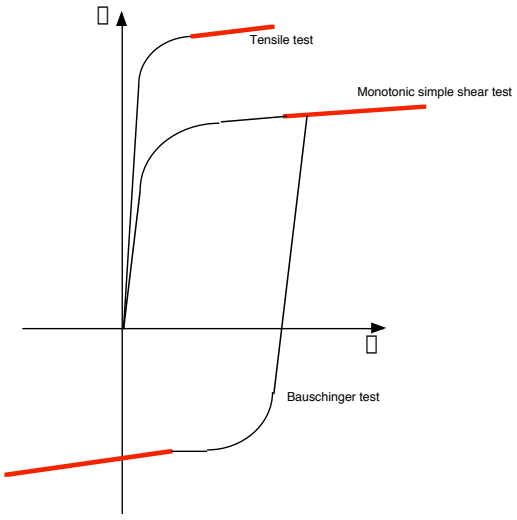

Figure 5.12 Saturation parameter identification: R_{SAT}, X_{SAT0}, S_{SAT}. Lower work hardening, at larger strains.

Parameters m, C_X and X_{SAT0}, are fitted to the beginning of the reversed flow curve of Bauschinger tests as shown in Figure 5.13.

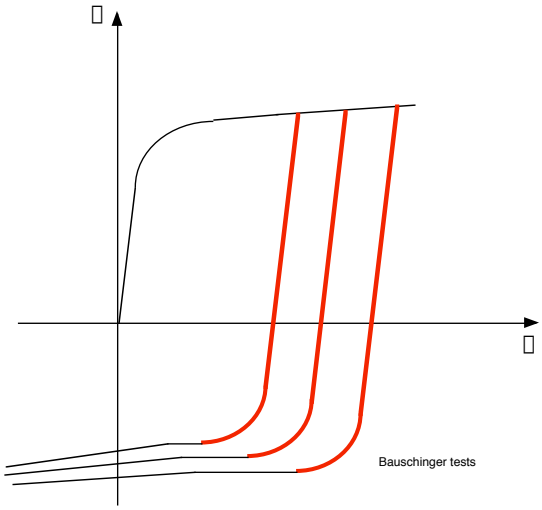

Figure 5.13 Identification of Bauschinger effect parameters: m, C_X, X_{SAT0}. Reversed flow curve of Bauschinger tests.

The parameter n_P has an influence only when $P_D < 0$ (Equation 2.83), as evidenced by the case when [illegible]. The higher the pre-strain is, the higher the value of P_D. In the case where the structure is completely polarized ($P_D = 1$), inversing the load induces $N_1 = -N_2$, then $P_D = -1$ and $g = 0$. The parameter is identified with the second strain path of a Bauschinger test (Figure 5.14). Figure 5.15 illustrates the influence of the parameter n_P on the function g.

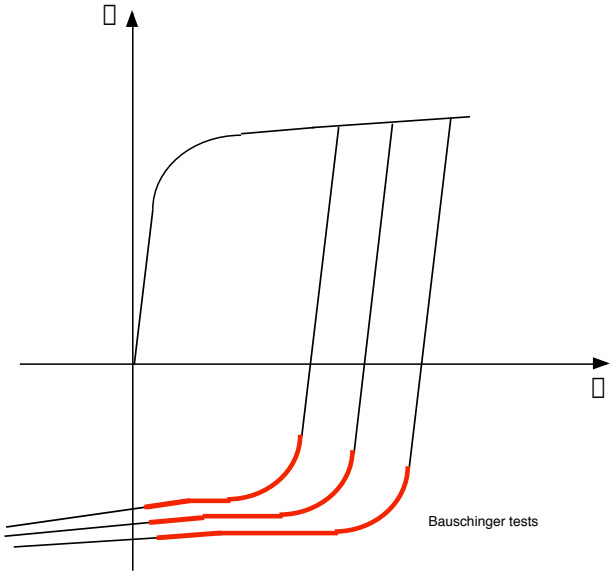

Figure 5.14 Identification of n_P.

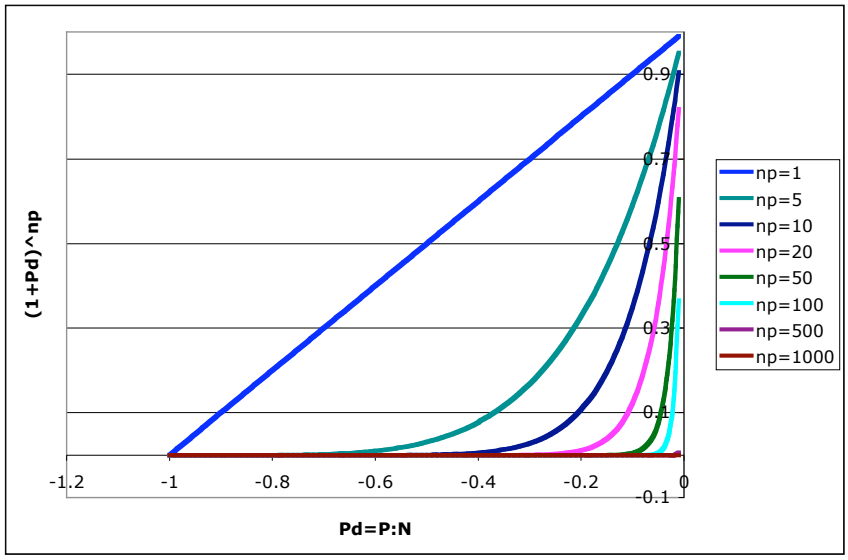

Figure 5.15 Influence of parameter n_P on the function g.

Finally, C_{SL}, n_L and q are identified with the second strain path of the orthogonal test, as in Figure 5.16.

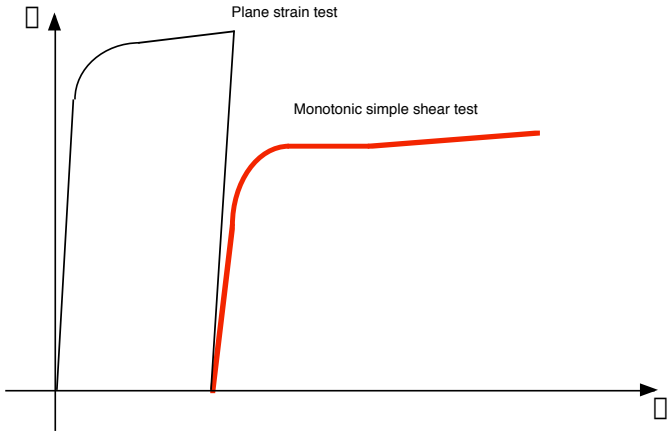

Figure 5.16 Second strain path of an orthogonal test: C_{SL}, n_L and q identification.

Likewise, the influence of some material parameters on the mechanical test has been studied. The data for finite element simulations of Bauschinger and orthogonal tests, performed for the DP600 (0,7 mm thickness), in Table 4.1 and Table 4.2.
The saturation speed and the saturation parameters have the same influence on the flow stress curve as the parameters described for the Voce law and for Armstrong-Frederick (Figure 5.7 to Figure 5.10). The influence of new parameters is studied below.

The parameter n_P describes the work hardening stagnation after imposing a reverse load (depending on the amount of pre-strain). The influence of this parameter is shown in Figure 5.17.

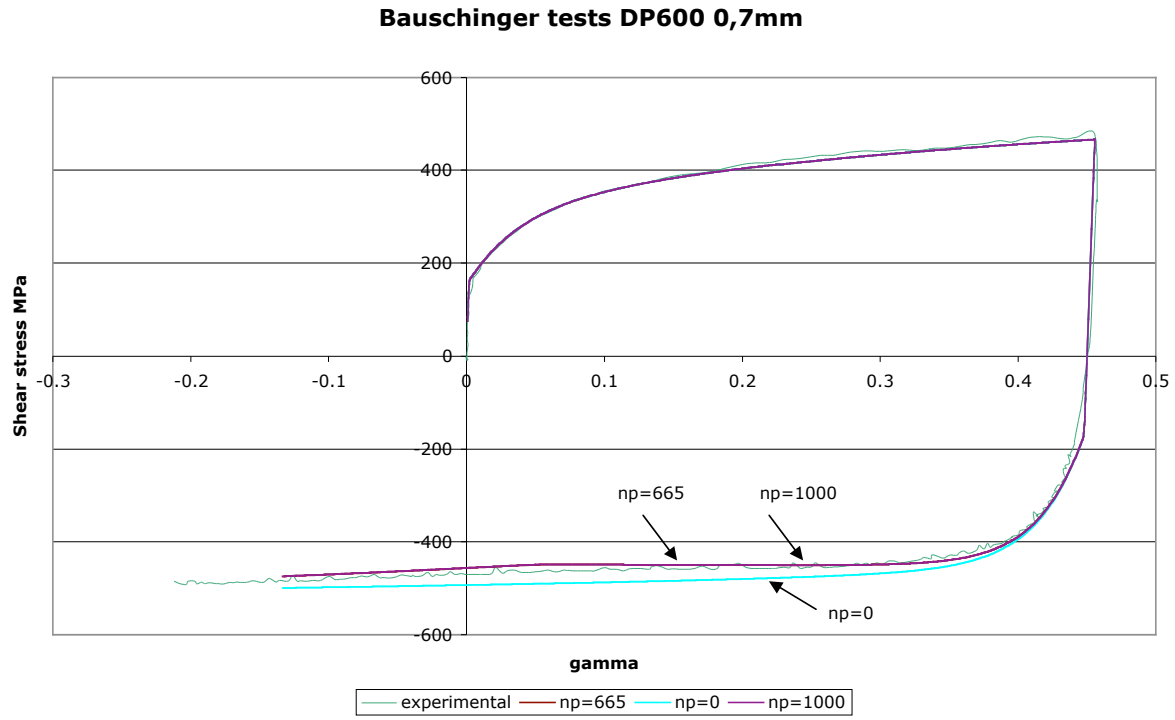

Figure 5.17 Influence of parameter n_P on a Bauschinger test.

Parameter m describes the contribution of the persistent dislocation structures to isotropic or kinematic hardening. This parameter's influence on the flow stress can be seen in Figure 5.18, where $m \in [0 , 1]$.

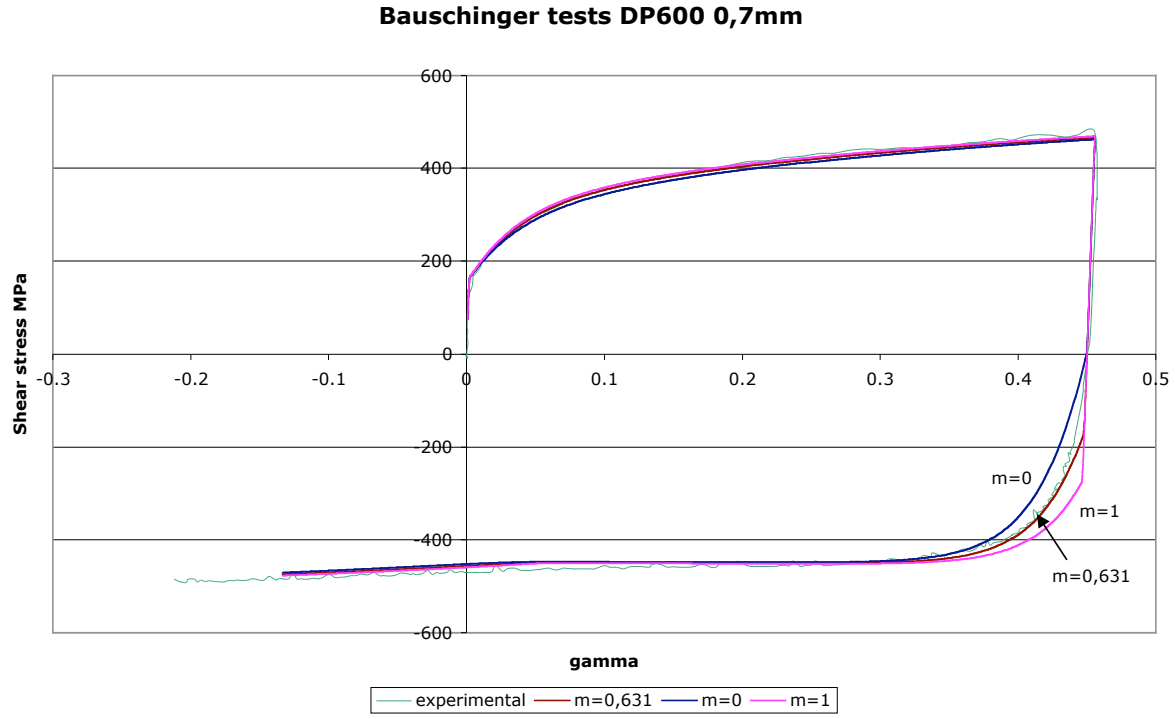

Figure 5.18 Influence of the parameter m in a Bauschinger test.

The influence of parameters C_{SL}, q, n_L, and m is studied on an orthogonal test. The simulated test is a plane strain test followed by a simple shear test. Figure 5.19 to Figure 5.23 show only the second loading flow stress.
Figure 5.19 shows the influence of the saturation speed parameter C_{SL} during the second load, whereas Figure 5.20 shows a detail of the zone where the parameter has greater influence.

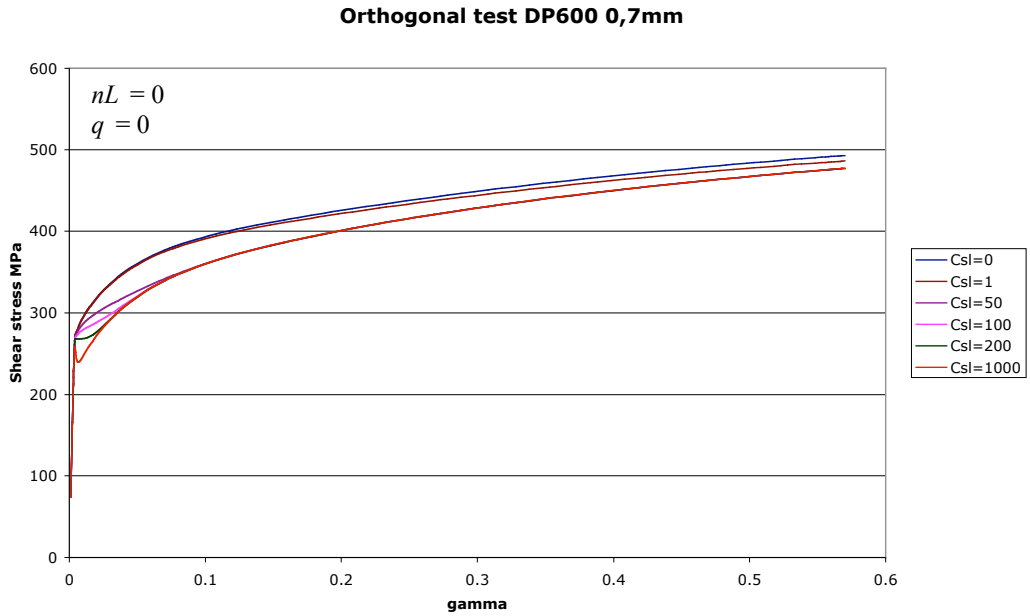

Figure 5.19 Influence of the parameter C_{SL} on the second loading in an orthogonal test.

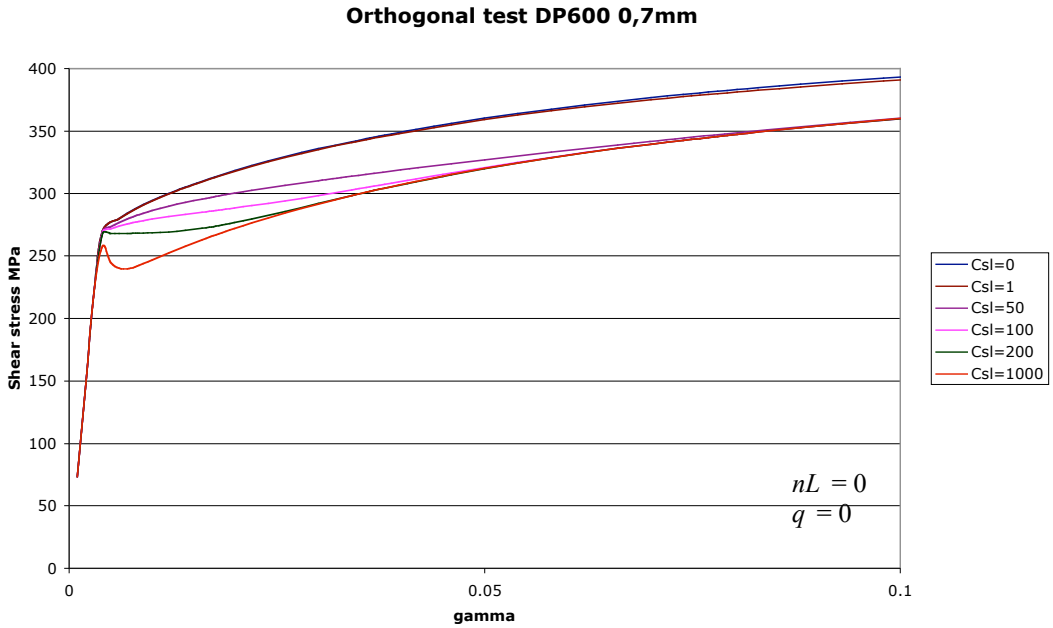

Figure 5.20 Zoom of the influence of the parameter C_{SL} on the second loading in an orthogonal test.

The parameter q has an influence on the amplitude of the stress, as is shown in Figure 5.21.

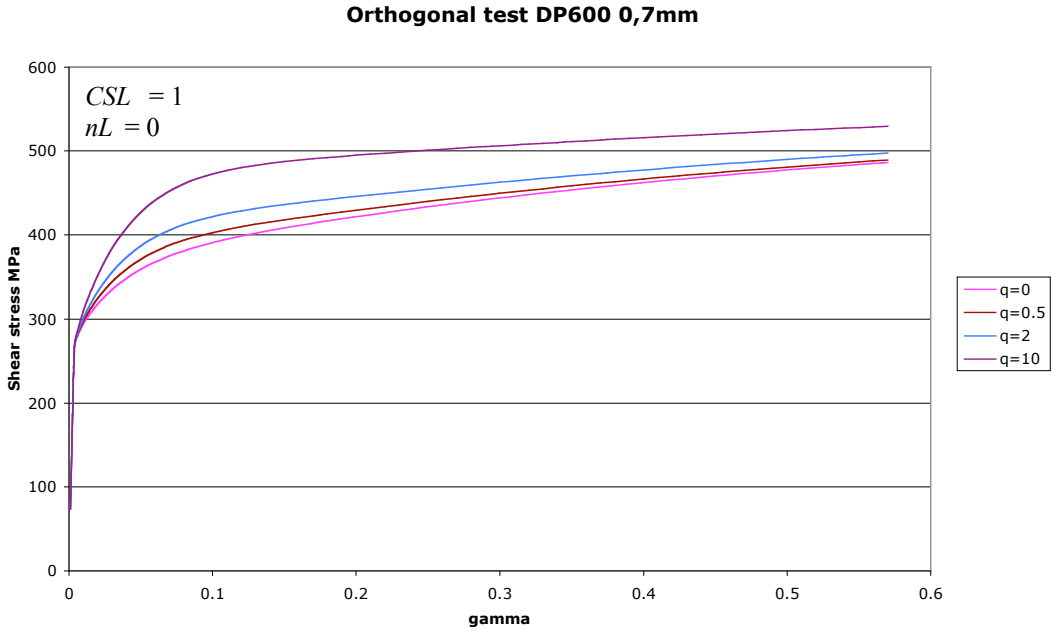

Figure 5.21 Influence of the parameter q on the second loading in an orthogonal test.

The influence of the amount of pre-strain is included in the factor $(Z/S_{SAT})^{nL}$ of Equation 5.46, where $Z = |\mathbf{S}_L|$. When the pre-strain is very small ($Z << S_{SAT}$), the evolution of $\mathbf{S}_L$ is negligible, whereas when the pre-strain is large, Z approaches S_{SAT} and the evolution of $\mathbf{S}_L$ is restored. (See Chapter 2 and Annex A for complementary information.)

The influence of the parameter n_L on $(Z/S_{SAT})^{nL}$ can be seen in Figure 5.22. One may observe that $(Z/S_{SAT})^{nL} \in [0\ ,\ 1]$, and it directly multiplies the saturation speed parameter C_{SL}.

$$\overset{\circ}{\mathbf{S}}_L = C_{SL}\left(\frac{Z}{S_{SAT}}\right)^{nL}\mathbf{S}_L\dot{p} \tag{5.46}$$

Figure 5.23 shows the influence of n_L for an 11% of amount of pre-strain.

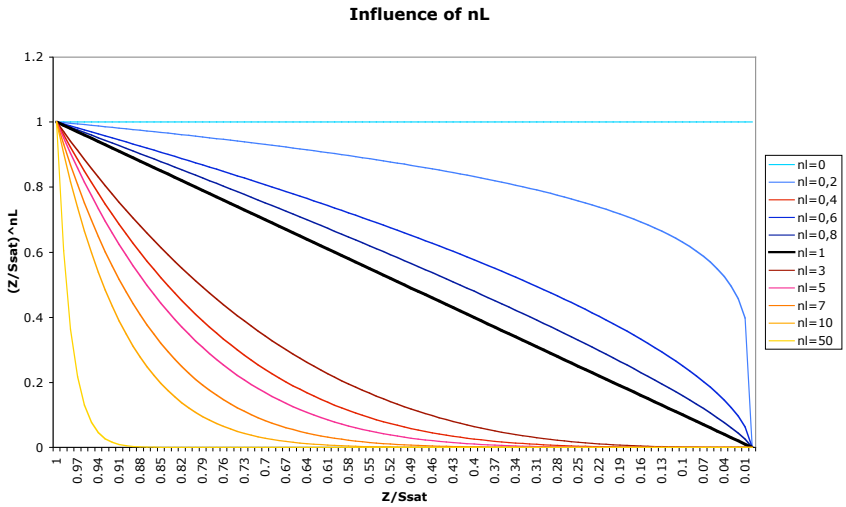

Figure 5.22 Influence of the parameter n_L on the factor multiplying the speed saturation C_{SL}.

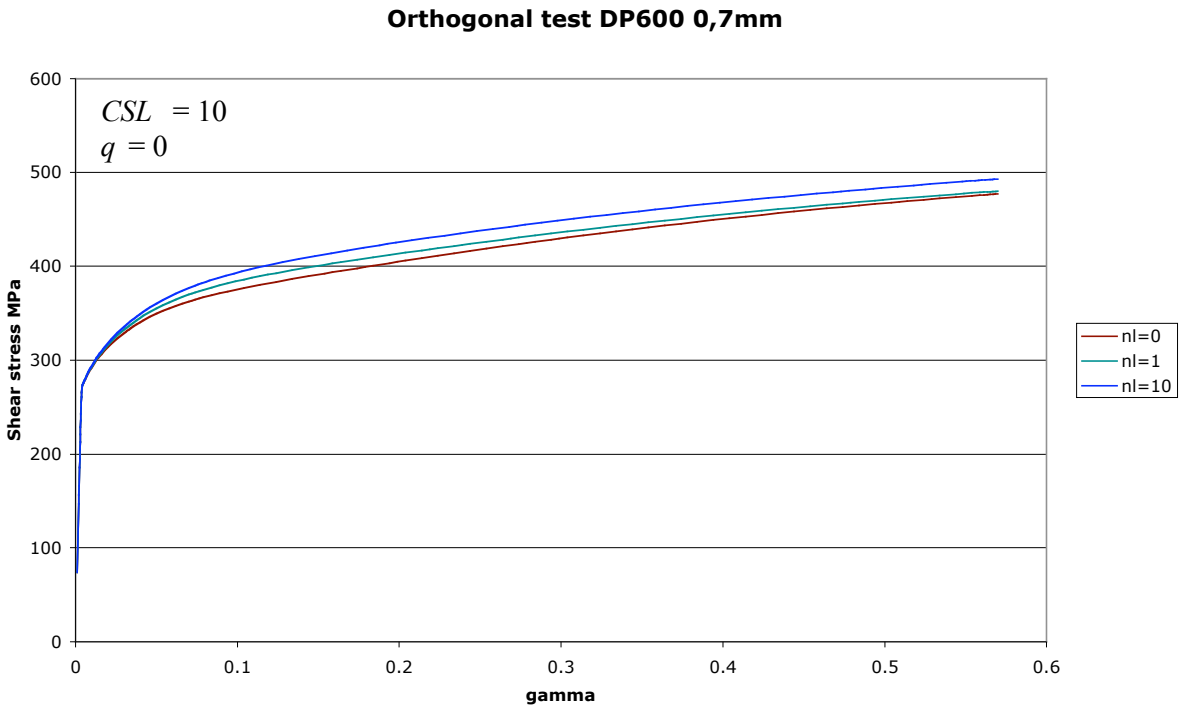

Figure 5.23 Influence of the parameter n_L on a second path of an orthogonal test.

As it appears in Figure 5.24, the parameter *m* influences the second load in an orthogonal test. This parameter, as well as in the Bauschinger test case, defines the yield stress of the subsequent load.

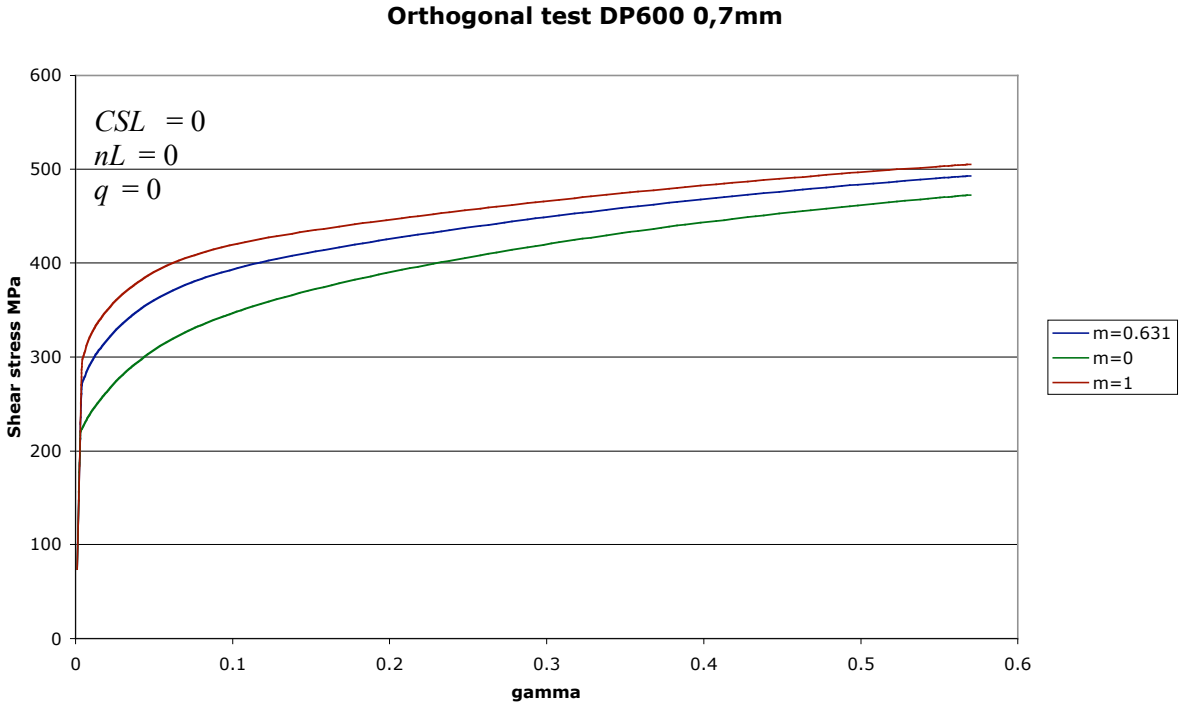

Figure 5.24 Influence of the parameter *m* on a second path of an orthogonal test.

For reference purposes, Table 5.3 summarizes the Teodosiu and Hu hardening law identification procedure.

Identification step *i*	**Teodosiu and Hu hardening law identification**	
	Parameters	Mechanical tests
1	R_0	Tensile test (offset method)
2	m, C_R, R_{SAT}, C_X, X_{SAT0}, C_{SD}, S_{SAT}, C_P *Rough estimation*	Tensile test Monotonic simple shear Bauschinger test (small pre-strain)
3	C_R, C_X, C_{SD}, C_P *More accurate identification*	High work hardening part of: Tensile test Monotonic simple shear Bauschinger test (small pre-strain)
4	R_{SAT}, X_{SAT0}, S_{SAT} *More accurate identification*	Low work hardening part of: Tensile test Monotonic simple shear Bauschinger test (small pre-strain)
5	m, C_X, X_{SAT0}	Beginning of the reversed flow curve of Bauschinger test (at different pre-strain)
6	n_P	Part of the reversed flow curve of Bauschinger test (at different pre-strain) containing work hardening stagnation
7	q, C_{SL}, n_L	Second strain path of the orthogonal test
8	m, R_0, C_R, R_{SAT}, C_X, X_{SAT0}, q, C_{SD}, C_{SL}, S_{SAT}, n_P, n_L, C_P	All tests

Table 5.3 Teodosiu and Hu identification procedure.

Each identification *i* (Table 5.3) is performed by *Optim* and *Lagamine* (except for *i*=1) is applied to those tests, or their parts, defined in the right hand column in a sequential approach. Parameters identified in step (i – 1) are kept constant for identification *i* except those more accurate definition exists currently more accurately defined.
A detailed study on the evolution of internal variables evolution as a function of the amount of pre-strain and strain-path change can be found in Bouvier et al., 2005 and de Montleau, 2004.

5.4 Material characterization

The aim of this section is to characterize of the following materials: IF DC06 (0,8 mm thick), dual phase DP1000 (1,6 mm thick) and S320GD (of 0,69 mm thick).
To study the material behavior a series of, tensile, plane strain, simple shear, Bauschinger and orthogonal tests are performed.

The tensile test is performed in a standard electro-mechanical tensile test machine with mechanical grips of 20 kN capacity, the specimen is deduced from a European standard.
Strain measures are taken with strain gauges (rosettes, strain measure capacity up to 5%) for the identification of the elastic parameters (E, ν) and the determination of the yield limit (σ_y).
Aramis® system is used to measure the strain field in order to compute the Lankford coefficients. Strain gauges perform better for small strains rather than the optical (Annex D). Stress is computed from load cell data.
The tensile test is performed at a constant ram speed of 1mm/min during the elastic portion followed by a speed of 5mm/min.
The effect of the phenomenon called "S shape" (Bockler at al., 1987), observed when loads are applied out of the orthotropy directions, is neglected. This phenomenon produces a loss of homogeneity in the stress and strain field and can be prevent using special grips (Habraken, 2001).

The rest of the tests (plane strain, simple shear, Bauschinger and orthogonal) are performed in the bi-axial machine describe in Chapter 3 and Chapter 4. In every case the piston speed is remains constant at 0,005 mm/s. Strain measures are taken with the Aramis® optical system and stress from the load cell.

5.4.1 IF steel DC06

Elastic parameters

Elastic parameters are obtained from uni-axial tensile tests.
Figure 5.25 shows the procedure used. Uni-axial tensile specimens are loaded and unloaded several times at small strains (in order to avoid the decrease of stiffness due to damage). Then, as is shown in Figure 5.26 for the RD, Figure 5.27 for the TD and Figure 5.28 for 45° from the RD, the slopes of the linear part are computed and averaged. The average values appear in Table 5.4.

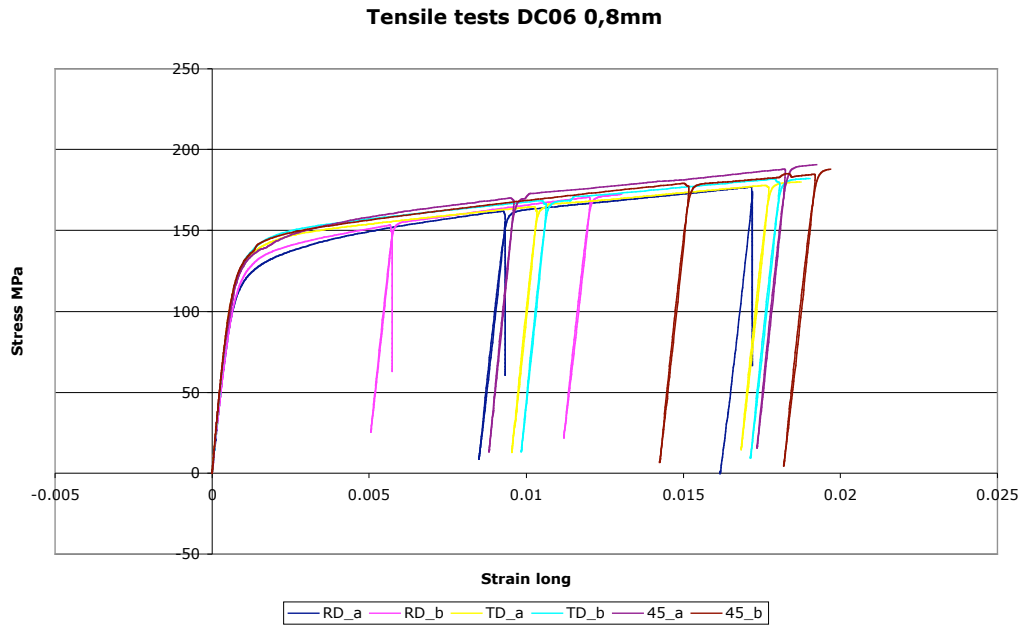

Figure 5.25 Uni-axial tensile test to measure Elastic modulus and Poisson's coefficient. DC06 0,8mm.

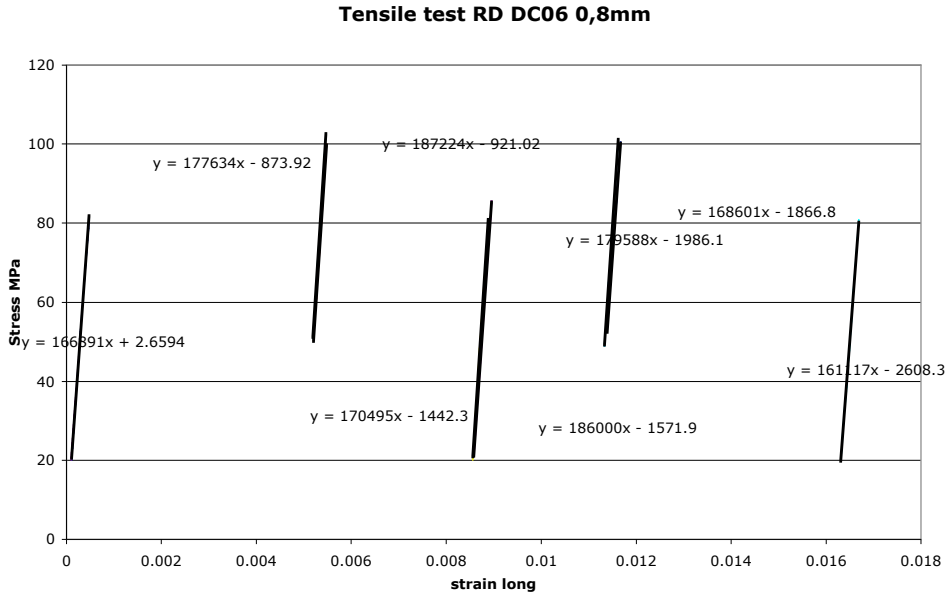

Figure 5.26 Elastic modulus computed at the RD. DC06 0,8mm.

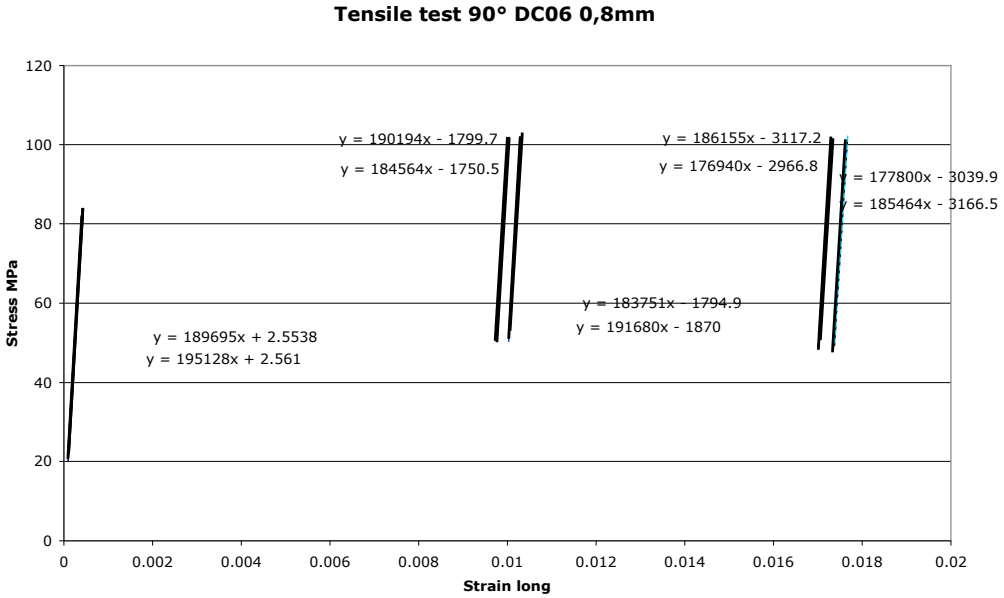

Figure 5.27 Elastic modulus computed at the TD. DC06 0,8mm.

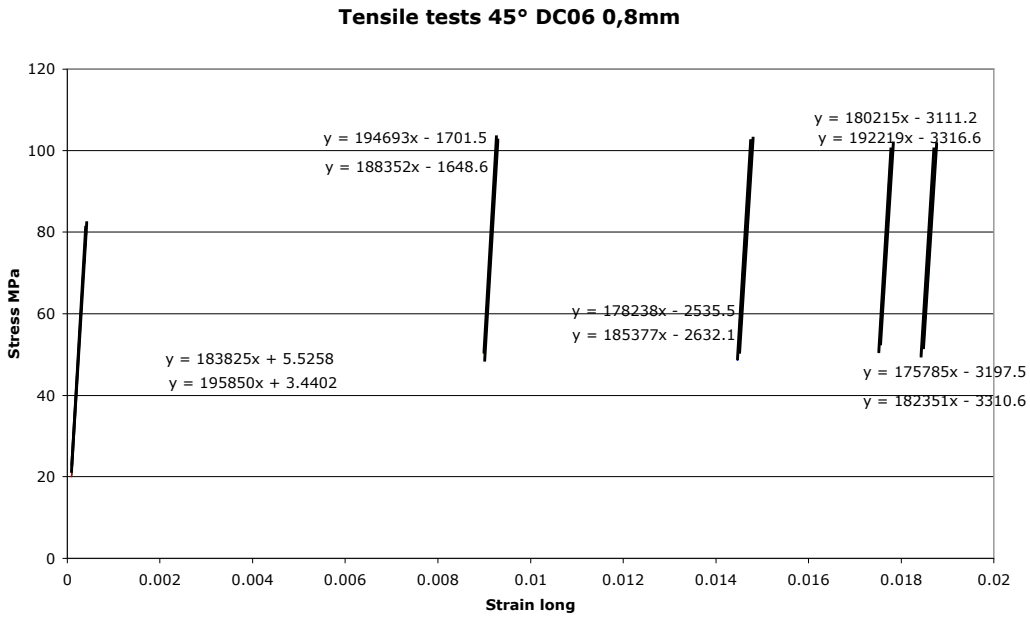

Figure 5.28 Elastic modulus computed at 45° from RD. DC06 0,8mm.

DC06 0,8 mm		Elastic modulus *E* MPa	Poisson's coefficient ν
0°	Average	174694	0,345
	N° Tests	8	4
	Range	[161117 – 187224]	[0,337 – 0,349]
45°	Average	185691	0,338
	N° Tests	10	5
	Range	[175785 – 195850]	[0,308 – 0,356]
90°	Average	186137	0,379
	N° Tests	10	4
	Range	[176940 – 195128]	[0,369 – 0,395]
AVERAGE		183053	0,350

Table 5.4 Elastic parameters for DC06 0,8mm.

Lankford coefficients

Lankford coefficients are measured from uni-axial tensile test data at RD, 45° from RD and TD. The stress – strain curves for the three cases are shown in Figure 5.29.
The procedure to measure anisotropy coefficients is demostrated in Figure 5.30 and Figure 5.31 for a single case (RD). Figure 5.30 shows the plastic strain tensor as a function of time, The function is approximated by a linear equation in the range of 10% to 30% of longitudinal plastic strain. The values of the slopes of the linear approximations give the plastic strain rate. The anisotropy coefficient is computed by the ratio of the width and the thickness plastic strain rates.
Alternatively, Figure 5.31 shows a procedure in which the width plastic strain is plotted as a function of the thickness plastic strain. The slope of the linear range gives the anisotropy coefficient. This is an approximation of the previous computation.

Table 5.5 shows the anisotropy coefficients computed, for both cases, using total strain measurements and Table 5.6, those for plastic strains measurements.
It can be observed that there is not a great difference between one method and the other or even neglecting the elastic part. In this work, the anisotropy coefficients computed out of the plastic strain rate have been used for material identification (values in red in Table 5.6).

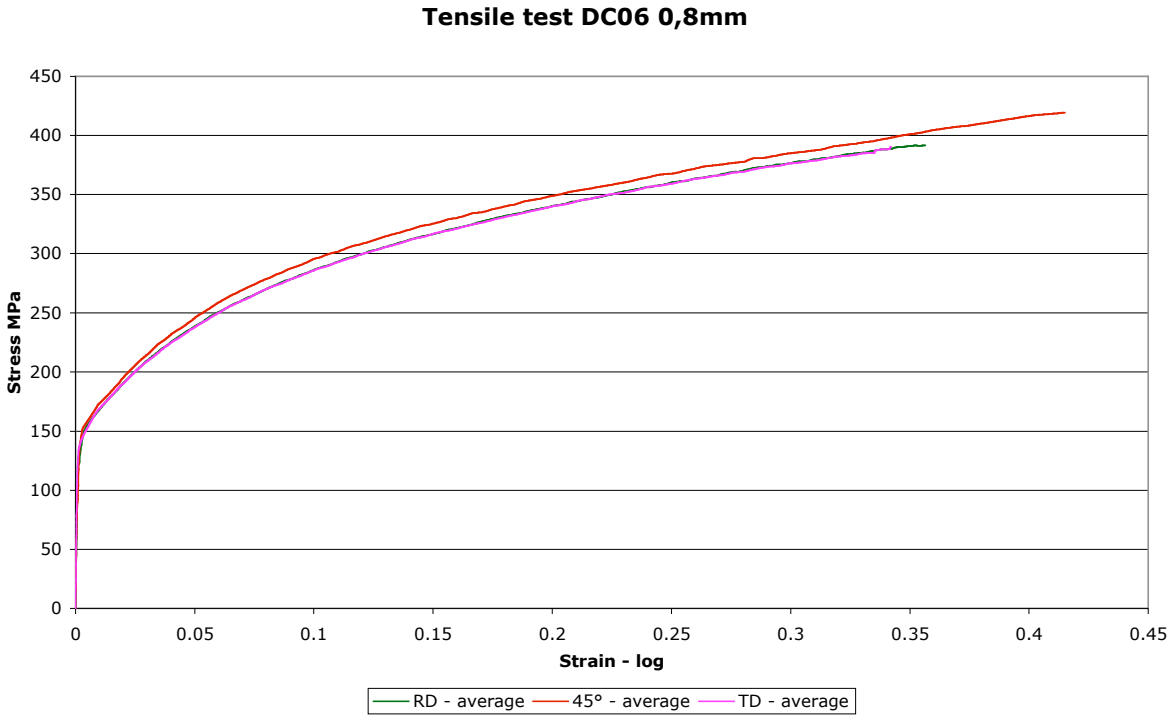

Figure 5.29 Tensile tests for a DC06 0,8mm.

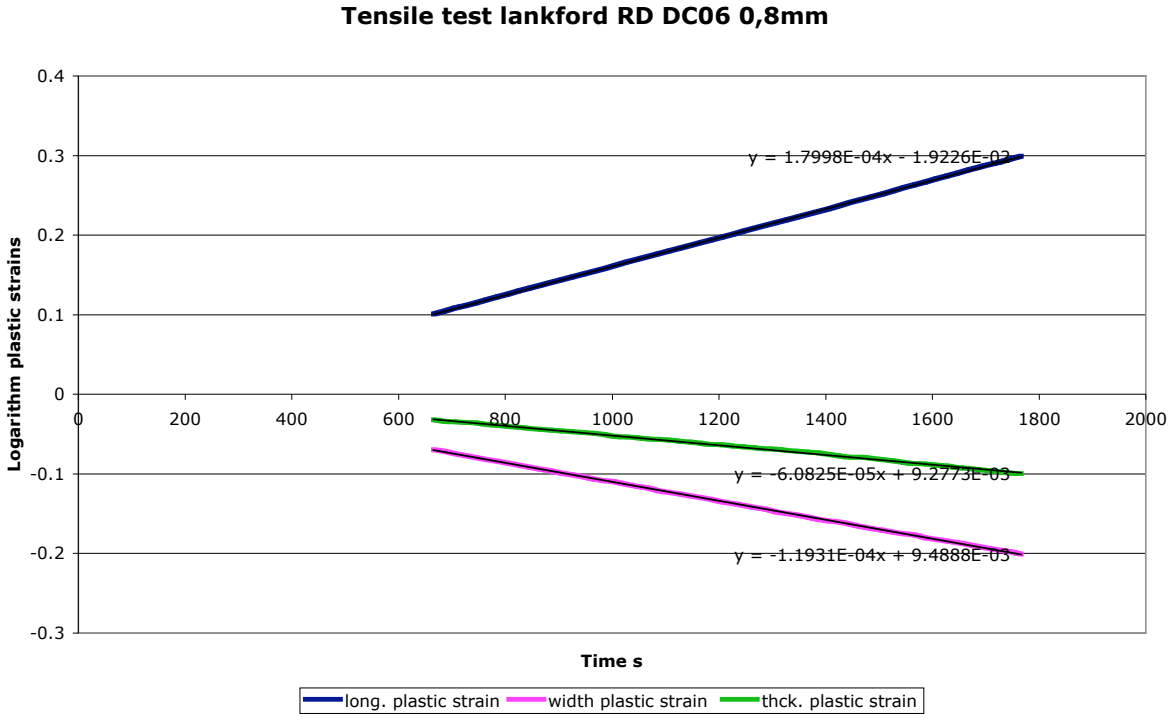

Figure 5.30 Plastic strain rate components for a uni-axial tensile test. DC06 0,8 mm.

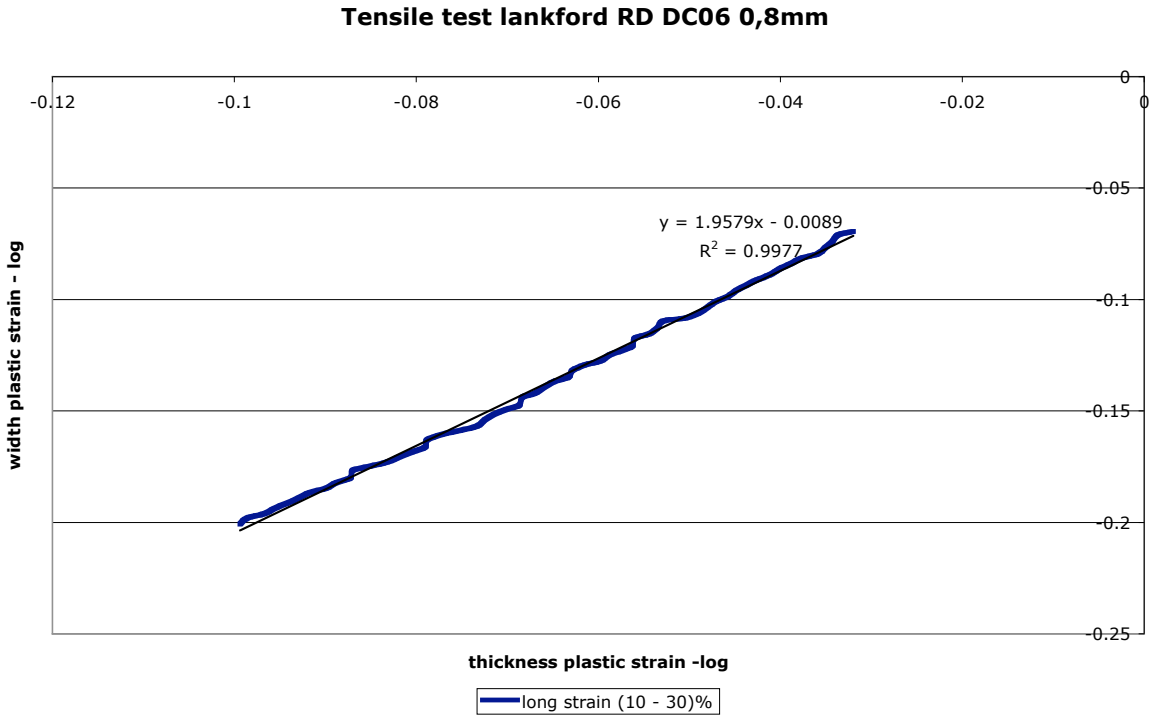

Figure 5.31 Anisotropy coefficient for a uni-axial tensile test. DC06 0,8 mm.

DC06 0,8 mm		Total strain				
		$\frac{d\varepsilon_{long}}{dt} x10^{-4}$	$\frac{d\varepsilon_{width}}{dt} x10^{-4}$	$\frac{d\varepsilon_{thick}}{dt} x10^{-4}$	$r = \frac{d\varepsilon_{with}}{d\varepsilon_{thick}}$	$r = \frac{\varepsilon_{with}}{\varepsilon_{thick}}$
0°	Average	1,8142	-1,2041	-0,61006	1,9586	1,9779
	N° Tests	4	4	4	5	5
	Range	[1,7818 – 1,8507]	[-1,2197 – -1,1883]	[-0,63101 – -0,59347]	[1,9096 – 2,0009]	[1,9329 – 2,0025]
45°	Average	1,8337	-1,1471	-0,6884	1,6637	1,6664
	N° Tests	3	3	3	3	3
	Range	[1,8044 – 1,8539]	[-1,1617 – -1,1273]	[-0,69585 – -0,67710]	[1,6539 – 1,6746]	[1,6561 – 1,6782]
90°	Average	1,8860	-1,3550	-0,53092	2,5478	2,5537
	N° Tests	3	3	3	3	3
	Range	[1,8641 – 1,8984]	[-1,3679 – -1,3468]	[-0,54797 – -0,51727]	[2,4584 – 2,5971]	[2,4644 – 2,6037]
$\bar{r}$		1,9661				
Δr		0,2997				

Table 5.5 Anisotropy coefficients using total strain measures DC06 0,8mm.

DC06 0,8 mm		Plastic strain				
		$\frac{d\varepsilon_{long}}{dt} x10^{-4}$	$\frac{d\varepsilon_{width}}{dt} x10^{-4}$	$\frac{d\varepsilon_{thick}}{dt} x10^{-4}$	$r = \frac{d\varepsilon_{with}}{d\varepsilon_{thick}}$	$r = \frac{\varepsilon_{with}}{\varepsilon_{thick}}$
0°	Average	1,8103	-1,2030	-0,60890	1,9599	**1,9799**
	N° Tests	4	4	4	5	5
	Range	[1,7777 – 1,8470]	[-1,2186 – -1,1871]	[-0,62989 – -0,59223]	[1,9090 – 2,0030]	[1,9346 – 2,0045]
45°	Average	1,8317	-1,1460	-0,68726	1,6647	**1,6675**
	N° Tests	3	3	3	3	3
	Range	[1,8007 – 1,8500]	[-1,1605 – -1,1262]	[-0,69470 – -0,67598]	[1,6549 – 1,6757]	[1,6573 – 1,6792]
90°	Average	1,8820	-1,3538	-0,52976	2,5511	**2,5570**
	N° Tests	3	3	3	3	3
	Range	[1,8602 – 1,8944]	[-1,3667 – -1,3456]	[-0,54677 – -0,51612]	[2,4616 – 2,6006]	[2,4676 – 2,6071]
$\bar{r}$		1,9680				
Δr		0,3004				

Table 5.6 Anisotropy coefficients using plastic strain measures DC06 0,8mm.

Initial yield surface

Eight experimental tests are performed in order to define the initial yield surface. From these tests, the stress – strain curves are represented in Figure 5.32.

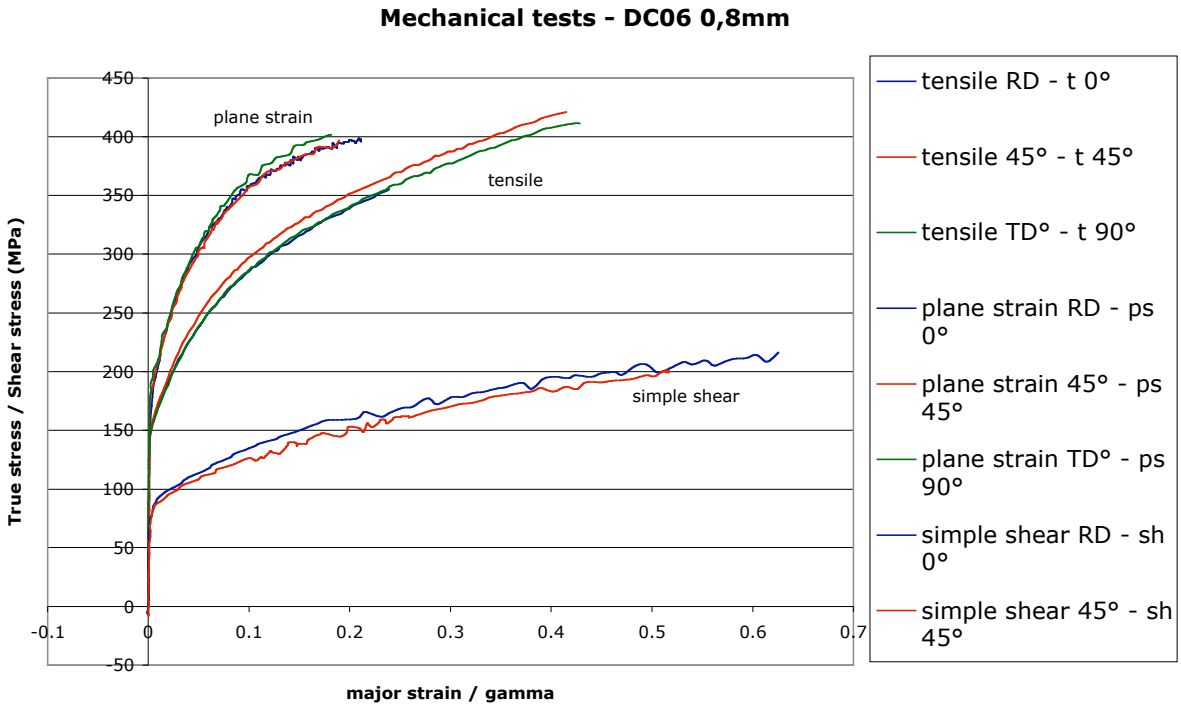

Figure 5.32 Mechanical tests on a DC06 0,8mm.

The yield stress for uni-axial tensile tests at different angles with respect to the RD are in Table 5.7. The offset is set to an arbitrary plastic strain value $\bar{\varepsilon}_0^p = 0{,}2\%$.

DC06 0,8 mm		$\sigma_y\left(\bar{\varepsilon}_0^p = 0{,}2\%\right) MPa$
0°	Average	140,47
	N° Tests	2
	Range	[138,57 – 142,36]
45°	Average	149,58
	N° Tests	2
	Range	[149,09 – 150,07]
90°	Average	149,67
	N° Tests	2
	Range	[148,02 – 151,31]
AVERAGE		147,67

Table 5.7 Initial yield stress for uni-axial stress state. DC06 0,8mm

To define plastic contours, the plastic work for arbitrary values of $\bar{\varepsilon}_0^p$ is computed from the uni-axial tensile test data (Table 5.8). The points are plotted, in the principal directions, in Figure 5.33. To plot these points in the $(\sigma_{11},\sigma_{22},\sigma_{12})$ axis, the transformation given in Equation 3.5 is used. The coordinates appear in Table 5.9 and Table 5.10 for two different strain levels.

$\bar{\varepsilon}_0^p$	W^p	σ_{11}^{UN} $(\theta = 0°)$ MPa	σ_{11}^{UN} $(\theta = 45°)$ MPa	σ_{11}^{UN} $(\theta = 90°)$ MPa	σ_{11}^{PS} $(\theta = 0°)$ MPa	σ_{11}^{PS} $(\theta = 45°)$ MPa	σ_{11}^{PS} $(\theta = 90°)$ MPa	σ_{12}^{SSH} $(\theta = 0°)$ MPa	σ_{12}^{SSH} $(\theta = 45°)$ MPa
0,2%	0,254	140,47	149,58	149,67	165,9	180,93	187,81	83,43	82,38
0,5%	0,762	153,30	163,61	159,33	191,12	193,18	201,32	92,60	88,95
1%	1,596	172,26	176,83	171,84	206,68	208,04	208,87	98,88	95,46
2%	3,423	193,82	198,51	192,72	235,78	236,11	236,00	108,5	105,04
3%	5,453	211,68	217,81	211,03	261,00	256,63	261,12	115,68	111,90
4%	7,644	226,49	234,50	227,06	281,28	277,11	279,79	124,24	118,94
5%	9,974	239,29	248,90	240,20	294,50	290,27	295,41	131,98	124,89
10%	23,24	286,80	296,40	287,80	346,94	342,55	350,22	158,80	146,51
20%	54,78	340,22	349,34	341,23	391,54	391,15	397,44	189,29	184,31

Table 5.8 Experimental yield stresses for different offset plastic strain. DC06 0,8mm.

Test $\bar{\varepsilon}_0^p = 0{,}2\%$	$\sigma_{11} MPa$	$\sigma_{22} MPa$	$\sigma_{12} MPa$
Tensile RD	140,47	0	0
Tensile TD	0	149,67	0
Tensile 45°	73,84	73,84	73,84
Plane strain RD	165,9	108,02	0
Plane strain TD	107,93	187,81	0
Plane strain 45°	120,68	120,68	60,25
Simple shear RD	0	0	83,45
Simple shear 45°	-82,38	82,38	0

Table 5.9 Coordinates in the $(\sigma_{11},\sigma_{22},\sigma_{12})$ axis for $\bar{\varepsilon}_0^p = 0{,}2\%$. DC06 0,8mm.

Test $\bar{\varepsilon}_0 = 0{,}5\%$	$\sigma_{11} MPa$	$\sigma_{22} MPa$	$\sigma_{12} MPa$
Tensile RD	153,3	0	0
Tensile TD	0	159,33	0
Tensile 45°	81,81	81,81	81,81
Plane strain RD	191,12	118,40	0
Plane strain TD	113,28	201,32	0
Plane strain 45°	123,30	123,30	69,87
Simple shear RD	0	0	92,60
Simple shear 45°	-88,95	88,95	0

Table 5.10 Coordinates in the $(\sigma_{11},\sigma_{22},\sigma_{12})$ axis for $\bar{\varepsilon}_0 = 0{,}5\%$. DC06 0,8mm.

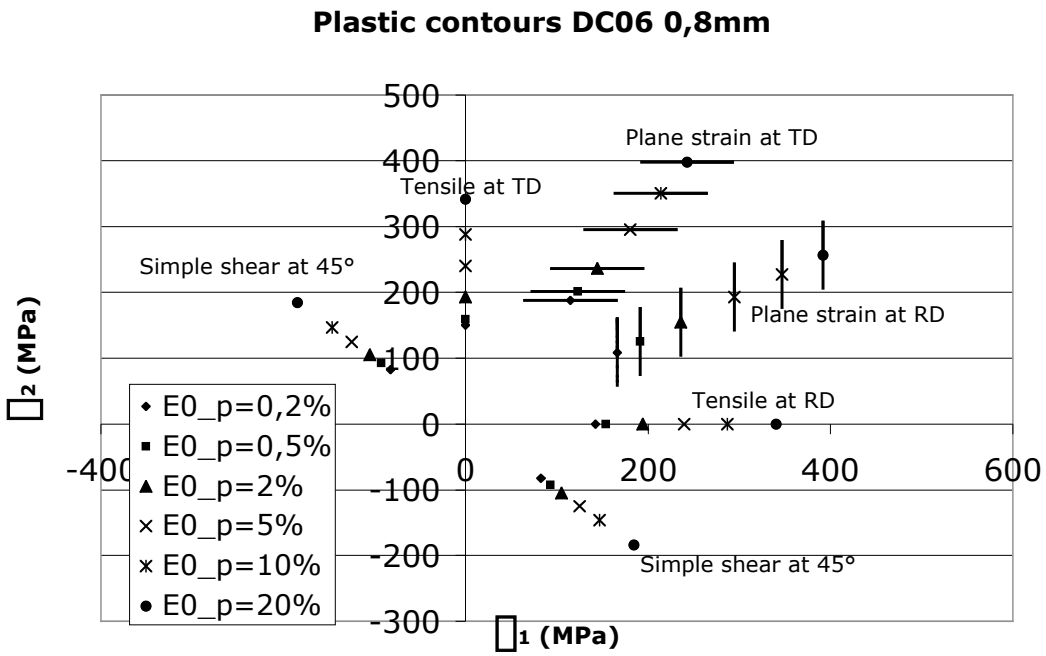

Figure 5.33 Contours of plastic work.

Hill 1948 material parameters are optimized for different strain levels. Table 5.11 and Table 5.12 show these optimized parameters together with the parameters identified using the Lankford coefficients. In Table 5.11, coefficients are optimized using only stress measures while in other cases (Table 5.12) the optimization is achieved by combining stress and strain measures.

Plastic contours at small strain levels approximate the yield surface, shown in Figure 5.34 to Figure 5.36 for three different cases. Figure 5.34 is obtained from parameters optimized at $\bar{\varepsilon}_0 = 0{,}5\%$ and $\alpha = 0$ (i.e., using only stress measures), Figure 5.35 from $\bar{\varepsilon}_0 = 0{,}5\%$ and $\alpha = 1$ (i.e., using Lankford coefficients) and Figure 5.36 from $\bar{\varepsilon}_0 = 0{,}5\%$ and $\alpha = 0{,}5$ (i.e., combining stress and strain measures).

$\bar{r}_0 = 0$	Identification method	H	F	G	N
Hill 1948	Lankford	1,33	0,52	0,67	2,58
	$\bar{r}_0 = 0{,}2\%$	1,04	0,67	0,96	2,85
	$\bar{r}_0 = 0{,}5\%$	1,13	0,69	0,87	2,76
	$\bar{r}_0 = 2\%$	1,16	0,87	0,84	3,04
	$\bar{r}_0 = 5\%$	1,17	0,84	0,83	3,03
	$\bar{r}_0 = 10\%$	1,14	0,88	0,86	3,04
	$\bar{r}_0 = 20\%$	1,01	0,99	0,99	2,98

Table 5.11 Material parameters for $\bar{r}_0 = 0$.

$\bar{r}_0 = 0{,}5$	Identification method	H	F	G	N
Hill 1948	Lankford	1,33	0,52	0,67	2,58
	$\bar{r}_0 = 0{,}2\%$	1,30	0,54	0,70	2,78
	$\bar{r}_0 = 0{,}5\%$	1,31	0,55	0,69	2,75
	$\bar{r}_0 = 2\%$	1,31	0,58	0,69	2,86
	$\bar{r}_0 = 5\%$	1,31	0,57	0,69	2,84
	$\bar{r}_0 = 10\%$	1,31	0,58	0,69	2,86
	$\bar{r}_0 = 20\%$	1,30	0,59	0,70	2,91

Table 5.12 Material parameters for $\bar{r}_0 = 0{,}5$.

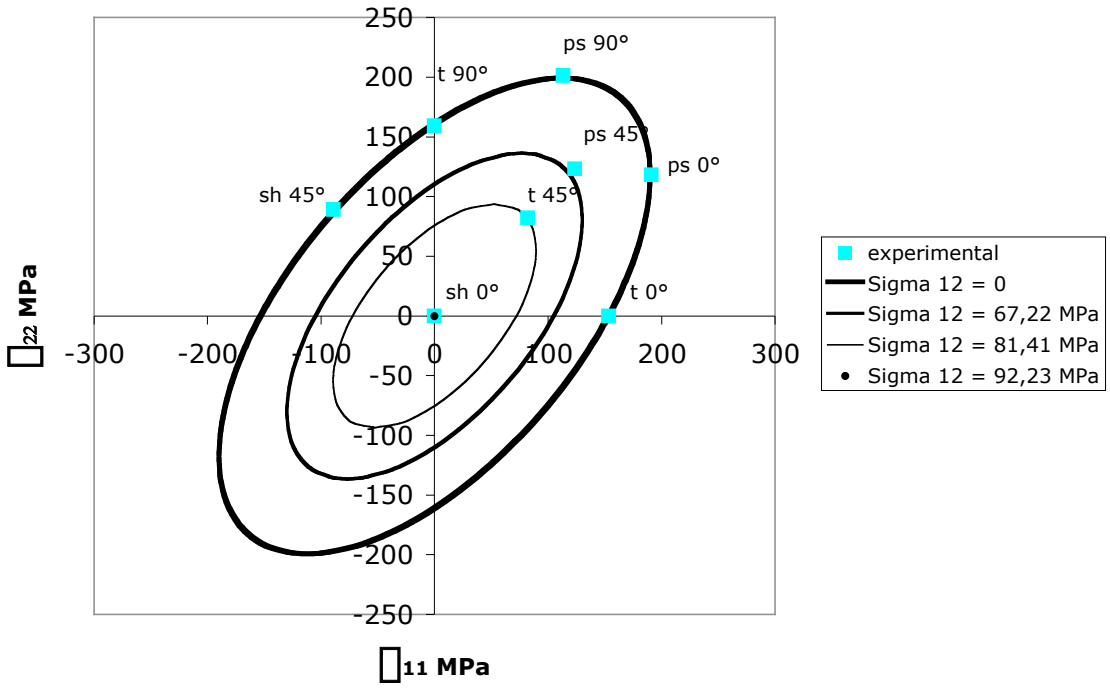

Figure 5.34 Yield surface identified using only stress measurements $\bar{r}_0 = 0{,}5\%$. DC06 0,8mm.

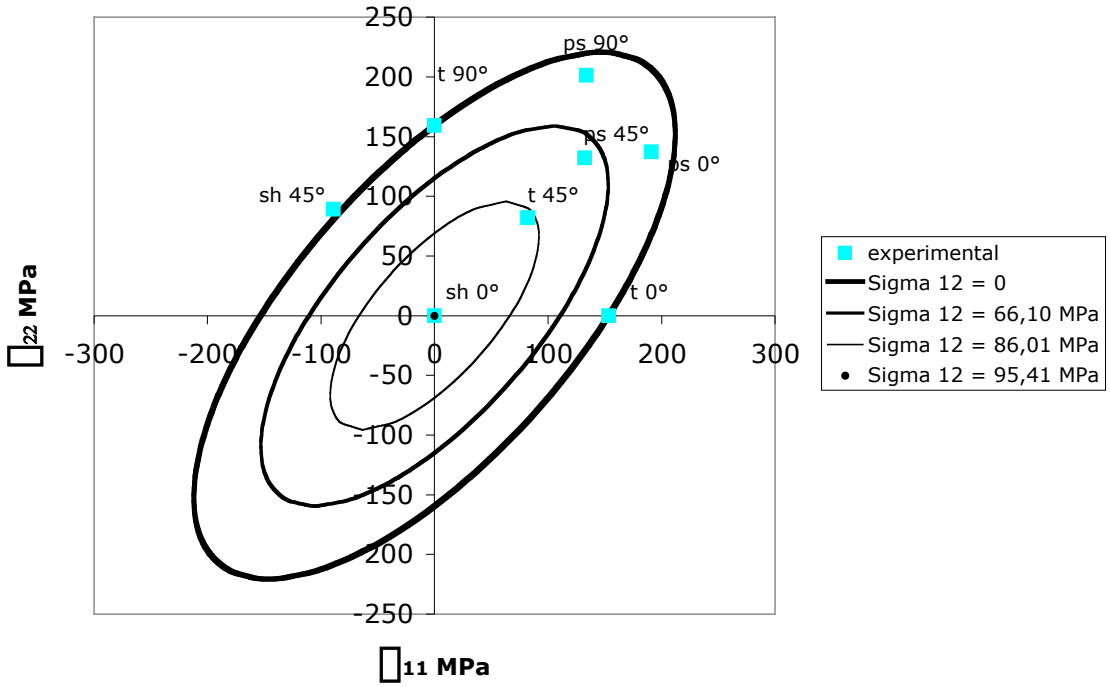

Figure 5.35 Yield surface identified using only strain measurements $\sigma_0' = 0{,}5\%$. DC06 0,8mm.

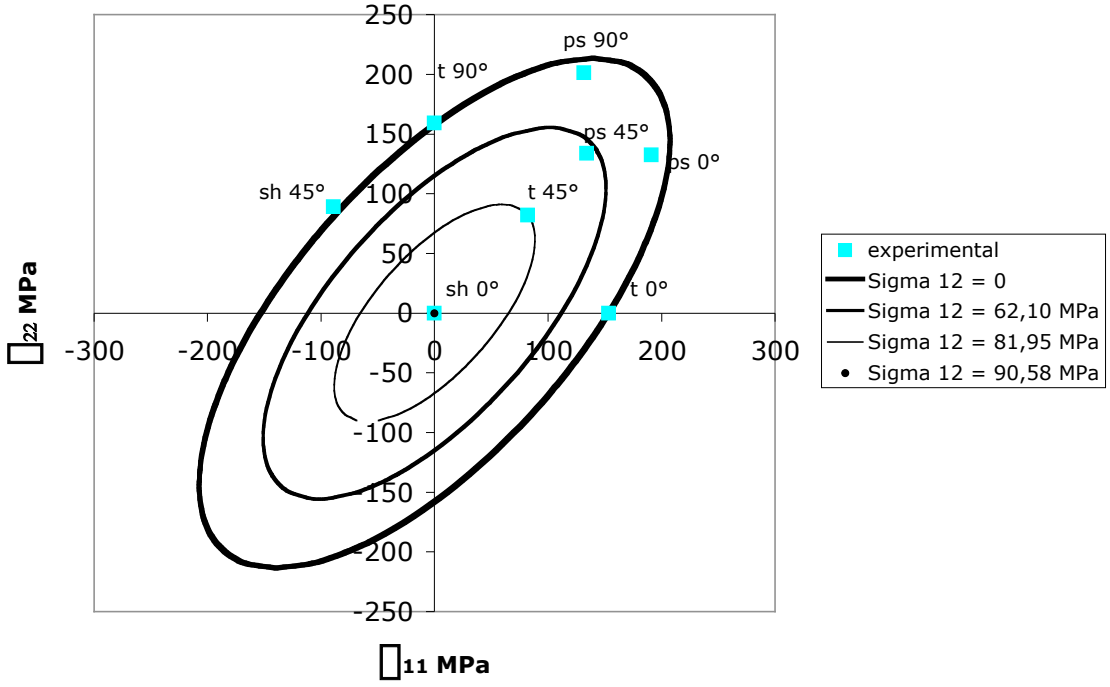

Figure 5.36 Yield surface identified combining stress and strain measurements ($\alpha = 0{,}5$) $\sigma_0' = 0{,}5\%$. DC06 0,8mm.

The differences between experimental points and the predicted surfaces in the σ_{12} axis are detailed in Table 5.13.

Test	$\sigma_{12} MPa$ Tensile 45°	$\sigma_{12} MPa$ Plane strain 45°	$\sigma_{12} MPa$ Simple shear RD
Experimental	81,81	69,87	92,60
$\varepsilon_0^p = 0{,}5\%$ - $\beta = 0$	81,41	67,22	92,23
$\varepsilon_0^p = 0{,}5\%$ - $\beta = 1$	86,01	66,10	95,41
$\varepsilon_0^p = 0{,}5\%$ - $\beta = 0{,}5$	81,95	62,10	90,58

Table 5.13 Experimental and predicted points in the σ_{12} axis.

The yield surface shape is compared in Figure 5.37 for three cases: material identification using only the strain measurements and material identification using only stress measures at $\varepsilon_0^p = 0{,}5\%$ and $\varepsilon_0^p = 20\%$. The experimental points are normalized with respect to σ_y.

Clearly, it can be seen that the yield function, identified with yield stress points, is more accurate at predicting stress states, but this implies a lack of accuracy at describing the flow rule as Lankford coefficients are not recovered.

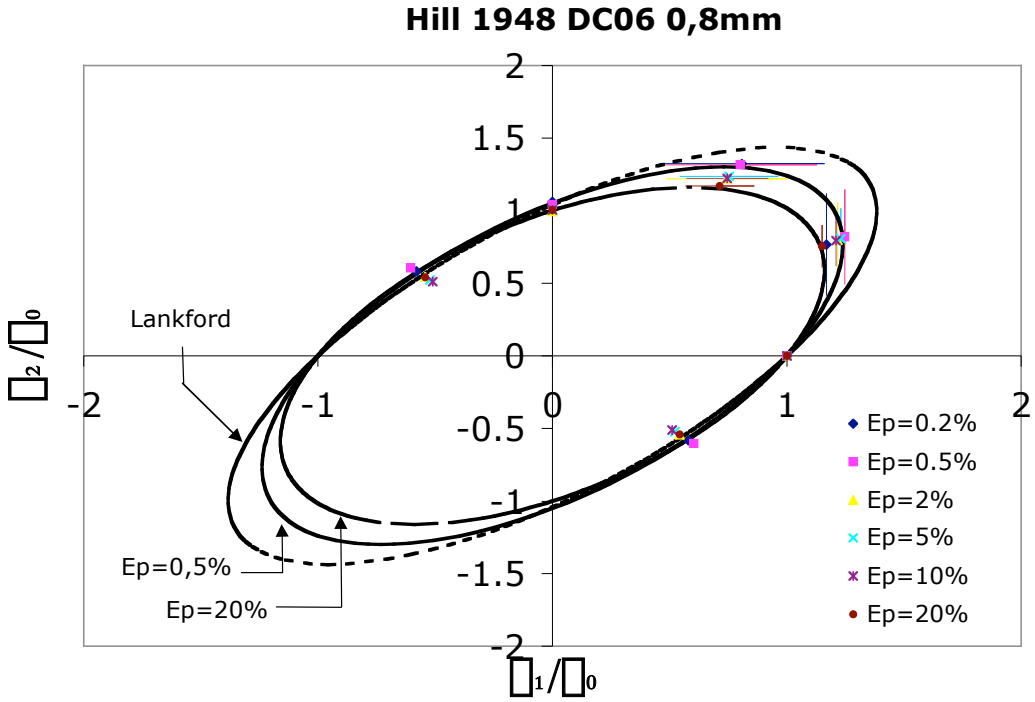

Figure 5.37 Hill 1948 yield surface shape for different cases. DC06 0,8mm.

Note that work contours for $\varepsilon_0^p = 0{,}2\%$ or $\varepsilon_0^p = 0{,}5\%$ are actual yield loci, while contours plotted for higher strain levels assume no kinematic hardening and no texture evolution or damage process. These phenomena result in the case that the material that has undergone a large plastic strain in a plane strain or shear test is actually different and can no longer be identified by only one work contour. It is not surprising, then, that the "yield locus" plotted for $\varepsilon_0^p = 20\%$ is different and has no real meaning. To describe the material in large strain, both the texture model evolution that computes the actual yield locus shape and hardening models must be coupled. However, the fact that Lankford coefficients are constant with plastic strain suggests that texture evolution is weak during the tensile test. Checking the texture evolution for other loadings could be useful and may provide some interesting information.

The same analysis done for Hill 1948 is performed for the Hosford 1979 yield criterion. Table 5.14 and Table 5.15 show the identified material parameters for two cases at different strain levels.

$\square = 0$	Identification method	H	F	G	a
Hosford 1979	Lankford	0,66	0,26	0,34	6
	$\square_0^{\square} = 0{,}2\%$	0,58	0,17	0,42	6
	$\square_0^{\square} = 0{,}5\%$	0,72	0,18	0,28	6
	$\square_0^{\square} = 2\%$	0,70	0,30	0,30	6
	$\square_0^{\square} = 5\%$	0,75	0,24	0,25	7
	$\square_0^{\square} = 10\%$	0,79	0,20	0,21	8
	$\square_0^{\square} = 20\%$	0,60	0,37	0,40	6

Table 5.14 Material parameters for $\square = 0$.

$\square = 0{,}5$	Identification method	H	F	G	a
Hosford 1979	Lankford	0,66	0,26	0,34	6
	$\square_0^{\square} = 0{,}2\%$	0,66	0,26	0,34	6
	$\square_0^{\square} = 0{,}5\%$	0,66	0,26	0,34	6
	$\square_0^{\square} = 2\%$	0,67	0,26	0,33	6
	$\square_0^{\square} = 5\%$	0,67	0,26	0,33	6
	$\square_0^{\square} = 10\%$	0,67	0,26	0,33	6
	$\square_0^{\square} = 20\%$	0,66	0,26	0,34	8

Table 5.15 Material parameters for $\square = 0{,}5$.

As one may observe Table 5.14 and Table 5.15 clearly demonstrate the influence of the weight factor $\square$ in the stabilization of material parameters. Figure 5.38 shows the yield surface shape for four cases: material identification using only the strain measurements (Lankford coefficients), material identification using only stress measures at $\square_0^{\square} = 0{,}5\%$, material identification using only stress measures at $\square_0^{\square} = 20\%$ with a = 6 imposed, and material identification using only stress measures at $\square_0^{\square} = 20\%$ with a = 8 optimized. The experimental points are normalized with respect to $\square_y$.

It can be observed that the yield function plot with a = 6 produces the same shape for every case. From this remark, it can be concluded that uni-axial tensile tests are enough for the material identification. In addition, the normality rule is respected.

The low shape evolution between $\square_0^{\square} = 0{,}5\%$ and $\square_0^{\square} = 20\%$ seem to suggest that the Hosford 1979 description is less sensitive to texture evolution, damage, and kinematic hardening. This yield locus description does not, therefore, fulfil the interest of this work since it neglects shear stress present in general loading cases.

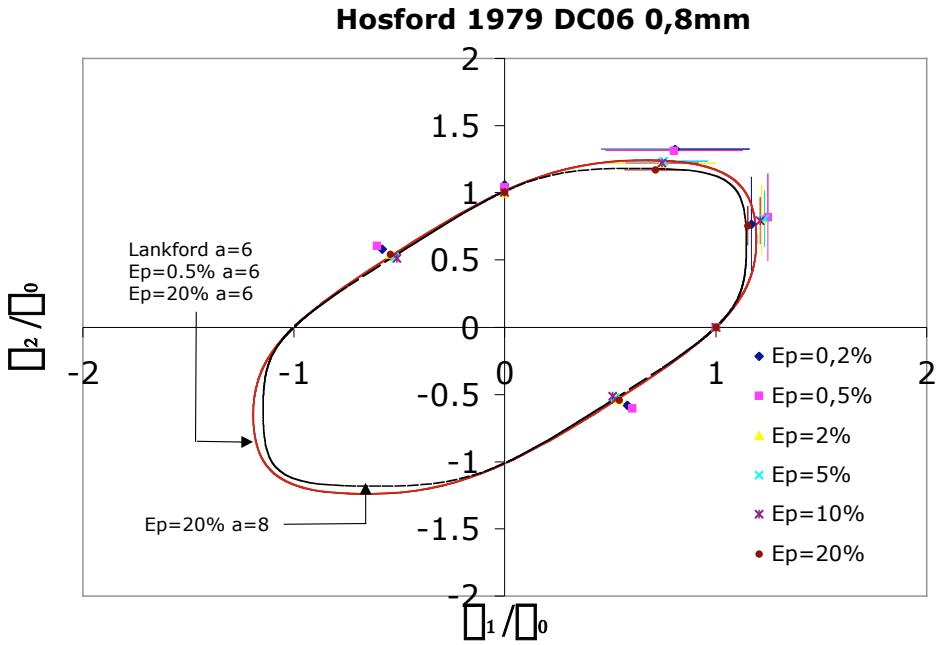

Figure 5.38 Hosford 1979 yield function shape. DC06 0,8mm.

Finally, four selected cases are compared with the yield function shape predicted by a texture-based description *Minty* (see Section 2.4 for details). These cases are presented in Table 5.16 and plotted in Figure 5.39 and Figure 5.40.
Figure 5.39 clearly shows that Hill 1948 identified by Lankford coefficients is far from plane strain experimental points, when the other three models, Minty, Hosford 1979, and Hill 1948 based on experimental points, provide more accurate results.
Kuwabara (Kuwabara et al., 2002) measured work contours for the same material using a bi-axial machine (see Section 3.2). The bi-axial stress state adimensional points, measured at different levels of plastic strain ($\bar{\varepsilon}_0 = 0{,}05\%$, $\bar{\varepsilon}_0 = 0{,}2\%$, $\bar{\varepsilon}_0 = 1\%$, and $\bar{\varepsilon}_0 = 4\%$), are included in Figure 5.39. These points coincide well with Hosford 1979 and Hill 1948 (by experimental stress points) predictions.
Note that the Minty model could be linked with a more advanced microscopic model such as the *Lamel* model (Van Houtte et al., 2005) to improve its prediction. At the time of the current thesis, this work is still in progress.

Comparing Hill 1948 based on experimental points, Minty, and experimental points at different shear levels (Figure 5.40 and Table 5.17) show that for this IF steel, the Hill 1948 description seems more efficient.

Yield function	Identification method	*H*	*F*	*G*	*N*	*a*
Hill 1948	Lankford coefficients	1,33	0,52	0,67	2,58	-
Hill 1948	Experimental points at $\bar{\varepsilon}_0 = 0{,}2\%$	1,04	0,67	0,96	2,85	
Hill 1948	Experimental points at $\bar{\varepsilon}_0 = 0{,}5\%$	1,13	0,69	0,87	2,76	-
Hosford 1979	Anisotropy coefficients	0,66	0,26	0,34	-	6

Table 5.16 Material parameters, chosen cases. DC06 0,8mm.

In order to check the shear stress predictions Hill 1948 and Minty are compared in Figure 5.40. The shear stress values appear in Table 5.17.

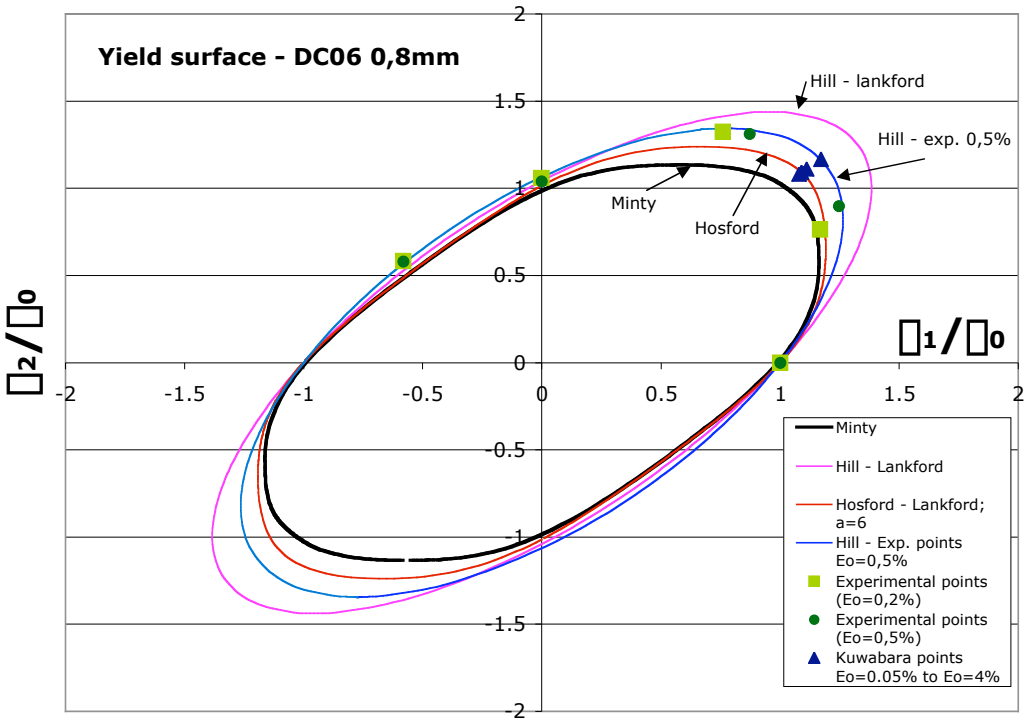

Figure 5.39 Yield function shape for different criteria. DC06 0,8mm.

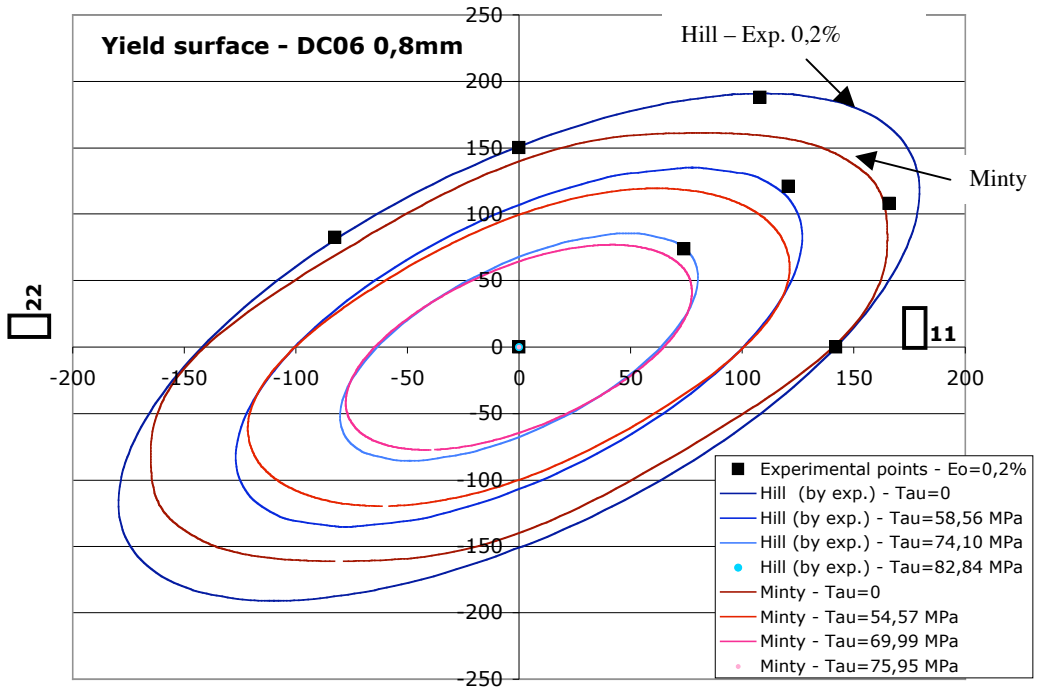

Figure 5.40 Hill 1948 and Minty yield function shape. DC06 0,8mm.

Test	$\tau_{12} MPa$ Tensile 45°	$\tau_{12} MPa$ Plane strain 45°	$\tau_{12} MPa$ Simple shear RD
Experimental at $\gamma_0 = 0{,}2\%$	73,84	60,25	83,45
Hill 1948 $\gamma_0 = 0{,}2\%$	74,10	58,56	82,84
Minty	69,99	54,57	75,95

Table 5.17 Shear stress at $\gamma_0 = 0{,}2\%$. DC06 0,8mm.

Hardening parameters

Figure 5.41 and Figure 5.42 present mechanical tests complementary to the monotonic tests shown in Figure 5.32.
Figure 5.41 shows four Bauschinger tests at different amounts of pre-strain. These tests highlight the presence of the Bauschinger effect, as well as the influence of the amount of pre-strain on the flow stress stagnation when reversing the load.
Figure 5.42 illustrates an orthogonal test and Figure 5.43 shows the second loads of orthogonal tests performed at 10% and 15% of pre-strain. The results exhibit a work-hardening stagnation dependent on the amount of pre-strain.
Due to experimental evidence, the Teodosiu and Hu hardening law is chosen to describe the material behavior of this steel.

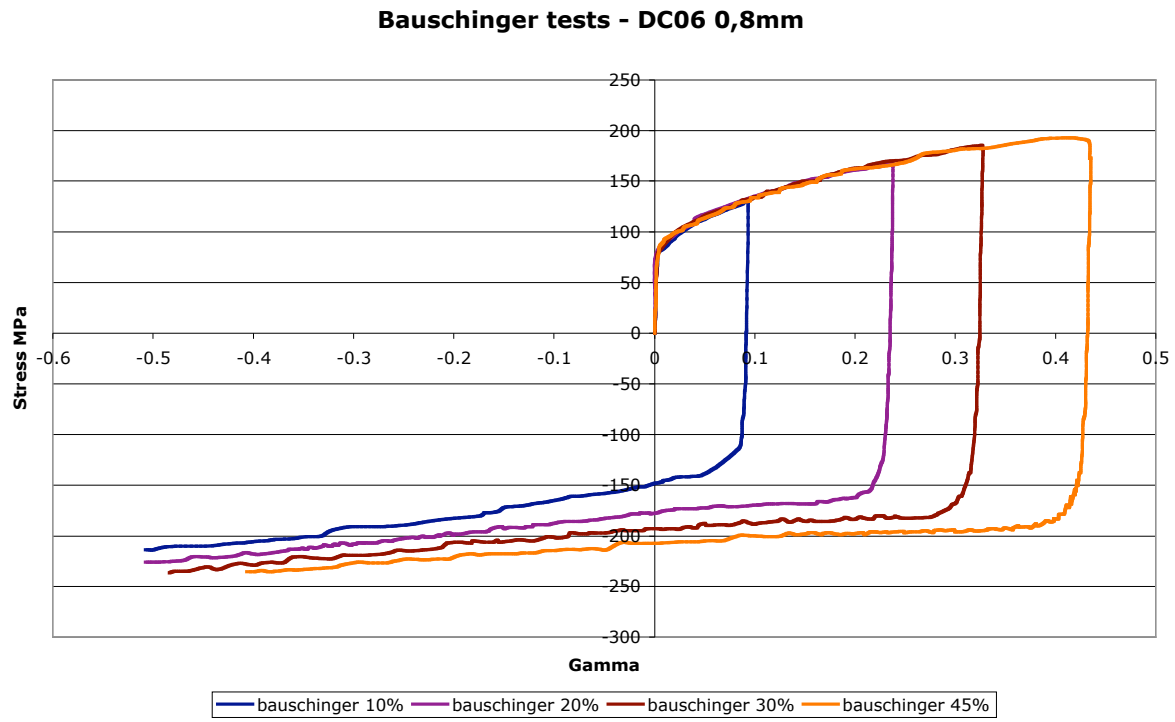

Figure 5.41 Bauschinger tests at different amounts of pre-strain.

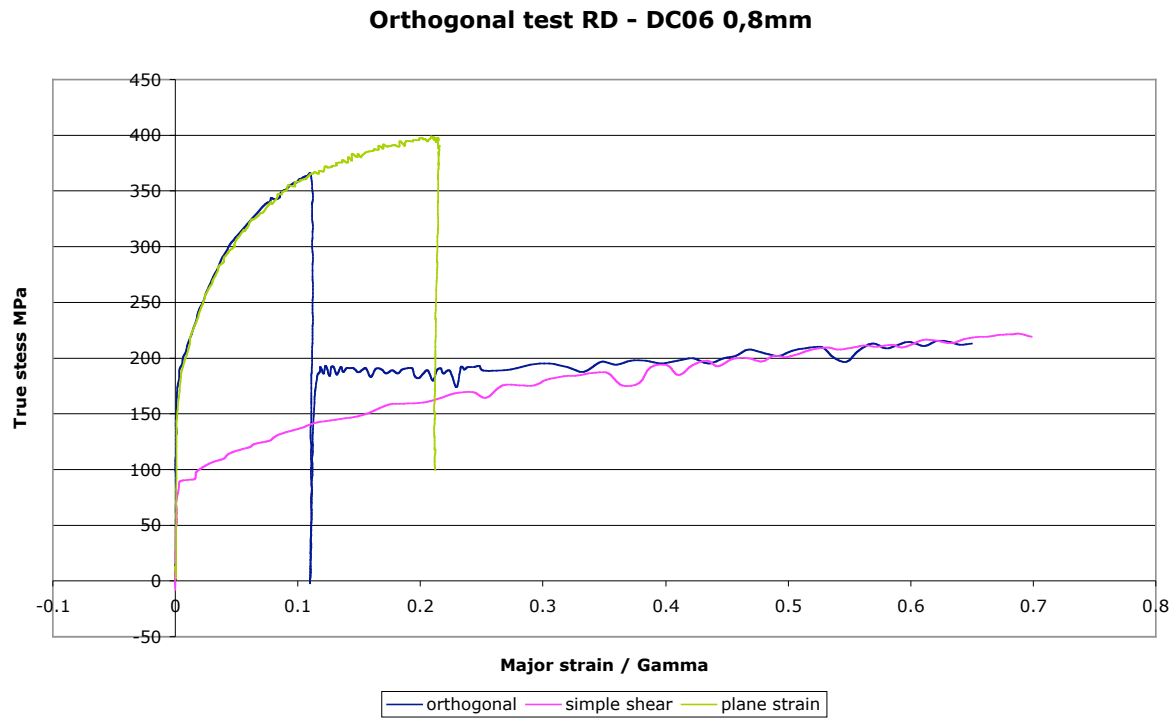

Figure 5.42 Orthogonal test, plane strain test followed by a simple shear test.

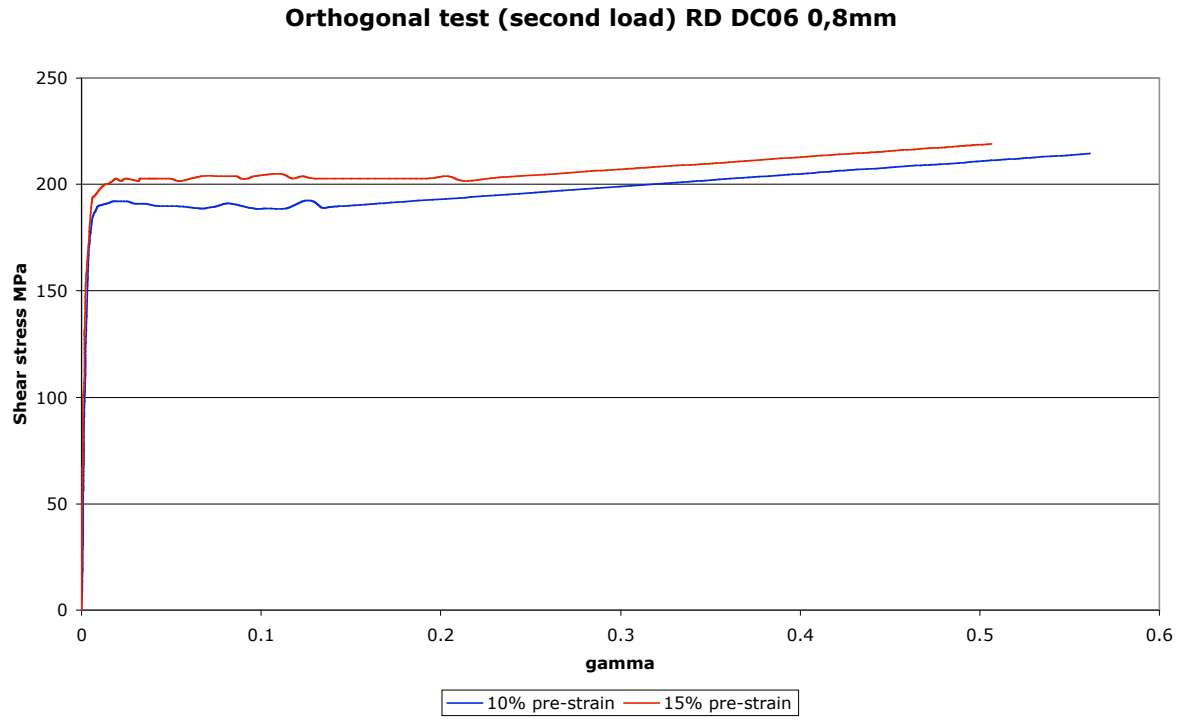

Figure 5.43 Orthogonal test (second load) at different pre-strain levels.

The initial yield surface is described by the Hill 1948 yield criterion according to the parameters fitted using the experimental points at $\gamma_0 = 0{,}5\%$ (Table 5.11 and Table 5.16). These parameters remain constant since no texture evolution is taken into account.
As mentioned earlier, the Teodosiu and Hu hardening law describes the yield surface evolution. The material parameters are fitted using the procedure summarized in Table 5.3.

The final parameters are shown in Table 5.18 and the predicted curves appear in Figure 5.44 and Figure 5.45.
Two main comments must be made with respect to the hardening parameters' identification. The first involves the Hill 1948 parameter N, which is fitted using the monotonic simple shear stress curve in order to take into account the probable texture evolution under this state. The second is linked to the back-stress saturation speed parameter C_X. This parameter has a strong influence on the subsequent flow stress curves (Bauschinger and orthogonal tests). Figure 5.44 and Figure 5.45 show the influence of this parameter on the respective flow stress and the difficulty in reconciling the conflicting results. Finally, the parameter $C_X = 150$ is kept since it describes the beginning of the monotonic curves more accurately (Figure 5.44). The parameters q, C_{SL}, n_L, from the evolution equation of the tensor $\mathbf{S}_L$ (associated with the latent part of the persistent dislocation structures) are not enough to describe the subsequent flow stress of an orthogonal test.

Hill 1948 material parameters (Equation 2.59)												
F			G			H			$N=M=L$			
0,69			0,87			1,13			3,26*			
Teodosiu and Hu hardening parameters (Section 2.5)												
R_0	C_R	R_{SAT}	C_X	X_{SAT0}	m	q	C_{SD}	C_{SL}	S_{SAT}	n_p	n_L	C_P
140,47 MPa	19,2	67,7 MPa	150	21,56 MPa	0,3	2,69	3,27	4,61	246,83 MPa	50	0,38	1,67

Table 5.18 DC06 0,8mm material parameters. *This parameter is fitted using the monotonic simple shear test experimental curve.

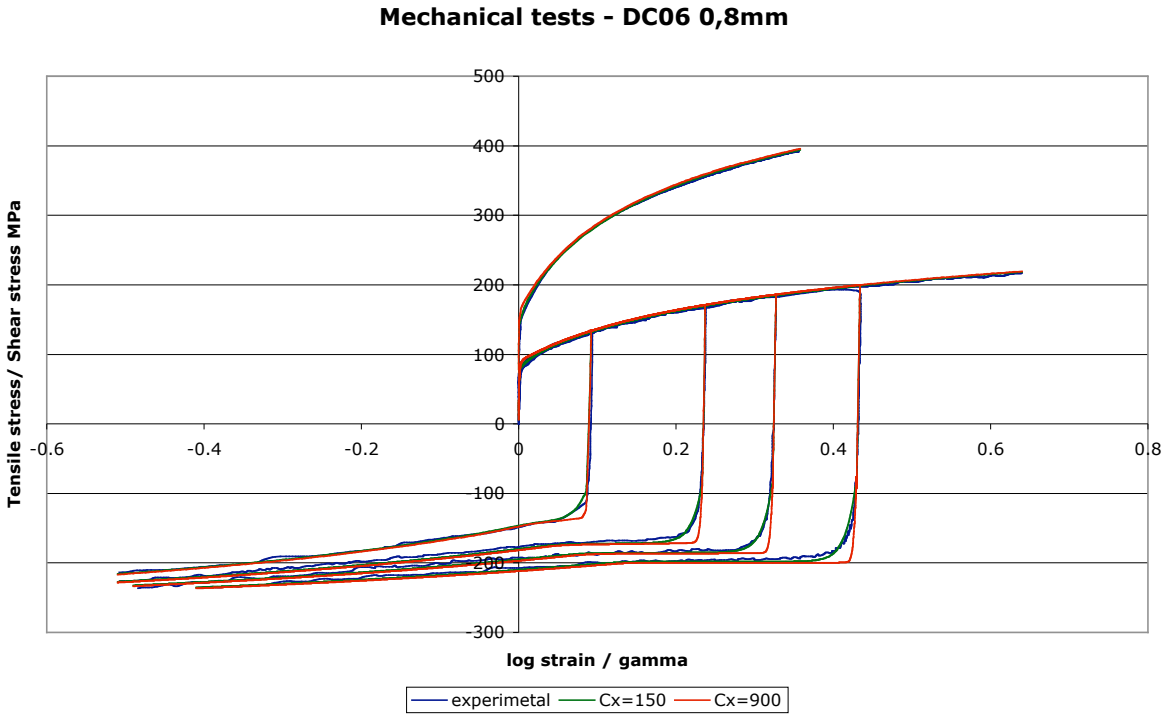

Figure 5.44 Mechanical tests simulations using parameters from Table 5.18.

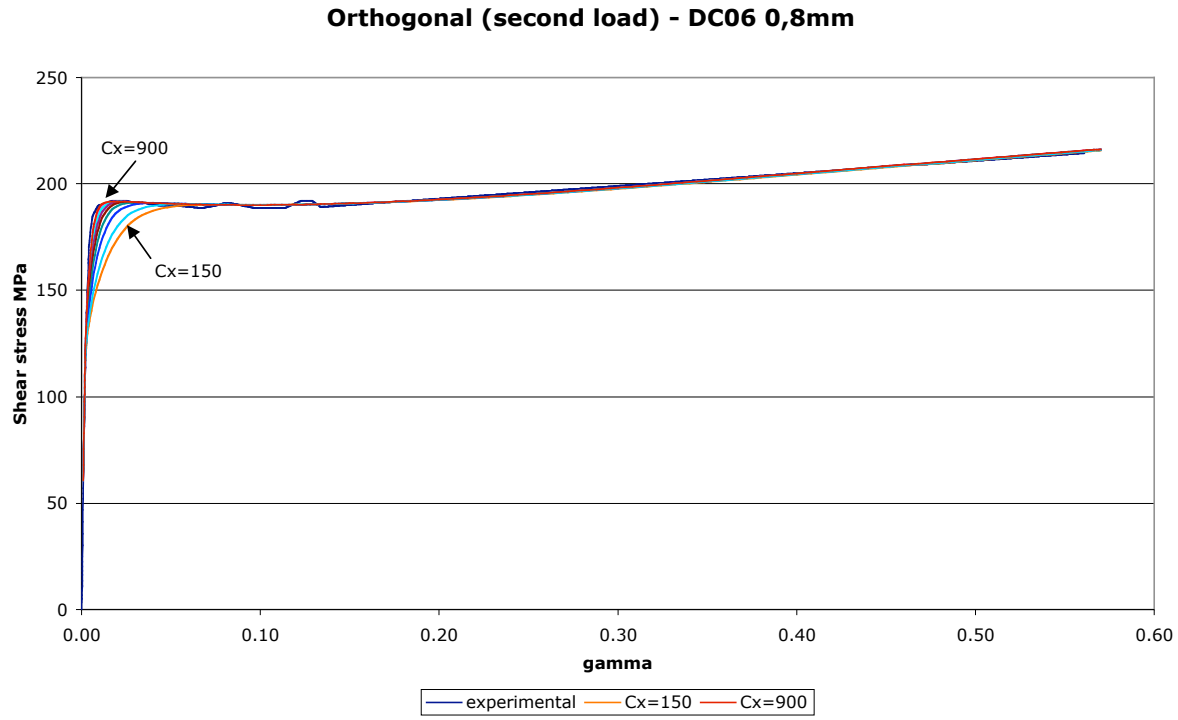

Figure 5.45 Orthogonal test simulation using parameters from Table 5.18.

A finite element simulation of a plane strain test in the RD is performed in order to validate the parameters established in Table 5.18. The finite element strategy is the same as the one used in Section 4.1.1, i.e., a 707-element mesh (Figure 4.8) and the data appearing in Table 4.1.
The experimental data are compared with the results of stress – strain curves for:

- Hill 1948 fit with Lankford coefficients,
- Hill 1948 fit with experimental data at $\bar{\varepsilon}_0^p = 0{,}5\%$,
- Hill 1948 fit with experimental data at $\bar{\varepsilon}_0^p = 20\%$,
- Minty (initial texture).

Each case is coupled with the Teodosiu and Hu hardening law.

In order to reproduce the conditions of the experimental test, the stress is measured from the computed resulting force divided by the actual area (Equation 4.2), which, in turn, is computed from the initial area and the thickness reduction computed at the center of the specimen (Equation 4.5). The longitudinal strain data is also computed at the center of the specimen.
Figure 5.46 provides the results. It can be seen that the constitutive model identified using Lankford coefficients predicts a higher strain than the other approaches. The results predicted by the model identified by stress values coincide with those predicted by the texture model and with the experimental curve up to a strain of 10%. Beyond this amount of strain, localization takes place (localization is not included in the models used).

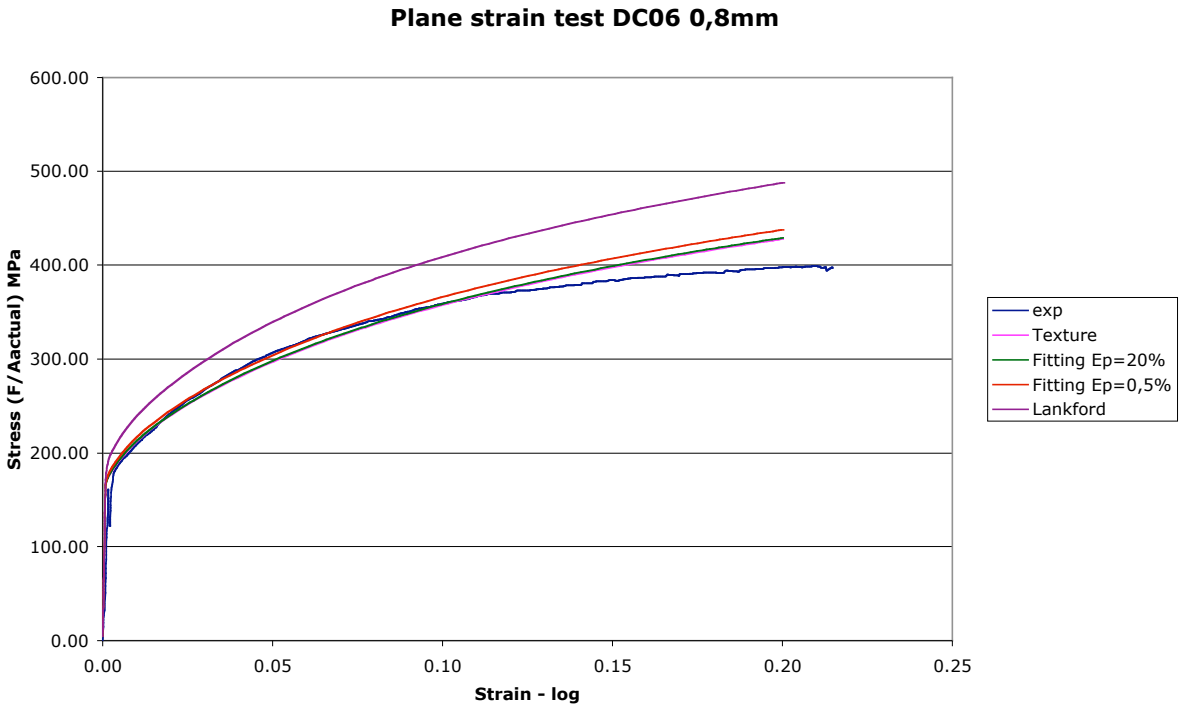

Figure 5.46 Plane strain test. DC06 0,8mm

5.4.2 Dual phase steel DP1000

Elastic parameters

The procedure for measuring the elastic parameters is similar to the one used for the DC06 in the previous section. Table 5.19 contains average parameters of tests performed in the RD, the TD and at 45° from the RD.

DP1000 1,6 mm		Elastic modulus E MPa	Poisson's coefficient
0°	Average	183695	0,290
	N° Tests	12	7
	Range	[170226 – 204798]	[0,268 – 0,308]
45°	Average	190669	0,301
	N° Tests	11	9
	Range	[172425 – 209173]	[0,263 – 0,322]
90°	Average	188723	0,287
	N° Tests	11	9
	Range	[171337 – 208824]	[0,258 – 0,312]
AVERAGE		188439	0,295

Table 5.19 Elastic parameters for DP1000 1,6mm.

Anisotropy coefficients

To compute the anisotropy coefficients, the plastic strain rate obtained from uni-axial tensile tests in the RD, the TD and at 45° from the RD are used. The stress-strain curves appear in Figure 5.47 as do the strain rates shown in Figure 5.48 for a particular case.
Computed average values are summarized in Table 5.20.

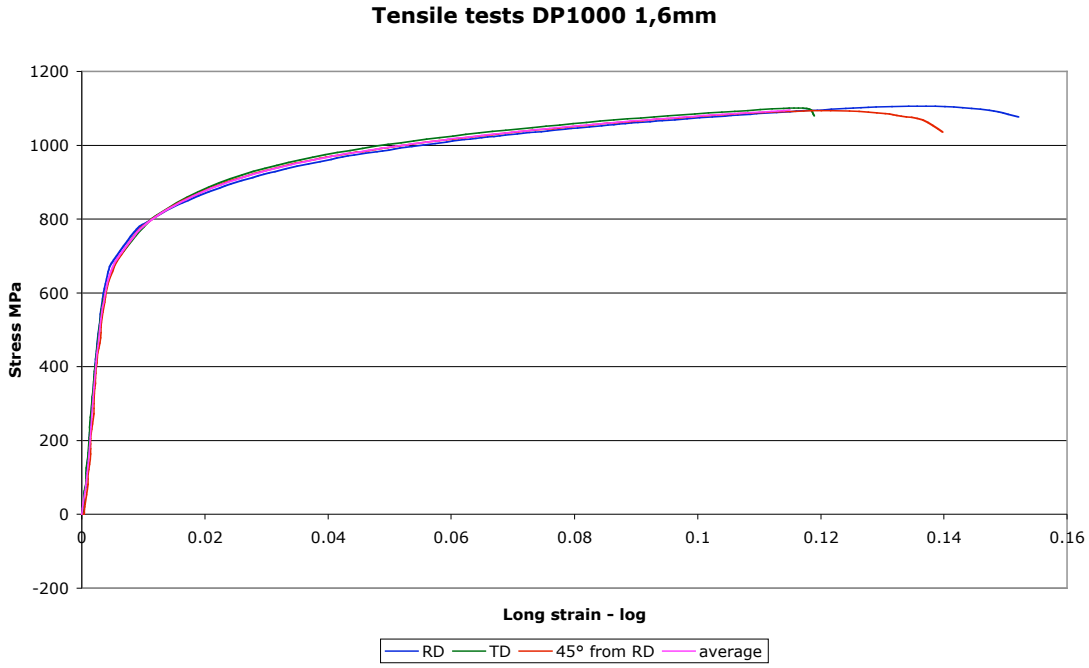

Figure 5.47 Tensile tests for a DP1000 1,6mm.

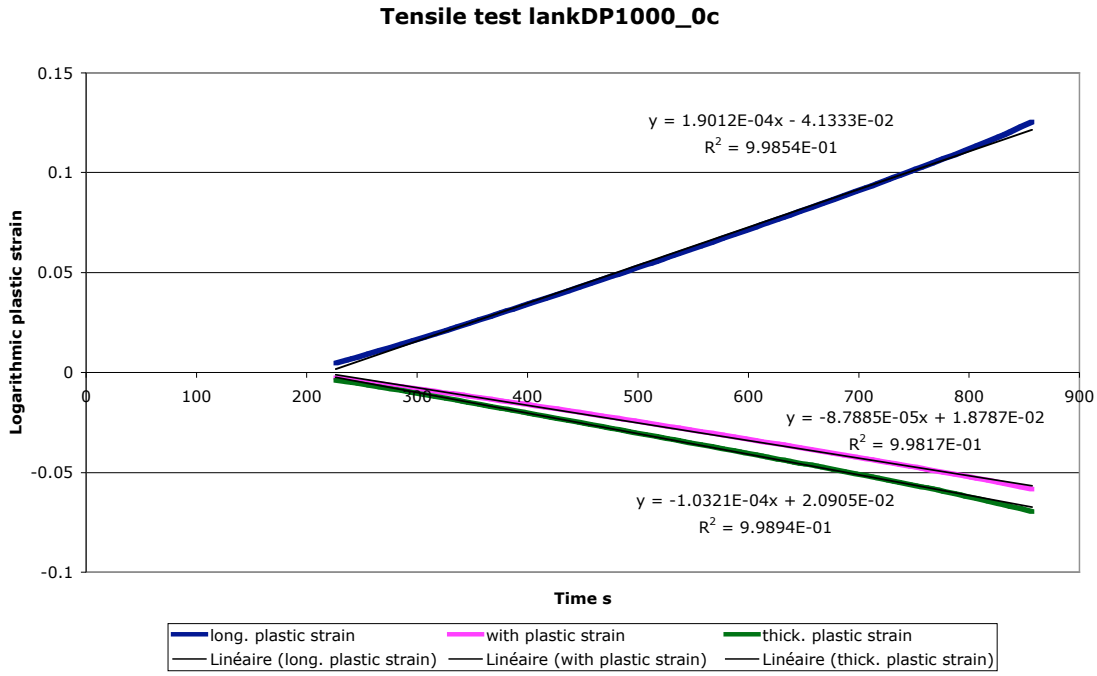

Figure 5.48 Plastic strain rate components for a uni-axial tensile test. DP1000 1,6mm.

DP1000 1,6 mm		Plastic strain			
		$\frac{d\varepsilon_{long}}{dt} x10^{-4}$	$\frac{d\varepsilon_{width}}{dt} x10^{-4}$	$\frac{d\varepsilon_{thick}}{dt} x10^{-4}$	$r = \frac{\varepsilon_{with}}{\varepsilon_{thick}}$
0°	Average	1,8908	-1,0214	-1,0214	**0,8596**
	N° Tests	3	3	3	3
	Range	[1,8254 – 1,9427]	[-1,0474 – -0,98382]	[-1,0474 – -0,98382]	[0,8516 – 0,8639]
45°	Average	2,0834	-1,0486	-1,0486	**0,9964**
	N° Tests	4	4	4	4
	Range	[2,0099 –2,1243]	[-1,0743 – -1,0092]	[-1,0743 – -1,0092]	[0,9810 – 1,0163]
90°	Average	1,9814	-1,0604	-1,0604	**0,8799**
	N° Tests	3	3	3	3
	Range	[1,9318 – 2,0548]	[-1,1094 – -1,0269]	[-1,1094 – -1,0269]	[0,8610 – 0,8926]
$\bar{r}$		0,9331			
Δr		-0,0633			

Table 5.20 Anisotropy coefficients using plastic strain measures DP1000 1,6mm.

Initial yield surface

Initial yield surface is described using the Hill 1948 yield criterion. The initial yield stress in the RD is used.
Table 5.21 shows the yield stress in the RD, the TD and at 45° from the RD (values measured at $\varepsilon_0 = 0{,}2\%$).
Table 5.22 presents the Hill 1948 material parameters computed using the Lankford coefficients (Equation 5.13 to Equation 5.15). Here, the chosen method has significant effect since the material is nearly isotropic.

DP1000 1,6 mm		$\sigma_y(\varepsilon_0 = 0{,}2\%) MPa$
0°	Average	697,34
	N° Tests	2
	Range	[692,77 – 701,90]
45°	Average	679,06
	N° Tests	2
	Range	[677,69 – 680,42]
90°	Average	665,20
	N° Tests	2
	Range	[664,71 – 665,69]
AVERAGE		680,16

Table 5.21 Initial yield stress for uni-axial stress state. DP1000 1,6mm.

Yield criterion	*H*	*F*	*G*	*N*
Hill 1948	0,925	1,051	1,076	3,182

Table 5.22 Hill 1948 material parameters. DP1000 steel 1,6 mm.

Hardening parameters

Monotonic simple shear tests (Figure 5.49) and Bauschinger tests are performed at different amounts of pre-strain (Figure 5.50 to Figure 5.53) to complement the uni-axial tensile tests.

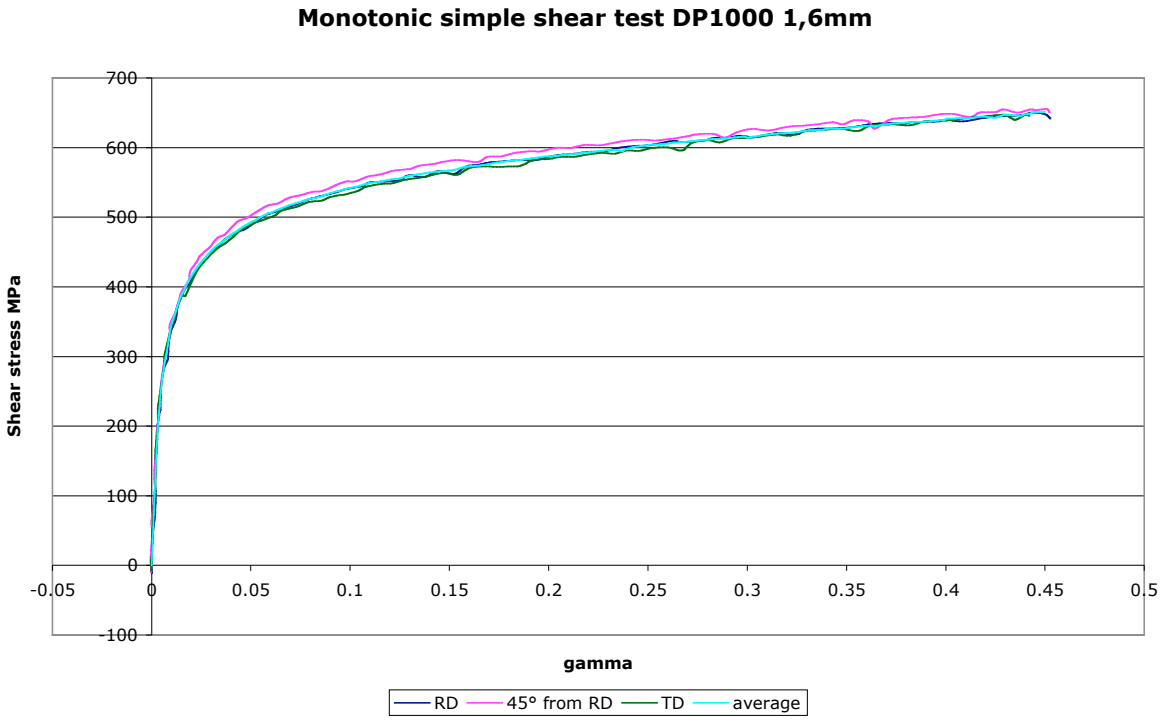

Figure 5.49 Monotonic simple shear tests. DP1000 1,6mm.

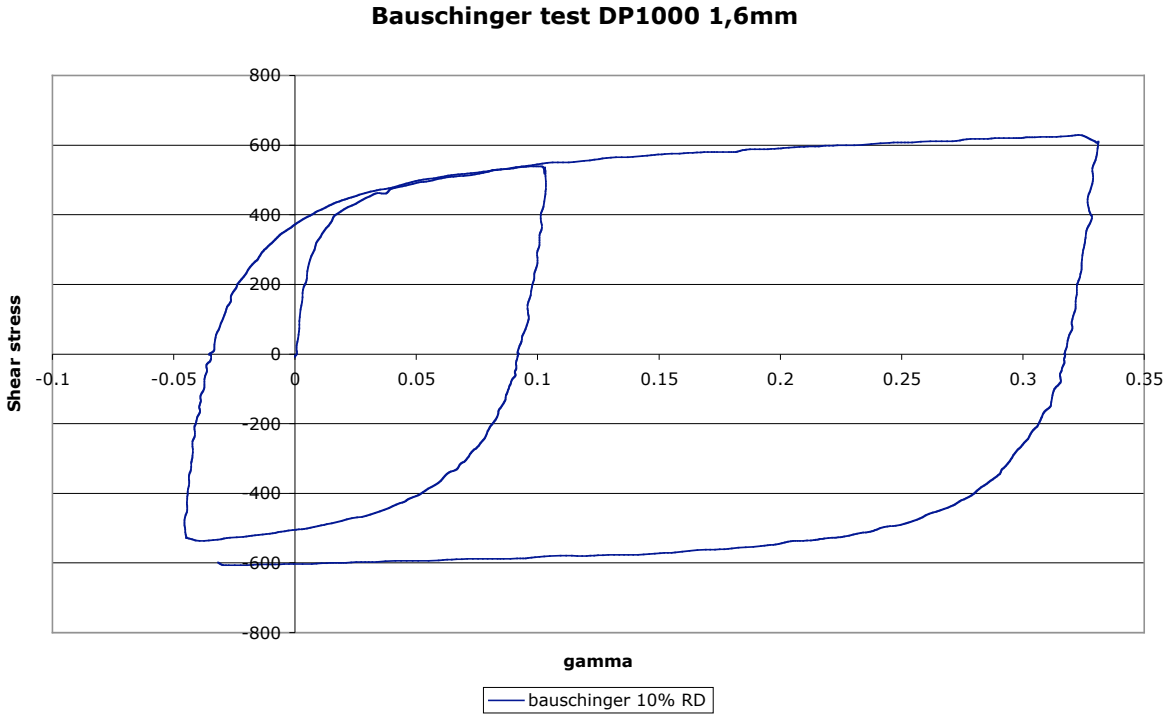

Figure 5.50 Bauschinger test in the RD (10% of pre-strain). DP1000 1,6mm.

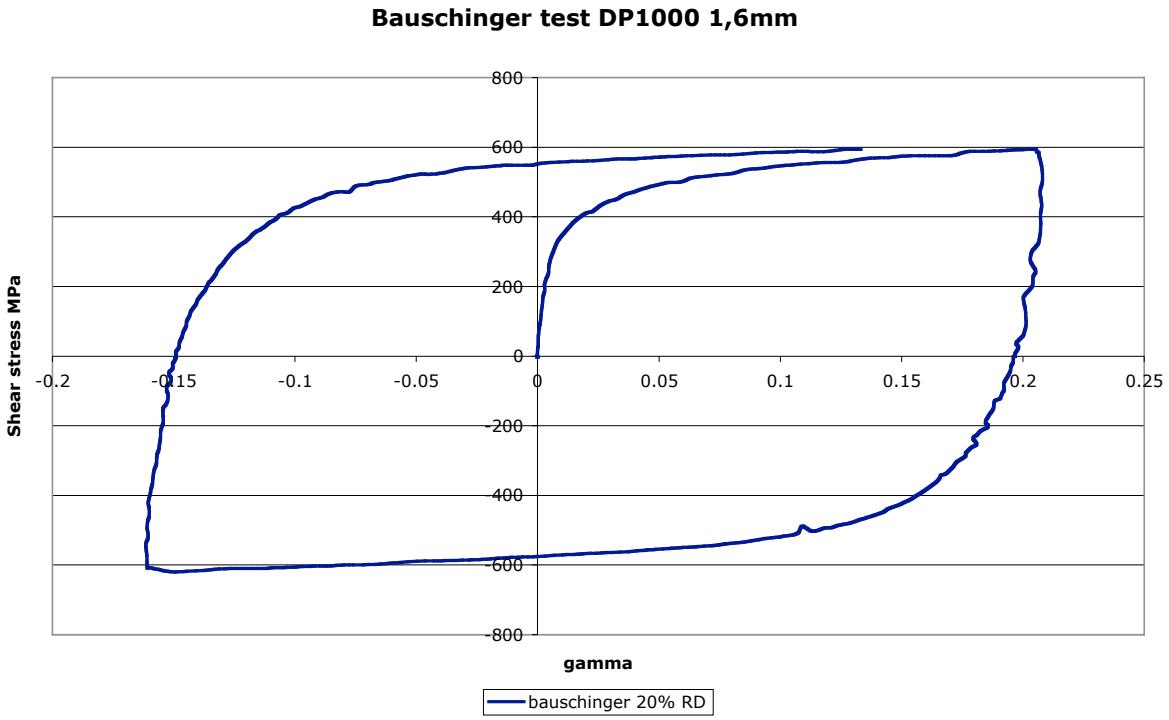

Figure 5.51 Bauschinger test in the RD (20% of pre-strain). DP1000 1,6mm.

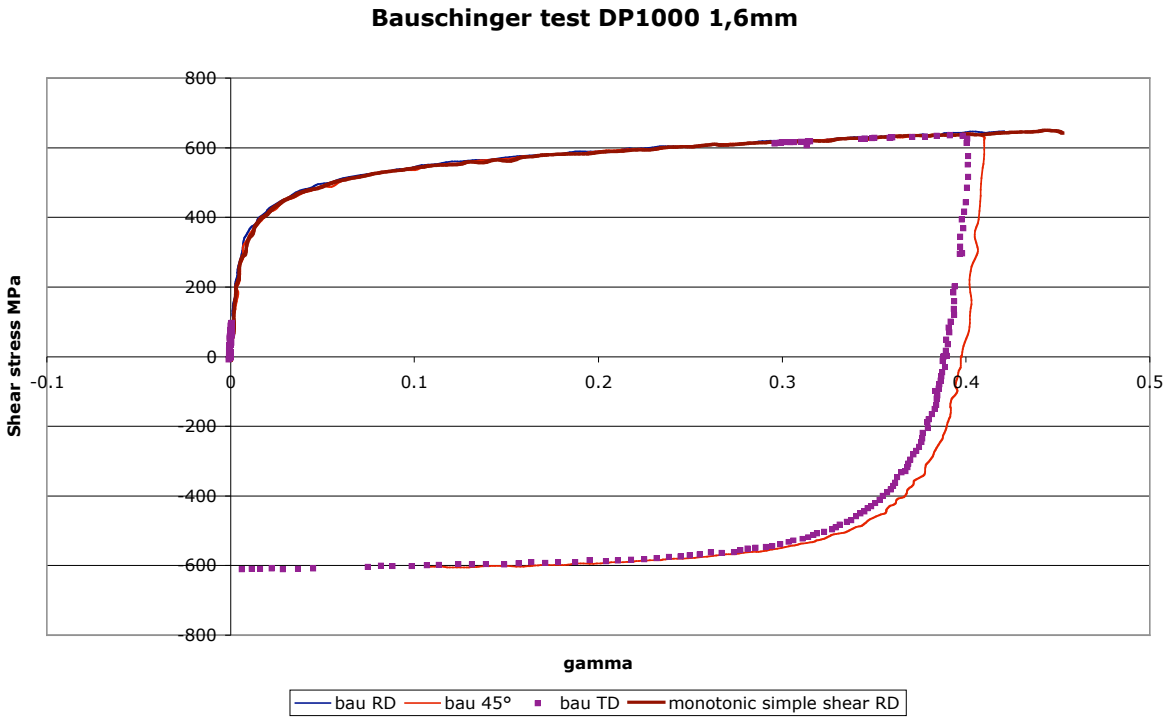

Figure 5.52 Bauschinger test in the RD (40% of pre-strain). DP1000 1,6mm.

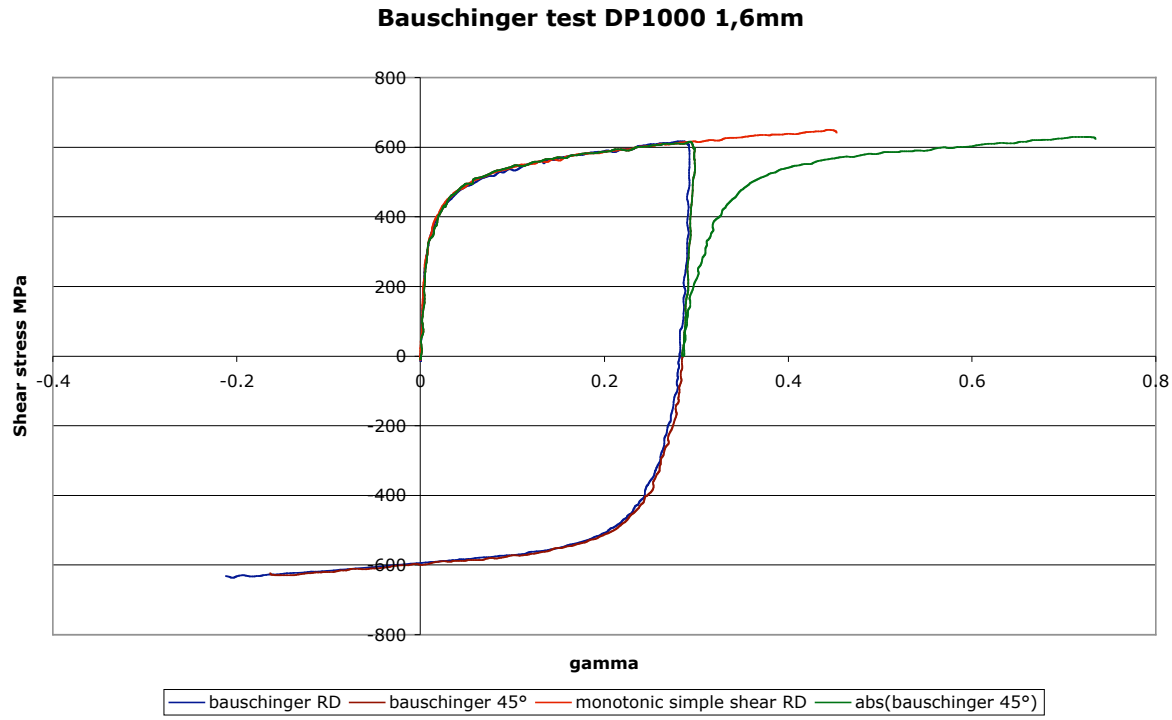

Figure 5.53 Bauschinger test at different angles from the RD (30% of pre-strain). DP1000 1,6mm.

Two main observations can be deduced: the amount of pre-strain doesn't have any influence on the subsequent strain path, whereas the Bauschinger effect is considerable.
This material is then characterized by the isotropic hardening (Swift Type, Equation 2.67) and by kinematic hardening (Armstrong-Frederick, Equation 5.45) in order to study the effect of the work-hardening induced anisotropy.
Swift law material parameters are fitted with uni-axial tensile test in the RD. The best fit is obtained with the parameters appearing in Table 5.23 and plotted in Figure 5.54.

Swift type hardening law – Material parameters	
K	1626 MPa
ε_0	0,00487
n	0,17

Table 5.23 Material isotropic hardening parameters for DP1000 1,6 mm.

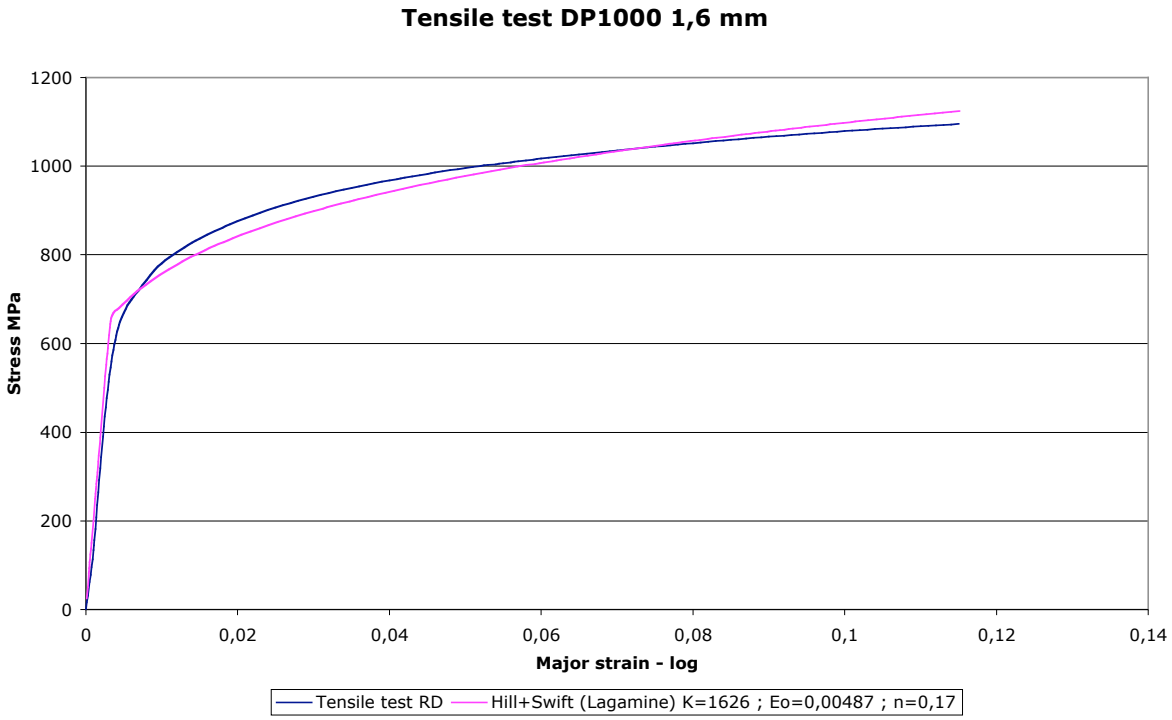

Figure 5.54 Tensile test simulation using Swift law.

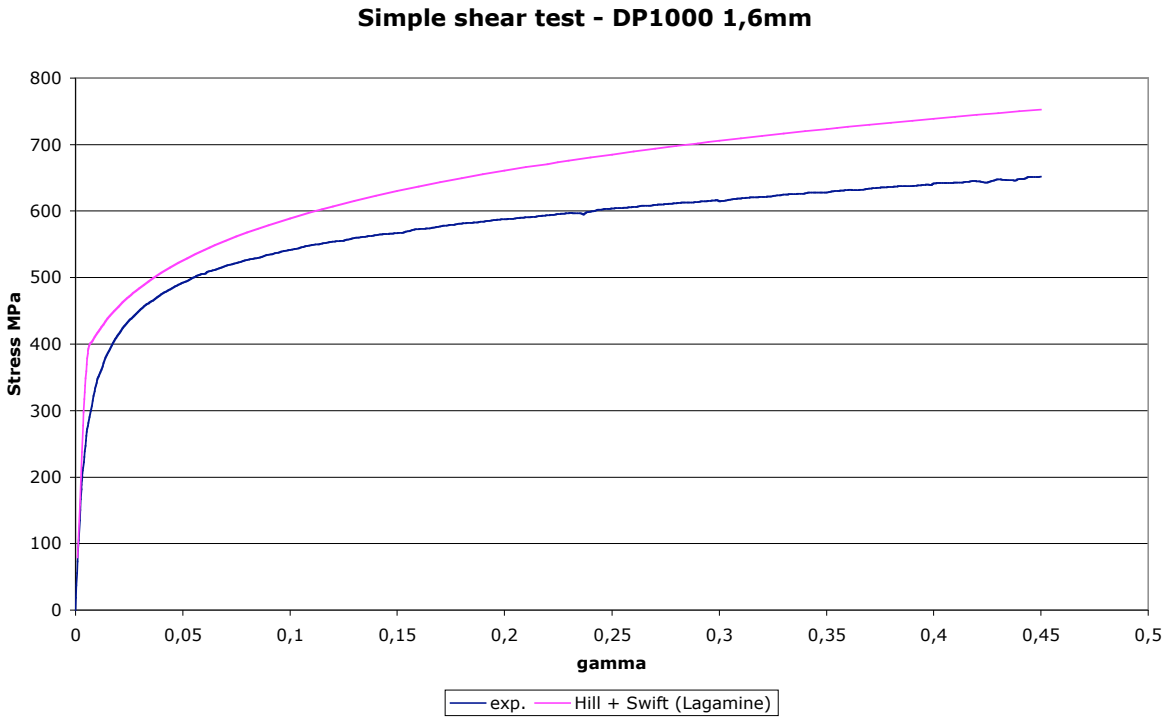

Figure 5.55 Simple shear test simulation using Swift law.

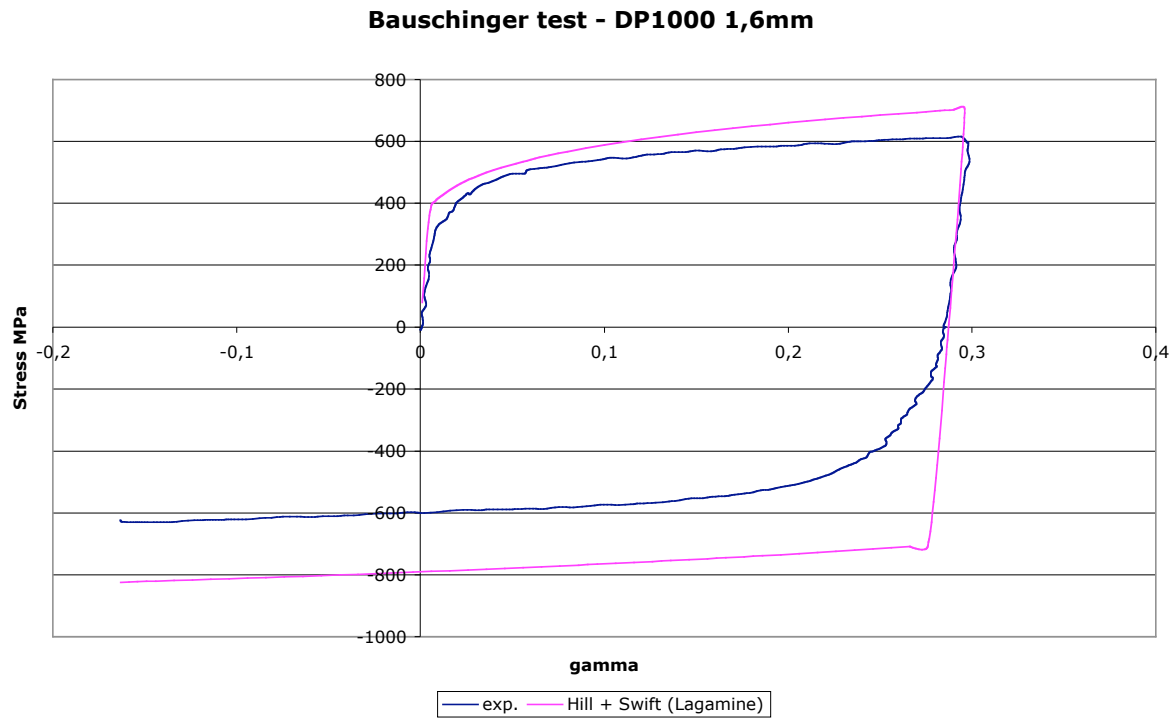

Figure 5.56 Bauschinger test simulation using an isotropic hardening law.

Figure 5.55 shows that the Swift law cannot predict the simple shear state in monotonic loads. A modification in the initial yield stress parameter *N* in Table 5.22 (the one exhibiting a larger influence over the shear state) can correct this difference, as is shown in Figure 5.57 for *N*=3,68. Even if the improvement is evident, this is not a proper solution, because it will produce errors in predicting material behavior when loads are applied outside the material axes, i.e., uni-axial tensile test at 45° from the RD.
Evidently, this law cannot predict the Bauschinger effect, as shown in Figure 5.56.

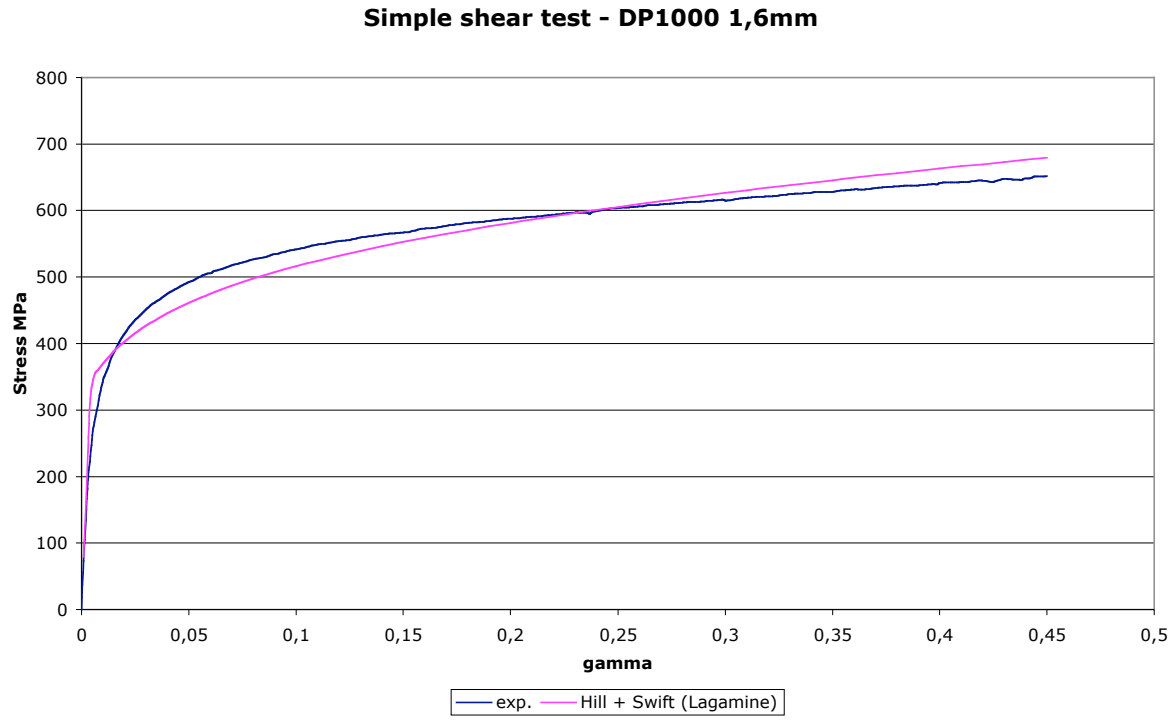

Figure 5.57 Simple shear test simulation using Swift law with N=3,68.

Table 5.24 contains the material parameters for the Armstrong-Frederick hardening law. Tensile, simple shear and Bauschinger tests are simulated with these parameters, and they are plotted respectively in Figure 5.58, Figure 5.59 and Figure 5.60. These curves include the simulated results using the Swift law in order to visualize the difference.

Armstrong-Frederick hardening law – Material parameters	
$\square_y$	697,34 MPa
C_X	43,7
X_{sat}	199 MPa

Table 5.24 Material kinematic hardening parameters for DP1000 steel 1,6 mm.

In conclusion, isotropic hardening does not conform for this material; only kinematic hardening and the Hill 1948 model properly model the material behavior under uni-axial tensile and simple shear states.

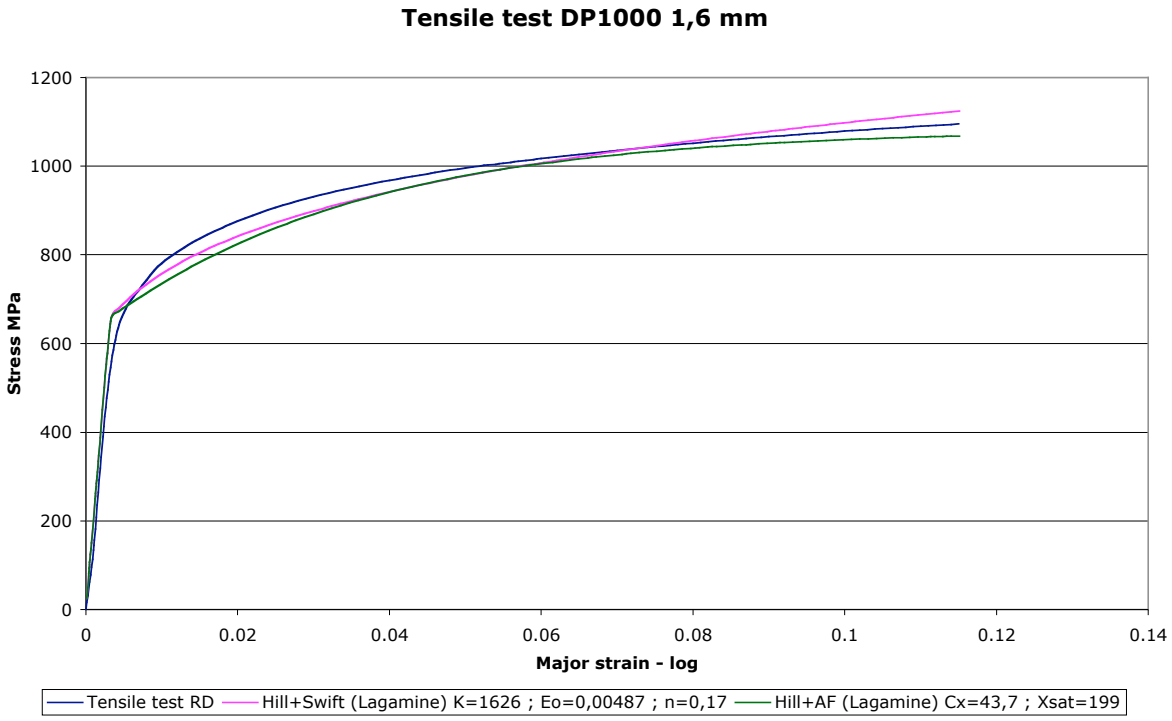

Figure 5.58 Tensile test simulation using Armstrong-Frederick hardening law.

Figure 5.59 Simple shear test simulation using Armstrong-Frederick hardening law.

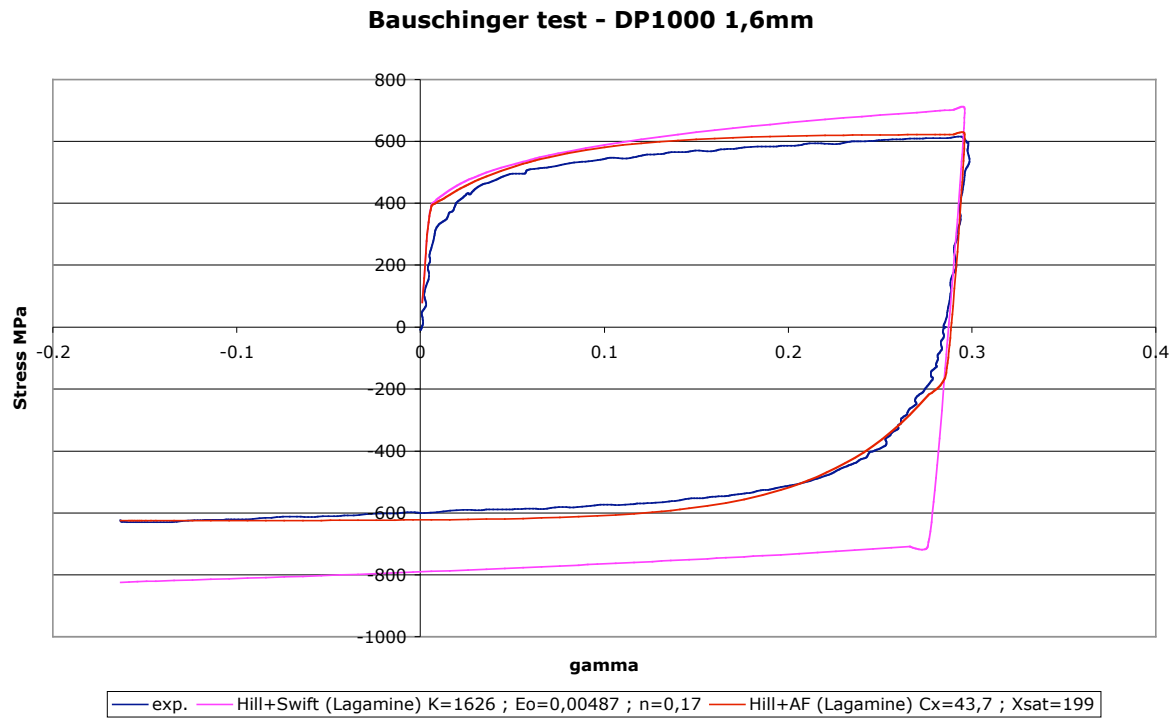

Figure 5.60 Bauschinger test simulation using Armstrong-Frederick hardening law.

5.4.3 Steel S320GD

Elastic parameters

The data obtained from a uni-axial tensile test is used to compute the elastic parameters. The parameters are approximated to E = 200000 MPa and ν = 0,3. Judging by our results, the elastic parameters do not have a great influence on the yield surface and on hardening material parameters identification.

Anisotropy coefficients

Anisotropy coefficients, as explained above for the other materials, are computed from the plastic strain rate obtained from uni-axial tensile tests in the RD, the TD and at 45° from the RD. The stress-strain curves appear in Figure 5.61.
Computed average values are summarized in Table 5.25.

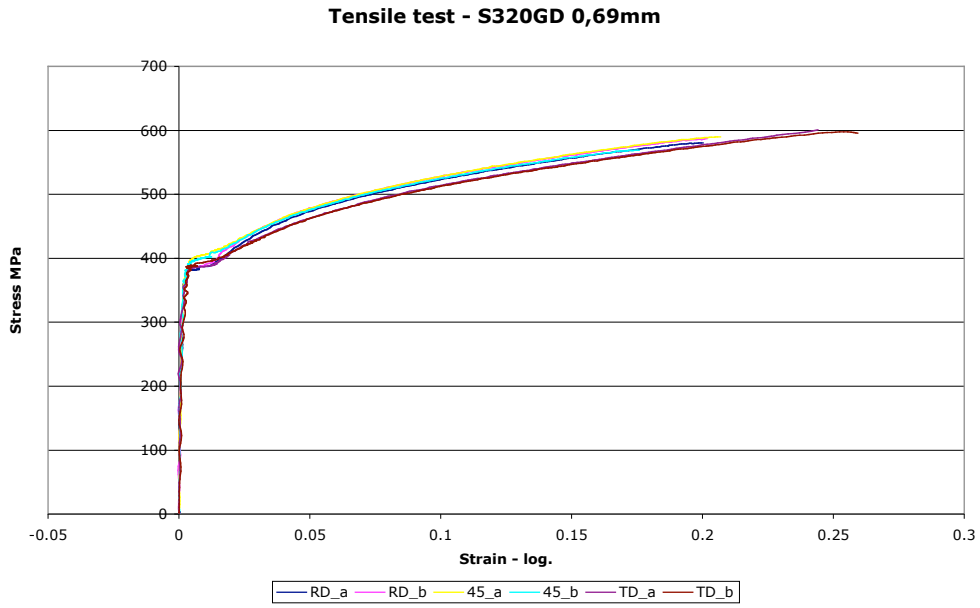

Figure 5.61 Tensile tests for a S320GD 0,69mm.

Lankford coefficients			
r_0	r_{45}	r_{90}	$\bar{r}$
0,9	0,76	0,98	0,85

Table 5.25 Lankford coefficients.

Initial yield surface

At this point in the research, as further improvement of the hydraulic pistons has been judged necessary, the current method of stress points has not been applied as the new configuration of the bi-axial testing machine will largely improve its accuracy. The simple identification by Lankford coefficients was used. Time constraints have likewise hindered further applications.
Initial yield surface is described with the Hill 1948 yield criterion. The initial yield stress in the RD is used.
Table 5.26 shows the yield stress in the RD, the TD and at 45° from the RD (values measured at $\varepsilon_0 = 0{,}2\%$).
Table 5.27 presents the Hill 1948 material parameters computed using the Lankford coefficients (Equation 5.13 to Equation 5.15).

S320GD 0,69 mm		$\sigma_y(\varepsilon_0 = 0{,}2\%)MPa$
0°	Average	328,87
	N° Tests	2
	Range	[327,84 – 329,84]
45°	Average	342,2
	N° Tests	2
	Range	[340,88 – 343,52]
90°	Average	321,2
	N° Tests	2
	Range	[321,84 – 320,55]
AVERAGE		336,62

Table 5.26 Initial yield stress for uni-axial stress state. S320GD 0,69mm.

Yield criterion	*H*	*F*	*G*	*N*
Hill 1948	0,95	0,97	1,05	2,55

Table 5.27 Hill 1948 material parameters. S320GD 0,69mm.

Hardening parameters

In addition to the tensile tests (Figure 5.61), monotonic simple shear, Bauschinger and orthogonal tests at the RD are performed in order to characterize the hardening behavior of this steel. Both, Bauschinger and orthogonal tests are performed at different amounts of pre-strain.
Figure 5.62, Figure 5.63 and Figure 5.64 show respectively the monotonic simple shear test, Bauschinger tests and an orthogonal test. Figure 5.65 represents the second load of the orthogonal tests at different amounts of pre-strain.
The tests highlight the presence of the Bauschinger effect, as well as the influence of the amount of pre-strain on the stress stagnation when reversing the load and for an orthogonal strain path change.
This material presents a similar behavior to DC06. Using the same identification method, Teodosiu and Hu hardening law parameters are identified and appear in Table 5.28. The predicted curves appear in Figure 5.65 to Figure 5.68.

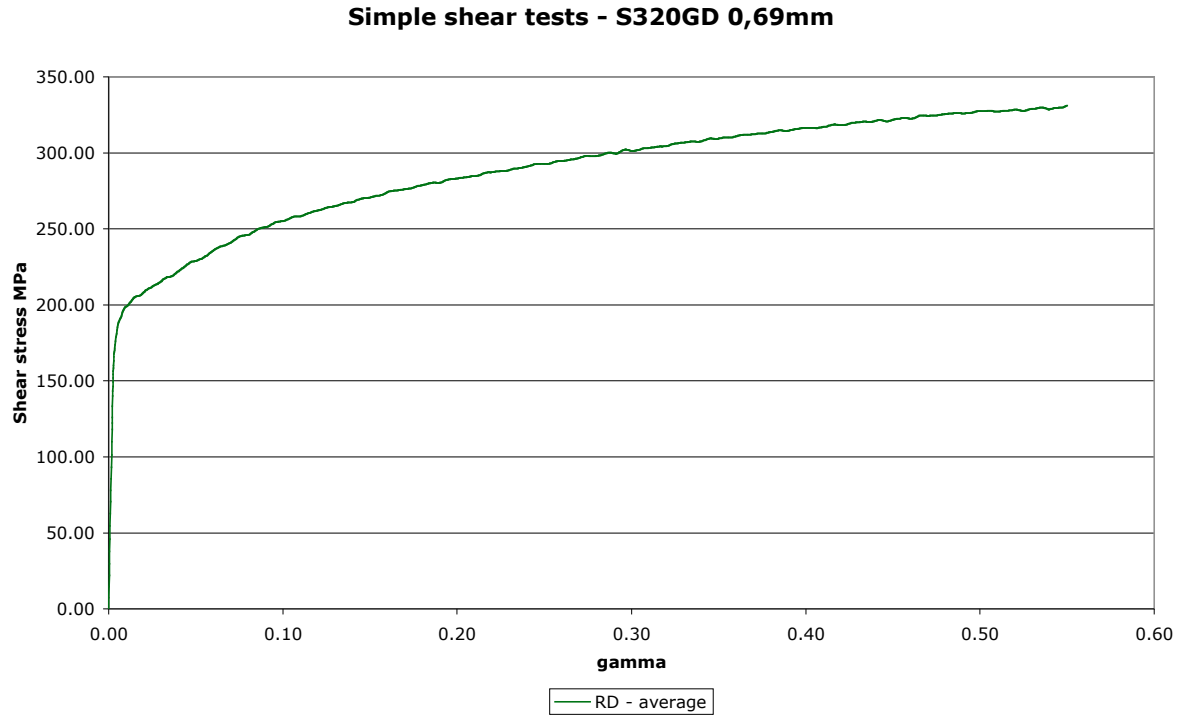

Figure 5.62 Monotonic simple shear test.

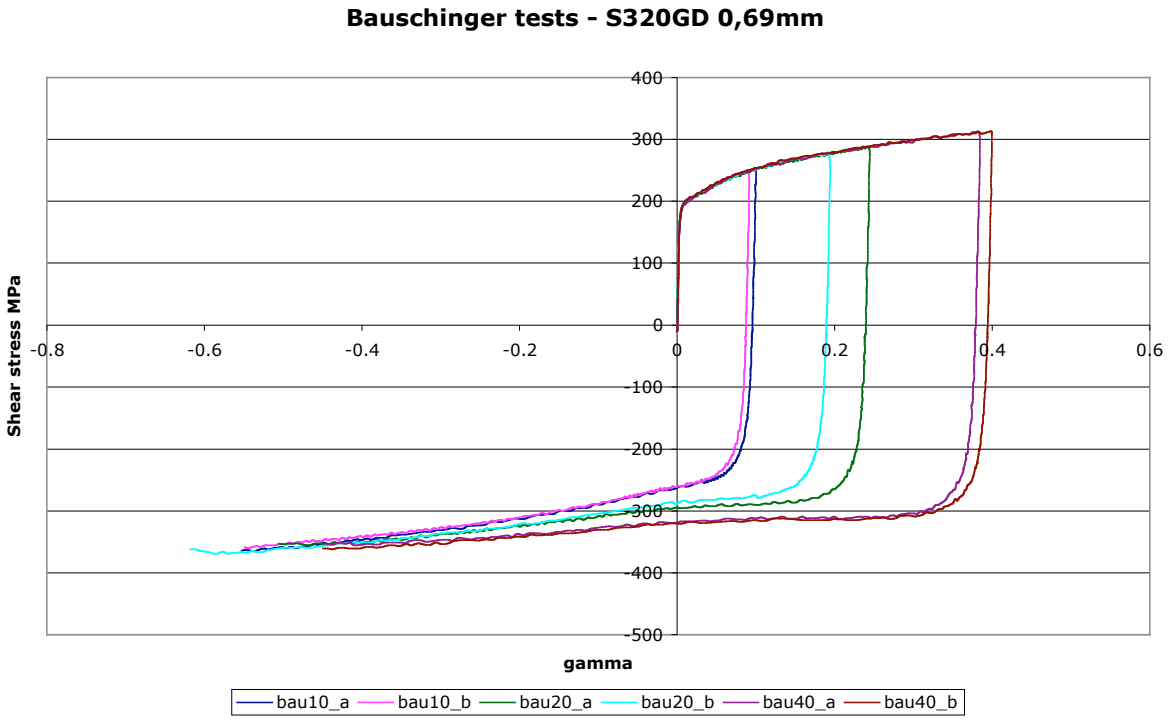

Figure 5.63 Bauschinger test at different amounts of pre-strain.

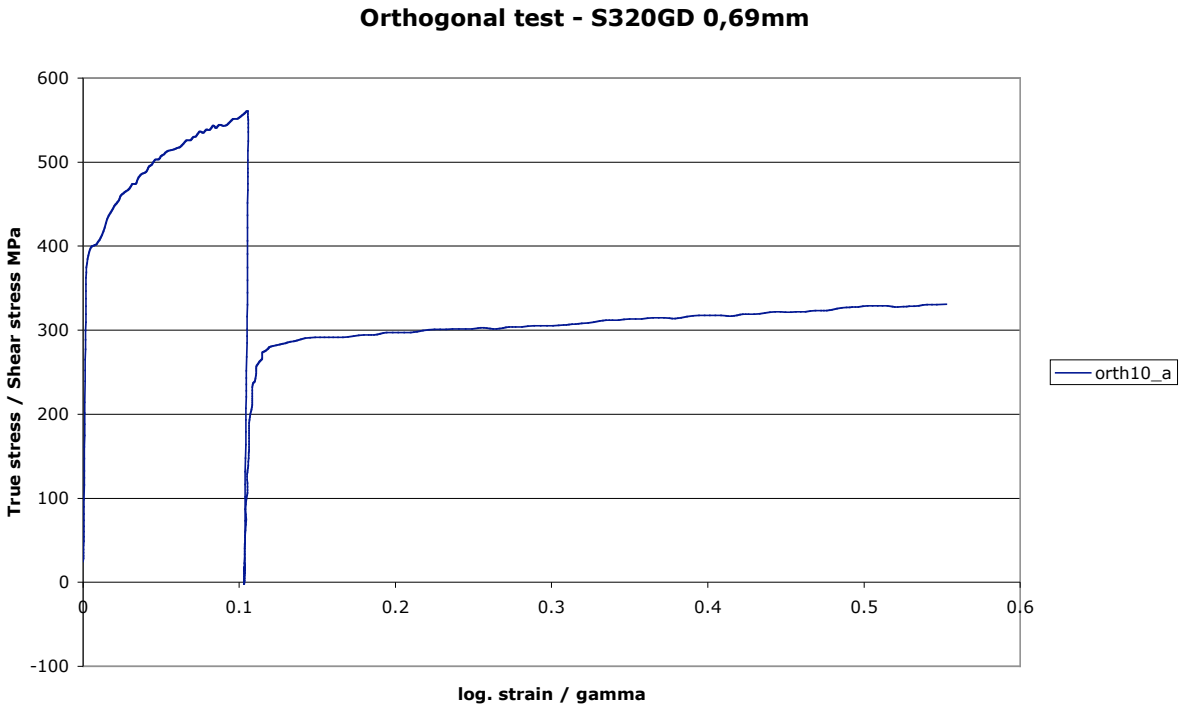

Figure 5.64 Orthogonal test with 10% of pre-strain.

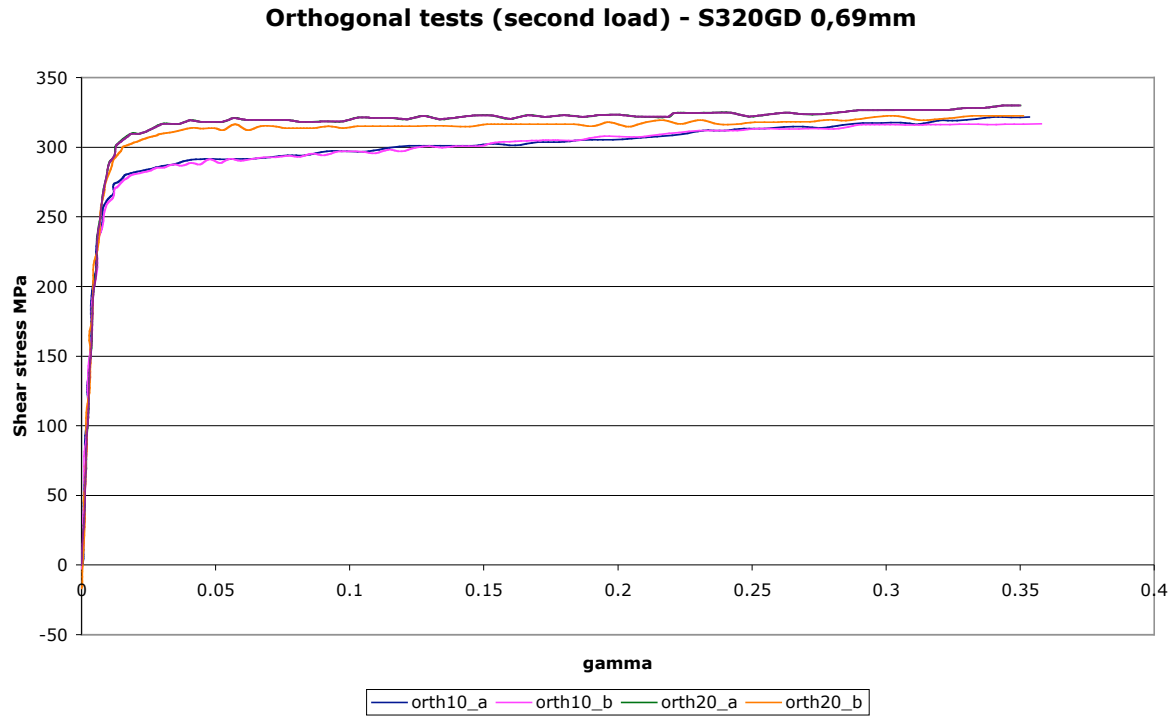

Figure 5.65 Orthogonal tests (second load) at 10% and 20% of pre-strain.

Hill 1948 material parameters (Equation 2.59)											
F		G		H		$N=M=L$					
0,97		1,05		0,95		3,56*					
Teodosiu and Hu hardening parameters (Section 2.5)											
R_0	C_R	R_{SAT}	C_X	X_{SAT0}	m	q	C_{SD}	C_{SL}	S_{SAT}	n_p	n_L	C_P
328,87 MPa	17,13	44,26 MPa	105,99	80,43 MPa	0,3	6	3,33	4	292,60 MPa	52,86	0	1

Table 5.28 S320GD 0,69mm material parameters. *This parameter is tuned up using the monotonic simple shear test experimental curve.

The same remarks established for DC06 can be applied here. The parameter N of Hill 1948 is optimized using the monotonic shear test and it is somewhat difficult to predict the orthogonal test flow stress. Figure 5.69 shows simulations using two different sets of parameters. As one may observe, the effect of increasing the parameter C_X is the same as the one observed for DC06.

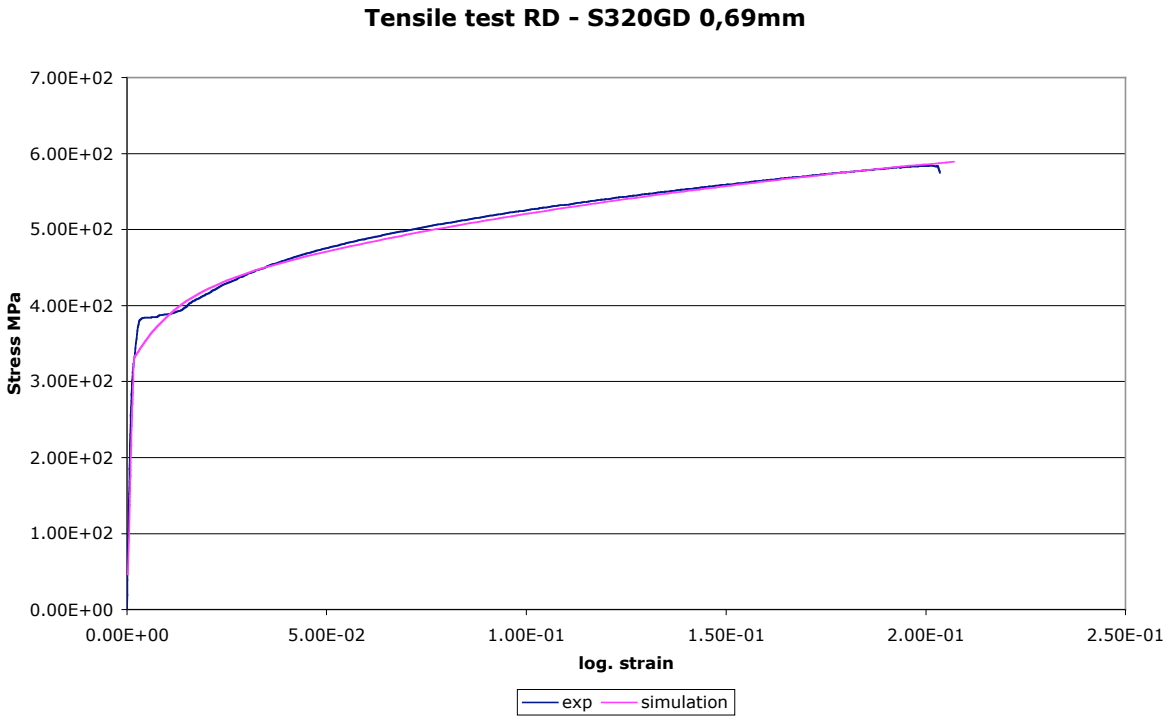

Figure 5.66 Tensile test, experiment and simulation, S320GD 0,69mm.

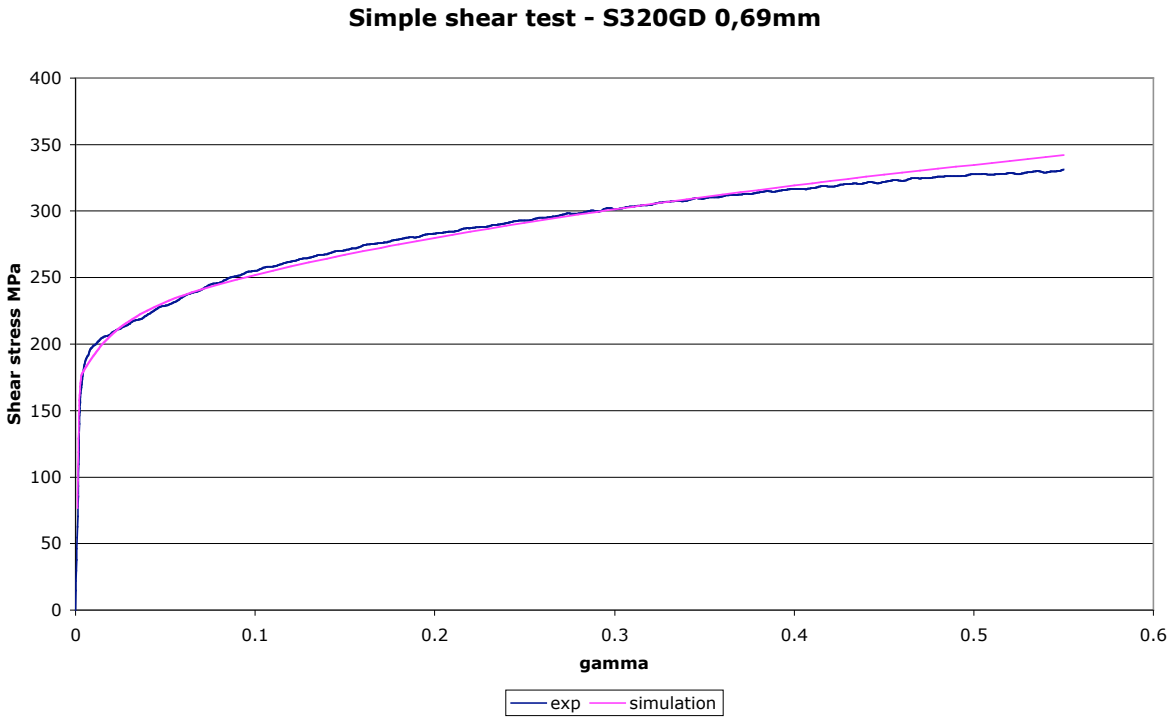

Figure 5.67 Simple shear test, experiment and simulation, S320GD 0,69mm.

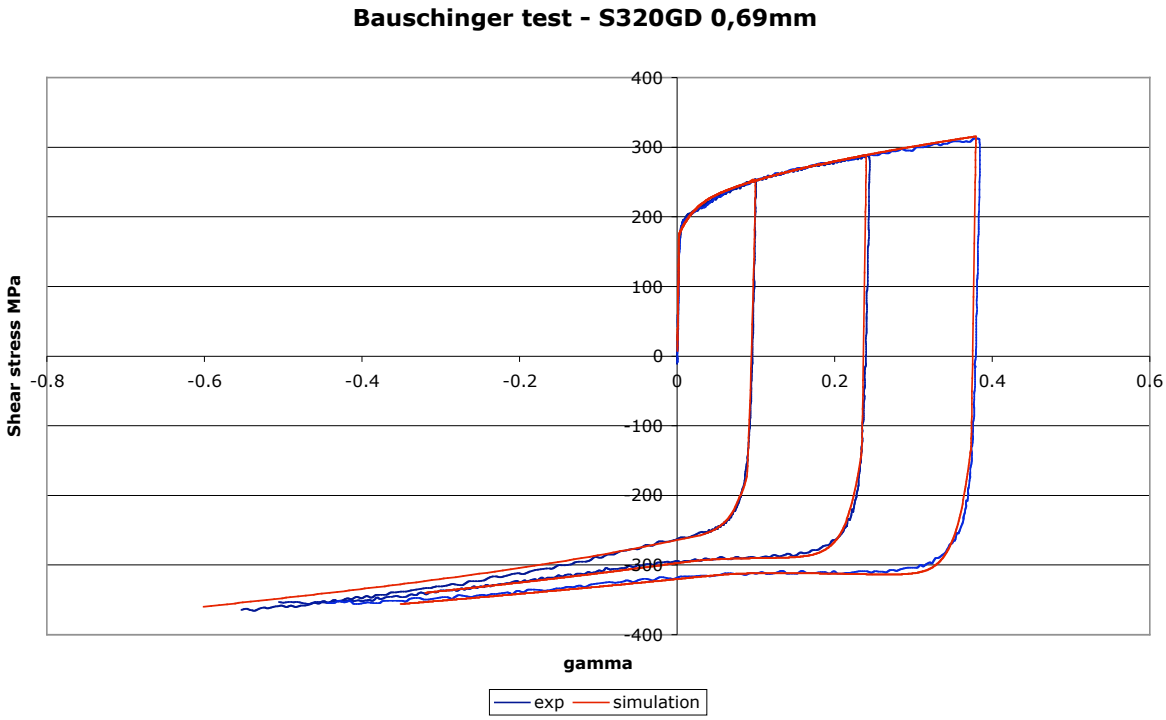

Figure 5.68 Bauschinger test, experiment and simulation, S320GD 0,69mm.

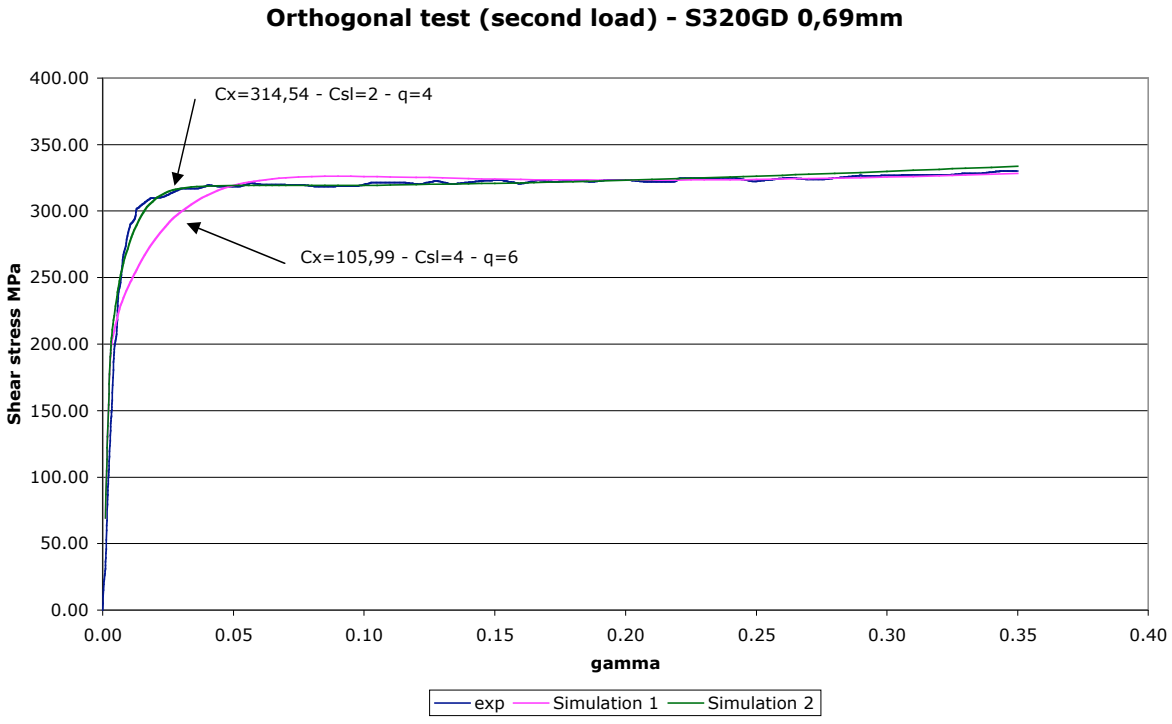

Figure 5.69 Orthogonal test S320GD 0,69mm.

5.5 Conclusions

Throughout this chapter, the object has been to study the identification of the material parameters of constitutive laws capable of accurately describing sheet metal behavior at room temperature.
The identification is divided into three parts: elastic behavior, initial yield surface and work hardening model. The study is focused on the last two characteristics, while assuming and isotropic elasticity.
To identify the initial yield surface, two methods have been studied and compared. One is based on the strain measurements (Lankford coefficients) and the other, on stress measurements (plastic work contours).

The first method requires three uni-axial tensile tests performed in the RD, the TD and at 45° from the RD using a standard tensile test machine and normalized tensile specimens. In addition, the strain field is obtained by an optical strain gauge (Aramis®). The strains measured allow us to compute the Lankford coefficients, which describe the material anisotropy. Lankford coefficients have been linked to the material parameters of Hill 1948 and Hosford 1979 yield criteria by the flow rule (a classical method that can be found in the literature).
The second method, based on stress measurements, requires several mechanical tests in order to reproduce the yield stress tensor in different zones of the yield locus of the material. Uni-axial tensile tests performed in the RD, the TD and at 45° from the RD allow us to identify three points on the yield surface. In addition, plane strain and simple shear tests performed (in the RD, TD and 45° from RD) in the bi-axial machine, described in Chapter 3 and Chapter 4, permits the identification of five additional points (since simple shear in RD is equivalent to simple shear in TD). Material parameters of Hill 1948 and Hosford 1979 yield criteria are optimized in order to minimize an error function established between the experimental and theoretical stress points. Since this method is based on (initial yield) stress measurements at different stress states, a coherent general definition of initial yield stress must be established. In this work, therefore, the initial yield stress is defined at equivalent plastic work. In turn, the reference plastic work is computed from the uni-axial tensile test at the RD.

Due to the mechanical conditions, it is impossible, due to the mechanical conditions, to compute the whole stress tensor for the plane strain and simple shear states directly from the measurement. Hence, in order to determine the “lost” terms, the following hypotheses are used: at small deformations, a simple shear test can be used to approximate a pure shear state (only one stress component computed with load cell data), and the missing stress component in the plane strain state is linked to the one computed with the load cell data using the flow rule and the strain field measurements, as shown in Section 5.2.2.

In the next step the two methods have been compared in the identification of the initial yield surface of the DC06 steel. The initial yield surface for this material is described with Hill 1948, Hosford 1979 (both identified using Lankford coefficients and stress measurements), and Minty (texture based) yield criteria. These criteria have then been compared with the measured yield stress points for tensile, plane strain, simple shear in the RD, TD and 45° from RD (measured at M&S Laboratory) and the bi-axial stress point (Kuwabara et al., 2002).

The results reveal that Hosford 1979 yield criterion accurately describes the initial yield locus (defined by the experimental points) no matter which identification method is used. However, its main drawback is the lack of the shear state description. The Hill 1948 criterion identified

using stress data is as accurate as Hosford 1979 in stress prediction, but it does not respect the normality rule (as is the case using Lankford identification). Likewise, the Hill 1948 identified using Lankford coefficients cannot predict the plane strain state or the bi-axial stress state. The Hill 1948 criterion identified using stress data and Hosford 1979 can predict the bi-axial stress state while Minty does not.

The Hill 1948 criterion identified using stress performs well but it requires a high accuracy in stress and strain measurements. As mentioned in the conclusions of Chapter 4, the bi-axial machine does not have a very high precision at low loads; therefore, the computation of stresses does not ensure good accuracy. This explains why additional "bi-axial points" corresponding to simultaneous shear and tensile states have not been added as initially planned at the outset of this thesis. Further modifications (changing hydraulic pistons for electromechanical actuators) will improve the stress determination accuracy and would enable the achievement of this goal. In the meantime, the yield surface for the other two materials (DP1000 and S320GD) is described by Hill 1948 identified with Lankford coefficients.

To characterize the strain-induced anisotropy of the materials, the following tests are performed in the RD: uni-axial tensile, plane strain, simple shear, Bauschinger (at different amounts of pre-strain) and orthogonal (at different amounts of pre-strain).
DC06 and S320GD exhibit similar behavior, i.e., flow stress does not saturate before the rupture, Bauschinger effect, and work-hardening stagnation dependent on the amounts of pre-strain when strain-path changes occur. Most appropriate for this situation, the hardening law proposed by Teodosiu and Hu has been chosen to describe the behavior of those materials.

Optimization of the material parameters has allowed us to obtained the material identification as described in Section 5.3.4 (summarized in Table 5.3). The optimized parameters perform well in describing the strain-induced anisotropy present in the reverse strain-path change, while for the orthogonal case they cannot predict the behavior of the flow stress at the beginning of second load. In order to resolve this problem, the reason for this is being studied. The orthogonal test, as mention in Chapter 3, can be performed by a successive simple shear – simple shear test, tensile – simple shear test or plane strain – simple shear test. If this last is chosen, the yield criterion must be able to describe that stress state.
One last point involves the influence of the parameter N of the Hill 1948 yield criterion on the hardening law identification. This parameter plays an important role in the shear state description. Since most of the tests used for the identification present a simple shear state behavior, it is important to include this parameter in the identification procedure.

Finally, the DP1000 presents a high Bauschinger effect and one may observe that the flow stress is not influenced by the amount of pre-strain when reversing the load (orthogonal tests have not been performed due to the capacity limitations of the bi-axial machine). It is proven that a kinematic hardening (Armstrong-Frederick) can accurately describe the behavior of this material. In the future, this material will be identified with the Teodosiu and Hu hardening law in order to improve accuracy.

CHAPTER 6
CONCLUSIONS AND PERSPECTIVES

The aim of this thesis is the identification of material parameters of phenomenological constitutive laws capable of accurately describing sheet metal behavior under large deformations at room temperature.

The thesis starts with a brief description of the concepts of kinematics, strains and stresses of a continuum body under large deformations. A general constitutive equation, relating stress and deformation in a rate form, is developed by using classic concepts of plasticity theory such as yield function, plastic flow rule and hardening constitutive laws. Of these concepts, our interest is focused on the identification of yield functions able to identify material anisotropy, such as Hill 1948 and Hosford 1979, as well as hardening constitutive laws able to predict strain-induced anisotropy such as the Teodosiu and Hu hardening law. Other classic approaches like the isotropic Swift or Voce laws and the kinematic Armstrong – Frederick hardening models are also a matter of interest. The choice of these constitutive laws is due to their wide use in several finite element codes.

Before defining the experimental equipment required to be used for the material identification, a general study of stress – strain states is performed. The stress states that easily define the initial yield stress are as follows: uni-axial tensile, tensile plane strain, bi-axial tensile and pure shear. The strain states that best suit the study of the strain-induced anisotropy are: uni-axial, tensile plane strain and simple shear (this last attaining large deformations). The effect of strain-path changes can be studied by successively combining these strain states.
After a review of testing equipment used to reproduce the required mechanical states, the decision to build the Miyauchi device and a bi-axial test machine was made. The Miyauchi device is particularly suitable for a reverse simple shear test and can be implemented in any tensile test machine. The specimen geometry used here has been designed to have a wide deformation zone in order to allow the extraction of pre-strained specimens to be tested in the bi-axial machine. The bi-axial testing machine is able to perform plane strain and simple shear tests separately or simultaneously. The small size of its specimen enables us to cut them off from the Miyauchi specimen deformation areas.
An optical strain gauge is used to measure the strain field directly from the material, thereby avoiding error sources such as sliding or machine rigid displacements.

The first step in the validation of the bi-axial mechanical tests is the verification of the homogeneity of the strain and stress fields. As for the first, the verification process is, straight forward, in that strain field homogeneity can be verified experimentally using the optical strain gauge information. On the other hand, stress field homogeneity has to be studied by finite element simulations. The analysis consists in comparing the stress field values (by

taking an average value from each finite element) with the global stress obtained from the force per unit of area. It has been shown that this last measurement can accurately represent the stress average value. These results are also compared with the results obtained for a single element analysis, concluding that a single element is representative of the material behavior at the center of the specimen having a negligible relative error with respect to the average value. The homogeneity test confirms that the stress computation can be directly obtained from available data such as load and current area; in addition, the central point can be taken as a representative point of the specimen deformation area.

The second step is to show that the required mechanical tests can be carried out with this testing machine. Experimental results are compared with finite element simulations of the tests (material being identified by another laboratory) leading to a satisfactory correlation. Similarly, the Miyauchi simple shear test is validated by an identical method.

The behavior of three steels (DC06, DP1000 and S320GD) is characterized by performing uni-axial tensile, plane strain, simple shear, Bauschinger and orthogonal mechanical tests in the RD, TD and at 45° from the RD. The elastic parameters and the initial yield stress are identified using uni-axial tensile tests, and strains measured using strain gauges. The Lankford coefficients are computed from strain data measured with an optical strain gauge from uni-axial tensile tests in the RD, TD and 45° from RD.
DC06 yield stress is identified for three yield criteria: Hill 1948, Hosford 1979 and Minty (texture-based). Hill 1948 and Hosford 1979 are identified using strain measurements (Lankford coefficients) and stress measurements of the yield stress at different stress states (defining equivalent plastic work contours). Both criteria identified with the two methods are compared with the Minty description and initial yield stress experimental points (uni-axial tensile, plane strain, pure shear and bi-axial).
The results show that Hosford 1979 yield criterion is the one which best represents the initial yield surface in the principal stresses. Both identification methods give similar results; hence, this criterion can be identified with only two tensile tests (in the RD and TD). However, this criterion is not suitable for the description of shear states.
The Hill 1948 identified with Lankford coefficients is not able to predict states accurately other than uni-axial tensile ones. The same criterion identified using stress measurements presents an accuracy similar to Hosford 1979 yield criterion but it does not respect the normality rule.
Hill 1948 criterion identified using stress measures and Hosford 1979 predict the bi-axial stress state point better than Minty.
The yield surface identification using stress measurements gives good results, but it requires a high level of accuracy in stress and strain measurements. To improve the measurement accuracy, hydraulic pistons will be replaced with electromechanical actuators. In the meantime, DP1000 and S320GD yield surfaces are described with Hill 1948 criterion identified with the Lankford coefficients.

The Teodosiu and Hu hardening law is used to describe the DC06 and S320GD hardening behavior in order to predict the transient behavior that appears after strain-path changes.
The material identification is carry out by optimizing of the material parameters between a finite element simulation and the experimental curves. The optimized set of parameters is able to describe the flow stress behavior after a reversed strain-path change and the influence of the pre-strain in the flow stress transient behavior, while for the orthogonal case, the same set of parameters cannot predict the behavior of the flow stress at the beginning of a second load. At the time of publication, the reason for this discrepancy is still being studied.

DP1000 presents a high Bauschinger effect and it can be seen that the flow stress is non-reactive to the amount of pre-strain when reversing the load. This material behavior is described by the Armstrong and Frederick kinematic hardening law.

In future tests, in order to improve the accuracy of the measurement of loads (at low load levels) in the bi-axial testing machine, the hydraulic pistons will be replaced by electromechanical actuators. This change will allow the application of the stress measurement method to yield surface determination and the study of the material behavior under combined loads (simultaneous plane strain and simple shear tests) initially planned for this thesis (Figure 6.1).
The grip wedges will be also replaced for others having a geometry that is suitable for the clamping thicker specimens.

It is recommended for the characterization of the initial yield stress in the plane strain stress state to use plane strain specimens presenting necking as the one shown in Figure 3.21. The reason is that this geometry ensures the precision of the test since the geometry at the measurable zone will remain constant and will be no longer dependent on the gap between the grips. The plane strain test is very sensitive to the geometry.

The use of the Miyauchi device in the study of strain-path changes other than those presented in this work will be studied.

The bi-axial machine is being used for aluminum characterization (Flores et al., 2005) and it will be used for titanium characterization (in the frame of the projects SEMPER, PAI and TITAERO). In addition, some tests are being performed to study the influence of the percentage of ferrite and perlite on the steel mechanical behavior in order to develop new steel grades (Arcelor).

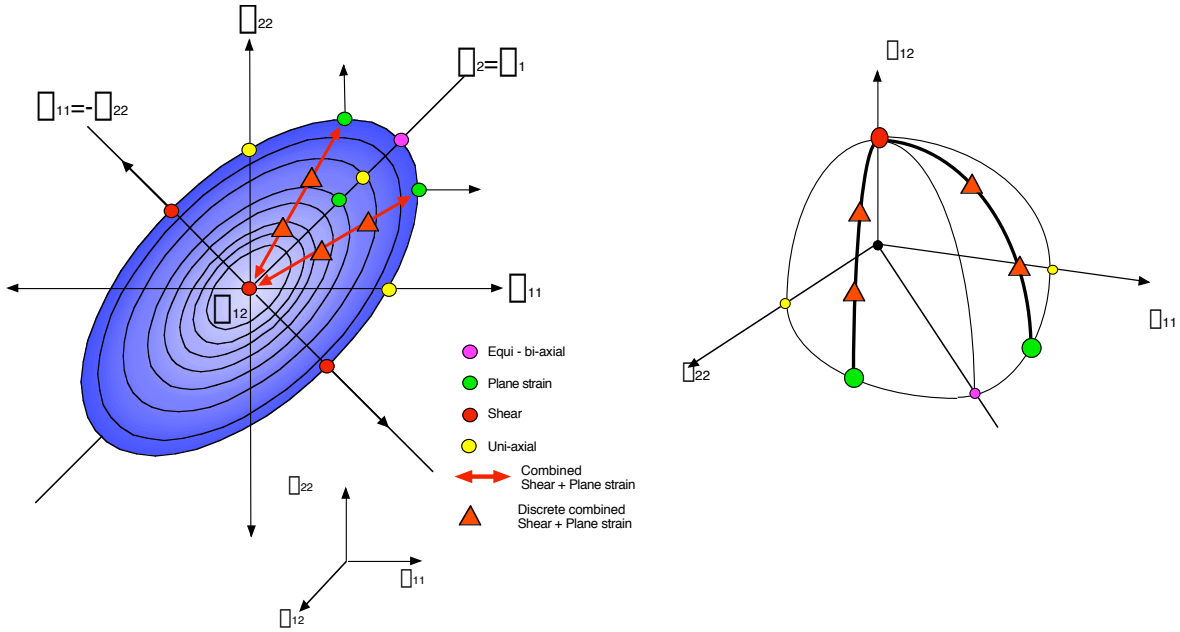

Figure 6.1 Discrete points in yield surface obtained by combined loads.

Future areas of research will focus on:

- The study of texture evolution during large deformations.
- The comparison with experimental measurements of material axis rotation as in finite element simulation of the orthogonal material axis (Hughes, 1983) has to be defined either by the use of Mandel spin (Peeters et al., 2001b), corrotational formulation (Jetteur and Cescotto, 1991), Jaumann approach (Hughes, 1983), the gradient constant symmetry velocity tensor (Munhoven and Habraken, 1995), definitions as the Mandel spin, the Jaumann correction, and the gradient constant symmetry velocity tensor (reference) or a variant proposed by Ponthot, 2002. A first approach has already been published in Lelotte et al, 2005.
- The experimental validation of new yield criteria of hexagonal closed packed metals such as the one proposed by Cazacu et al., 2005 (Figure 6.2).

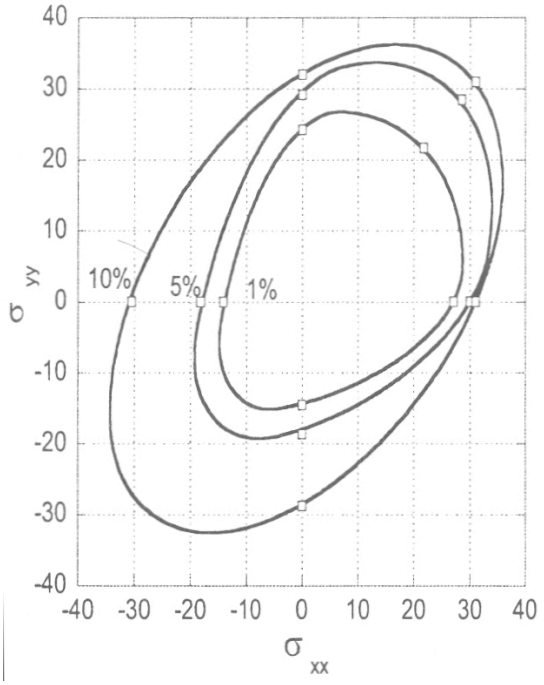

Figure 6.2 Comparison between the plane stress yield loci for a Mg.-0,5% Th sheet predicted by Cazacu et al., 2005 (solid lines) and the experiments (symbols). Cazacu et al., 2005.

ANNEX A

PHENOMENOLOGICAL MICROSTRUCTURAL-BASED HARDENING MODEL BY TEODOSIU AND HU

A.1 Introduction

This Annex is a review of several articles dealing with the phenomenological microstructural-based model proposed by Teodosiu and Hu. Before defining the experimental characterization procedure, it is first necessary to understand the model's micro-structural roots, a goal which this section seeks to address.
The Teodosiu and Hu's model describes large strains as well as the influence of strain-path changes and the amount of pre-strain on the flow stress. Four internal variables are included and 13 material parameters are required.
This law was first developed for BCC mono-crystals (Hu, 1992) and then it has been applied successfully to IF steel sheets (Bouvier et Haddadi, 2001, Brasseur et al., 2001, Hoferlin, 2001, Li et al., 2003, etc.). Further applications for dual phase steels and aluminum can be found in Bouvier et al., 2002.
This model review is divided into five steps (experimental, macroscopic observations, microscopic observations, mathematical model and identification). Section A.2 describes, in a general way, the tests required to identify certain phenomena. Section A.3 describes the macroscopic observation of the flow stress, while the fourth section explains the microstructural roots of the phenomena. In Section A.5, the mathematical model is described. An identification procedure is proposed in Section A.6 and, finally, some conclusions are established.

A.2 Mechanical tests

The different mechanical tests, which are required to identify the 13 material parameters, must be able to reproduce all the phenomena that the model can describe.
The most often performed tests are address below (Bacroix et al, 1994, Bouvier and Haddadi, 2001, Rauch, 1998, Rauch and Schmitt, 1989, Teodosiu and Hu, 1998):

Simple shear test

This test enables the material to reach large strains and the influence of the amount of pre-strain can be studied by performing several reversed simple shear tests (inversing the load) at different amounts of pre-strain.

Orthogonal test or cross test

This test enables the study of a strong strain-path change case. It can be performed in several ways, two of them being: 1. Tensile test + subsequent simple shear test of a specimen obtained from the former tensile specimen, 2. Simple shear test + a subsequent simple shear test of a specimen obtained from the former sheared specimen. In both cases, the subsequent test must be performed in the direction perpendicular to the first one in order to have a maximum effect.

More information about the tests and the required equipment can be found in Flores, 2003. In what follows, some important details are recalled concerning the strain-path changes study using a simple shear test (Bacroix et al., 1994 and Rauch and Schmitt, 1989) and the symmetry of the orthotropic metal sheets (Rauch, 1998).

The parameter α, initially proposed by Schmitt, is used to characterize the changes in strain-paths. This parameter is given by:

$$\alpha = \frac{\mathbf{d}_1 : \mathbf{d}_2}{|\mathbf{d}_1||\mathbf{d}_2|}. \tag{A.1}$$

Here, the sub-index represents the load sequence and $\mathbf{d}_i$ the strain rate tensor. A colon denotes the double-contracted tensor product and $|\mathbf{d}| = \sqrt{\mathbf{d} : \mathbf{d}}$.
The (quasi-)monotonic, (quasi-)Bauschinger and orthogonal tests are defined by α = 1, -1 and 0, respectively. When the two strain rate tensors correspond to simple shear, this expression can be rewritten as (Bacroix et al., 1994):

$$\alpha = (\operatorname{sgn}\dot{\gamma}_1)(\operatorname{sgn}\dot{\gamma}_2)\cos 2\beta, \tag{A.2}$$

where $\dot{\gamma}_1$ and $\dot{\gamma}_2$ are the shear strain rates during pre-strain and strain, and β is the angle between the two shearing directions.
The test used in Bacroix et al., 1994 is the Miyauchi test (see also Flores, 2003). Figure A.1 shows a diagram of the deformed specimen with the conventions of the reference frames. Two symmetrical zones can be distinguished corresponding to opposite signs of $\dot{\gamma}_1$. Table A.1 indicates the angle β for a second strain-path in order to obtain monotonic, orthogonal or Bauschinger sequences.

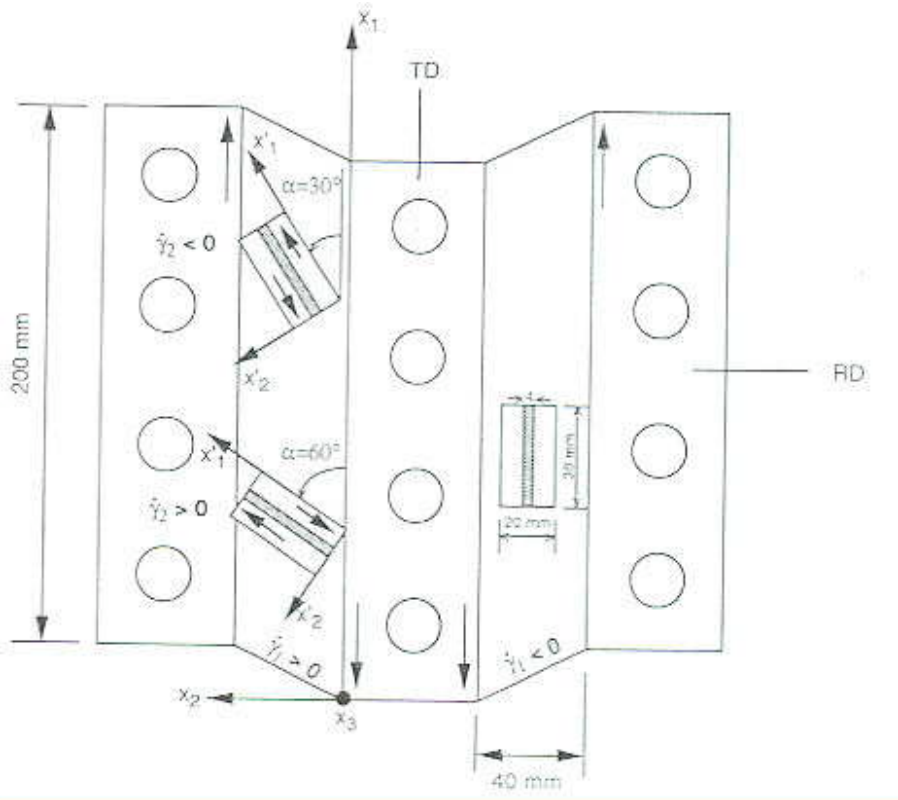

Figure A.1 Reference frames. Bacroix et al., 1994.

	1	0	-1
(> 0)	0°	45° or 135°	90°
(< 0)	90°	45° or 135°	0°
Sequence	Monotonic	Orthogonal	Bauschinger

Table A.1 Test sequences for >0. Simple shear test + subsequent simple shear test. Bacroix et al., 1994.

Rauch and Schmitt, 1989 study strain-path changes by sequences of tensile tests followed by simple shear tests. The simple shear test specimens are obtained from those used in the tensile test cut at a different angle from the tensile axis (coincident with the rolling direction). Table A.2 shows the angle for a second strain-path in order to obtain monotonic, orthogonal or Bauschinger sequences.

	0,92	0	-0,92
	45°	90°	135°
Sequence	Pseudo–monotonic	Orthogonal	Pseudo-Bauschinger

Table A.2 Test sequences. Tensile test + simple shear test. Rauch and Schmitt, 1989.

Rauch, 1998 shows that, for orthotropic materials, a test performed at 180°- corresponds to a test performed at (see Figure A.2). This result is applicable to the Miyauchi test symmetry.

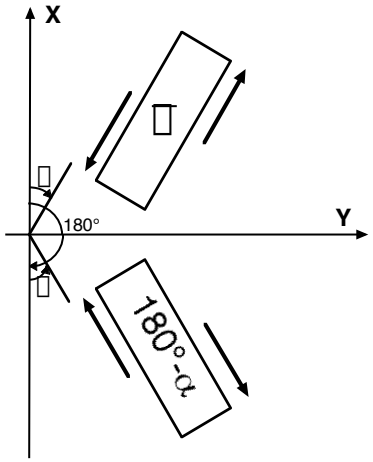

Figure A.2 For orthotropic sheets, an experiment performed at (180°-) corresponds to . Rauch, 1998.

A.3 Macroscopic observations

Figure A.3 and Figure A.4 show examples of the stress – strain curves obtained for these different mechanical tests.

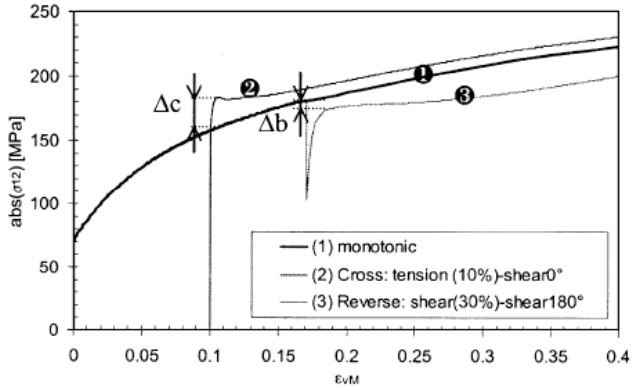

Figure A.3 Mechanical tests for an IF Steel. Peeters et al., 2001.

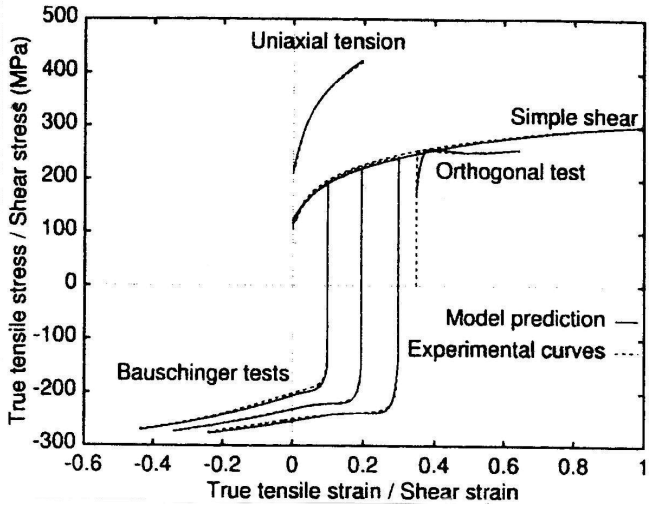

Figure A.4 High-strength steel ZstE180BH. Modelled by Teodosiu hardening law. Bouvier and Haddadi, 2001.

The simple shear monotonic test enables the material to attain high plastic strain levels. This test can be easily reversed, making it possible to study the strain-path change characterized by $\alpha = -1$ and the influence of the amount of pre-strain. The experimental results show three facts:

- Bauschinger effect (lower yield stress at the subsequent reversed strain-path).
- The work-hardening shows a transient stagnation stage after the load is reversed, followed by a resumption of the flow stress.
- The size of the work-hardening stagnation depends on the amount of pre-strain.

The results of the experimental orthogonal test ($\alpha = 0$) elicit the following observations (Teodosiu and Hu, 1998):

- After a subsequent orthogonal deformation, the flow stress is always higher than during the monotonic deformation, at the same accumulated strain.
- When the amount of pre-strain is small, the work-hardening rate is always positive.
- When the amount of pre-strain is large, first a work-softening occurs followed by a resumption of the work hardening.

A.4 Microstructural observations

The microstructural observations give an explanation for the phenomena described in the previous section. The conclusions established here are a summary of the following works: Peeters et al., 2001, Rauch and Thuillier, 1993, Rauch, 1989, Rauch and Schmitt, 1989, Teodosiu and Hu, 1995.

Monotonic test

The event called "deformation-induced micro-structural organization" is the formation and the evolution of low-energy dislocation structures (LEDS). These LEDS gradually form whenever a sufficient amount of monotonic deformation is allowed for along the same deformation path.
For a monotonic deformation, along the same strain-path, several slip systems are activated in the grains. The dominant LEDS are planar persistent dislocation structures called dislocation sheets or CBBs (Cell-block boundaries by Peeters et al., 2001) more or less parallel to the main slip planes.
During plastic deformation, the dislocation sheets polarized, i.e., an excess of mobile dislocations of one sign is stopped at one side of the dislocation sheet, and of the opposite sign on the other side of the dislocation sheet (Peeters et al., 2001).

Reverse test

The Bauschinger effect observed when performing a reverse test is caused by microscopic internal stresses present after the pre-strain and unloading. Such back-stresses are attributed to polarization. This polarity will cause an asymmetry of slip resistance and thus a drop in flow stress when reversing the load.
The polarization is also responsible for the observed work-hardening stagnation. When the load is reversed, the "polarity" dislocations can escape from the dislocation sheets and can be annihilated with dislocations in the cell-block interiors (Peeters et al., 2001).

The resumption of the flow stress is due to the re-polarization (in an opposite sense) of the dislocation sheets when increasing the strain in the new strain-path.

Orthogonal test

As mentioned before, at the subsequent strain-path of an orthogonal test, two main kind of phenomena can be observed: a higher flow stress and a transient zone depending on the amount of pre-strain.
The higher flow stress is due to the fact that the dislocation sheets act as obstacles for the new mobile dislocations (new slip systems, that were latent, are activated when changing the strain path, but also **at rotation!**).
The transient behavior, immediately after the second load, depends on the amount of pre-strain. For small pre-strains, the work-hardening rate is low but positive, and for large pre-strains, it can became negative. Peeters et al., 2001 explain that this behavior is associated with micro-localizations of plastic flow, which lead to the development of **microbands**. They are roughly parallel to the plane of a newly activated slip system. Then, these microbands cut through the old dislocation sheets and produce channels for easy glide of the mobile dislocations.
After increasing strain in the second path, microbands also increase and disintegrate the pre-existing structure. Then, at an even larger strain, microbands saturate and are transformed into dislocation sheets.

A.5 Mathematical model

This microstructural-based hardening law was first proposed in Hu, 1992, then some improvements, generalizations and applications can be found in Hu, 1994, Teodosiu and Hu, 1995, Teodosiu and Hu, 1998, Hoferlin, 2001 and Bouvier et al., 2002.
The first version of the law contained three internal variables. P described the polarity-dependent behavior due to persistent dislocation structures. R was used to describe the dislocation rearrangement during the disintegration of preformed persistent microstructures and the formation of new dislocation structures. Finally, the back-stress X represents the influence of less stable dislocation rearrangements, such as pile-ups. The model was first limited to a one-dimensional case.
In the work presented by Hu, 1994, the internal variable R is renamed R_P and a new internal variable R_I is introduced. This new internal variable takes into account the influence of non-polarized dislocation structures on the flow stress.
The article presented by Teodosiu and Hu, 1995 introduced the three-dimensional generalized model. The internal variables are redefined and are represented by tensors. The back-stress is a second-order tensor $\mathbf{X}$ having the same dimension as stress. The polarity is a non-dimensional second-order tensor $\mathbf{P}$. The variables R_P and R_I are replaced by a fourth-order tensor $\mathbf{S}$. This tensor describes the directional strength of planar persistent dislocation structures. The choice of its order is due to the need to describe the anisotropic contribution of persistent dislocation structures to the flow stress. This work is the basis of the hardening model as it is known today.
More recent works (Bouvier et al, 2002 and Hoferlin, 2001) introduce a scalar internal variable R with the dimension of the stress, which takes into account the isotropic hardening caused by the statistically distributed dislocations.
In what follows, the evolution equations of the model are described (Teodosiu and Hu, 1995). For matters of simplicity, initial isotropy is assumed and rotations are not taken into account. Therefore, problems of objective derivatives are not treated here.

A.5.1 Yield condition

First, the yield condition is written as:

$$F \equiv \bar{\sigma} - R_0 - R - m|\mathbf{S}| = 0\,, \tag{A.3}$$

where $\bar{\sigma}$ is the equivalent stress (for instance, von Mises), R_0 is the initial yield stress and m is a material parameter.

A.5.2 Evolution law for variable R

The evolution law of the variable R is a Voce type:

$$\dot{R} = C_R\left(R_{SAT} - R\right)\dot{p}, \tag{A.4}$$

then, the solution is

$$R = R_{sat}\left(1 - e^{-C_R p}\right). \tag{A.5}$$

C_R and R_{SAT} are material parameters and $\dot{p}$ is the equivalent strain rate.

A.5.3 Evolution law for variable X

The back-stress is ruled by the following equation:

$$\dot{\mathbf{X}} = C_X\left[\frac{X_{SAT}}{\bar{\sigma}}(\mathbf{s} - \mathbf{X}) - \mathbf{X}\right]\dot{p}\,, \tag{A.6}$$

where **s** is the deviatoric stress tensor.
The dependence of **X** on the persistent dislocation structures is included in the scalar function $X_{\mathrm{SAT}}(\mathbf{S},\mathbf{N})$:

$$X_{SAT} = X_{SAT0} + (1 - m)\sqrt{q|\mathbf{S}|^2 + (1 - q)S_D^2} \tag{A.7}$$

with

$$S_D = \mathbf{N} : \mathbf{S} : \mathbf{N} \tag{A.8}$$

$\mathbf{N} = \dfrac{\mathbf{d}^p}{\left|\mathbf{d}^P\right|}$ is the current direction of the strain rate tensor.

By introducing the parameter $\sigma_S = S_D/|\mathbf{S}|$, the former equation can be written as:

$$X_{SAT} = X_{SAT0} + (1 - m)|\mathbf{S}|\sqrt{q + (1 - q)\sigma_S^2}\,. \tag{A.9}$$

X_{SAT0}, m and q are material parameters.

A.5.4 Evolution law for variable S and some remarks

This internal variable takes into account the directionality of the dislocation structures. As it was mentioned in Section A.4, specifically for the orthogonal test (strong path-change), dislocation structures associated with the subsequent direction of the strain rate evolve quite differently from the rest of the persistent structures (Teodosiu and Hu, 1995). In order to describe such evolutionary processes, and taking into account the definition of S_D, **S** is decomposed as:

$$\mathbf{S} = S_D \mathbf{N} \quad \mathbf{N} + \mathbf{S}_L \ . \tag{A.10}$$

S_D represents the strength associated with dislocations of the currently active slip systems, whereas $\mathbf{S}_L$ is associated with the latent part of the persistent dislocation structures.

The evolution of S_D follows the equation:

$$\dot{S}_D = C_{SD}\left[g\left(S_{sat} - S_D\right) - hS_D\right]\dot{p} \ . \tag{A.11}$$

This equation almost represents a Voce type (if g=1 and h=0). Functions g*(***P**,**N***)* and h*(***X**,**N***)* are two attenuation coefficients of the evolution of S_D upon stress reversal.
h is non-negligible only during a micro-plastic stage and its equation is:

$$h = \frac{1}{2}\left(1 - \frac{\mathbf{X}:\mathbf{N}}{X_{sat}}\right). \tag{A.12}$$

The presence of h enables us to evaluate the slight loss of S_D as **X:N** approaches its saturation value X_{SAT} (Teodosiu and Hu, 1995).
The function g describes the work-hardening stagnation and the resumption of the work-hardening after a subsequent reverse deformation. Specifically, by denoting P_D=**P:N,** the function is:

$$g = \begin{cases} 1 - \dfrac{C_P}{C_{SD} + C_P}\left|\dfrac{S_D}{S_{SAT}} - P_D\right| & \text{if } P_D \geq 0 \\ \left(1 + P_D\right)^{nP}\left(1 - \dfrac{C_P}{C_{SD} + C_P}\dfrac{S_D}{S_{SAT}}\right) & \text{otherwise.} \end{cases} \tag{A.13}$$

The evolution of **P** is seen in Equation A.16.
To understand the mechanism of this function, let us imagine performing a reversed test with a high amount of pre-strain. The material is first deformed at a constant strain rate direction $\mathbf{N}_1$, then at the end of this deformation the polarity tensor will be practically equal to $\mathbf{N}_1$ (see Equation A.16). At the subsequent reverse deformation $\mathbf{N}$=-$\mathbf{N}_1$, then P_D=-1 and g=0. Clearly, the evolution of S_D is zero. This last condition corresponds to a stagnation of the work-hardening (Teodosiu and Hu, 1995).

The tensor $\mathbf{S}_L$ associated with the latent part of the persistent dislocation structures evolves in the following way:

$$\dot{\mathbf{S}}_L = C_{SL}\left(\frac{Z}{S_{SAT}}\right)^{n_L}\mathbf{S}_L\dot{p} \tag{A.14}$$

where C_{SL} and n_L are material parameters

$$Z = |\mathbf{S}_L| = \sqrt{|\mathbf{S}|^2 - S_D^2}. \tag{A.15}$$

The factor $(Z/S_{SAT})^{nL}$ is introduced in order to explain the influence of the amount of pre-strain. When the pre-strain is very small, $Z<<S_{SAT}$, and the evolution of $\mathbf{S}_L$ is negligible, whereas when the pre-strain is large, Z approaches S_{SAT}, and the evolution of $\mathbf{S}_L$ is accelerated (Teodosiu and Hu, 1995).

A.5.5 Evolution law for variable P

The evolution law for the polarity is:

$$\dot{\mathbf{P}} = C_P(\mathbf{N} - \mathbf{P})\dot{p}, \tag{A.16}$$

where C_P is a material parameter.
Hoferlin, 2001 calls $P_D(\mathbf{N})$ the "Memory function" and establishes that upon a Bauschinger sequence, the stagnation of the flow stress is due to the progressive depolarization of the sheets, which provide mobile dislocations. Then, when the sheet is repolarized, the material has lost the memory of its forward pre-strain.

A.6 Identification strategy

Bouvier and Haddadi, 2001 propose the following strategy:

1. Identification of the set C_{SD}, C_P, C_X, C_R, R_{SAT}, S_{SAT}, X_{SAT0}, n_p by using monotonic tests and Bauschinger tests only.
2. Choosing the best fit for the parameters m, C_X, X_{SAT0}, with part of Bauschinger tests immediately following the stress reversal.
3. Identification of the set C_{SL}, n_L, q using only the orthogonal test.
4. Global identification of C_{SD}, C_P, C_X, C_R, R_{SAT}, S_{SAT}, X_{SAT0}, n_p, m, C_{SL}, n_L, q using experimental tests with limited variation intervals for each material parameter.

A more complete description of the identification procedure is presented in Chapter 5.

A.7 Conclusions

A review of several publications related to the micro-structural-based hardening law proposed by Teodosiu and Hu has been done. The goal of this review was to better understand the experimental phenomena in order to understand the evolution equations roots. The final objective is to establish an identification procedure.

ANNEX B

GRIPS PRESSURE

B.1 Hydraulic wedge grips series 647.10 (MTS, 1997)

The plan of the grip set is shown in Figure B.1a, its geometry in Figure B.1b and a detail view of the installation in Figure B.2. More relevant information pertaining to the grip set is presented in Table B.1 and Table B.2.

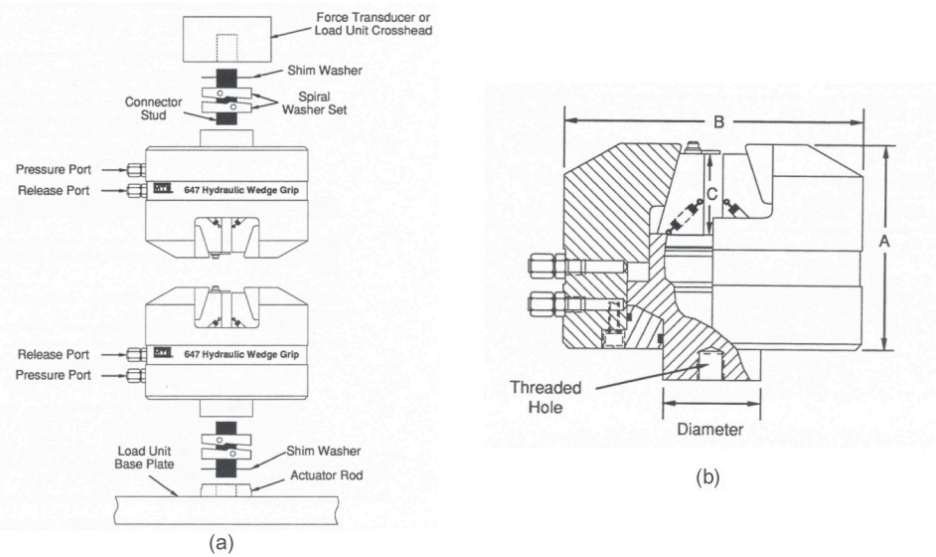

Figure B.1 (a) Typical grip mounting. (b) Grip dimensions.

Model	Monotonic tension capacity rating (kN)	Fatigue capacity rating (kN)	A (mm)	B (mm)	C[1] (mm)	Weight (per grip kg)	Maximum hydraulic preload grip pressure (MPa)
647.10	120	100	159	203	50 Side insert 63 Top insert	30	21

Table B.1 Grip ratings and physical specifications (SI metric).

[1] For side insertion, the length of the specimen which is contained in the wedges must be specified Side Insert "C" length. For top insertion, the length of the specimen which is contained in the wedges must be specified Top Insert "C" length minus at least 3mm, but no more than 6,35mm to prevent specimen slippage and wedge damage.

Model	Threaded Hole Size. SI metric	Diameter (mm)
647.10	M27 x 2 mm x 35,1 mm DP	73,03

Table B.2 Grip mounting specifications.

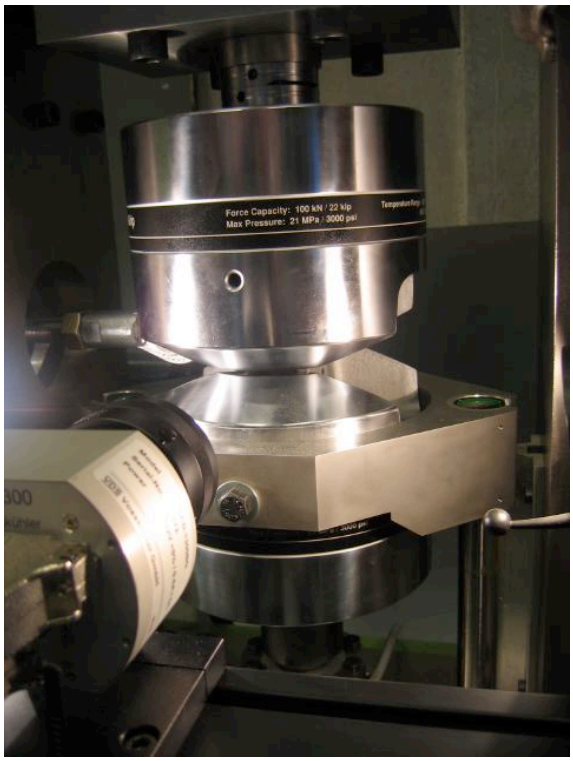

Figure B.2 Detail view of the installed grips.

B.2 Specimen gripping pressure

As grips are originally design for tensile tests, it is important to study the feasibility of using them under different conditions such as shear or combined tests. In this part, the required pressure for these three kinds of tests is determined.

Gripping pressure for tensile test

The user will define the pressure imposed on the grip to prevent slippage during the tensile test. The following procedure determines the minimum grip pressure required for a tensile test. The maximum grip pressure is limited for the grip model used at 21 MPa.

- Determine the maximum axial load to be applied to the specimen during the test. As stipulated before, (Chapter 3) F=50 kN.

- Calculate the minimum grip supply pressure according to the formula (MTS, 1997):

$$P(MPa) = \frac{10{,}4xF(kN)}{A(cm^2)} \tag{B.1}$$

where:

F = Maximum axial load applied to the specimen.
A = Area of the grip piston, in this case A=66,45 cm^2 (value taken from MTS, 1997).
P = Grip supply pressure.

$$P = \frac{10{,}4x50}{66{,}45} = 7{,}83MPa \ . \tag{B.2}$$

In conclusion, according to the value chosen for a tensile force F of 50 kN, the imposed pressure must be greater than 7,83 MPa and smaller than 21 MPa to prevent grip damage.

Gripping pressure for shear test (without pre-tension)

To identify the forces preventing slipping in a shear test, all the applied forces have to be determined as a function of the applied pressure P.
The actual clamping force (F_c) applied to the specimen is calculated by using Equation B.3, taken from the force equilibrium of Figure B.3 (where F_N is the normal force applied by the grip on the wedge and f_r is the friction force between the grip and wedge) and considering θ = 15° and the friction coefficient as μ = 0,06.

$$F_c = \frac{PA}{2}\left[\frac{\cos\theta - \mu\sin\theta}{\sin\theta + \mu\cos\theta}\right]. \tag{B.3}$$

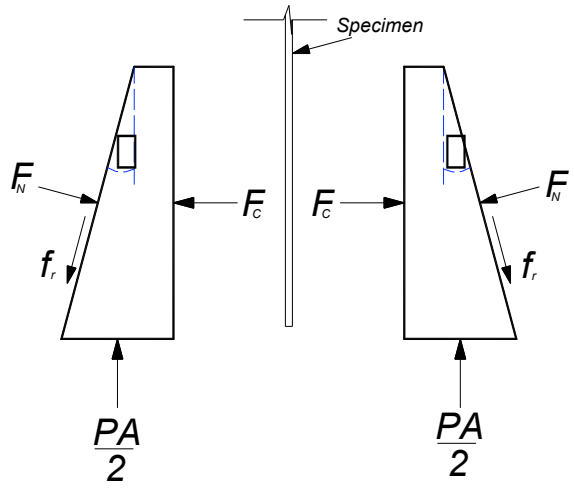

Figure B.3 Forces acting on the wedges.

Using the same diagram the following forces can be calculated:

$$F_N = \frac{PA}{2}\left[\frac{1}{\sin\theta + \mu\cos\theta}\right], \tag{B.4}$$

and

$$f_r = \frac{PA}{2}\left[\frac{\mu}{\sin\theta + \mu\cos\theta}\right]. \tag{B.5}$$

The following equation must be satisfied in order to determine the minimum pressure to be applied for carrying out only the shear test without previous tension:

$$\frac{F_S}{2} \leq f_r \ , \tag{B.6}$$

where F_s is the horizontal applied load producing shear. The coefficient 2 takes into account both wedges (left and right) and f_r is assumed to be the same in every direction.
As F_s=50 kN is the current maximum value of the horizontal loading cell, the applied pressure should be:

$$P = \frac{F_S}{\alpha A}\left(\sin\alpha + \mu\cos\alpha\right) = 39{,}7MPa \ , \tag{B.7}$$

which exceeds the designed pressure limit.
Hence, the maximum force is computed from the recommended limiting pressure (P=21MPa)

$$F_S = PA\left[\frac{\mu}{\sin\alpha + \mu\cos\alpha}\right] = 26{,}4kN \ . \tag{B.8}$$

Gripping pressure for combined test

The simple shear test implies the presence of a tensile force. The tension force F is then included in equations used in the computation of gripping pressure for a tensile test, that is:

$$F_c = \frac{PA + F}{2}\left[\frac{\cos\alpha - \mu\sin\alpha}{\sin\alpha + \mu\cos\alpha}\right], \tag{B.9}$$

$$F_N = \frac{PA + F}{2}\left[\frac{1}{\sin\alpha + \mu\cos\alpha}\right], \tag{B.10}$$

$$f_r = \frac{PA + F}{2}\left[\frac{\mu}{\sin\alpha + \mu\cos\alpha}\right]. \tag{B.11}$$

As friction force f_r (Equation B.11) increases due to the effect of the tensile force F, the applied shear force F_s (Equation B.6) can be greater than the one computed in Equation B.8.
Figure B.4 shows the allowed shear force F_s as a function of the tensile force F (Equation B.12) for the grip supply pressure P = 15 MPa and the maximum grip supply pressure P = 21 MPa.

$$F_S = \left(PA + F\right)\left[\frac{\mu}{\sin\alpha + \mu\cos\alpha}\right]. \tag{B.12}$$

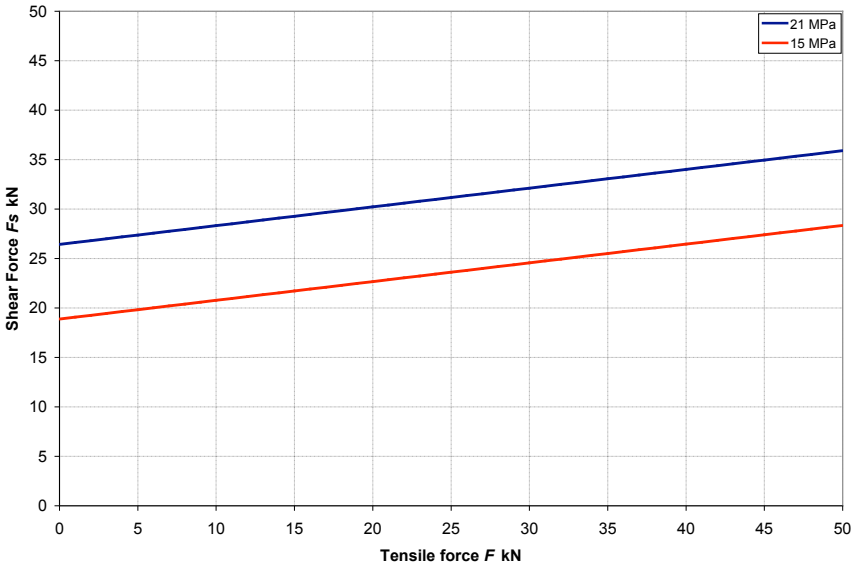

Figure B.4 Tension force – shear force.

ANNEX C

BI-AXIAL SPECIMEN GEOMETRY

The very first results obtained with the bi-axial machine clearly showed that sliding between the specimen and the grips occurs for a simple shear test. The following factors were studied in order to identify the problem: grip teeth rectification, grip teeth distribution and specimen geometry. This last was identified as the main source of sliding.
By reducing the clamping zone of the specimen, the pressure on it increases.
The first idea is to transform the geometry of Figure C.1a (the same shape as Figure 3.21) into a simpler one as shown in Figure C.1b. The measurable zone remains the same and the necking is eliminated.
In fact, necking has no influence on the simple shear test as the grips are localized in the neck (as in Figure C.2b).
During the plane strain test, the neck has a strain concentrator function in order to identify in advance the fracture zone. The plane strain test required to characterize the metal sheet does not attain a high strain level, so the neck can be neglected.

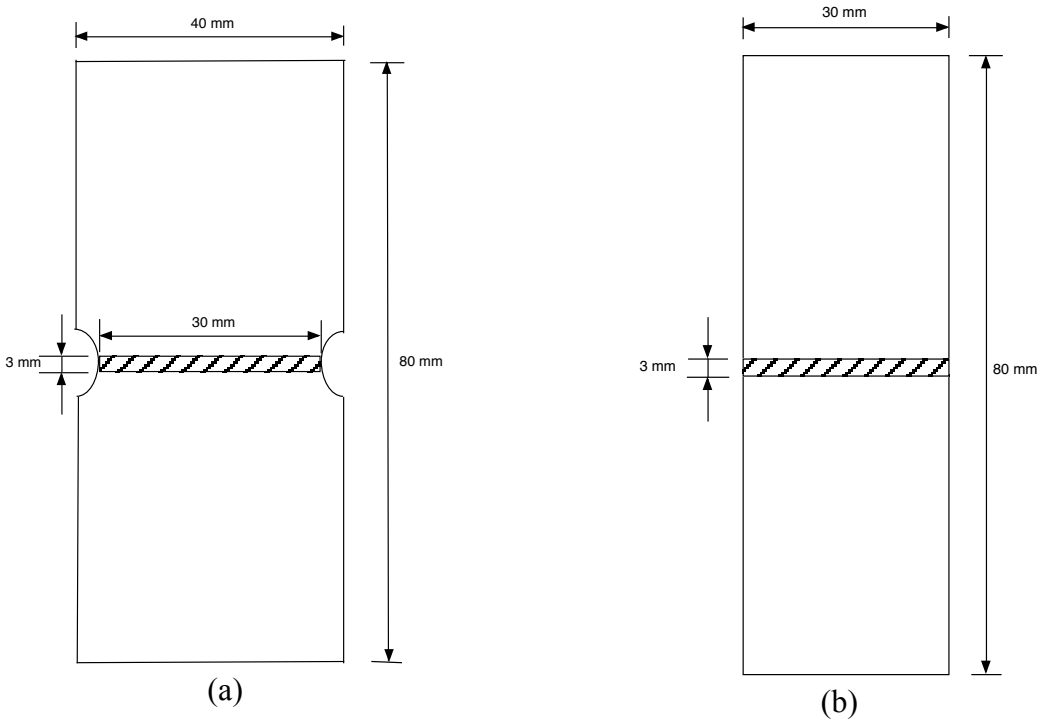

Figure C.1 Geometry of the bi-axial specimen.

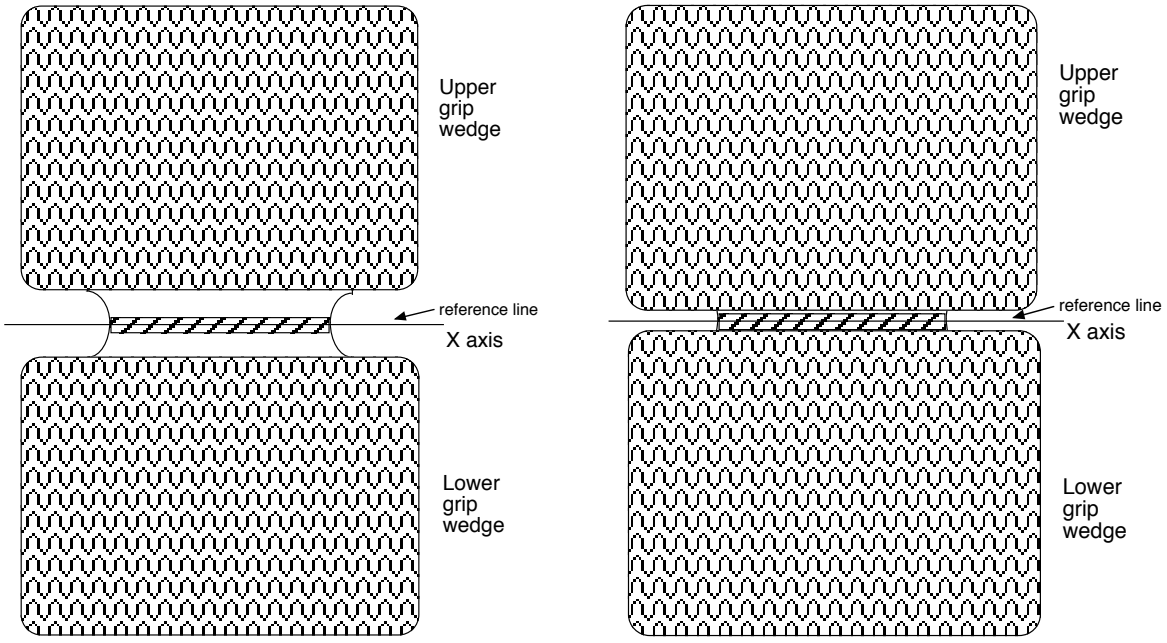

(a) (b)

Figure C.2 Clamping. a) Taking necking into account (for plane strain test). b) Neglecting necking (for simple shear test).

Figure C.3 gives the results of two tests, the first using Figure C.1a geometry (old geometry) and the second using Figure C.1b geometry (new geometry). Both are clamped as shown in Figure C.2b. Figure C.3 shows the shear deformation measured for a given horizontal displacement. These strains are measured by GOM system. It can be seen that with the new geometry, a higher strain can be obtained for the same imposed displacement. It can also be remarked that the mechanical adjustment is less than 0,5 mm.

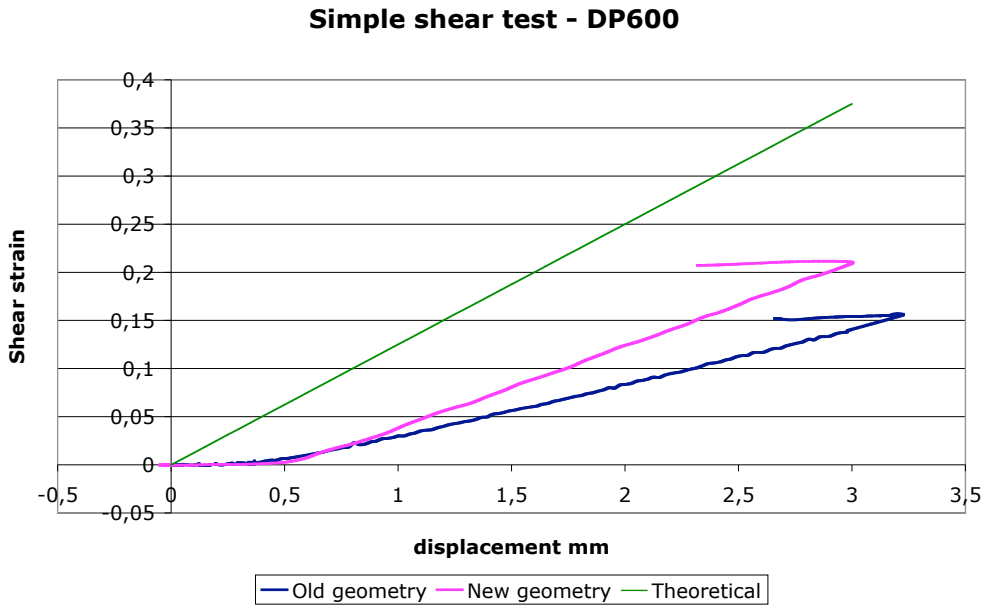

Figure C.3 Shear strain with respect to imposed displacement.

ANNEX D

ARAMIS® PARTICULAR CASE

This section focuses on the use of the Aramis® system for this particular case of deformation field measurements in the bi-axial machine, i.e., a 30mm x 3mm measurable zone. For more general details, see Gom, 2001.

D.1 Specimen preparation

The Aramis system computes the deformation gradient by comparing two images (two stages). The software must be able to recognize the material points of the first image in the second image.
Two factors are fundamental for success:

1. A contrasted pattern.
2. The choice of a proper facet size and facet step (Figure D.1).

To obtain contrasted irregular patterns the measurable area of the specimen can be painted in white with small black dots (Figure D.2a). Those small black dots must be well distributed all along the surface, otherwise a lighting problem may appear. First, it is recommended to use bright white, then matte black spray paint.
Once the images are taken, a measurable zone is selected and subdivided into facets (Figure D.2b). The facet size is the size of a facet in pixels and the facet step is the distance between the centers of two neighboring facets. Figure D.2b shows the size of a facet in green (9 pixels for this case) and yellow crosses mark the center of the facets. In this case, the facet step is the same as the facet size. Figure D.2c displays the deformed grid and Figure D.3 gives a detailed extract.
To compute displacements and strains accurately throughout the selected zone, a contrast must exist inside each facet, otherwise the facet at the final stage will not be recognized and, therefore not calculated. Figure D.4 shows two stages, where blue crosses in the final stage indicate that the facets were not calculated.
In conclusion, the facet size must be chosen as function of the pattern and the size of the measurable zone. For this particular case, sizes of 7 or 9 pixels are recommended but the pattern must be executed carefully. Higher facets may be used, but in that case, it is recommended to reduce the facet step.

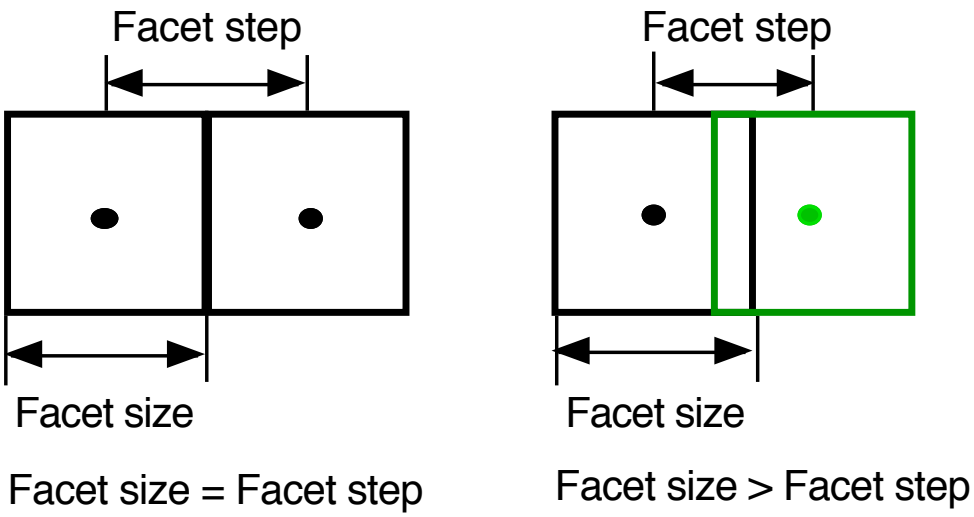

Figure D.1 Diagram of facet step and facet size definition.

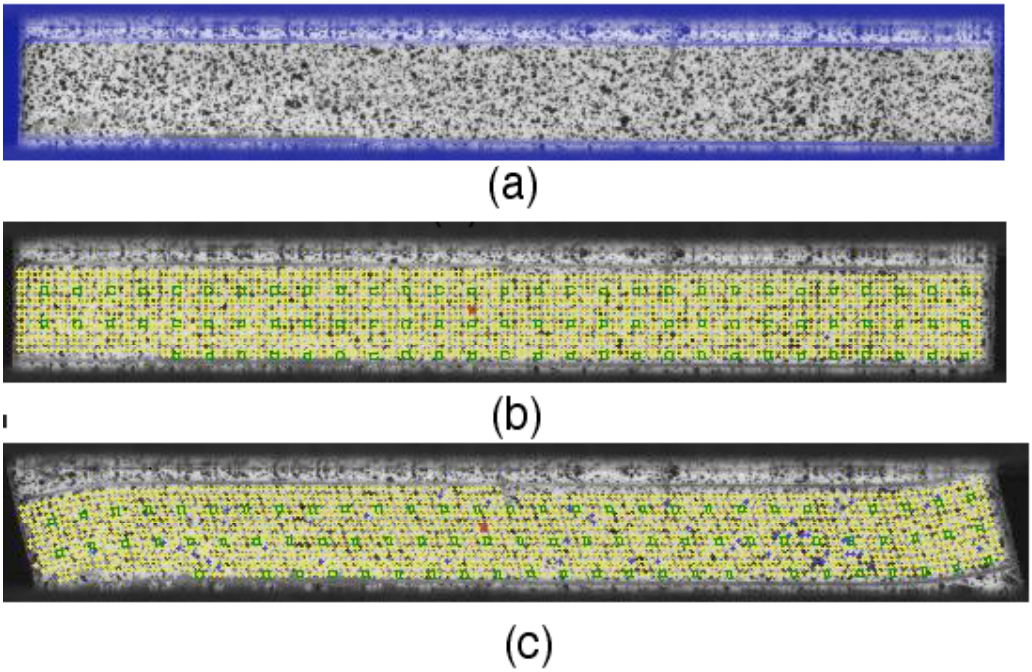

Figure D.2 a) Contrasted pattern. b) Grid selection. c) Deformed grid.

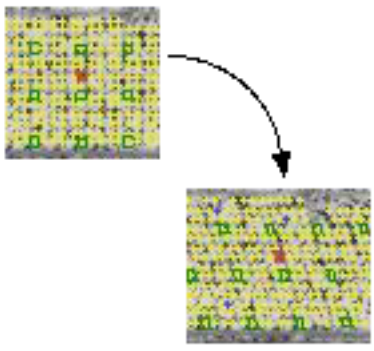

Figure D.3 Facet evolution.

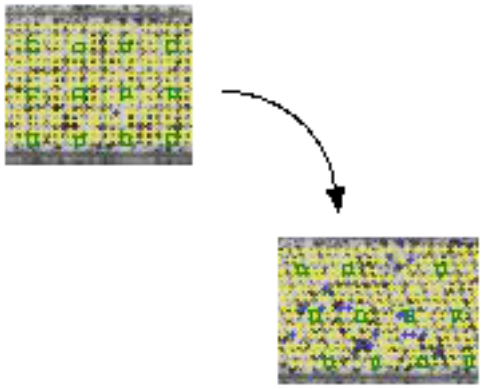

Figure D.4 Not calculated facets.

D.2 Lighting

Lighting is very important when taking pictures. It should be uniform all along the measurable zone and it is not recommended to spot the specimen directly.
After several trials and errors, it was found that the best solution was to place two lamps (12V, 20W) one in front of the other as shown in Figure D.5.

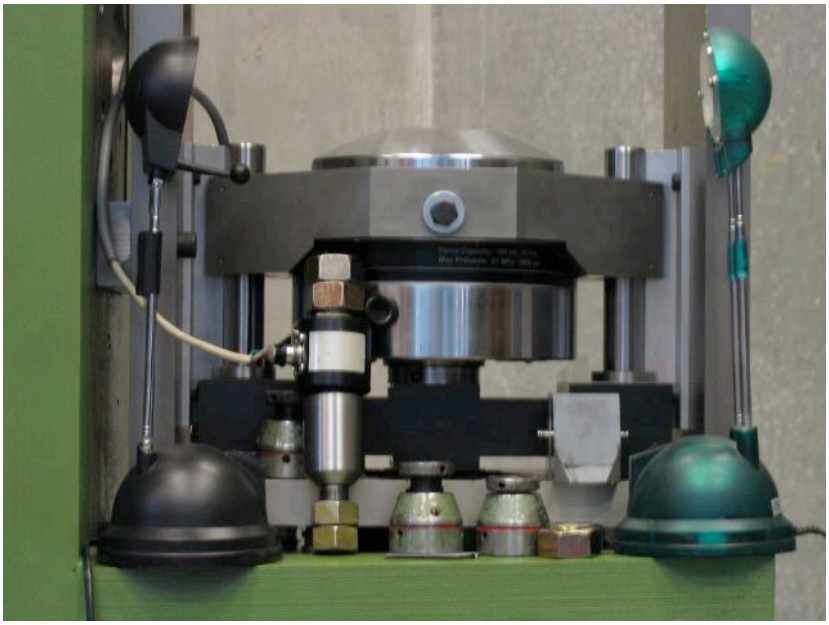

Figure D.5 Lamp locations.

D.3 Sensor parameters

The system includes an external controller for the image data acquisition. Input and output are available as separate BNC-connectors.
The signals of force and displacement coming from the pistons are set as input. However, as there are only two sources of input, either the force and displacement data acquisition can be done for one piston at a time, or the force (or displacement) for each piston may be taken separately.
These signals can be used as a trigger to record an image.

Sensor parameters are set as follows:

	A – IN 0	A – IN 1
Min	-50000	-10
Max	50000	10
Unit	N	mm

Table D.1 Sensor parameters.

D.4 Creating a new project in Aramis system

Two types of projects can be created: 2D or 3D. For the purposes of this work, only 2D is necessary. 3D projects were used for the first tests in order to verify grip alignment. Then, only 2D analyses are necessary since there are only planar deformations.
A new project is created using the function *File → New*. Once the function has been named, Aramis® creates a new directory that contains the project file (*.dap), subdirectories for the recorded images and the computed sub-projects of the individual steps. The parameters for the facet (*size* and *step*) and solution (*solve method*, *solve model*, *interpolation*, *accuracy* and *residuum*) must also be provided.
The facet parameters were already discussed in Section D.1. The solve method chosen to define a first approach is *single facet* for a matter of speed (the *multi facet* method will be discussed later in Section D.8), solve method is *total*, the *accuracy* is expressed in pixels (recommended 0,015 to 0,05), the *maximal residuum* is set to 15 and *interpolation* is used.
To determine the *maximal accuracy* parameter, it is important to know the resolution of the images. The CCD cameras take 1280x1024 pixels pictures. The picture area is approximately 35mm x 30mm, which implies that a single pixel is 0,027 mm, so a final accuracy of 0,015 pixels means 0,405 μm and 0,05 pixels equals 1,35 μm. The accuracy is chosen depending on the image's quality.

D.5 Making a measurement

In the menu bar of the Aramis® software the function *measurement* is found. This function is subdivided into:

- *Edit project.*
- *Add images.*
- *Project parameters.*
- *Start points.*
- *Solve project.*
- *Strain.*

Each of these functions must be followed in order.

Edit project

This command opens a window that gives all the information about the project. For example, it gives the option of changing the parameters set at the beginning or for eliminating unnecessary images.

Add images

This menu proposes four choices for image acquisition, namely: *load images*, *simple measurement*, *standard measurements* and *fast measurement*, of these, the most used choices are the *simple measurement* and the *standard measurement*.
The *simple measurement* opens a video window. The upper part of the image-recording dialog is used to control the video window. Each time the button *Snap image* is pressed, an image is recorded and a new project step is created in the measurement project.
The *standard measurement* menu is well explained in Gom, 2001. Briefly speaking, this function allows one to record images by using the input signals as a trigger.
A few recommendations can be established:

- Two or more images have to be recorded before starting the loading. This procedure can help to identify the error due to noise, lighting or other perturbations.
- If the elastic part is not negligible, it is better to control the image acquisition by using the force input signal. The plastic part is better controlled by the displacement signal.
- The image acquisition method can be switched at any time during the test.

Project parameter

Here, the *facet size*, the *facet step* and the *solve method* can be redefined. A mask containing the points to be computed is selected over the first image. Figure D.2a gives an example.

Start point

A start point must be chosen in the first picture before solving the problem. This point can be located at any place within the measurable zone. The point is then recognized by the application in the following pictures with the accuracy given at the beginning.

Solve project

After all preceding points have been developed, the project can be solved. A window is open giving information about the calculated or non-calculated facets.

Strain

The menu contains several options, but here we are only concerned with the option *Calculate strain (DAP)*.

Scale project

This point can be done before computing strains (former point). The *scale project* function is found in *Operations* → *Transformation* → *2d* → *Scale project*. It is convenient to draw a reference line in the specimen in order to scale the project using an accurate known value.

D.6 Manipulating data

There exist many functions to process the results, most of which can be found in the *Strain* menu.
For the purpose of the tests described here, the most useful points are:

- *Strain* → *Show* → *3d view* displays the displacement or strain field throughout the measurable zone.
- *Strain* → *Define section* → … visualizes the results in a specific section over one or several stages.
- *Strain* → *Multi stage analysis* provides one variable as a function of another for a single point of the computed zone. Some of the variables that can be treated are: AD0 and AD1 (input signals), Time, Strain X, Strain Y, Major and Minor strains, Shear strain, Displacement X, Y and Z, Mises strain, etc.
- *Strain* → *Statistic data* gives the statistical data of a computed step concerning a selected section.

The recommended strain computation for tensile and plane strain tests is the logarithmic strain (Equation 3.47), and for simple shear tests the Green-Lagrange strain (Equation 3.48).

D.7 Exporting data

Every computed item of data can be exported from Aramis® into data format using the function *File* → *Export*. Different formats can be chosen, although they are not flexible. The option *User Defined (all points)* or *(single point)* allows the user to choose the variables to be exported (a list of all the exportation variables can be found in pages 64-66 of Gom, 2001).
The export filters are defined by a **.expcfg* file. This file must be saved in the home directory *demo* in *.tom-cfg/config* .

- *User Defined (single point)*: the data of every stage of a single point is exported. This function is very useful when the characteristics (or values) of the points represent the entire computed zone. This is the case for the input values (AD0 and AD1) and the strain field for plastic deformation (this specimen geometry exhibits a homogeneous strain field).
- *User Defined (all points)*: this function is recommended when the values of the computed zone are non-homogenous, for instance, for the strain field during the first deformation stages. In this case, it is better to export the entire data field (for the visualized stage or for each one) and then to compute the average field value using another program. The average value of a data field cannot be exported.

D.8 Improving accuracy

If even higher accuracy is deemed necessary, the project can be solved using the *Multi facet* solving model. However, this model requires more computation time.

D.9 Optical system validation

D.9.1 Displacement computation

A displacement of 5mm is imposed on the horizontal piston of the bi-axial machine. An analog comparator is placed on the upper grip. The Aramis® system computes this displacement by comparing pictures taken at the initial and final stages of the specimen clamped at the upper grip (Figure D.6). Finally, the computed value is compared to the measured one by the analog comparator (Table D.2). No deformation is imposed on the material.

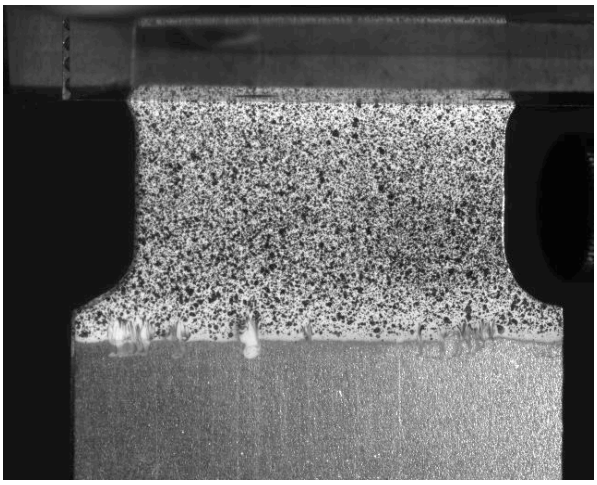

Figure D.6 Specimen clamped with the bi-axial machine.

Imposed displacement	Aramis	Analog
5,00 mm	4,94 mm	4,91 mm

Table D.2 Displacement measured using different apparatuses.

D.9.2 Moderately large strains computation

The performance of the Aramis® system in computing strain is tested in a tensile test. The computed logarithmic strain average of the measured zone is compared to those obtained by an analog extensometer (Figure D.7). The measure base, i.e., the initial distance between the upper and lower clip of the analog extensometer, is 50 mm.
Figure D.8 shows a flow stress curve obtained using both extensometers. Engineering stress is obtained from the load cell signal value divided by the initial specimen cross section.

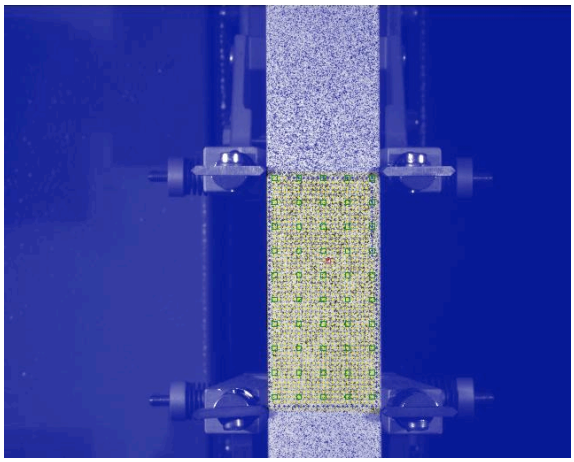

Figure D.7 Analog extensometer and Aramis® measured zone.

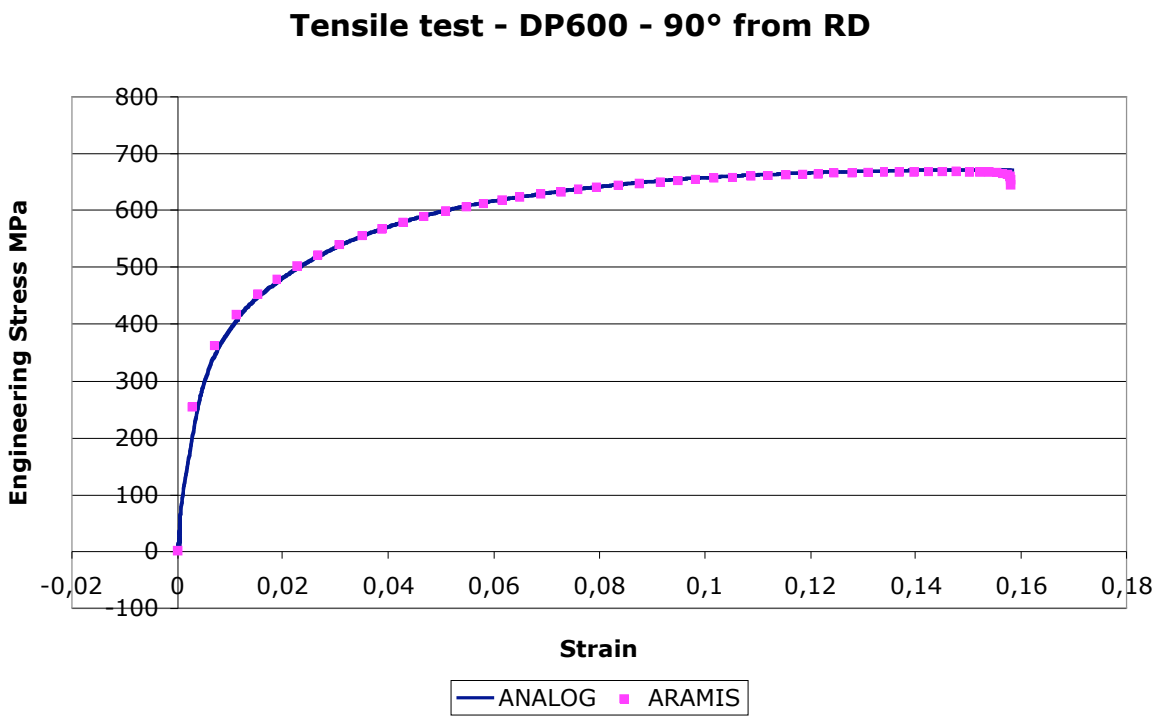

Figure D.8 Tensile test on a DP600 steel. Strains measured using an analog extensometer and Aramis® system.

D.9.3 Small strain computation

The average computed strains in the measured zone are compared with those obtained using strain gauges (Figure D.9). From Figure D.10 it is evident that there is a gap between the two curves, but their shapes remain very similar.

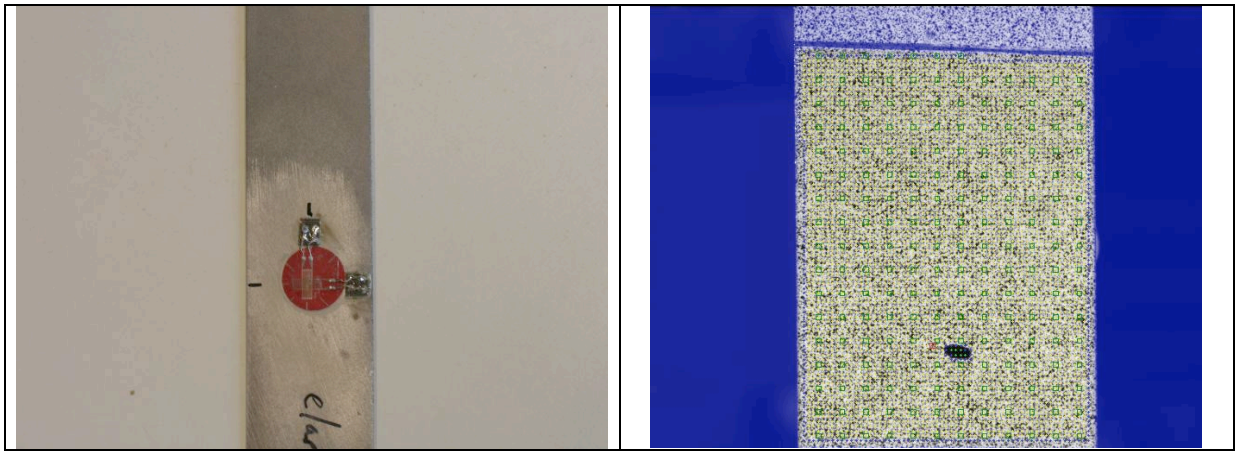

Figure D.9 Strain gauges and Aramis® measured zone.

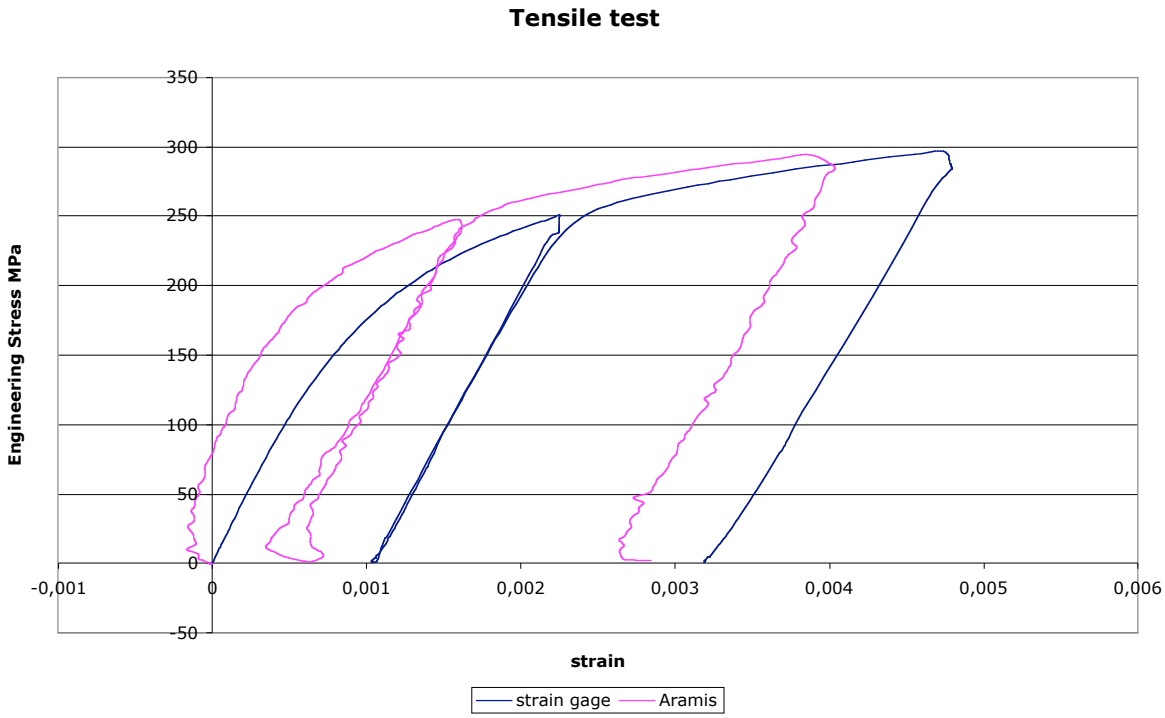

Figure D.10 Tensile test on a DP600 steel. Strains measured using a strain gauge and Aramis® system.

For our purposes, the origin of such a difference won't be studied in depth since the goal of the present work is not to study elastic parts.

BIBLIOGRAPHY

Arcan M., Hashin Z, Voloshin A., 1978. *A Method to Produce Uniform Plane–Stress States with Applications to Fiber–Reinforced Materials*. Experimental Mechanics 18, pp. 141 – 146.

Bacroix, B., Genevois, P., Teodosiu, C., 1994. *Plastic Anisotropy in Low Carbon Steels Subjected to Simple Shear with Strain Path Changes*. Eur. J. Mech., A/Solids, 13, n°5, pp. 661-675.

Banabic, D., Bunge, H.-J., Pöhlandt, K., Tekkaya, A. E., 2000. Formability of Metallic Materials. Springer (Ed.).

Barlat, F., Lege, D., Brem, J., 1991. *A Six-Component Yield Function for Anisotropic Materials*. International Journal of Plasticity (7) pp. 693 – 712.

Bockler, J.P., El Aoufi, L., Raclin, S., 1987. *On Experimental TestingMmethod for Anisotropy Materials*. Res. Mechanica (21) pp. 73 – 95.

Bouvier, S., Haddadi, H., 2001. *Modelling the Behaviour of a Bake-Hardening Steel Using a Dislocation Structure Based Model*. The 4th International ESAFORM Conference on Material Forming. University of Liege, Belgium, pp. 429-432.

Bouvier, S., Teodosiu, C., Haddadi, H., Tabacaru, V., 2002. *Anisotropic Behaviour of Structural Steel and Aluminium Alloys at Large Strains*. Proc. of the Sixth European Mechanics of Materials Conference on Non-linear Mechanics of Anisotropic Materials. University of Liege, Belgium, pp. 215 – 222.

Bouvier S., Alves, J. L., Oliveira, M. C., Menezes, L. F., 2005. *Modelling of Anisotropy Work-hardening Behaviour of Metallic Materials Subjected to Strain-path Changes*. Computational Materials Sciences (32) pp. 301 – 315.

Bouvier, S., Gardey, B., Haddadi, H., Teodosiu, C. 2005. *Characterization of the Strain-Induced Anisotropy of Rolled Sheets by using Sequences of Simple Shear and Uniaxial Tensile Tests*. Journal of Materials Processing Technology. To be published.

Bouvier, S., Haddadi, H., Levée, P., Teodosiu, C., 2005. *Simple Shear Test: Experimental Techniques and Characterizations of the Plastic Anisotropy of Rolled Sheets at Large Strains*. Journal of Material Processing Technology. To be published.

Brasseur, E. Hoferlin, E., Moriau, O., 2001. *Springback Analysis in Sheet Metal Forming with an Anisotropic Micro-macro Hardening Model*. Simulation of Materials Processing: Theory, Methods and Applications, Mori (Ed.) © Swets & Zeitlinger, Lisse, ISBN 90 2651 822 6.

Casotto S., Pascon F., Bruschi S., Habraken, A.M., 2005. *Thermo-mechanical-metallurgical Model to Predict Geometrical Distortions of Rings During Cooling Phase After Ring Rolling Operations*. International Journal of Machine Tools and Manufacture (45) pp. 657 – 664.

Castagne, S., Habraken, A. M., Cescotto, S., 2002. *Application of a Damage Model to an Aluminum Alloy*. International Journal of Damage Mechanics (1) n°4, pp. 367 – 392.

Catalogue LIF, 1996. Guidages Linéaires: Systèmes à Recirculation de Billes et Rouleaux, Systèmes de Guidages à Galets, Arbres et Douilles à Billes. INA Techniques Linéares. 93, route de Bischwiller BP 16, 67501 Haguenau Cedex.

Cescotto, S., Grober, H., 1985. *Calibration and Application of an Elastic-Visco-Plastic Constitutive Equation for Steels in Hot-Rolling Conditions*. Eng. Comp. (2) pp. 101 – 106.

Cescotto S., Charlier R., 1993 *Frictional Contact Finite Element Based on Mixed Variational Principles*. Int. Journal. of Numerical Methods in Engineering. (36) pp. 1681 – 1701.

Cescotto S. and Habraken A. M., 1996. *Contact between Deformable Solids the Fully Coupled Approach*. Special Issue of Journal of Mathematical and Computer Modelling.

Col, A., 2000. Characterization of SOLLAC Steels for 3 DS. Usinor. Internal Report.

Cozacu, O., Plunkett, B.,Barlat, F., 2005. *Orthotropic Yield Criterion for Mg Alloy Sheets*. The 5th ESAFORM Conference on Material Forming. Dorel Banabic (Ed.) Romania. Vol 1, pp. 379 – 382.

De Montleau, P., 2004. *Programation of the Teodoisu's Hardening Law*. Internal report, M&S Department, University of Liege.

Doghri, I., 2000. Mechanics of Deformable Solids, Linear and Nonlinear, Analytical and Computational Aspects. Springer (Ed.).

Doyoyo, M., Mohr, D., 2003. *Microstructural Response of Aluminium Honeycomb to Combined Out-of-plane Loading*. Mechanics of Materials 35 (2003) pp. 865 – 876.

Doyoyo, M., Wierzbicki, T., 2003. *Experimental Studies on the Yield Behaviour of Ductile and Brittle Aluminium Foams*. International Journal of Plasticity (19) pp. 1195 – 1214.

Duchêne, L., Godinas, A., Cescotto, S., Habraken, A.M., 2002. Texture evolution during deep-drawing processes. Journal of Materials Processing Technology, (125-126) pp. 110 – 118.

Duchêne, L., Habraken, A.M., 2005. *Analysis of the Sensitivity of FEM Predictions to Numerical Parameters in Deep Drawing Simulations*. European Journal of Mechanics - A/Solids.

Duchêne, L., de Montleau, P., El Houdaigui, F., Bouvier, S., Habraken, A.M., 2005. *Analysis of Texture Evolution and Hardening Behavior during Deep Drawing with an Improved Mixed Type FEM Element*. Proc. of 6th Int. Conf. and Workshop on Numerical Simulation of 3D Sheet Metal Forming Processes NUMISHEET 2005. Detroit, MI, U.S.A. Part A, pp. 409 – 414.

Dyduch M., Habraken A.M., Cescotto, S., 1992. *Automatic Adaptive Remeshing for Numerical Simulations of Metalforming*. Journal of Comp. Meth. in Appl. Mechanics and Engineering (101) pp. 283-298.

Flores, P., 2003. Experimental and Theoretical Development of Tensile – Shear Test on Metal Sheets. DEA presented at University of Liege.

Flores, P., Duchêne, L. Lelotte, T., Bouffioux, C., El Houdaigui, F., Van Beal, A., He, S., Duflou, J., Habraken, A.M. 2005. *Model Identification and FE Simulations: Effect of Different Yield Loci and Hardening Laws in Sheet Forming*. Proc. of 6th Int. Conf. and Workshop on Numerical Simulation of 3D Sheet Metal Forming Processes NUMISHEET 2005. Detroit, MI, U.S.A. Part A, pp. 371 – 381.

Genevois, P., 1992. Etude Experimentale et Modelisation du Comportement Plastique Anisotrope de Toles d'Acier en Grandes Transformations. Ph. D. Thesis, Institut National Polytechnique de Grenoble.

GOM, 2001. ARAMIS, Deformation Measurement using the Grating Method. GOM mbh, Braunschweig.

G'Sell C., Boni S., Shrivastave S., 1983. *Application of the Plane Simple Shear Test for Determination of the Plastic Behavior of Solid Polymers at Large Strains*. Journal of Material Science 18, pp. 903-918.

Habraken, A.M., Bourdouxhe, M., 1992. Coupled *Thermo-Mechanical-Metallurgical Analysis during the Cooling of Steel Pieces*. European Journal of Mechanics, A/Solids (11), n° 3, pp. 381 – 402.

Habraken, A.M., Charles J.F, Wegria J., Cescotto S., 1998. *Dynamic Recrystallization during Zinc Rolling*. International Journal of Forming Processes (1).

Habraken A. M. and Cescotto S., 1998. *Contact between deformable solids, the fully coupled approach*. Mathematical and Computer Modelling (28) n° 4 – 8, 153 – 169.

Habraken, A.M., 2001. Contributions to Constitutive Laws of Metals: Micro – macro and Damage Models. Aggregation in Higher Education Thesis. University of Liege.

Habraken, A.M., Duchêne, L., 2004. *Anisotropic Elasto-plastic Finite Element Analysis Using aSstress-strain Interpolation Method Based on a Polycrystalline Model*. International Journal of Plasticity (20) Issue 8-9, pp. 1525-1560.

Hill, R., 1950. The Mathematical Theory of Plasticity. The Oxford Engineering Sciences Series.

Hoferlin, E., 2001. Incorporation of an Accurate Model of Texture and Strain-path Induced Anisotropy in Simulations of Sheet Metal Forming. Ph. D. Thesis, Katholieke Universiteit Leuven.

Holzapfel, G., 2000. Nonlinear Solid Mechanics. A Continuum Approach for Engineering. John Wiley & Sons (Ed.).

Hora, P., Feurer, U., Wahlen, A., Reissner, J., 2000. *Methods for Handling of FEM Input and Output Data with the Goal of Higher Computational Reliability.* ECCOMAS 2000, Barcelona, Spain.

Hosford, W. F., 1998. *Reflections on the Dependence of Plastic Anisotropy on Texture*. Mater. Sci. Eng. A257, pp. 1 – 8.

Hosford, W.F. and Caddell, R., 1993. Metal Forming: Mechanics and Metallurgy. Prentice Hall (Ed.).

Hu, Z., 1992. Lois de Comportement des Métaux en Grandes Transformations tenant Compte de l'Evolution de la Microstructure. Doctoral Thesis. Institut National Polytechnique de Grenoble.

Hu, Z., 1994. *Work-hardening behavior of mild steel under cyclic deformation at finite strains*. Acta metal. mater. (42) N°10, pp. 3481 – 3491.

Hughes, TJR., 1983. *Theoretical Foundation for Large-scale Computations of Nonlinear Material Behavior*. Evanston, Illinois, Eds. Nemat-Nasser S., Asaro RJ., Hegemier GA., Martinus Nijhoff Publisher, Dordrecht, pp. 26 – 93.

Jetteur, P., Cescotto, S., 1991. *A Mixed Finite Element for the Analysis of Large Inelastic Strains*. International Journal of Numerical Methods in Engineering (31) pp. 229 – 239.

Khan, A., Huang, S., 1995. Continuum Theory of Plasticity. John Wiley & Sons (Ed.).

Knockaert, R., 2001. Numerical and Experimental Study of the Strain Localization During Sheet Forming Operations. Ph. D. Thesis, Ecole National Supérieure des Mines de Paris.

Kuwabara T., Ikeda S., Kuroda K., 1998. *Measurement and Analysis of Differential Work Hardening in Cold-rolled Steel Sheet under Bi-axial Tension*. Journal of Material Processing Technology 80 – 81, pp. 517 – 523.

Kuwabara, T., Van Beal, A., Iizuka, E., 2002. *Measurement and Analysis of Yiled Locus and Work-hardening Characteristics of Steel Sheets with Different r-values*. Acta Materialia (50) pp. 3717 – 3729.

Lelotte, T., Gerday, A.F., Flores, P. , Bouvier, S., Van Houtte, P., Habraken, A.M., 2005. *Axes Rotation during Simple Shear Test: Measurement and Predictions*. VIII Int. Conf. on Comp. Plasticity (COMPLAS VIII). Barcelona, Spain, pp. 1027 – 1030.

Li, K.P., Cescotto, S., 1997a. *A 8-Node Brick Element with Mixed Formulation forLarge Deformation Analyses*. Comp. Meth. in Appl. Mech. and Eng. (141) 157 – 204.

Li, K.P., Habraken, A.M., Bruneel, H., 1995. *Simulation of Square Cup Deep Drawing with Different Finite Elements*. Journal of Materials Processing Technology (50) n° 1-4, pp. 81 – 91.

Li, S., Hoferlin, E., Van Beale, A., Van Houtte, P., 2001. *Application of a Texture-based Plastic Potential in Earing Prediction of an IF Steel*. Advanced Engineering Materials (3) n° 12, pp. 990 – 994.

Li, S., Hoferlin, E., Van Beal, A., Van Houtte, P., Teodosiu, C., 2003. *Finite Element Modelling of Plastic Anisotropy Induced by Texture and Strain-path Change*. International Journal of Plasticity (19) pp. 647-674.

Li, X.K., Cescotto, S., 1996. *Finite Element Method for Gradient Plasticity at Large Strains*. International Journal of Numerical Methods in Engineering (39) pp. 619 – 633.

Li, X.K., Cescotto, S., 1997b. *A Mixed Element Method in Gradient Plasticity for Pressure Dependent Materials and Modelling of Strain Localization*. Comput. Methods Appl. Mech. Eng. (144) 287 – 305.

Mahgoub, E., Deng, X., Sutton, M., 2003. *Three-dimensional Stress and Deformation Fields around Flat and Slant Cracks under Remote Mode I loading Conditions*. Engineering Fracture Mechanics. To be published.

Mathonet, V. and Habraken, A. M., 2003. Manuel d'Utilisation du Programme d'Identification Paramètrique Optim. Projet Région Wallone: Caractérisation Rationnelle des propiétés à Chaud des Matériaux Métalliques.

Mistou, S., Karama, M., Desmars, B., Peres, P., 2003. *Caractérisation par Stéréocorrélation d'Images des Déformation d'une Liaison Collée Elastomèrique en Cisaillement*. Journée Scientifique AFM, Progrès Récents des Méthodes Optiques dans des Conditions Extrêmes – Grandes Déformations, Forte Localisation – en Mécanique Expérimentale.

Miyauchi, K., 1984. *A Proposal of a Planar Simple Shear Test in Sheet Metals*. Sci. Papers of I. P. C. R., vol. 78, p. 27.

Moreira, L. P., Ferron, G., Ferran, G., 2000. *Experimental and Numerical Analysis of the Cup Drawing Test for Orthotropic Metal Sheets*. Journal of Materials Processing Technology (109) pp. 78 – 86.

MTS, 1997. MTS Job N° 57.008-75. MTS Systems GmbH. Technical Documentations.

Munhoven S., Habraken, A.M., 1995. Application of an Anisotropic Yield Locus based on Texture to a Deep Drawing Simulation. Simulation of Materials Processing: Theory, Methods and Applications, Numiform '95, Shen SE, Dawson PR (Ed.), Balkema Rotterdam.

Orteu, J.-J., 2003. *3-D Computer Vision in Experimental Mechanics*. Belgian-French Workshop on Optical Methods. Introduction to Full Field Optical Measurement Techniques Application to Experimental Mechanics. K. U. Leuven-Belgium.

Pascon, F., Habraken, A.M., Bourdouxhe, M., Labory, F., 2000. *Modélisation des phénomènes thermomécaniques dans une lingotière de coulée continue*. Mec. Ind. (2000), (1) pp. 61 – 70.

Peeters, B., Seefeldt, M., Teodosiu, C., Kalidindi, S. R., Van Houtte, P., Aernoudt, E., 2001a. *Work-hardening/softening Behaviour of BCC Polycrystals during changing Strain Path: I. An Integrated Model based on Substructure and Texture Evolution, and its Prediction of the Stress-strain Behaviour of an Steel during Two-stage StrainPpath*. Acta mater. (49) pp. 1607 – 1619.

Peeters, B., Hoferlin, E., Van Houte, P., Aernoudt E., 2001b. *Assessment of Crystal Plasticity based Calculation of the Lattice Spin of Polycrystalline metals for FR implementation*. International Journal of Plasticity (17) pp. 819 – 836.

Petras, A., Sutcliffe, M. P. F., 2000, *Indentation Failure Analysis of Sandwich Beams*. Composite Structures (50) pp. 311 – 318.

Ponthot, J.P., 2002. Unified Stress Update Algorithms for the Numerical Simulation of Large Deformation Elasto-plastic and Elasto-viscoplastic Processes. International Journal of Plasticity (18) pp. 91 – 126.

Pijlman, H., 2001. Sheet Material Characterization by Multi-axial Experiments. Ph. D. Thesis, University of Twente.

Rauch, E. F., 1998. *Plastic Anisotropy of Sheet Metals determined by Simple Shear Tests*. Material Science and Engineering A241, pp. 179-183.

Rauch, E. F., 1989. *Flow Localization Induced by a Change in Strain Path in Mild Steel*. Materials Science and Engineering A111, pp. 71-80.

Rauch, E. F., Schmitt, J. H., 1989. *Dislocation Substructures in Mild Steel Deformed in Simple Shear*. Materials Science and Engineering, A113, pp. 441-448.

Rauch, E. F., Thuillier, S., 1993. *Rheological Behaviour of Mild Steel under Monotonic Loading Conditions and Cross-loading*. Material Science Engineering, A164, pp. 255-259.

Remy, M., Castagne, S., Habraken, A. M, 2002. *Progress in Microscopic Modeling of Damage in Steel at High Temperature*. International Journal of Forming Processes (5) n° 2-3-4, pp. 445 – 455.

Schmitt, J.-H., Aernoudt, E., Baudelet, B., 1985. *Yield Loci for Polycrystalline Metals without Texture*. Mater. Sci. Eng. (75) pp. 13 – 20.

Teodosiu, C., Hu, Z., 1995. *Evolution of the Intragranular Microstructure at Moderate and Large Strains*: Modelling and Computational Significance. Simulation of Material Processing: Theory, Methods and Applications, Shen & Dawson (Eds) © 1995 Balkema, Rotterdam. ISBN 90 5410 553 4, pp. 173-182.

Teodosiu, C., Hu, Z., 1998. *Microstructure in the Continuum Modelling of Plastic Anisotropy*. Proceedings of the 19th Riso International Symposium on Materials Science: Modelling of

Structure and Mechanics of Materials from Microscale to Product. Ed. J.V. Carstensen, T. Leffers, T. Lorentzen, O.B. Pedersen, B.F. Sorensen and G. Winther. Riso National Laboratory, Roskilde, Denmark, pp. 149-168.

Van Bael, A., 1994. Anisotropic Yield Loci Derived from Crystallographic Data and their Application in Finite-element Simulations of Plastic Forming Processes. Ph.D. Thesis, Katholieke Universiteit Leuven.

Van Houtte, P., Li, S., Seefeldt, Delannay, L., 2005. *Deformation Texture Prediction: from the Taylor Model to the Advanced Lamel Model.* International Journal of Plasticity (21) pp. 589 – 624.

Wang, J., Wagoner, R. H., 2004. *A New Hexahedral Solid Element for 3D FEM Simulation of Sheet Metal Forming*. Proc. of the 8th Numiform conference (2004) 712, Issue 1, pp. 2181 – 2186.

Winters, J., 1996. Implementation of a Texture-based Yield Locus into an Elasto-plastic Finite Element Code. Application to Sheet Forming, Ph.D. Thesis, Katholieke Universiteit Leuven.

Yoon, J. W., Barlat, F., Chung, K., Pourboghrat, F., Yang, D.Y., 2000. *Earing Predictions based on Asymmetric Nonquadratic Yield Function*. International Journal of Plasticity (16) pp. 1075 – 1104.

Zhu, Y. Y., Cescotto, S., 1992. *A Fully Coupled Elastoplastic Damage Modeling of Contact-impact between two Deformable Bodies. Structures under Shock and Impact.* II, Computational Mechanics Publications, P.S. Bulson, T. Telford (Ed.), pp. 113 – 133.

Zhu, Y. Y., Cescotto, S., 1994. *Transient Thermal and Thermomechanical Analysis by FEM*. Computers and Structures, 53 (2) 275 – 304.

Zhu, Y. Y., Cescotto, S., 1995. *Unified and Mixed Formulation of the 4-node Quadrilateral Elements by Assumed Strain Method: Application to Thermomechanical Problems.* International Journal of Numerical Methods in Engineering (38) pp. 685 – 716.

Zu, H., Rauch, E. F., Teodoisu, C., 1992. *Work-hardening behavior of mild steel under stress reversal at large strains*. International Journal of Plasticity (8) pp. 839 – 856.